



University of
Strathclyde
Glasgow

Centre for Doctoral Training in Medical Devices and
Health Technologies.
Department of Biomedical Engineering.

**Development of a modular microfluidic
platform for customisable *in vitro*
neuroscience models.**

Daniel Jackson Megarity

A thesis submitted in partial fulfilment of the requirements for
the degree of Doctor of Engineering.

2022

Declaration of authorship

This thesis is the result of the author's original research. It has been composed by the author and has not been previously submitted for examination which has led to the award of a degree.

The copyright of this thesis belongs to the author under the terms of the United Kingdom Copyright Acts as qualified by University of Strathclyde Regulation 3.50. Due acknowledgement must always be made of the use of any material contained in, or derived from, this thesis.

Signed: 

Date: 01st December 2022

Acknowledgements

To begin, I would like to thank my supervisors, Dr Michele Zagnoni and Dr Trevor Bushell, for the opportunity to complete this project and for their thorough advice, guidance and patience. I would like to thank the EPSRC and the CDT in Medical Devices and Health Technologies for providing the funding to complete this project, and to Carol McInnes, for all her help throughout.

I would like to thank everyone in the CMP for their friendship and support, and in particular the Microfluidics group – Ellis, Karla, Panicha, Sarah and Theresa – for their reassurance, encouragement and entertainment throughout my 3.5 years with them. It was a pleasure to work in such great company.

A special thanks to my flatmate and fellow EngD Daniel, for his friendship and support, and for keeping me sane throughout our 3 years living together. Thanks also to all my other close friends in Glasgow (particularly Clodagh, Lily, Mairi and Andrew) for making my time here a great experience. Finally, a massive thank you to my parents, Brian and Wendy, for their constant support and encouragement throughout my studies, without which I would never have gotten to where I am today.

Abstract

Central nervous system (CNS) disorders are the major public health problem in the developed world, leading to a huge societal and economic burden. These disorders are only set to increase given their long-term impact and the growing and ageing population. An increased understanding of the CNS under physiological and pathophysiological states is therefore essential to tackle the problem. However, many animal models have limited translational value, whilst traditional *in vitro* techniques fail to replicate the complex *in vivo* microenvironment. Conversely, microfluidic and organ-on-chip technologies can offer an opportunity to develop more physiologically relevant *in vitro* models of the CNS. These enable more precise cellular patterning and more complex network formation, ultimately providing enhanced experimental capabilities. Whilst microfluidic technology has been well established within neuroscience over the past two decades, there remains limited uptake outside labs with specialist microfabrication facilities required. Further, whilst there are some commercially available devices, there is limited customisable and reconfigurable options, restraining their potential. To increase the uptake and improve ease-of-use of the microfluidic technology, it must be readily accessible, without the need for additional complex equipment, and it must be user-friendly and reliable. A modular platform is therefore proposed, enabling user-defined device production with more flexibility to meet the needs of the individual. In this thesis a modular platform was developed consisting of multiple, individual microfluidic units that combine via a protrusion-intrusion interface on a pressure sensitive adhesive film. This allows components to be assembled in a user defined manner, enabling the creation of bespoke culture environments, making the technology customisable and appealing to novice users. Proof-of-concept experiments demonstrated functional connectivity between environmentally isolated hippocampal cultures across modules, alongside some example applications. This platform presents an opportunity to increase experimental capabilities in neuroscience, enabling the creation of bespoke circuits, and ultimately aid the development of novel therapies.

Contents

Declaration of authorship	1
Acknowledgements	2
Abstract	3
Contents	4
Figures	8
Abbreviations	17
Chapter 1. Background and introduction.	18
1.1. The human brain and nervous system.	18
1.1.1. Cellular components in the CNS.	18
1.1.1.1 Neurons.....	18
1.1.1.2. Glial cells.	19
1.1.2. Communication between neurons.	20
1.1.2.1. Action potential.....	20
1.1.2.2. Signal transmission at the synapse.....	21
1.1.3. Neuronal networks provide the basis for brain function.	23
1.2. CNS disorders.	25
1.2.1. Common disorders	26
1.2.1.1. Alzheimer’s disease.....	26
1.2.1.2. Parkinson’s disease.....	26
1.2.1.3. Epilepsy.....	27
1.2.2. Drug development for CNS disorders.	27
1.2.3. The blood-brain barrier.	28
1.2.4. The need for improved <i>in vitro</i> modelling.	29
1.2.4.1. Hippocampal neuronal cultures as a model system.	32
1.3. Microfluidic technology and its use in neuroscience.	33
1.3.1. Microfluidic device production.	33
1.3.2. Compartmentalised devices for neuroscience research.	34
1.3.2.1. Axonal isolation.....	35
1.3.2.2. Co-cultures and network studies.....	37
1.3.2.3. Disease models.....	38
1.3.3. 3D microfluidic cultures.	39
1.3.4. <i>In vitro</i> blood-brain barrier.	41
1.3.5. Analysis of neuronal cultures in microfluidic devices.	44
1.3.5.1. Immunocytochemistry and fluorescence imaging.	44
1.3.5.2. Electrophysiology and interfacing with microelectrode arrays (MEA).	46
1.3.5.3. Calcium (Ca ²⁺) imaging.....	47

1.3.6. Remaining challenges constraining microfluidic use.	49
1.4. Modular microfluidics.....	50
1.4.1. Existing modular microfluidic technology.	51
1.4.2. Body-on-a-chip devices.....	55
1.5. Project motivations and objectives.....	56
1.5.1. Thesis outline.....	58
1.5.2. Publications.	59
1.5.2.1. Journal articles.	59
1.5.2.2. Conference presentations.....	59
Chapter 2. Materials and methods.....	60
2.1. Materials.....	60
2.1.1. Equipment and materials.....	60
2.1.2. Chemicals and reagents.....	60
2.2. Microfluidic systems.....	62
2.2.1. Design.....	62
2.2.2. Master wafer fabrication.	63
2.2.3. Soft lithography.	64
2.2.4. Irreversible plasma bonding.....	65
2.2.5. Reversible bonding.	66
2.3. Production of modular components.....	66
2.3.1. Lego®-like modular platform.....	67
2.3.2. Press-fit PDMS-PMMA modular platform.....	68
2.3.3. Protrusion-intrusion interfacing modular platform.....	69
2.3.3.1. Double-casting procedure for enclosed interfaces.....	69
2.3.3.2. Assembly on glass slides.....	70
2.4. Device preparation for cell culture.	71
2.4.1. Priming devices using oxygen plasma.....	71
2.4.2. Priming devices using 70% ethanol.	72
2.5. Neuronal cell culture in microfluidic devices.....	72
2.5.1. Hippocampal dissection and cell isolation.....	72
2.5.2. Seeding devices with cells.....	73
2.5.3. α -synuclein pre-formed fibril seeding.....	74
2.6. Cell viability.	74
2.7. Immunocytochemistry.....	75
2.8. Ca^{2+} imaging.....	75
2.8.1. Microscope set up.	76
2.8.2. Ca^{2+} imaging protocols.	76
2.8.3. Ca^{2+} imaging analysis.	77

Chapter 3. Modular microfluidic platform development.	78
3.1. Introduction	78
3.2. PSA film substrates for reversible PDMS bonding and primary hippocampal cultures.	81
3.2.1. PSA and PDMS bonding.	81
3.2.2. Cell growth and functionality on PSA films.	82
3.2.2.1. Cell viability	82
3.2.2.2. Cell growth on the ThermalSeal® RTS film.	83
3.2.2.3. Cell functionality and network connectivity in cultures grown on the ThermalSeal® film.	86
3.3. Modular device production and assembly.	88
3.3.1. Lego®-like design.	88
3.3.1.1. PDMS blocks cast in 3D printed moulds.	89
3.3.2. Press-fitting design with acrylic enclosures.	91
3.3.3. Protruding tabs for interfacing modular components.	93
3.3.3.1. Laser-cut acrylic moulds to produce PDMS blocks with protrusions and intrusions.	93
3.3.3.2. Initial proof of concept of the protrusion-intrusion interfacing design.	94
3.3.3.3. Testing the robustness of the protrusion-intrusion interfacing with set parameters.	95
3.4. Discussion.	100
3.4.1. Cell growth and functionality.	100
3.4.2. Modular device assembly.	101
3.4.2.1. Lego®-like design.	101
3.4.2.2. Press-fitting design with acrylic enclosures.	102
3.4.2.3. Protruding tabs for interfacing modular components.	102
3.5. Conclusion.	104
Chapter 4. Modular devices for neuronal network formation.	106
4.1. Modules for neuronal network formation.	106
4.1.1. Double casting for enclosed modular interfaces.	106
4.1.2. Resultant PDMS modules.	107
4.2. Modular assembly and device production.	109
4.3. Primary hippocampal culture in modular devices.	114
4.3.1. Cell seeding in the different modules.	114
4.3.2. Primary hippocampal cultures in ethanol treated devices.	115
4.4. Design and production evaluation.	117
4.5. Discussion.	120
4.5. Conclusion.	122
Chapter 5. Research capabilities of the modular platform for neuroscience.	126

5.1. Connectivity and functional synaptic communication across the modular interface.	126
5.1.1. Functional synaptic connectivity across multiple modular interfaces.	128
5.2. Modular devices as tools to study neurodegenerative disease mechanisms <i>in vitro</i>.	135
5.3. Controlling neurite outgrowth to produce defined network connectivity.	137
5.4. Multi-module configurations for more complex <i>in vitro</i> models.	139
5.5. Discussion.	142
5.6. Conclusion.	145
Chapter 6. General discussion and evaluation.	146
6.1. Main thesis outcomes.	146
6.1.1. A substrate for reversible PDMS bonding and primary hippocampal cultures.	146
6.1.2. Modular components for reversible assembly.	147
6.1.3. Microfluidic priming in the absence of oxygen plasma.	148
6.1.4. Functional neuronal connectivity and disease modelling in modular devices.	149
6.2. Future work.	151
6.2.1. Fabrication and device preparation.	152
6.3. Conclusion.	158

Figures

Figure 1.1. Schematic highlighting the cellular components in the CNS. (A) Structure of a single neuron and (B) the glial cells surrounding a neuron. Image in (B) from ⁶..... 19

Figure 1.2. Schematic highlighting the sequence of events at the synapse upon arrival of an action potential. (1) Upon depolarisation, voltage gated calcium channels are opened, causing an influx of Ca^{2+} . (2) In response, synaptic vesicles can bind to the presynaptic membrane and neurotransmitters are released into the synaptic cleft. (3) Upon neurotransmitter binding with their receptors, changes in membrane permeability permit ion exchange, and a post synaptic potential is generated. (4) Whether an action potential is generated or not depends on whether the signal is excitatory or inhibitory. As a result, the signal is transmitted from the presynaptic neuron to the postsynaptic neuron. Action of the G-protein linked metabotropic, and the ionotropic receptors can also be seen on the postsynaptic membrane, with the activation of ionotropic receptors causing direct opening of ion channels. 22

Figure 1.3. Reconstructing neuronal networks is essential for better understanding of brain function and dysfunction. (A) The hippocampus formation is implicated in various disorders including (i) Alzheimer's disease and (ii) depression. Whilst one particular subregion may be implicated initially (EC in (i) and Sub in (ii)), the connectivity between regions (arrows) can lead to effects elsewhere. Figure recreated with permission from ³⁴. (B) An in vitro model of the basal ganglia (BG) circuit has been developed as a tool to better understand neurodegenerative disorders and for eventual pre-clinical drug screening. Figure recreated from ⁴³ (open access). (C) An in vitro model of the prefrontal cortex (pfCx), hippocampus and amygdala circuit demonstrated variable cell behaviour when cells from differed regions were cultured separately to when cultured as part of a network. Figure recreated with permission from ⁴⁴..... 24

Figure 1.4. Schematic of the blood-brain barrier. (A) Cellular organisation and (B) structure of the BBB, with the tight junction creating the main barrier to transport across it. Image recreated with permission from ⁸³..... 29

Figure 1.5. The most common microfluidic devices used in neuroscience research consist of two isolated culture chambers interconnected by a series of microchannels. (A) Schematic highlighting (i) a two-chamber compartmentalised device based on the Taylor design. Each culture chamber is connected to an inlet and outlet well, with (ii) a microchannel array between each culture chamber that isolates the somas and only permits the growth of neurites. (C) Image taken with permission from ¹²⁴ showing neurite outgrowth in microchannels of increasing lengths when cells were seeded in the left culture chamber. MAP2 staining shows dendrites while tau staining shows axons and demonstrates how increasing the microchannel length restricts connections between chambers to axonal connections only... 35

Figure 1.6. Microchannels between culture compartments enable the creation of distinct microenvironments. (A) Image taken with permission from ¹²² to demonstrate environmental isolation. Fluorescein was added to the neuritic side, with a hydrostatic pressure gradient from the somal side preventing leakage or diffusion of fluorescein. Fluorescein isolation in the neuritic side was maintained after (i) 1 and (ii) 15 hours. (iii) A graph of normalised fluorescence intensity against time, indicating no leakage of fluorescein between the two compartments. (B) Image reproduced with permission from ¹³⁶ shows the process of axotomy using vacuum aspiration through a central channel across the microchannels and the neurites (i) prior to axotomy and (ii) following axotomy. 36

Figure 1.7. Diode and tapered microchannels allow for more defined and organised network architecture in microfluidic devices. (A) Tapered microchannels have been used to recreate the basal ganglia circuitry: (i) schematic of the circuit showing directionality of neurites dictated by the orientation of tapered microchannels; (ii) schematic of the device for recreating the circuit, showing the different regions; (iii) a representative example of a PDMS device seeded with the desired cells and stained with DAPI (blue) and β III-tubulin (green).

Images reproduced with permission from ⁴³. (B) More complex microchannel geometries can also be used to define axonal outgrowth: (i) schematic demonstrating how the shapes can control the growth direction, with (ii) examples including triangular, zigzag and spine-like structures. These are orientated to encourage growth from the source to the target chamber. Images taken from ¹³⁸ (open access: CC BY 4.0)..... 38

Figure 1.8. Phase guides and micropillars are used to create microenvironments for 3D cell culture in microfluidic devices. (A) Schematic of a device utilising a phase guide to contain the injected gel within the desired channel. This small barrier reduces the capillary pressure to contain the gel-air interface meniscus prior to polymerisation. Image taken from ¹⁶³ (CC BY 4.0). (B) Schematic of a device that uses equally spaced posts to contain the gel within its channel. The pressure difference between the channel and the gaps prevents the gel escaping into the adjacent channel. Image taken with permission from ¹⁶⁴..... 40

Figure 1.9. A simple, 2D microfluidic in vitro BBB model (SyM-BBB). Figure recreated with permission from ⁸². (A) Schematic of the device highlighting the different regions and features. (B) Results from a permeation assay using FITC-Dextran in 3 different device conditions, from L-R: device had no endothelial cells (ECs) seeded in outer channel; device had ECs in outer channel but not astrocyte conditioned media (ACM) in central chamber; device had both ECs in outer channel and ACM in central chamber. The reduced presence of FITC-Dextran in the central chamber of the right-most condition indicates less permeation through the ‘barrier’ and so tight junction formation. Scale bars show 500 μm 42

Figure 1.10. A microfluidic in vitro BBB model has been created to investigate the effects of neurodegenerative disease on its integrity. Images taken from ¹⁶⁹(open access: CC BY 4.0). (A) A schematic of the device showing the layout and composition of the channels. (B) A permeability assay using FITC-dextran showed a significant increase in permeability of the barrier in the AD model. (C) Immunofluorescent staining showed a decrease in expression of tight junction proteins in the AD model, indicating disruption to the barrier. (D) The neurotoxic effects of thrombin were more prevalent in the AD model, confirming the disrupted barrier enables increase permeation of this and subsequent increased cell death. (E) The restorative effects on the barrier of the drug Etodolac were confirmed with a decrease in permeability following treatment vs untreated controls (DMSO). (F) Etodolac treated AD models also showed a decrease in cell death following application of thrombin, confirming restorative effects on the barrier. For B-F, * = $p < 0.05$, ** = $p < 0.01$, *** = $p < 0.001$, **** = $p < 0.0001$ 43

Figure 1.11. Immunofluorescent staining allows visualisation of the cell networks formed and indicates the proteins and structures present. (A) Cellular networks formed within microfluidic culture chambers separated by microchannel arrays, where neurites (green, β III-tubulin) cross between chambers while astrocytes (GFAP, red) do not. (B-D) Immunocytochemistry also enables visualisation of the neurites within microchannels (green, β III-tubulin) and subsequently the presence of synaptophysin (red), which can indicate synapse formation between cell populations. A & B taken from ¹²⁵ (open access: CC BY 4.0) and C & D taken with permission from ¹³⁴. Scale bars = (A) 100 μm and (B) 20 μm 45

Figure 1.12. Interfacing microfluidic and MEA technology enables stimulation/recording of whole cell population activity as well as spatially and temporally controlled stimulation/recording. (A) Primary rat hippocampal cells cultured on a 3Brain MEA platform. Electrodes shown by black squares, β -III tubulin stained green, and neuron nuclei/NeuN stained red. (B) Structural connectivity of the neuronal network developed, showing a high degree of connectivity and branching between the cells. (C) Example of PDMS microfluidic device and MEA platform for improved spatial and temporal manipulation. A-B taken from ¹⁷⁹ (open access CC BY 4.0) and C taken with permission from ¹⁸⁰..... 46

Figure 1.13. Ca^{2+} -sensitive dyes enable the analysis of calcium mediated signalling in neuronal populations cultured in microfluidic devices. (A) Under fluorescence microscopy, the intensity of the dye changes in response to stimulation. The bright white spots

highlighted in a and b represent regions of interest corresponding to the neuron/astrocyte soma. (B) Fluorescence intensity trace for a single neuron, showing an increase in intensity following both indirect (KCl') and direct (KCl) stimulation. C) Analysis confirmed that both neurons and astrocytes show significantly increased frequency of calcium events following indirect stimulation using glutamate (G') compared with direct vehicle (V') application. * = $p < 0.05$, *** = $p < 0.001$. Images taken with permission from ¹³⁴. 48

Figure 1.14. Microfluidic assembly blocks provide a good example of interlocking between modular components. (A) Improved MAB concept from ¹⁹⁹ showing (i) individual component layout, (ii) an example of an assembled device and (iii) the silicon mould used to speed up production of the PDMS modules. Images taken with permission from ¹⁹⁹. (B) Recent example of modular PDMS components from ²⁰⁰ showing (i) a schematic of a building block with lateral tongue/groove mechanism and male/female connection for stacking, and (ii) representative examples of PDMS blocks of different footprints. Scale bar shows 2 mm. Images taken from ²⁰⁰ (open access CC BY 4.0). 52

Figure 1.15. Lego® has inspired multiple modular microfluidic designs due to its accessibility, consistency between components and ease of use. (A) PDMS blocks have been produced based on the dimensions of a 2x2 Lego® brick. (i-ii) Representative example of a PDMS cast, with studs for 3D interfacing and small intruding tabs for 2D interfacing. (iii-iv) Example 3D device assembled using the PDMS Lego® bricks, with the blue channel running over the red. Images taken with permission from ¹⁹⁸. (B) Existing Lego® have also had channels micromilled directly into their sides then sealed using a transparent adhesive film. (i-ii) Schematic of the platform showing individual blocks assembled into a multifunctional device. (iii) An individual Lego® brick showing the machined channel and an O-ring for a leak-free seal at the interface between adjacent bricks. (iv) Multiple blocks were produced, each with individual functions. Image taken with permission from ²⁰². 54

Figure 1.16. Microfluidic multi-system organ-on-a-chip devices have been developed. (A) Schematic of a 4-system physiome-on-a-chip device. (B) 10-system physiome-on-a-chip device comprised of a 7-system chip (left) and 3-system chip (right), each with a mixing well for linking the separate cultures, connected via tubing. Image recreated from ²¹⁷ (open access CC BY 4.0). 56

Figure 2.1. Example photomasks used to create devices in a two-layer photolithography process. (A) An example of an acetate mask (well and culture chambers) and glass-chrome mask (microchannels) overlaid to show the positions of the microchannels. Red circles indicate alignment features. (B) The length of microchannels in the glass-chrome mask was 7.5 mm, as opposed to the desired 500 µm between culture chambers. This allows for misalignment of the acetate mask on top and allows multiple designs to work with one glass-chrome mask layout. 62

Figure 2.2. Schematic representation of the photolithography procedure for patterning microfluidic features in SU8. (A) The photolithography two-stage process of SU8 deposition. (i) The first layer is patterned onto the silicon wafer then (ii) the second layer is aligned on the first layer and (iii) the final SU8 pattern can be hard baked and silanised prior to soft lithography. (B) First layer of SU8 on the silicon wafer, representing the microchannels. (C) Second layer of SU8 aligned on the first layer to form the channel and well features. 64

Figure 2.3. Schematic representation of the soft lithography procedure for producing PDMS devices and plasma bonding to glass. (A) Schematic of the soft lithography process. (i) PDMS was cast on the silicon wafer and once cured, (ii-iii) the device cut to size ready for bonding. (B-C) Schematic showing (B) the PDMS on the wafer and (C) individual devices cut from the cured PDMS. (D) To permanently bond devices, (i) the PDMS and a glass coverslip were exposed to oxygen plasma and (ii) brought into contact, forming an enclosed microfluidic device. 65

Figure 2.4. Schematic representation demonstrating moulding of PDMS on silicon wafers for more consistent device shape and size. (A) The mould was (i) clamped to the silicon wafer and (ii) PDMS was poured into the holes. After curing, the mould was removed

from the wafer, with (B) individual devices dislodged from the mould and wells biopsy punched as before. 67

Figure 2.5. Schematic of the various methods tested for developing a modular platform.

(A) The initial Lego[®]-like design consisted of (i) PDMS blocks with stud holes for (ii) assembling on a studded baseplate. (B) The second design used the same PDMS blocks, but these were press-fit into acrylic enclosures. (C) The final design consisted of protruding tabs, either as (i) a protrusion or (ii) an intrusion for (iii) interfacing as a complete device. 68

Figure 2.6. Schematic representation of the doubling casting for producing PDMS modules with an enclosed interface.

Mould 1 contained the protrusion-intrusion layout to match the SU8-silicon wafer, while mould 2 contained the footprint to build wells only. (A) Mould 1 was clamped to the wafer, with (B) PDMS cast in the holes, degassed and cured for 30 minutes. (C) Mould 2 was aligned on top of mould 1 and re-clamped. (D) Degassed PDMS was poured to fill the holes formed by the sandwiched moulds and cured for 3 hours before demoulding the formed modules. (E) Finally, modules were dislodged from the moulds, with wells biopsy punched and excess PDMS trimmed. 70

Figure 2.7. Schematic representation of device assembly on glass slides using a double-sided adhesive tape.

A glass substrate improves structural stability of modular devices assembled on the ThermalSeal[®] PSA. (A) To create the stable substrate (i) the 3M 96042 double-sided tape was bonded to a glass-slide followed by (ii) the ThermalSeal[®] single-sided PSA as the culture substrate (iii) to form the base. (B) (i) Modules were then bonded sequentially (ii-iii) to create the desired device configuration. 71

Figure 2.8. Schematic representation of the Ca²⁺ imaging experiment in 2-chamber devices, highlighting fluidic/environmental isolation.

(A) All wells have the same volume of HBS at the beginning of the experiment. (B) A fluidic imbalance is created by removing solution from right side wells, this becomes the direct side (A side). (C) Glutamate was added to the top right well and the fluidic imbalance prevents it diffusing into the indirect side. (D) KCl (grey) was added to the top left well (B side). 77

Figure 3.1. Schematic of the various methods tested for developing a modular platform.

(A) The initial Lego[®]-like design consisted of (i) PDMS blocks with stud holes for (ii) assembling on a studded baseplate. (B) The second design used the same PDMS blocks, but these were press-fit into acrylic enclosures. (C) The final design consisted of protruding tabs, either as (i) a protrusion or (ii) an intrusion for (iii) interfacing as a complete device. 80

Figure 3.2. Hermetic PDMS-PSA sealing was confirmed using the fluorescent compound calcein.

(A) Calcein remained within the device channels (green), confirming a sufficient seal between PDMS and the ThermalSeal[®] PSA film. (B) Microchannels remain open and are not blocked by the pressure applied for bonding. Scale bars show 250 μm 82

Figure 3.3. PSA substrates enable the growth of healthy primary hippocampal cultures.

(A-B) Representative images of hippocampal cultures grown in one device bonded to the ThermalSeal[®] film and stained with PI (red) and Hoechst (blue). Whilst both images are from the same device and the same culture, the viability calculated in images varied from (A) 94.9% to 43.9%. (C-E) Representative brightfield images of cells in devices plasma bonded to (C) glass, (D) bonded to the ThermalSeal[®] RTS PSA, or (E) bonded to the ARseal[™] 90880 PSA after 10 DIV. Image in (E) demonstrates the poor imaging associated with the adhesive layer in the ARSeal[™], with bubbles present on its surface. (F) Cell viability was comparable after 14 DIV when grown on the various substrates. Scatter chart shows mean \pm S.E.M. Scale bars = 100 μm 84

Figure 3.4. Primary hippocampal cultures seeded in monolithic devices bonded to the ThermalSeal[®] RTS film are healthy with normal growth and morphology after 13 DIV.

(A) Cellular distribution is evident throughout culture chambers. (B) β III-tubulin staining shows neurite growth (green) through microchannels, with no evidence of astrocytic processes (red) beyond the channel entrances. (C) growth of both neurons and astrocytes forming intertwined networks in the hippocampal cultures. Green = β III-tubulin, red = GFAP and blue = DAPI. Scale bar shows 200 μm 85

Figure 3.5. Staining in microchannels revealed synaptic vesicle formation in primary hippocampal cultures seeded in monolithic devices on the ThermalSeal® film. (A-B) synaptophysin staining (orange) indicates synaptic vesicle formation within the neurites crossing the microchannels, evident by punctate staining (white arrows). Green = β III-tubulin, red = GFAP, orange = synaptophysin. Scale bar shows 100 μ m.	86
Figure 3.6. Hippocampal cultures grown in monolithic devices bonded to the ThermalSeal® PSA film are functional and synaptically connected. (A) The Fluo-8 AM Ca^{2+} -sensitive dye highlights cellular network formation and neurite outgrowth after 14 DIV. (i) Intracellular calcium can be seen in both cell somas and their processes, with (ii) neurites entering microchannels to enable connectivity between compartments. Scale bars = 200 μ m. (B) The increase in Ca^{2+} events in response to G (applied to chamber A, blue) and KCl (applied to chamber B, black) after 10-12 DIV indicates cells are functional and synaptic communication occurs between environmentally isolated hippocampal cultures. Scatter chart shows mean \pm S.E.M., n = 116 cells in chamber A (blue) and 82 cells in chamber B (black) of 3 devices from 3 separate cultures. A one-way ANOVA with Tukey's multiple comparison's test was used to compare values. **** = p < 0.0001 vs baseline.	87
Figure 3.7. A Lego®-like method failed to produce a watertight seal at the interface between modules. (A) PDMS blocks assembled into two-chamber devices on a baseplate with (i) 2 mm diameter studs and (ii) 1 mm diameter studs prior to pipetting food dye into wells. (B) Representative examples of multi-module devices following the addition of food dye on (i) a baseplate and (ii) after being removed from the baseplate. All configurations failed to seal, with leakage at the interface between adjacent modules. (C) Representative examples showing (i) the rough, layered surfaces of 3D printed modules that failed to seal fully at the interface both (i-ii) between PDMS modules and (i, iii) to the PSA film. Scale bars = 5 mm.	90
Figure 3.8. Laser cutting provided more consistent feature sizes than 3D printing. The three materials used were 3D printed resin, laser cut acrylic and milled acrylic. Scatter plot shows mean \pm SD with n \geq 20 for each condition. Grey dashed line indicates nominal width as set in drawing files.	91
Figure 3.9. Moulded PDMS blocks press-fit into laser cut PMMA did not produce watertight seals. Examples of press-fit modules in the acrylic enclosures showing a lack of seal between PDMS and acrylic, with dye present around the interface. (A-B) two-chamber device configuration assembled from 2 modules and (C-D) two-chamber device configuration assembled from 3 modules.	92
Figure 3.10. Schematic highlighting the interference fit condition between protrusions and intrusions. (A) Schematic to show that an interference or press-fit condition is achieved when P > I. (B) A nominal width of 6 mm for both protrusions (P) and intrusions (I) resulted in a large 'overlap' of between 0.33 and 0.64 mm, whereas reducing the nominal protrusion widths to 5.7 mm or 5.8 mm enabled a more stable interference fit of 0 to 0.43 mm. Scatter plot shows mean \pm SD. P = protrusion and I = intrusion. Grey dashed lines indicate nominal dimension given in CAD.	94
Figure 3.11. Protrusion-intrusion interfacing demonstrated leak-free assembly. This method relies on an interference press-fit condition at the interface with conformal PDMS-PDMS bonding. (A-B) Moulded PDMS modules with simple channels to assess feasibility. Red circles indicate where PDMS/vacuum grease may be deposited to seal the system. (C) An example of a perfectly sealed interface, with no fluid escaping the channel. Scale bars show 5 mm.	95
Figure 3.12. Schematic highlighting the parameters identified to help properly test the protrusion-intrusion design. (A) Example mask used to test the protrusion-intrusion system and the effects of the pre-defined parameters. Red outlines indicate the module positions when moulded. (B) Schematic of a device to highlight the parameters – the amount of overlap between protrusion and intrusion (A), the distance between the edges of the channel and the protrusion (B) and the relationship between P and I.	96

Figure 3.13. Laser cutting produces consistent dimensions for a range of nominal values. (A-D) The measured widths remain consistent for each value tested, with (E) a linear regression plot demonstrating an R^2 value of 0.997 indicating the consistency of laser cutting across a range of values. Graphs created using GraphPad Prism and Excel. Scatter plots show mean \pm SD and $n = 6-9$. Grey dashed lines indicate nominal dimension given in CAD. P = protrusion and I = intrusion.	97
Figure 3.14. The effect of the parameters on sealing was assessed in modular protrusion-intrusion devices. Representative examples given of configurations that were (A) sealed, (B) semi-sealed, and (C) not sealed. (D) Values of P-I (amount of overlap at the interface) plotted according to sealing. (E) P/I (ratio between the widths of the protrusions and intrusions) plotted according to sealing. (F) Depth of interface (A, 2/4/6 mm) plotted according to sealing. (G) Distance between channel and edge of protrusion (B, 2/4/6/8 mm) plotted according to sealing. These results represent a range of protrusion/intrusion widths (6-18 mm). Scatter plots show mean \pm SD. Scale bars = 2 mm. ns = non-significant and * = $p < 0.05$ (Y vs N).	99
Figure 3.15. Schematic demonstrating the excess PDMS that runs under moulds. (A) Schematic representation of moulds sitting above SU8. (B) Representative example of cast PDMS modules. Once cured, the excess PDMS requires trimming which can damage the interfacing surfaces. Scale bar shows 5 mm.	104
Figure 4.1. Schematic representation of the interface between protrusion and intrusion modules. (A) The main (i) protrusion and (ii) intrusion modules with widths P and I respectively and (iii) a combined two-module protrusion-intrusion device with enclosed interface. (B) A press-fit condition is achieved if $P > I$	108
Figure 4.2. Representative examples of the four individual PDMS modules moulded in laser cut acrylic. The four main module types include (A) one protrusion, (B) one intrusion, (C) one protrusion and one intrusion combined and (D) four intrusions combined. Scale bars = 5 mm.	108
Figure 4.3. Representative examples of devices using the four module styles in various configurations. Examples include (A) the common two-chamber and (B) three-chamber devices, along with (C) a four-chamber device with modules connected in series. Larger configurations include (D) a five-chamber device, with four modules independently connected to the central intrusion module, demonstrating parallel network formation, and (E) a six-chamber device with modules connected in series. Scale bar = 10 mm.	110
Figure 4.4. Microchannels were not blocked by the adhesive following assembly of modular devices. Results here are for a two-module device that was oxygen plasma treated and the chamber shown is from a protrusion module with integrated microchannels. The calcein was added to the intrusion module to the right of the microchannel array, not shown in these images. (A) Beginning with empty wells, (i) 75 μ l of calcein was added to the top right well followed by the bottom right well. (ii) This caused calcein to flow across the microchannels to the left side. (B) (i) 75 μ l of water was added to the left top well, (ii) causing the gradient to retract. (iii) The water in the left chamber stabilised and the gradient reformed due to the still larger volume on the right side. (C) (i) The top left well was filled with water (ii) forcing the calcein to fully retract due to the larger volume on the left compared with the right. Scale bars = 100 μ m.	111
Figure 4.5. Well imbalances between culture chambers were maintained over the course of 30 minutes. Calcein was added to chamber 1 (target chamber) and a fluorescent image taken (A) immediately and after (B) 30 minutes. Images with (top) and without (bottom) brightfield. (C) Fluorescence intensity chart across the 2 chambers initially (blue) and after 30 minutes (orange). This highlights that there was no increase in fluorescence in chamber 2 and a reduction in chamber 1, indicating that passive flow does not occur from target to non-target chambers. Dashed white/black line indicates location of modular interface and beginning of microchannel region whilst solid line indicates end of microchannel region and beginning of chamber 2. Scale bars = 500 μ m.	112

Figure 4.6. 70% ethanol is a suitable alternative to oxygen plasma treatment for initiating flow through devices. (A) Beginning with empty wells, (i) 75 μ l of calcein was added to the top right well followed by the bottom right well (ii) forcing calcein to flow across the microchannels to the left side. (B) (i) 75 μ l of water was added to the left top well, causing the gradient to retract. (ii) The water level in the left chamber stabilises and the gradient reforms due to the still larger volume of calcein on the right side. Scale bars = 100 μ m. 113

Figure 4.7. Poor cell adhesion was observed with initial cultures in modular devices that had been primed with ethanol. Primary hippocampal cultures stained after 13 DIV with β III-tubulin shown in green and GFAP shown in red. (A) A two-chamber modular device bonded to PSA film was primed using 70% ethanol followed by addition of PLL for 1 hour. Large cellular aggregates were observed in culture chambers (white solid box) with poor cell distribution overall. White dashed line represents the interface. (B) However, neurites enter microchannels between compartments indicating the modular interface does not pose a barrier to cellular connectivity between components. Scale bars = 200 μ m. 116

Figure 4.8. An increased incubation time with PLL demonstrated improved cellular distribution in modular devices primed with ethanol. Improved cellular distribution throughout culture chambers of both the intrusion (left) and protrusion modules of a two-chamber device, with subsequent neurite outgrowth through microchannels. Green = β III-tubulin and red = GFAP. Scale bar = 500 μ m. 117

Figure 4.9. Priming modular components with ethanol can lead to disruptive bubble formation in culture chambers. (A) Bubble nucleation was observed in the corner of channels at the modular interface, suggesting insufficient sealing. (B) Air gaps were seen forming along the length of culture chambers suggesting surface tension effects also contribute to this problem, with the hydrophobic PDMS repelling the water. Arrows indicate air gaps and bubbles in chambers. Scale bars = 500 μ m. 119

Figure 4.10. Bubble/air gap formation was observed in monolithic devices and modular devices sealed with PDMS. (A) Small bubbles were observed in culture chambers of hermetically sealed monolithic devices. (B) Air gap in a channel of a modular device sealed with PDMS after incubation overnight at 5% CO₂/37°C. This represents a major disruption to flow through the device thus making it unusable. Arrows indicate air gaps and bubbles. Scale bars = 2 mm. 120

Figure 5.1. Healthy growth and morphology of primary hippocampal cultures is observed in 2-module devices. (A) Cellular distribution was evident throughout culture chambers of both the protrusion (left) and intrusion (right) modules, with neurites (B) able to cross the modular interface and (C) grow throughout the microchannels. Green = β -III tubulin, red = GFAP and blue = DAPI. Scale bars = 500 μ m (A) and 100 μ m (B-C). 127

Figure 5.2. Hippocampal cultures grown in modular devices are functional and synaptically connected across the protrusion-intrusion interface. (A) Schematic of a 2-module device. (B) Representative fluorescence intensity traces for a synaptically connected cell in chamber A (blue) and chamber B (black). NFU = normalised fluorescence units. (C) An increase in Ca²⁺ events in response to G and KCl indicates hippocampal cultures are functional and synaptic connectivity occurred between the cultures of separate modules. Scatter chart shows mean \pm S.E.M. n = 223 cells in chamber A and 170 cells in chamber B of 3 separate devices/cultures. **** = p < 0.0001. (D) Representative images during (i) the baseline period; (ii) the period following addition of G to chamber A; and (iii) the period following the addition of KCl to chamber B. White dashed lines indicate boundary between culture chambers and microchannel region in the centre. 128

Figure 5.3. Healthy growth of hippocampal cultures in a 3-module device, with neurites observed across multiple protrusion-intrusion interfaces. (A-C) Uniform neuronal cell distribution throughout the culture chambers of the three individual components. (D) Neurites are again able to cross the modular interface with (E) a presence throughout microchannels

indicating connectivity across the three modules. Green = β III-tubulin, red = GFAP, blue = DAPI. Scale bars = 2 mm (B) and 100 μ m (C-E)..... 130

Figure 5.4. 0 Mg²⁺ HBS induced an increase in calcium response in 2-module devices following an incubation period. (A) Schematic and timeline of the experiment. (B) 0 Mg²⁺ HBS induced continued activity in the directly stimulated chamber A (blue points) and an increase in activity in the synaptically connected chamber B (black points) following an incubation period, which was absent with a control (normal HBS, right). Charts show mean \pm S.E.M., n = 63 cells in direct chamber and 37 cells in the indirect chamber from 1 device loaded with 0 Mg²⁺ and 19 cells in direct chamber and 15 cells in the indirect chamber from 1 device loaded with the control. A one-way ANOVA was used to compare events over baseline period (t = 0 – 2 minutes), the period following addition of the stimulant/control (t = 2 – 10 mins) and the post-incubation period (t = 20 – 30 mins). * = p < 0.05, ** = p < 0.01 and **** = p < 0.0001. (C) Representative images taken during the Ca²⁺ imaging experiment at (i) t = 0 minutes; (ii) t = 2 minutes, after 0 Mg²⁺ HBS addition; (iii) t = 10 minutes; and (iv) t = ~ 20 minutes, following the incubation period. 132

Figure 5.5. Functional synaptic connectivity was observed in 3-module devices. (A) Schematic and timeline of Ca²⁺ imaging experiments in 3-module devices. (B) (i) 0 Mg²⁺ HBS induced increased activity in both chamber 2 (left) and chamber 3 (right) following an incubation period, (ii) which was absent with normal Mg²⁺ HBS..... 133

Figure 5.6. Functional synaptic connectivity was observed across the three chambers in 3-module devices. Increase in Ca²⁺ events in both chambers 2 (green) and 3 (blue) with addition of the 0 Mg²⁺ HBS (0 Mg²⁺, left), compared with normal HBS (HBS, right). Chart shows mean \pm S.E.M., n = 65 cells in chamber 2 and 57 cells in chamber 3 from 2 devices/cultures loaded with 0 Mg²⁺ HBS and 13 cells in chamber 2 and 30 cells in chamber 3 from 1 device/culture loaded with normal HBS. One-way ANOVA used to compare events over the baseline period (t = 0 – 2 mins), the period following addition of the 0 Mg²⁺ HBS/normal HBS (t = 2 – 10 mins) and the post-incubation period (t = 20 – 30 mins). *** = p < 0.001, **** = p < 0.0001, ns = non-significant. 134

Figure 5.7. Modular devices can be used as tools for investigating neurodegenerative disease mechanisms. PFFs were added to one module (red highlighted chamber 1) after 7 DIV, with cells fixed and stained after 14 DIV. Hydrostatic pressure gradients were induced towards the target chamber, ensuring environmental isolation, and preventing flow of PFFs into non-target chambers. 135

Figure 5.8. The addition PFFs induced phosphorylation of α -synuclein in primary hippocampal cells cultured in a modular device. Representative images taken in (A) target chamber (Chamber 1); (B) non-target chamber 2; and (C) non-target chamber 3 of a 3-module device (**Figure 5.7**) 7 days after the addition of PFFs to the target chamber (14 DIV). pSer129 staining in the target chamber indicated internalisation and phosphorylation of α -synuclein fibrils, with subsequent transfer of pathology to a fluidically isolated but synaptically connected non-target chamber 2, evident by both punctate and thread-like features (red). Pathological staining was absent in chamber 3. Red = pSer-129- α Syn and green = β III-tubulin. Scale bars = 100 μ m (top and middle row of images) and 5 μ m (i-vi). (D) Th level of pSyn was calculated as a percentage of the level of β III-tubulin, demonstrating a reduction in the non-target chamber 2 (n = 2 images from each chamber of 1 device). 136

Figure 5.9. Edge-guided microchannels can be used in modular devices to either permit or inhibit neurite outgrowth between culture chambers. (A) Representative (i) brightfield image of PDMS heart-arrow microchannels and (ii) schematic highlighting permissive (green) and inhibitive outgrowth (red). (B) Confirmation of microstructure abilities, with (i) permissive neurite growth in the forward orientation (green) and (ii) inhibited neurite growth in the reverse orientation (red). Red and green = β III-tubulin. White dashed line indicates the modular interface and edge of microchannel region, while solid white line indicates edge of adjacent culture chamber in a 2-module device. Scale bars = 200 μ m (A) and 500 μ m (B). 137

Figure 5.10. The heart-arrow microstructures stalled neurite outgrowth when cells were seeded in the inhibitive chamber. (A) Edge guidance of neurites, highlighting (i) permissive growth with cells seeded in the growth enabling chamber, but (ii) blocking/stalling of neurite growth when cells were seeded in the growth inhibiting chamber. (B) Representative images of the microstructures with cells seeded in the growth inhibiting chamber highlighting where the neurites have been stalled and blocked from crossing the entirety of the microchannel region. Red = β III-tubulin. White dashed line indicates the modular interface and edge of microchannel region, while solid white line indicates edge of adjacent culture chamber. Scale bars = 100 μ m. 138

Figure 5.11. Uniform cell distribution throughout a multi-module 4-chamber device configuration. The modular platform provides greater flexibility to design user-specific devices above monolithic equivalents. Here, all modules are interconnected in series as shown in (A). (B) Uniform cell distribution throughout the individual modules with (C-D) neurites able to cross the modular interface. Red dashed box indicates area imaged. White dashed lines indicate the outline of individual modules. Green = β III-tubulin, red = GFAP. Scale bars = 2 mm (B) and 100 μ m (C-D). 139

Figure 5.12. Parallel cell network formation is possible using the modular platform. In addition to serial connectivity, the modular platform enables the production of devices with modules connected in parallel. Here, a 5-chamber device was produced with 4 protrusion modules each independently connected to a central all-intrusion module as shown in (A). (B) Uniform cell distribution evident throughout all modules and (C-E) neurites can cross the modular interfaces, which enables connectivity between cells of the separate modules. Red dashed box indicates device area imaged. White dashed lines indicate the outline of individual modules. Green = β III-tubulin and red = GFAP. Scale bars in = 2 mm (B) and 100 μ m (C-E). 140

Figure 5.13. Uniform cell distribution with module-module connectivity can be achieved in larger device configurations. The modular platform enables the production of much larger devices, as demonstrated by a 6-chamber device with all modules connected in series, shown in (A). This provides the flexibility to create more complex in vitro networks and subsequent novel assays, beyond that available with typical monolithic equivalents. (B) Uniform cell distribution evident throughout all modules and (C-G) neurites again cross the modular interface enabling connectivity between cells of separate modules. Red dashed box indicates device area imaged. White dashed lines indicate the outline of individual modules. Green = β III-tubulin and red = GFAP. Scale bars = 2 mm (B) and 100 μ m (C-G). 141

Figure 6.1. The Form3 produces more consistent moulds with values closer to the desired width than those produced by laser cutting acrylic sheets. (A) The Form3 printer (left) produces moulds with dimensions closer to the intended values than laser cutting (right). Dashed outlines indicate the intended nominal values. (B) Difference between intended and actual dimensions of protrusions (P) and intrusions (I) using the Form3 and laser cut acrylic. Scatter plot shows mean \pm SD, n = 6-26. 153

Figure 6.2. Schematic representation demonstrating the use thick film resists for creating smaller interfacing regions with improved alignment features. (A) Example mask design for (i) protrusion and (ii) intrusion. (B) PDMS could first be cast directly on the wafer to produce the interfacing features, then (C) further PDMS moulded to build the modules height and integrate open wells for (D) an enclosed device. 154

Figure 6.3. Schematic representation highlighting other features of interest for integrating into the modular platform and increasing the potential applications. This includes (A) more complex edge-guiding patterns with tapering to encourage re-routing and long-term inhibitive outgrowth, (B) micropillars in place of the microchannels to enable 3D culture conditions, and (C) an axotomy channel that runs perpendicular to the straight-edge microchannels to allow an investigation of axonal regenerative properties and response to injury. 157

Abbreviations

AD	Alzheimer's disease
AMPA	amino-3-hydroxy-5-methylisoxazolepropionic acid
AP	Action potential
BBB	Blood-brain barrier
BSA	Bovine serum albumin
CNS	Central nervous system
DALY	Disability-adjusted life years
DIV	Days <i>in vitro</i>
E/IPSP	Excitatory/inhibitory post synaptic potential
EDTA	Ethylene-di-amine tetra-chloro-acetate
FBS	Foetal bovine serum
G/YFP	Green/yellow fluorescent protein
GABA	γ -aminobutyric acid
GFAP	Glial fibrillary acidic protein
GPCR	G-protein coupled receptor
HBS	HEPES-buffered saline
HPMC	Hydroxypropyl methylcellulose
IPA	Isopropanol/isopropyl alcohol
iPSC	Induced pluripotent stem cell
NDD	Neurodegenerative disorder
NFU	Normalised fluorescence unit
NMDA	N-methyl-D-aspartate
PBS	Phosphate buffered saline
PD	Parkinson's disease
PDMS	Polydimethylsiloxane
PFA	Paraformaldehyde
PFF	Pre-formed fibril
PLL	Poly-l-lysine
PLO	Poly-l-ornithine
PMMA	Polymethylmethacrylate
PNS	Peripheral nervous system
PSA	Pressure-sensitive adhesive
ROI	Region of interest
RT	Room temperature
SLA	Stereolithography

Chapter 1. Background and introduction.

1.1. The human brain and nervous system.

The human brain has been described as the most complex object in the universe. It is certainly the most complex organ in our body, with control over our every thought and body process and is unique in its ability to think and feel. It is our consciousness and is responsible for our behaviour, emotions and memory, and ensures we continue to breathe, and our hearts keep beating. The brain is part of the wider nervous system encompassing the central nervous system (CNS) and peripheral nervous system (PNS). The CNS, consisting of the brain and spinal cord, acts as the control centre. It interprets sensory inputs and decides the response based upon the environment and past experiences. The PNS serves as a link between the CNS and the rest of the body, conveying the sensory information to the CNS and relaying its response to the effectors which in turn carry out a defined task. The brain has multiple different regions, working together to carry out the complex functions required of the nervous system. It consists mainly of nervous tissue, which is a highly dense network of cells, with the main functional and structural unit being the neuron. The complexity of the brain is thanks to the huge number of these neurons, estimated at around 86 billion, with trillions of synaptic connections forming complex and tangled networks to create functional circuits^{1,2}. The other cell types within the brain encompass the neuroglia, which are essential for proper neuronal function and provide protection and homeostatic stability.

1.1.1. Cellular components in the CNS.

1.1.1.1 Neurons.

Neurons are highly specialised cells, responsible for communication, in the form of nerve impulses between each other and the rest of the body. They differ from other cell types due to their inability to renew and divide, with no widespread capacity for neurogenesis, however they do have extreme longevity^{3,4}. Many different subtypes exist throughout the brain regions; however, they all have a degree of similarity in how they function. Neurons can broadly be classed as excitatory, inhibitory or neuromodulatory, and the transmission of a signal therefore depends on the neuron subclass involved^{2,5}. All neurons have a cell body or soma, with processes known as dendrites and axons extending from this (**Figure 1.1A**). The dendrites are the main receptive regions, through which incoming signals from other neurons are relayed to the cell soma. Each neuron has multiple dendrites and can interface with many other neurons. However, they each have only one axon which can extend to many different lengths with branches along its surface and numerous terminal branches at the end. The axon is the

conducting region of the neuron and carries the incoming signal between neurons, in the form of an action potential. Each terminal branch ends with a synapse where the arriving action potential causes the release of neurotransmitters or chemical signals, which in turn excite or inhibit surrounding neurons in close contact. This allows the continuation of the signal through the network.

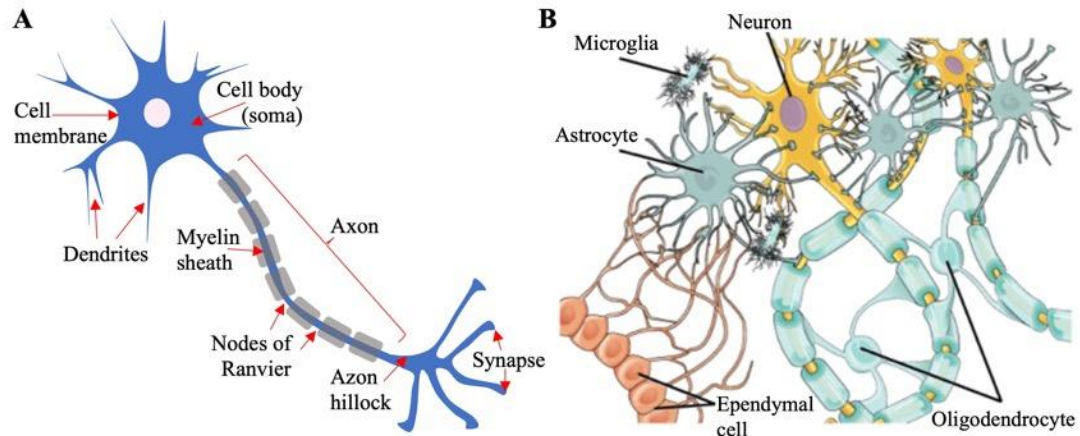


Figure 1.1. Schematic highlighting the cellular components in the CNS. (A) Structure of a single neuron and (B) the glial cells surrounding a neuron. Image in (B) from ⁶.

1.1.1.2. Glial cells.

The neuroglia are much smaller than neurons but make up around half the brains mass, with a similar number of these cells to the neurons ^{1,7}, (**Figure 1.1B**). While the role of neurons is the transmission of nerve impulses, the neuroglia are the supportive cells. Originally thought to function simply as ‘nerve glue’, it is now understood they have a much more important protective role. Glial cells provide nutrient support and maintain homeostasis and are responsible for producing the myelin sheath, which enables saltatory conduction and proper neuronal functioning. The main glia in the CNS are astrocytes, oligodendrocytes and microglia. The microglia function as the innate immune system, providing a protective role by acting as phagocytic cells, which is of vital importance as the blood-brain barrier prevents immune system access to the CNS under healthy conditions ⁸. They monitor the health of neurons, and upon the death of a neuron or invasion by microorganisms, they engulf and destroy the debris. Oligodendrocytes are the myelinating cells of the CNS, forming the myelin sheath around axons to enable saltatory conduction. Cell processes form the sheath by wrapping around the axon in layers, and each axon will have multiple segments of myelin. The spaces between each are the nodes of Ranvier where the ion channels are concentrated, resulting in the signal ‘leaping’ between each, increasing the speed of transmission ⁹. Astrocytes are the most abundant glial cells in the CNS and serve a range of important

functions. They provide anchorage between neurons and nutrient supply lines and help with exchange between the two by altering capillary permeability^{3,10}. Further, they play a role in maintaining the blood-brain barrier and may affect neurodegenerative disease progression, such as Alzheimer's where they been shown to uptake amyloid- β ¹¹. They also have a role in maintaining the extracellular environment by regulating the pH and removing or redistributing extracellular K^+ ¹². Further, they help in regulating synaptic transmission through their ability to uptake glutamate and GABA by direct contact with the synapse, where the two neurons and an astrocyte form a tripartite synapse^{13,14}. Ultimately this helps prevent overstimulation and neurotoxic effects caused by prolonged glutamatergic activity.

1.1.2. Communication between neurons.

The propagation of a signal within and between neurons is a complex process involving changes to the membrane potential and neurotransmitters. Each neuron has a resting membrane potential that can be altered, which is essential to transmit a signal along its axon. The presence of special proteins, called ion channels, on the cell membrane allow the exchange of charged ions between the inside and outside of a cell. This in turn alters the potential across the membrane. The resting membrane potential of a neuron is around -70mV, where the inside of the cell is negatively charged relative to the outside^{3,5,15}. These changes in membrane potential are classed as depolarisation or hyperpolarisation. At rest, there is a high concentration of potassium ions (K^+) inside the cell while outside the cell there is a high concentration of sodium (Na^+) ions, balanced by chloride (Cl^-) ions. The cell membrane is selectively permeable, with a much greater permeability to K^+ than Na^+ and Cl^- , enabling travel through leakage ion channels. Other gated channels open upon changes to the membrane potential (voltage-gated) or upon binding of a neurotransmitter (chemically or ligand-gated). The ATP driven Na^+-K^+ pump maintains the concentration gradient and stabilises the membrane potential¹⁶.

1.1.2.1. Action potential.

An action potential (AP), or nerve impulse, allows the transmission of a signal over a long distance through an axon. An AP is generated upon depolarisation of the cell membrane, that is, the membrane potential becomes less negative. Depolarisation is initiated either in response to neurotransmitters or from another area of the membrane that has already been depolarised. For an AP to be generated, a threshold (~ -55 mV) must be met, and it is an all or nothing phenomenon. Once this is reached, voltage-gated Na^+ channels open, causing an influx of Na^+ ions into the cell, making the interior progressively less negative. This depolarisation causes

the voltage-gated Na^+ channels to close, stopping the entry of Na^+ into the cell, and voltage-gated K^+ channels to open, causing an efflux of K^+ out of the cell. This has the effect of repolarising the membrane to its resting potential, however excessive efflux of K^+ results in a period known as hyperpolarisation ($\sim -90\text{mV}$)^{3,15}. This prevents a new AP being immediately generated in the same area and so the signal is propagated along the length of the axon. The speed of an AP varies throughout the body, with those in neural pathways mediating reflexes, for example, travelling much faster than others. The speed depends on several factors including the diameter of the axon, with wider axons propagating APs faster due to reduced resistance, and the degree of myelination¹⁷. In unmyelinated axons, an AP must be generated at every point along the membrane to prevent the signal decaying. However, in myelinated axons, the myelin sheath acts as an insulating layer around the axon and is split into sections, with nodes of Ranvier between each¹⁸. Ion exchange and subsequently depolarisation can only occur at points where the axon is unsheathed, enabling the APs to propagate rapidly throughout the length of the axon. Indeed, the speed of propagation of impulses in myelinated axons is up to 150 m/s versus around 0.5-10 m/s for unmyelinated axons¹⁹.

1.1.2.2. Signal transmission at the synapse.

The synapse enables signal transfer between neurons, with any one neuron having thousands of connections with other neurons, resulting in 100s of trillions of synapses^{3,20}. The vast majority of synapses are chemical, where the axon terminal of the presynaptic neuron is separated from the postsynaptic neuron by the synaptic cleft. This prevents nerve impulses transmitting directly, and so neurotransmitters fulfil this role. Chemical synapses are either inhibitory, hyperpolarising the postsynaptic membrane, or excitatory, depolarising the postsynaptic membrane. When an AP arrives at the axon terminal, the depolarisation causes voltage-gated Ca^{2+} channels to open, allowing the influx of Ca^{2+} into the terminal (**Figure 1.2**). The Ca^{2+} acts as an intracellular messenger, enabling synaptic vesicles to bind with the axon membrane and release their neurotransmitters into the synaptic cleft²¹. Neurotransmitters diffuse across the cleft to the postsynaptic membrane where they bind to receptors on ligand-gated ion channels. Once bound, the ion channels open, allowing the exchange of ions across the membrane, altering its potential. However, the resulting action depends on the receptor to which the neurotransmitter binds, and the channel controlled. Broadly, there are two main types of receptors, ionotropic receptors and G-protein coupled (GPCR) or metabotropic receptors (**Figure 1.2**). Upon neurotransmitter binding, ionotropic receptors undergo conformational changes that result in direct opening of ion channels. GPCRs bind neurotransmitter

resulting in a signalling cascade and activation of G-proteins that can subsequently alter voltage-gate ion channel permeability and cell excitability.

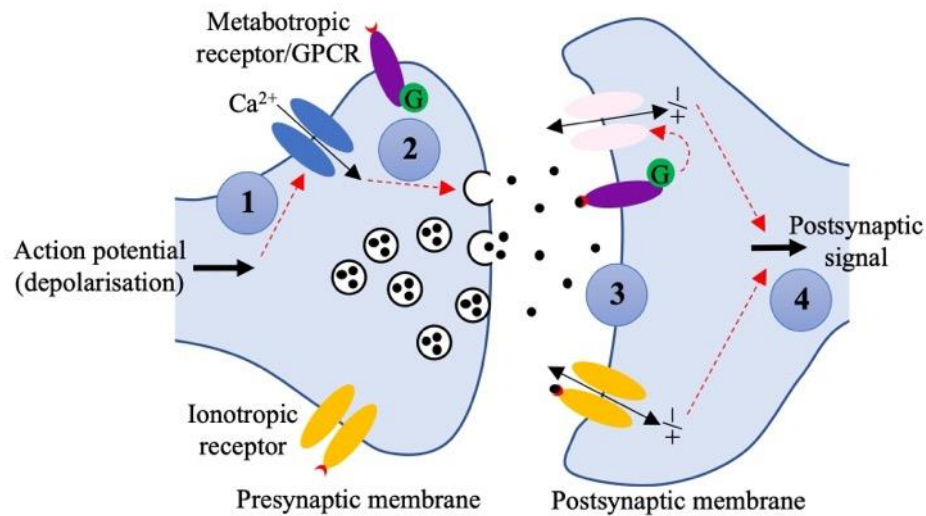


Figure 1.2. Schematic highlighting the sequence of events at the synapse upon arrival of an action potential. (1) Upon depolarisation, voltage gated calcium channels are opened, causing an influx of Ca^{2+} . (2) In response, synaptic vesicles can bind to the presynaptic membrane and neurotransmitters are released into the synaptic cleft. (3) Upon neurotransmitter binding with their receptors, changes in membrane permeability permit ion exchange, and a post synaptic potential is generated. (4) Whether an action potential is generated or not depends on whether the signal is excitatory or inhibitory. As a result, the signal is transmitted from the presynaptic neuron to the postsynaptic neuron. Action of the G-protein linked metabotropic, and the ionotropic receptors can also be seen on the postsynaptic membrane, with the activation of ionotropic receptors causing direct opening of ion channels.

The main excitatory neurotransmitter in the brain is glutamate and in turn, glutamate receptors are responsible for most excitatory synaptic transmission. Ionotropic glutamate receptors include N-methyl-D-aspartate-sensitive receptors (NMDA receptors), amino-3-hydroxy-5-methylisoxazolepropionic acid-sensitive receptors (AMPA receptors), and kainate-sensitive receptors and are located mainly on the postsynaptic membrane⁵. Kainate receptors are also present on the presynaptic membrane and recent evidence points to the presence of NMDA receptors here also^{22,23}. NMDA receptors have the highest affinity for glutamate but activate slower than AMPA receptors. As a result, non-NMDA receptor activation is necessary to depolarise the neuron, in turn allowing activation of NMDA receptors²⁴. Activation of ionotropic receptors opens the ion channels enabling cations to cross the cell membrane, resulting in an influx of Na^+ and efflux of K^+ . Here, as the influx of Na^+ is greater and faster than the efflux of K^+ , a net depolarisation of the membrane occurs initially. If the threshold is

reached, then an excitatory post synaptic potential (EPSP) is generated and, if strong enough, helps generate an AP on reaching the axon hillock ²⁵. Activation of GPCRs modulate ion channel activity through signalling cascades. On the postsynaptic membrane, GPCRs modulate K^+ and Ca^{2+} ion channel activity to induce depolarisation and increase excitability ^{24,26}. On the presynaptic membrane they have been shown to decrease both excitatory (glutamatergic) and inhibitory neurotransmission by inhibiting Ca^{2+} influx through voltage-gated channels and directly preventing exocytosis of synaptic vesicles, subsequently inhibiting neurotransmitter release ^{25,27–29}. GPCRs can also induce a signalling cascade that leads to a release of Ca^{2+} from the endoplasmic reticulum ²⁴.

Conversely, γ -aminobutyric acid (GABA) is the main inhibitory neurotransmitter in the CNS. The main GABA receptors are the ionotropic $GABA_A$ and $GABA_C$ receptors, and the metabotropic $GABA_B$ receptor. On the postsynaptic membrane, $GABA_A$ activation causes the ion channel to open allowing an influx of Cl^- to the cell, lowering the potential and causing hyperpolarisation (inhibitory post synaptic potential/IPSP) ³⁰. This prevents depolarisation, lowering the excitability of the network as the potential moves farther from the threshold and reduces the likelihood of an AP being generated at the axon hillock. $GABA_B$ receptors are found both on the presynaptic membrane and the postsynaptic membrane and are coupled with K^+ and Ca^{2+} ion channels. Binding of GABA results in either activation of postsynaptic K^+ channels, causing an influx and hyperpolarisation to reduce excitability, or inhibition of presynaptic Ca^{2+} channels which reduces presynaptic Ca^{2+} influx and inhibits neurotransmitter release ^{26,28,30}.

1.1.3. Neuronal networks provide the basis for brain function.

As the control centre of our body, organisation within the brain is complex. Billions of neurons and trillions of synapses are arranged into functional networks throughout various structurally and functionally distinct regions ^{2,31–33}. The ability to carry out tasks therefore relies on sufficient circuitry with both excitatory and inhibitory neurons throughout these different areas. Whilst the neuron can be considered the main structural unit, it is these networks that encompass the main functional unit, essential for interpreting and relaying complex information throughout the body. As a result, any dysfunction or disruption of these circuits can lead to an array of disorders. For instance, hippocampal networks have been implicated in a variety of disorders including Alzheimer's disease, epilepsy, PTSD, anxiety and depression. The hippocampal formation is composed of the hippocampus, itself made up of various distinct subregions (CA1, CA2, CA3), along with the dentate gyrus (DG), subiculum and

entorhinal cortex (EC) ^{34,35}. Here, the main input to the hippocampus is via the EC, which connects to the ‘trisynaptic pathway’ where the DG carries the signals to the CA3, the CA1 and finally the subiculum. Further, the EC can also directly connect with the CA3, CA1 and subiculum. Whilst a particular disease may affect a particular subregion, the interconnectivity means that other regions can become affected overtime (**Figure 1.3A**). Further, in Alzheimer’s disease and other neurodegenerative disorders, there is evidence that the pathological features can spread to other regions via synaptically connected networks ^{36–40}. It is therefore essential to look at reconstructed networks as a whole, rather than individual neurons, in order to fully understand brain function in healthy and diseased states and how a particular disorder can spread across regions ⁴¹. Further, the plasticity within the CNS provides a basis for constant change and reorganisation of these networks in response to new events, experiences and injury ⁴². This phenomenon is essential for development, learning and memory.

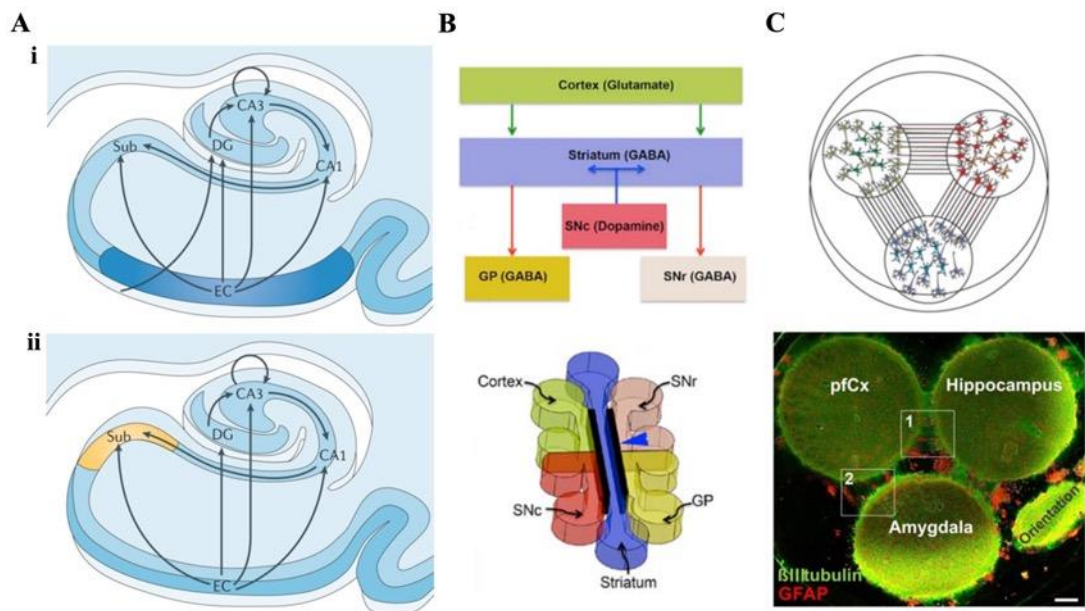


Figure 1.3. Reconstructing neuronal networks is essential for better understanding of brain function and dysfunction. (A) The hippocampus formation is implicated in various disorders including (i) Alzheimer’s disease and (ii) depression. Whilst one particular subregion may be implicated initially (EC in (i) and Sub in (ii)), the connectivity between regions (arrows) can lead to effects elsewhere. Figure recreated with permission from ³⁴. (B) An in vitro model of the basal ganglia (BG) circuit has been developed as a tool to better understand neurodegenerative disorders and for eventual pre-clinical drug screening. Figure recreated from ⁴³ (open access). (C) An in vitro model of the prefrontal cortex (pfCx), hippocampus and amygdala circuit demonstrated variable cell behaviour when cells from differed regions were cultured separately to when cultured as part of a network. Figure recreated with permission from ⁴⁴.

Several studies have investigated the functional activity of neurons derived from different regions, highlighting the diversity between these and the networks produced⁴³⁻⁴⁸. A recent publication demonstrated an *in vitro* basal ganglia (BG) circuit, with distinct placement of the neuronal subtypes and directed connectivity between these to more accurately recreate the precise network connectivity⁴³ (**Figure 1.3B**). They were able to demonstrate functional connectivity between the regions, highlighting the potential of such a development in offering a tool to better understand neurodegenerative disease, given the implication of BG degeneration in such disorders, as well as offering a more relevant platform for pre-clinical drug screening. Another example cultured neurons from the prefrontal cortex, hippocampus and amygdala both separately and in an interconnected circuit (**Figure 1.3C**)⁴⁴. They demonstrated initially that cells from these regions differ in both cell morphology and protein expression, as well as in their electrical activity. After culturing the cells in an *in vivo*-like circuit, changes in each cellular region's behaviour were observed. This again highlights the importance of considering networks formed between different regions as a whole, rather than individual cultures, in order to properly study both normal functioning networks as well as their dysfunction in disease states⁴¹. Another *in vitro* model has been created to investigate the protective mechanisms that help to prevent widespread damage across environmentally isolated but synaptically connected neuronal populations⁴⁹. This study demonstrated the importance of networks for limiting spread of disease and injury, with the potential to upregulate the intrinsic neuroprotective effects for a range of disorders where network dysfunction is implicated. Ultimately, a greater understanding of the precise dynamics within neuronal networks in both normal and disease states is essential for interpreting the direct and subsequent indirect effects of potential drug treatments.

1.2. CNS disorders.

CNS disorders are the second leading cause of death globally (9 million deaths), behind cardiovascular disorders, representing an increase of 39% from 1990⁵⁰. Indeed, studies have described these disorders as the major public health problem in the developed world and it is estimated that one third of all European citizens, around 179 million people, suffer from at least one CNS disorder⁵¹. This is a striking figure and results in combined direct and indirect spending of €798 billion per year in Europe, representing 35% of the total cost of disease here⁵². Further, using disability-adjusted life years (DALYs) as a measure of disease burden, combined CNS disorders are the leading cause (276 million in 2016), with both deaths and DALYs increasing compared with the age standardised rates⁵⁰. Some of the major disorders associated with the CNS include neurodegenerative disorders (NDD), of which Parkinson's

(PD) and Alzheimer's (AD) diseases are the most common. NDDs are those which cause neuronal death and subsequent loss of function in both the CNS and PNS. Other conditions include neurodevelopmental disorders (e.g., autism and ADHD) and psychiatric or mental health disorders (e.g., depression, schizophrenia), as well as epilepsy, neuropathic pain, and stroke. In the UK, Alzheimer's disease and other dementias are the leading cause of death, with an increase from 3.58% to 12.37% of total deaths between 2005 and 2019⁵³. This compares with ischaemic cardiovascular disorders that showed a decrease from 17.39% to 10.46% over the same period. Further, patients with long-term CNS disorders, particularly neurodegenerative conditions, continue to have the lowest quality of life among sufferers of long-term conditions. Considering that these disorders disproportionately affect older patients, an ageing and increasing population is only set to increase the prevalence and associated costs.

1.2.1. Common disorders

1.2.1.1. Alzheimer's disease.

AD is a progressive and irreversible condition ultimately resulting in dementia, the loss of memory and cognitive function, and a majority of cases are in those 65 and older. AD accounts for 60-70% of all dementia cases and it is estimated that there are around 0.8-1 million people in the UK living with dementia, set to double to around 2 million by 2050. This also has major economic implications, with the cost to the UK economy predicted to more than double from an estimated £24 billion to £60 billion by 2050^{53,54}. The underlying cause is not yet fully understood; however, a range of factors are thought to be complicit including age, genetics, environment and lifestyle. The main characteristic pathologies are amyloid- β plaques and neurofibrillary tau tangles resulting from misfolding of proteins⁵⁵. How the two pathologies are related, and which ultimately causes the disease cascade has long been pondered. It is believed that formation of amyloid- β plaques and neurofibrillary tangles are independent events. However, evidence suggests that AD is triggered by changes to the amyloid precursor protein, rather than plaque formation, and that the tau pathology causes its progression⁵⁶. Better understanding the interplay between the two pathologies is particularly important for therapy development, as drugs targeted at reducing amyloid- β plaques alone have typically shown poor clinical outcomes⁵⁷.

1.2.1.2. Parkinson's disease.

PD is the second most common NDD after AD, with around 145,000 people living with the disease in the UK in 2020 and anticipated to increase by a fifth in 2030, to around 172,000 people⁵⁸. Worldwide, a conservative estimate would be for the number of sufferers to double

by 2050, however given the increasing population age this is expected to be much greater ⁵⁹. The main symptoms of PD are motor function impairments including tremors and stiffness, but others such as speech difficulties, neuropsychiatric symptoms (depression and cognitive decline), sleep disorders and incontinence are experienced ⁶⁰. The main pathological features in PD are the progressive loss of dopaminergic neurons in the basal ganglia and the formation of Lewy bodies, which are accumulations of phosphorylated α -synuclein ⁶¹. The underlying cause of this is unknown; however, genetics and environmental factors are presumed to play a role, in some combinatory fashion. There is evidence to suggest that the misfolded, phosphorylated α -synuclein acts in a prion-like manner, whereby the phosphorylation or misfolding of downstream endogenous α -synuclein is initiated, causing the pathology to spread throughout the CNS ⁶². Recent evidence has also pointed to the role of tau in PD, perhaps by interacting with the α -synuclein, however research is ongoing to determine the exact mechanisms involved ⁶¹.

1.2.1.3. Epilepsy.

Epilepsy is defined as the tendency for recurrent, unprovoked seizures which themselves are uncontrollable, hypersynchronous bursts of neuronal activity due to an imbalance between excitation and inhibition. Seizures are generally classed as focal or generalised, depending on the network area affected and whether it is localised to one hemisphere or both, or as epileptic spasms, which do not last longer than 1-3 seconds ^{63,64}. Generalised seizures occur in networks between both hemispheres and their manifestation depends on the subtype. For example, absent seizures present as a blank stare with no response to external stimuli, whilst myoclonic and tonic-clonic seizures involve motor dysfunction and uncontrollable muscle movements (jerking). Epilepsy affects around 600,000 people in the UK, with 87 new diagnoses each day. It is estimated to cost the NHS around £1.5 billion annually and results in 100,000 emergency admissions ⁶⁵. There is no known cause in around 65% of cases, however epileptic seizures may occur following head injury, a brain tumour or during the onset of neurodegenerative disorders. Further, there are possible genetic components behind the cause of epilepsy, with genes governing synaptic regulation, cell growth and other cellular functions thought to be implicated ⁶⁶.

1.2.2. Drug development for CNS disorders.

Without thorough knowledge of the underlying aetiology of the disease, it is difficult to identify targets for potential therapy. Even with this, the success/approval rate of drugs targeting CNS disease is half of that for non-CNS targets (6.2% for CNS and 13.3% for non-

CNS) and approval takes significantly longer (19.3 months for CNS and 14.7 months for non-CNS) ⁶⁷. It is also worth noting that most successes are for established therapeutic targets, rather than novel interventions for modifying or curing disease. Given that drug candidates here tend to fail later down the development line, large investments have already been made ⁶⁸. Further investment is therefore difficult to obtain given the risk associated and may be seen as an unattractive business model. For example, dementia is the only condition in the top 10 causes of deaths in the UK without any approved disease-modifying treatments ^{53,54}. Overall, the failure rate of neurodegenerative disease-modifying treatments at the clinical stage can be as high as 100%, compared with around 20% in oncology ^{67,69}. This highlights the need for more significant investment in studying CNS disorders and finding potential therapeutics. For instance, despite the cost of dementia to UK health and social care being greater than that of cancer and heart disease combined (£11.9 billion vs £7.5 billion), the investment in research is substantially lower (£90 billion vs £710 million) ^{54,70}.

Targeting diseases such as neurodegenerative conditions, stroke and traumatic brain injuries have the least success rate ⁶⁷. This is unsurprising given the widespread neuronal cell death that occurs and the lack of widespread regenerative capabilities in the CNS. As a result, treatments tend to focus on easing the conditions or symptoms associated with the disease in question, rather than providing an outright cure. However, there are currently 17 AD disease-modifying treatments undergoing Phase 3 trials with the FDA, suggesting progress is being made ⁷¹. An example of a symptom-reducing therapy is the use of acetylcholinesterase (AChE) inhibitors to reduce the breakdown of acetylcholine (ACh) and increase the levels in the brain ⁷²⁻⁷⁴. Acetylcholine is a widespread neurotransmitter implicated in various physiological processes including learning and memory, attention, and stress response ⁷⁴. AChE inhibitors have been shown to improve cognitive function in mild and severe AD for short periods (1-3 years), however do not alter the disease progression ⁷⁴. Recently however, several studies have pointed to the potential of AChE inhibitor-based drugs for preventing amyloid- β aggregation ^{72,73}.

1.2.3. The blood-brain barrier.

The brain presents its own unique challenge in the form of the blood-brain barrier (BBB), described as the most important limiting factor in drug discovery ⁷⁵. The BBB consists of brain endothelial cells (ECs), the capillary basement membrane, astrocyte end feet and pericytes, all of which are essential for its normal functioning (**Figure 1.4**) ^{3,76}. These components in turn create three layers through which substances from the capillaries must pass, with tight

junctions (TJ) between the endothelial cells forming the major barrier. Here, only small lipophilic molecules can cross freely, with essential nutrients such as glucose crossing via transporters, and larger molecules such as insulin requiring endocytic uptake ⁷⁷. The BBB is therefore highly restrictive and tightly regulates the movement of ions and molecules between blood and the CNS. This helps maintain a stable environment to ensure proper functioning and provides protection from toxins, pathogens, inflammation and injury ^{78,79}. However, this results in the movement of drugs between the blood and the CNS being highly restricted, requiring any molecule to be of a small size (<500 Da) and typically lipid soluble ^{80,81}. Indeed, 98% of small molecule drugs (500 Da – 1 kDa) do not cross the BBB as a result of the TJ ^{75,76,82}. This therefore presents the greatest challenge for delivery of therapeutics to the CNS via the blood, and so contributes to the escalating prevalence of disease. Further, the BBB can become disrupted in some disorders including multiple sclerosis, stroke, epilepsy and Alzheimer's disease. As a result, there may be a disruption to ionic homeostasis, signalling and a greater chance of interactions with the immune system, leading to further progression of the disease ⁷⁸. It is thought that these diseases affect the protein components of the TJ, resulting in increased permeability. Understanding the BBB and how to overcome it is therefore essential for developing new and efficient drug treatments and therapies as well as for better understanding disease progression.

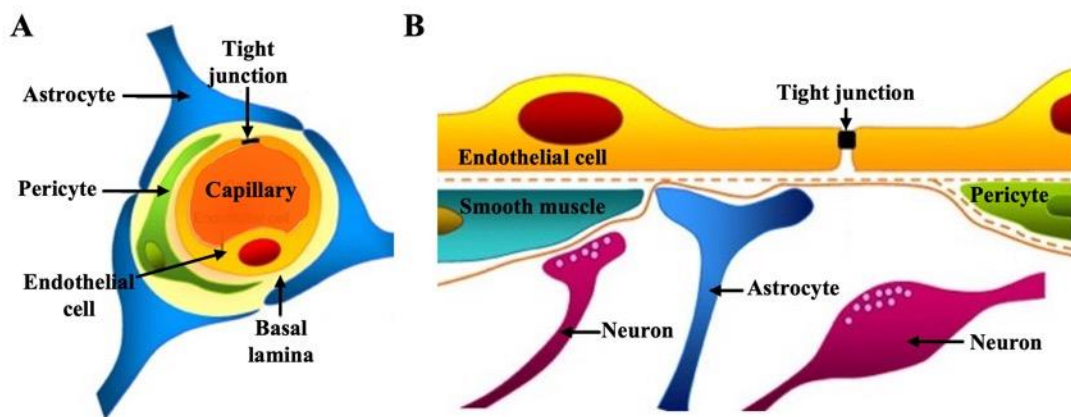


Figure 1.4. Schematic of the blood-brain barrier. (A) Cellular organisation and (B) structure of the BBB, with the tight junction creating the main barrier to transport across it. Image recreated with permission from ⁸³.

1.2.4. The need for improved *in vitro* modelling.

Given there are up to 90 billion neurons in the brain with 100+ trillion synaptic connections, it is no surprise that this organ is difficult to interpret ^{5,84}. An understanding of the underlying cellular structures, cell-cell communication and circuit dynamics in simple organisms has been well documented. However, one neuron can create connections with thousands of others and

the networks are constantly changing throughout development⁴². This plasticity further allows remodelling in response to new experiences throughout life⁸⁵. Correct functioning of the nervous system relies on variable circuits throughout the brain regions interconnecting to produce coordinated actions³³. The difficulty is therefore in interpreting the complex networks, circuitry and pathways formed, which is needed to then have a better understanding of proper function, as well as dysfunction. This is particularly useful in disease where there is no underlying pathology but a clear behavioural impact, for example mental health disorders, caused by dysregulated circuits⁸⁶. Overall, there remains a generally poor understanding of the underlying pathophysiology and mechanisms behind CNS disorders⁸⁷.

To properly study the underlying physiology in the normal and diseased brain, developing appropriate models is essential. There is much debate on what type of model is best, with these typically being *in vitro* or *in vivo*. While some animals such as rodents may possess similarities to humans, in terms of physiology and potentially genetics, they are unable to reproduce the critical features needed for sufficient developmental and circuit dynamic studies relating to human disease^{41,88}. There is particular difficulty in recapitulation of neurodegenerative diseases, such as Alzheimer's, as this does not naturally occur in rodents and so must be induced through gene manipulation. Further issues come down to the limited lifespan of such animals and so a thorough study of a disease that occurs over decades is difficult to model^{89,90}. For example, mouse AD models express the mutations associated with the disease leading to amyloid- β plaque formation or tau associated neurofibrillary tangles. However, the use of genetically induced pathology leads to overexpression of the amyloid protein, which does not accurately model the sporadic and heterogenous nature of the disease, and it has been difficult to induce the pathological features associated with tau accumulation⁹⁰. Ultimately, there is difficulty in interpreting the behavioural and cognitive effects of these protein aggregates, as would be seen in humans, and subsequently determining if their breakdown reverses the effects⁶⁷. The use of animal models also brings into question the ethics of keeping and breeding laboratory animals, as well as the associated upkeep costs. There is a desire here to move away from wasteful animal use towards a more sustainable and humane culture of *in vivo* experimentation, when necessary, namely through the 3R's initiative by the National Centre for the Replacement, Reduction and Refinement of animals in research (NC3Rs).

Whilst animal models remain important tools for investigating potential treatments within a whole, multi-system organism, the difficulty in translating such models can lead to bottlenecks in the drug development process. For example, clinical trials of drugs aimed at treating AD

conditions had a 0.4% success rate between 2002 and 2012⁹¹. Further, only 7% of drugs in development for all CNS disorders will eventually make it onto the market, compared with 20% for cardiovascular disorders and an average of 12% across all areas⁹². Of the 53 new drugs receiving FDA approval in 2020, none of these were for treating Alzheimer's disease or its symptoms. However, 5 of the approved agents were classed as disease-modifying therapies for neurodegenerative disorders (including 1 for multiple sclerosis) suggesting that progress is being made in finding and developing appropriate biomarkers for therapeutic targets^{71,93}. The BBB also has a major effect on drug development, due to restrictions in the size of molecules that can readily cross it⁹⁴. Thus, *in vitro* models able to recapitulate this structure would be useful as a screening tool prior to expensive and lengthy clinical studies. This should help in selecting the drug candidates most likely to enter the CNS, while discarding those that are most likely to fail, increasing the predictive power of *in vitro* models and ultimately reducing costs in the development process.

Traditional *in vitro* methods of studying neurons involve 2D cultures grown on glass coverslips or another hard substrate. Whilst animal derived cells provide a rapid and convenient method for producing simple *in vitro* network models, they fail to replicate the complex physiological microenvironments within the brain. However, the advent of induced pluripotent stem cells (iPSCs) provides the ability to generate more relevant cells with a specific phenotype, maturity and infinite lifespan and is more in line with the 3R's initiative for more humane research⁹⁵⁻⁹⁷. Whilst *in vitro* models would not reproduce the behavioural and cognitive effects of a disease, the use of patient-derived cells, with the specific genetic profile of the patient, alongside improved spatiotemporal control could enable more predictable outcomes and improve the clinical relevancy of the model^{32,98,99}. Further, using substrates with more appropriate mechanical properties is attractive to more accurately mimic the *in vivo* microenvironment¹⁰⁰. For instance, the elastic modulus/stiffness of CNS tissue is in the Pa – kPa range whilst typical cell culture substrates have a modulus in GPa range¹⁰¹. Research has shown that the stiffness of the substrate effects cell behaviour and ultimately cell survival and growth, with no one-size-fits-all approach given the heterogeneity of the nervous system¹⁰¹. It is also known that the substrate stiffness can influence the fate of stem cell, with stiffer substrates required to help direct lineage into bone tissue, but softer matrices required for brain and muscle tissue^{100,102}. Therefore, there is an increased demand for *in vitro* models that use iPSCs and enable the manipulation of the cellular microenvironment. Suitable methods include the use of microfluidics, 3D culture conditions, generating brain organoids or through a combination of these. Brain organoids are an exciting technology that provide a

greater level of complexity above traditional *in vitro* techniques, offering self-organisation of multiple cell types, with great potential for investigating disease on a system level¹⁰³⁻¹⁰⁵. However, the technology is still in the early stages, with issues including consistency and reproducibility, a lack of sufficient nutrient delivery and circulatory system, and ethical and moral dilemmas that may come with increasingly complex and advanced structures^{105,106}. Besides this, microfluidic technology offers an ability to generate more precise microenvironments, enabling spatial and temporal manipulation of fluidically isolated but synaptically connect neuronal populations^{107,108}. Further, if using animal-derived cells, the reproducible and more relevant environments provided in microfluidic cultures ultimately enables a reduction in the number of animals required.

1.2.4.1. Hippocampal neuronal cultures as a model system.

Despite their issues, *in vitro* models using animal derived cells are easy to implement, offering a rapid and convenient source of information for a range of neuronal studies¹⁰⁹. Dissociated hippocampal cultures are one of the most commonly used neuronal culture systems for *in vitro* models and are an accepted approach for investigating electrophysiological, morphological and developmental properties^{110,111}. The hippocampus is of particular relevance as it is easily accessible, it is implicated in several diseases including epilepsy and neurodegenerative disorders such as Alzheimer's, and it is associated with learning and memory²⁰. The cells isolated are typically a mix of neurons and astrocytes and show defined periods of maturation, form complex networks following dissociation and enable high quality imaging. Further, primary hippocampal cultures begin to show signs of synaptogenesis after 3-7 days, peaking around day 14¹¹⁰. This high density of synaptic connectivity achieved within a short period enables analysis of network dynamics and signalling as a short-term culture system. The manipulation and observation of these neurons on a cellular level is achievable through common methods including electrophysiology and fluorescence microscopy. In addition, the use of P0-P3 rodent pups provide networks with both excitatory and inhibitory neurons, providing more physiological relevancy and activity and provide a direct source of astrocytes, unlike embryonic cultures (E17-18), which help ensure the survival of cultures^{109,112,113}. Further, these properties make such primary cultures amenable to studying seizure activity for better understanding epileptic network activity¹¹⁴. Overall, the hippocampus provides a rapid and convenient method for producing simple *in vitro* network models and enabling analysis within 14 DIV.

1.3. Microfluidic technology and its use in neuroscience.

Microfluidics is concerned with the handling and manipulation of fluids at the microscale and nanoscale. Microfluidic devices typically have features in the range of 10s – 100s of micrometres resulting in non-turbulent or laminar, predictable, and highly ordered flow that can be precisely controlled¹¹⁵. As a result, microfluidics offers great advantages for recreating biological systems by enabling defined spatial arrangement. This provides a level of control over the growth and guidance of cellular features, and a reduction of reagents and cells is required over traditional techniques. Further, the flow properties offer a more appropriate environment for cells, enabling controlled nutrient flow and the ability to manipulate the cellular environment spatially and temporally¹¹⁶. This is particularly useful in neuroscience as it provides the ability to arrange and interconnect different regions with specific cell types and conditions, similar to the *in vivo* brain which consists of 52 interconnected regions (Brodmann regions) each with distinct cellular organisation and complex circuitry^{31–33,41}.

Currently, a large portion of the microfluidics industry is focused on chemistry and chemical diagnostics, with extensive exploration for creating point of care diagnostics. This enables miniaturisation of the process, enabling reduced analyte consumption and associated costs, increased sensitivity, and reduced analysis times¹¹⁷. This is particularly useful for developing countries where financial resources are limited, and often the expensive laboratory equipment and personnel required for their operation are unavailable. Further, the leading causes of deaths in these countries are infectious diseases such as HIV/AIDS, measles and malaria, where thorough diagnosis can help prevent the spread and reduce the mortality rate¹¹⁸. Other fields where microfluidics have an impact are genetic analysis, single-cell analysis, drug discovery, and DNA amplification¹¹⁵. Ultimately, for microfluidics to become an established technique in any one field, the benefits it provides must outweigh the challenges associated with moving away from the traditional techniques¹¹⁹.

1.3.1. Microfluidic device production.

For producing microfluidic devices, replica moulding via soft lithography is the most established method and is a relatively simple process. Photolithography is used to generate moulds with the microfluidic features in a photoresist, then a liquid polymer is poured over and allowed to set. To create a complete device, the set polymer containing the microfluidic features is bonded to a substrate such as glass or another piece of the polymer, enclosing the channels. SU8 is a widely used photoresist as it provides high resolution and aspect ratios, with features down to a few microns or 100s of nanometres, and is durable, allowing multiple

moulding and demoulding without damage¹²⁰. The most widely used polymer in microfluidics is polydimethylsiloxane (PDMS) and is particularly useful in biomedical applications due to its gas permeability and biocompatibility. Further, the optical transparency allows easy interfacing with microscopy equipment as a means of imaging and analysis. However, this method of production typically requires clean room facilities, limiting the potential for its use outside of specialised labs. Other techniques for producing microfluidic devices include hot embossing, 3D printing and injection moulding. Photo and soft lithography remain the most appropriate method of production for reliably achieving the microscale features used in brain-on-a-chip type devices¹²¹. Ultimately, the specialist equipment required for in-house device production limits the potential for microfluidic use outside of labs with the necessary microfabrication knowledge and facilities. This highlights the need for developing a more accessible and reconfigurable easy-to-use platform to make microfluidic technology more appealing to novice users. This would enable greater flexibility in device production, without the restraints imposed by fixed designs and commercially available options.

1.3.2. Compartmentalised devices for neuroscience research.

The most common device type used for neuroscience studies consists of compartmentalised culture chambers interconnected by an array of microchannels orientated perpendicular to the culture channel (**Figure 1.5**). The first major design for this type of device came from the Taylor group¹²², based on the Campenot chamber¹²³, and incorporating modifications to improve regional isolation and neurite outgrowth. This work has been cited extensively in the literature and has been the design of choice for many applications in neuroscience^{108,124–134}. The success of this design is a result of using established microfabrication techniques, namely photo/soft lithography, and replica moulding, as well as the reduced reagent volume and cell numbers required per assay over more traditional culture techniques. Further, the ability to independently manipulate individual interconnected regions is a major attraction. As discussed previously, the brain is unique in its complexity and contains multiple regions with distinct microenvironments and numerous neuronal subtypes. Neuronal processes become highly branched and extend increasingly complex networks throughout the various regions and environments. Network formation is reliant on proper axonal guidance, synapse formation and the subsequent synaptic activity. Therefore, compartmentalisation provides the ability to isolate a cell soma from axons, create co-cultures, recreate specific networks with distinct microenvironments, and directly manipulate cells in an individual compartment. Further, the microchannels permit only neurites to enter, enabling guidance of axons between chambers.

This in turn allows more complex network formation, and a means of studying axonal and synaptic behaviour.

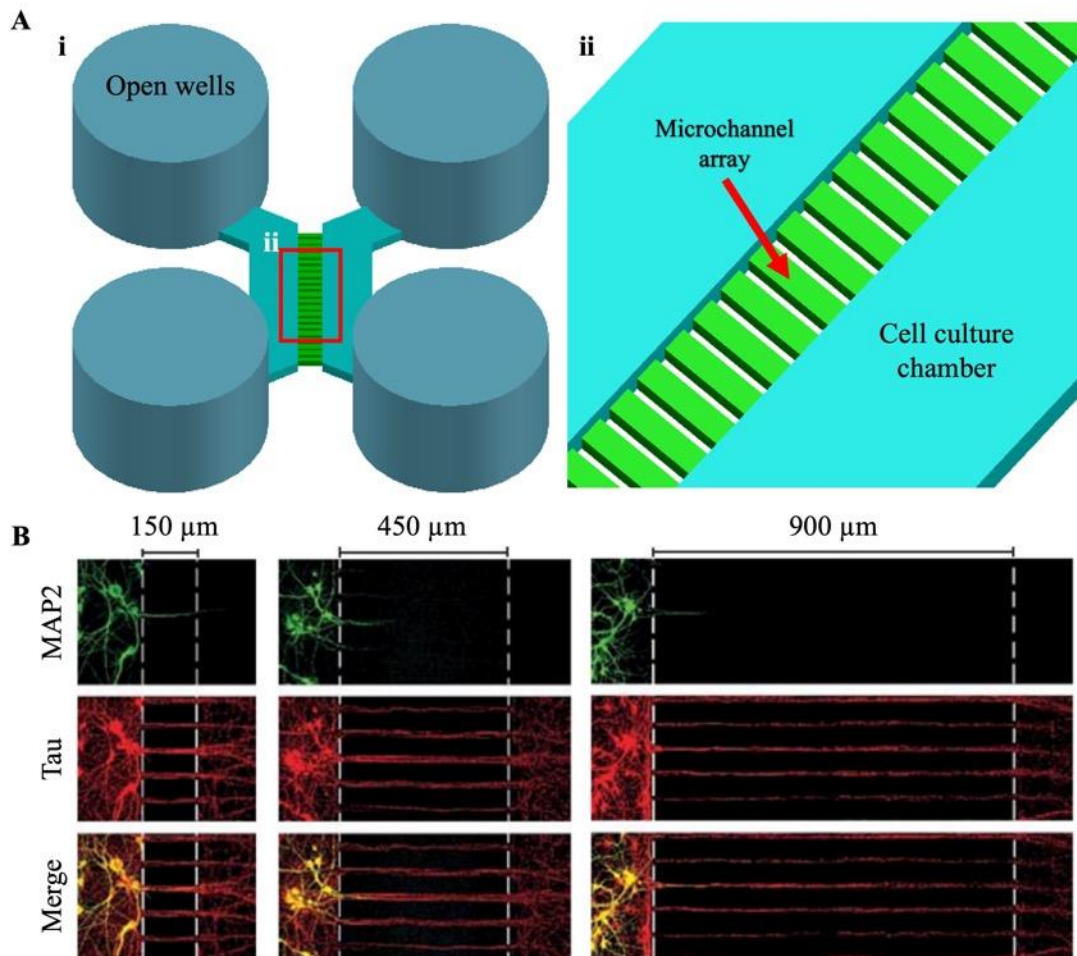


Figure 1.5. *The most common microfluidic devices used in neuroscience research consist of two isolated culture chambers interconnected by a series of microchannels. (A) Schematic highlighting (i) a two-chamber compartmentalised device based on the Taylor design. Each culture chamber is connected to an inlet and outlet well, with (ii) a microchannel array between each culture chamber that isolates the somas and only permits the growth of neurites. (C) Image taken with permission from ¹²⁴ showing neurite outgrowth in microchannels of increasing lengths when cells were seeded in the left culture chamber. MAP2 staining shows dendrites while tau staining shows axons and demonstrates how increasing the microchannel length restricts connections between chambers to axonal connections only.*

1.3.2.1. Axonal isolation.

The initial study from the Taylor group demonstrated guided neurite outgrowth through microchannels, with the isolation of these from the soma ¹²². Further, they established a method of selectively applying chemical insults to the neurons in individual compartments by altering

the fluid levels in the wells. The hydrostatic pressure generated, along with the high fluidic resistance in the microchannels, prevents leaching between compartments. By using a fluorescent compound, this fluidic isolation was shown to remain for at least 15 hours (**Figure 1.6A**). Another study from the Taylor group tested various microchannel lengths and found that those of at least 450 μm ensure only axons can completely transverse to the adjacent chamber, with dendrites prevented from doing so ¹²⁴ (**Figure 1.5B**). Microchannels for isolated axonal outgrowth also enable the application of a chemical insult or mechanical dissection directly to axons in order to study injury and regeneration ¹³⁵. For example, a two-chamber device was modified with a central channel running perpendicular to the microchannels, allowing simultaneous axotomy of all axons, via vacuum aspiration (**Figure 1.6B**) ¹³⁶. Further, these compartmentalised chambers enable one to study synaptic activity, such as synaptic competition between neuronal populations ¹³⁷, or for simply visualising and manipulating these individually from the rest of the cell ¹²⁶.

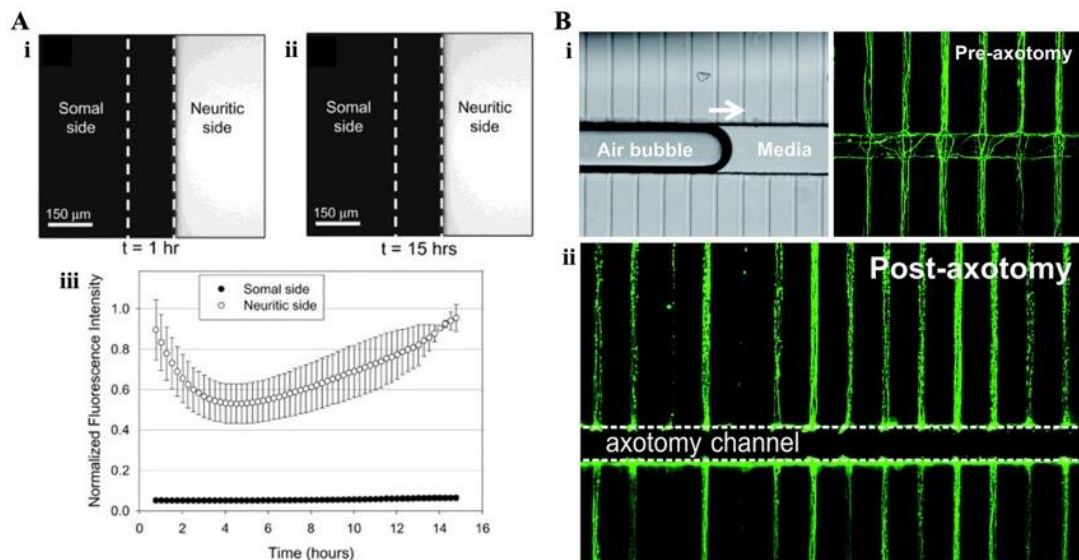


Figure 1.6. Microchannels between culture compartments enable the creation of distinct microenvironments. (A) Image taken with permission from ¹²² to demonstrate environmental isolation. Fluorescein was added to the neuritic side, with a hydrostatic pressure gradient from the somal side preventing leakage or diffusion of fluorescein. Fluorescein isolation in the neuritic side was maintained after (i) 1 and (ii) 15 hours. (iii) A graph of normalised fluorescence intensity against time, indicating no leakage of fluorescein between the two compartments. (B) Image reproduced with permission from ¹³⁶ shows the process of axotomy using vacuum aspiration through a central channel across the microchannels and the neurites (i) prior to axotomy and (ii) following axotomy.

1.3.2.2. Co-cultures and network studies.

Compartmentalisation enables studying of the interaction between different, separated, but functionally connected cell types and their isolated manipulation. Interactions between neurons and microglia have been studied to gain an insight into the phagocytosis of the latter on degenerating axons¹²⁷, and between oligodendrocytes and neurons to study myelination in the CNS¹²⁸. Further, compartmentalised devices have been used for creating co-cultures of neurons and other cells of the body. For example, the neuromuscular junction can be studied by seeding neurons in one compartment and muscle cells in another¹²⁹, or the functional connectivity between neurons and cardiomyocytes studied by seeding these in adjacent chambers¹³⁰. Likewise, compartmentalisation enables the investigation of different networks by culturing neurons from specific CNS regions in adjacent chambers. Cortical-thalamic networks have been recreated to study the firing patterns between the co-cultures⁴⁷ as well as how the effects of a chemical insult in one region affects activity in the other¹³². A ‘multiregional’ device with three interconnected chambers, each containing cells from either the prefrontal cortex, hippocampus, or amygdala has been developed⁴⁴. Here, differences in cell composition and electrophysiology in these cultures as compared to cells that had been cultured separately was demonstrated, highlighting the importance of these multi-regional models for creating more physiologically appropriate networks.

Beyond the use of simple linear microchannels, tapered or ‘diode’ microchannels have been validated for enabling unidirectional axonal growth via edge guidance of neurites^{138,139}. This has the potential to improve network dynamics by orienting and directing synaptic activity, producing more defined and ordered network architecture, similar to those found *in vivo*. Using such directionality, a more complex platform has been created to replicate the basal ganglia circuitry as a model for studying its function and dysfunction (**Figure 1.7A**)⁴³. The device consists of four chambers all independently connected to a central chamber via tapered microchannels. Calcium imaging was used to demonstrate functional connectivity between regions, however more work is needed to improve maturity of the circuit and enable more long-term measurements. Whilst this provides an exciting example of more complex, *in vivo*-like network formation, the fixed layout of the device ultimately restricts its use to that which it was designed for. Recently, more complex microchannel geometries have also been investigated for controlling directionality¹³⁸. These asymmetric shapes can trap any neurites transecting in the ‘reverse’ direction, inhibiting outgrowth between culture chambers (**Figure 1.7B**). This allows the creation of predefined circuits for more accurate network dynamics and *in vivo* like characteristics.

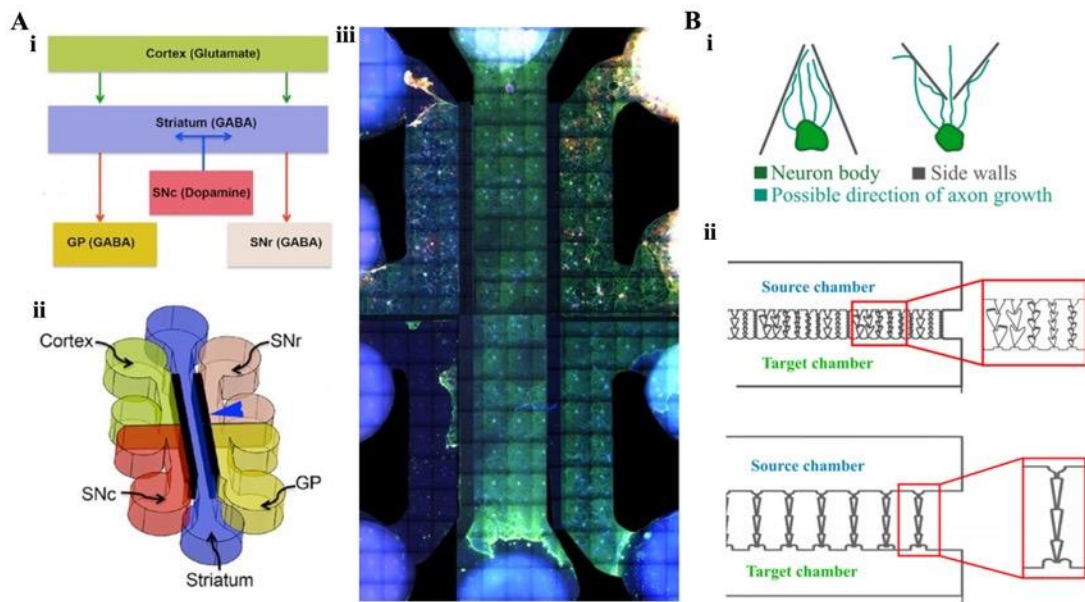


Figure 1.7. Diode and tapered microchannels allow for more defined and organised network architecture in microfluidic devices. (A) Tapered microchannels have been used to recreate the basal ganglia circuitry: (i) schematic of the circuit showing directionality of neurites dictated by the orientation of tapered microchannels; (ii) schematic of the device for recreating the circuit, showing the different regions; (iii) a representative example of a PDMS device seeded with the desired cells and stained with DAPI (blue) and β III-tubulin (green). Images reproduced with permission from ⁴³. (B) More complex microchannel geometries can also be used to define axonal outgrowth: (i) schematic demonstrating how the shapes can control the growth direction, with (ii) examples including triangular, zigzag and spine-like structures. These are orientated to encourage growth from the source to the target chamber. Images taken from ¹³⁸ (open access: CC BY 4.0).

1.3.2.3. Disease models.

Various microfluidic models of NDD have been created ¹⁴⁰. There have been several studies using microfluidic devices to investigate both tau ^{141–146} and amyloid ^{147–150} hypotheses in Alzheimer's disease. A three-chamber device has been used to create interconnected networks of diseased and healthy neuronal populations in AD ¹³³. Cortical cells were seeded in the two outer chambers, while the central chamber allowed synaptic connections between the neuronal networks. To induce a diseased state, okadaic acid was added to one side causing hyperphosphorylation of tau, as seen in Alzheimer's disease. A gradient was generated between the two chambers in the central chamber, ensuring only the diseased side was directly affected. This model would allow an investigation of AD propagation or an evaluation of how a particular drug affects healthy and diseased populations. Another device has been developed

to investigate microglial response to soluble and insoluble amyloid- β states. This provides an insight into microglial accumulation at amyloid- β plaques and the subsequent neurotoxic and neuroinflammatory response¹⁵¹. This device varies from the standard compartmentalised platforms with a central, circular chamber for the amyloid- β surrounded by another circular chamber. An array of microchannels connects the two and these act as migration channels for the microglia.

Further, there have been numerous studies that used microfluidic devices to study pathological spread of α -synuclein in Parkinson's disease^{39,152-155}. A three-chamber device has been used with tapered microchannels to ensure axonal growth unidirectionally from the proximal chambers to the distal chamber⁴⁰. Human iPSCs were seeded in both outer chambers, and neurites were extended from the proximal chamber, creating a unidirectional network. α -synuclein aggregation was initiated in the proximal chamber by addition of 'fibrils' or 'ribbons', themselves aggregates of the phosphorylated α -synuclein that can seed in cultured cells and induce endogenous α -synuclein phosphorylation¹⁵⁶⁻¹⁵⁸. They were able to demonstrate uptake of exogenous fibrils with subsequent axonal transport and neuron-neuron pathological spread resulting in endogenous α -synuclein aggregation in the distal chamber, confirming the prion-like properties of phosphorylated α -synuclein, within a human cell model. This research offers potential for advancing pre-clinical models and would enable the use of patient-derived cells for more predictive drug discovery and treatment selection.

1.3.3. 3D microfluidic cultures.

2D microfluidic cultures provide a good platform for circuit studies, allowing interaction with other cell types through co-culture and providing more dynamic distribution of oxygen and nutrients. Further, the compartmentalisation enables fluidic isolation between chambers and thus regional manipulation. They also enable simple analysis through imaging techniques including immunocytochemistry and functional calcium imaging⁴¹. However, cultures grown in a 2D environment do not fully recapitulate the brain microenvironment. Further, there have been observed differences in viability, morphology, differentiation and protein expression of cells cultured in 2D versus 3D environments¹⁵⁹. It is therefore of interest to culture cells in a more physiologically relevant matrix to mimic as best possible the native brain extracellular matrix (ECM). To do this, gel-based systems are some of the most widely used 3D culture methods and can be combined with microfluidics.

In microfluidic 2D cultures, cells are suspended in cell media and inserted into the culture chambers where they grow on a suitable culture substrate. Subsequently, media and chemical insults can be directly applied over these cells by addition to the same channel. However, in 3D cultures, cells are normally suspended in a suitable hydrogel^{160–162} which fills the entire channel before polymerising. The injection of this gel must be controlled so that it remains in the desired channel but creates an interface with adjacent perfusion channels. Any chemical insult or fresh media can then be applied via a perfusion channel, allowing nutrients or reagents to diffuse across the gel. Other cell types can also be added in these adjacent channels where they become embedded in the polymerised gel.

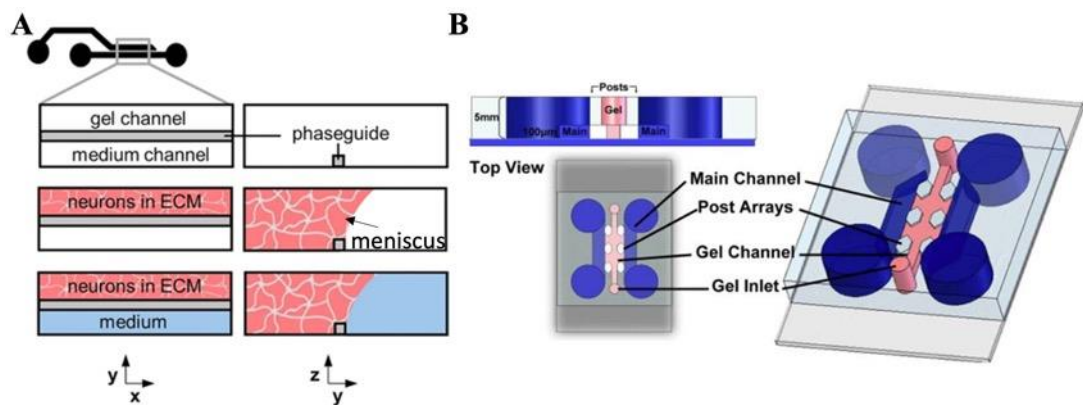


Figure 1.8. Phase guides and micropillars are used to create microenvironments for 3D cell culture in microfluidic devices. (A) Schematic of a device utilising a phase guide to contain the injected gel within the desired channel. This small barrier reduces the capillary pressure to contain the gel-air interface meniscus prior to polymerisation. Image taken from¹⁶³ (CC BY 4.0). (B) Schematic of a device that uses equally spaced posts to contain the gel within its channel. The pressure difference between the channel and the gaps prevents the gel escaping into the adjacent channel. Image taken with permission from¹⁶⁴.

Phase guides were first introduced to control the liquid-air interface^{165,166}. Here, a small barrier is added along the channel to alter its surface energy. As a result, capillary pressure is reduced and, as liquid enters, the meniscus formed between liquid and air aligns itself along the barrier before passing over. This forces the liquid to fill the entire space, preventing the entrapment of air and dead angles. In the case of 3D culturing, phase guides have been demonstrated in microfluidic chips to control gels prior to their polymerisation and ensure they remain in the desired channel (**Figure 1.8A**)^{163,167}. An alternative to these phase guides is the use of regularly spaced micropillars or posts that run the length of the channel (**Figure 1.8B**). Whilst the capillary action at the micropillar gap aims to draw the liquid across, the channels ultimately remain hydrophobic and so the large surface tension created will prevent the gel

escaping into adjacent channels prior to polymerisation¹⁶⁴. These pillars have been used in devices with varying numbers of channels for BBB applications^{168–171}. Both types of structure ensure there is an interface between each channel enabling their components to interact with each other.

1.3.4. *In vitro* blood-brain barrier.

As discussed previously, the BBB presents a major challenge to drug discovery in neuroscience. Therefore, the development of *in vitro* models enable studying of the complex interactions at the BBB, the effects it has on CNS disease pathogenesis and how membrane permeability is altered, and ultimately aid in the discovery of suitable therapeutics able to penetrate the barrier¹⁷². The combination of microfluidics and 3D cell culture therefore presents an ideal solution for *in vitro* model development. Numerous BBB models have been created with varying complexity, depending on the culture conditions and cell types used^{81,82,92,168,169,171,173}. As preclinical models, these can provide a more reproducible, cheaper and less invasive option than animal models, without the associated ethical considerations. Both static and dynamic BBB models, including the Transwell® insert, have been used to study permeability and transport kinetics for drug discovery⁸¹. However, these once again fail to replicate the precise microenvironments that microfluidics can offer.

One of the earliest and simplest microfluidic BBB models consisted of a PDMS device with a central chamber surrounded on both sides by smaller channels and micropillars in-between to enable communication between channels (**Figure 1.9A**)⁸². Rat brain endothelial cells were cultured in the outer channels and perfused continuously to provide shear effects. Subsequently, astrocyte conditioned medium (ACM) was perfused through the central chamber. To study the permeability of the *in vitro* barrier, FITC-dextran was perfused through the outer channels and its presence observed for in the central chamber (**Figure 1.9B**). The decreased permeation of FITC-dextran in the cell-ACM condition can be attributed to tight junction formation in the endothelial cell layer. In comparison to Transwell® inserts, the SyM-BBB device showed a significant reduction in FITC-dextran permeation, indicating its greater relevancy for drug delivery studies. Further, western blotting confirmed the SyM-BBB device had an increased presence of tight junction molecules compared with a Transwell® model.

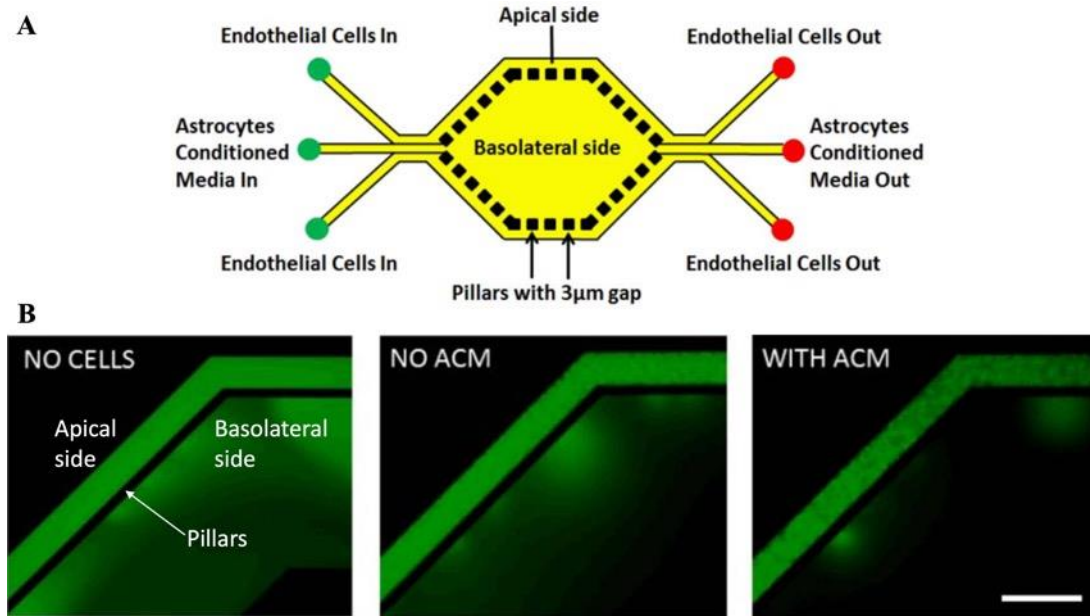


Figure 1.9. A simple, 2D microfluidic in vitro BBB model (SyM-BBB). Figure recreated with permission from ⁸². (A) Schematic of the device highlighting the different regions and features. (B) Results from a permeation assay using FITC-Dextran in 3 different device conditions, from L-R: device had no endothelial cells (ECs) seeded in outer channel; device had ECs in outer channel but not astrocyte conditioned media (ACM) in central chamber; device had both ECs in outer channel and ACM in central chamber. The reduced presence of FITC-Dextran in the central chamber of the right-most condition indicates less permeation through the 'barrier' and so tight junction formation. Scale bars show 500 μm .

Other, more complex models have also been developed. BBB dysfunction is seen in the early stages of NDD, with a disruption in the endothelial layer and subsequently the tight junctions, impairing its resistance to permeation ^{169,174}. Understanding the molecular mechanisms behind this is essential to developing novel strategies for treating such conditions. A recent microfluidic model has been developed to address this, with the device having both neuron and BBB chambers (**Figure 1.10A**) ¹⁶⁹. The neuronal section contained either FAD (familial Alzheimer's disease) mutation expressing cells (ReN-AD) or wild-type cells (ReN-WT, control), both from the ReN human neural progenitor cell line, whilst the BBB section contained brain endothelial cells (bECs). Using FITC-dextran, a significant increase in the permeability of the barrier was seen in the AD model compared with that of the wild-type model (**Figure 1.10B**). Immunofluorescent staining highlighted the presence of tight junction proteins in the endothelial layer, with a decrease in expression in the AD model, indicating this influences permeability (**Figure 1.10C**). Further, a significant increase in cell death in the AD model was observed in the presence of thrombin, indicating barrier breakdown and

subsequent increased permeation (**Figure 1.10D**). Finally, an anti-inflammatory drug was used to assess if barrier integrity can be restored, with treated AD models showing a decrease in permeability compared to untreated controls (**Figure 1.10E**), whilst also showing a decrease in the neurotoxic effects of thrombin (**Figure 1.10F**). These results indicate that restoring the barrier integrity may be a potential target for drugs in Alzheimer's disease. Overall, this model has shown similarities to the *in vivo* BBB and has the potential to aid in drug screening and investigating how the barrier is disrupted under various conditions.

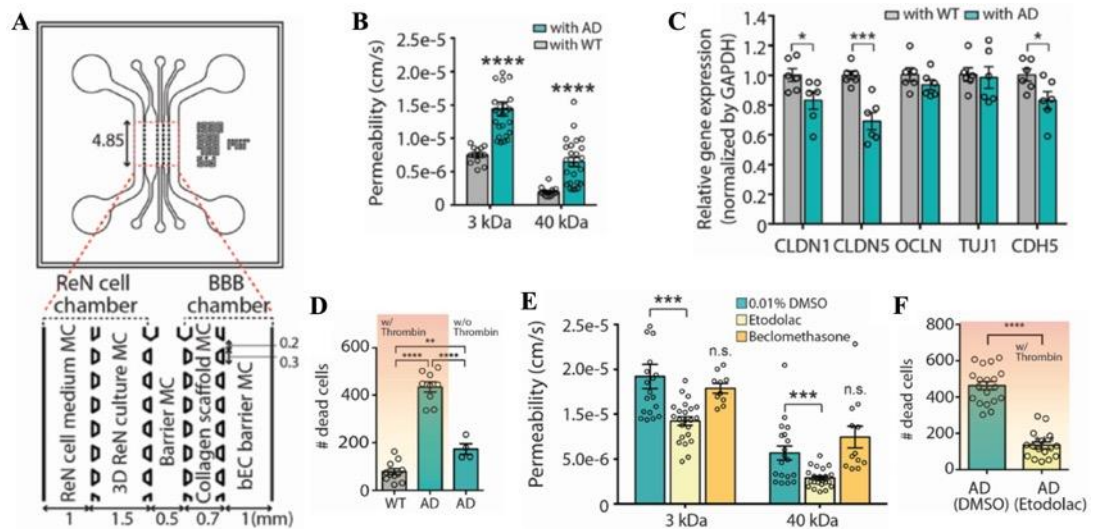


Figure 1.10. A microfluidic *in vitro* BBB model has been created to investigate the effects of neurodegenerative disease on its integrity. Images taken from ¹⁶⁹(open access: CC BY 4.0). (A) A schematic of the device showing the layout and composition of the channels. (B) A permeability assay using FITC-dextran showed a significant increase in permeability of the barrier in the AD model. (C) Immunofluorescent staining showed a decrease in expression of tight junction proteins in the AD model, indicating disruption to the barrier. (D) The neurotoxic effects of thrombin were more prevalent in the AD model, confirming the disrupted barrier enables increase permeation of this and subsequent increased cell death. (E) The restorative effects on the barrier of the drug Etodolac were confirmed with a decrease in permeability following treatment vs untreated controls (DMSO). (F) Etodolac treated AD models also showed a decrease in cell death following application of thrombin, confirming restorative effects on the barrier. For B-F, * = $p < 0.05$, ** = $p < 0.01$, *** = $p < 0.001$, **** = $p < 0.0001$.

1.3.5. Analysis of neuronal cultures in microfluidic devices.

Various methods can be employed to investigate microfluidic neuronal cultures. Some of the most common methods include electrophysiology for investigating the electrical signalling of neurons, immunofluorescent staining to image the structures present and determine protein expression, and calcium imaging as a measure of functionality and signalling in synaptically connected networks.

1.3.5.1. Immunocytochemistry and fluorescence imaging.

Immunofluorescent staining is one of the most common methods used for analysing cultured cells. This can give an indication as to the cellular growth and morphology, highlighting any structures of interest, depending on the type of study. Immunocytochemical staining typically involves targeting the proteins of interest using primary antibodies, followed by tagging these using the appropriate fluorescently conjugated secondary antibodies, with visualisation using subsequent fluorescence microscopy. This gives no functional information, however, and if investigating intracellular targets, cells must be fixed and permeabilised prior to staining. Common targets for neuronal cultures include: β III-tubulin, a marker for neurons; glial fibrillary acidic protein (GFAP), a marker for astrocytes; synaptophysin, a marker for synaptic vesicles which can indicate synapse formation and cell-cell communication; and microtubule-associated protein (MAP-2), a marker for the soma and dendrites. Immunocytochemistry also allows for identification of specific neurons. Staining for VGLUT1/2 (vesicular glutamate transporter) or glutaminase will highlight glutamatergic neurons, while staining for VGAT (vesicular inhibitory amino acid transporter) or GAD65/67 (glutamate decarboxylase) can highlight GABAergic neurons¹⁴⁰. Within microfluidic devices, immunofluorescent staining provides visualisation of the network formation between cells (**Figure 1.11A**) as well as the connections formed across fluidically isolated chambers via microchannels and subsequently an indication of synaptic connectivity (**Figure 1.11C-D**)^{124–126,134}.

Immunofluorescence imaging may also be used to study neurodegenerative diseases and their progression. By staining for α -synuclein and its phosphorylated form, one can investigate the progression of Parkinson's disease. By looking specifically at the phosphorylated form, it is possible to investigate how this induces downstream phosphorylation of regular α -synuclein throughout a network or how it is transported between cells^{40,175}. It is also possible to study Alzheimer's disease by staining for amyloid- β and tau proteins^{133,151,176}. Analysing the levels and accumulation of both under various conditions can again give an indication as to the progression and spreading mechanisms of the disease. In blood-brain barrier models with

endothelial structures, targets of interest include tight junction proteins such as claudin and occludin, or transporters such as P-glycoprotein^{82,140,169,171}. An increased expression of these along an endothelial cell layer indicates tight junction formation and low permeability, as in a fully functional BBB. Besides immunofluorescence, fluorescently labelled dextran, such as fluorescein isothiocyanate-dextran (FITC-dextran), is commonly used for assessing the endothelial barrier permeability^{82,169,171}. Using dextran of various molecular mass under different conditions will give an indication as to how functional the barrier is. If a larger mass can pass freely, shown by an increase in fluorescence, then this indicates an impairment in functionality and increased permeability.

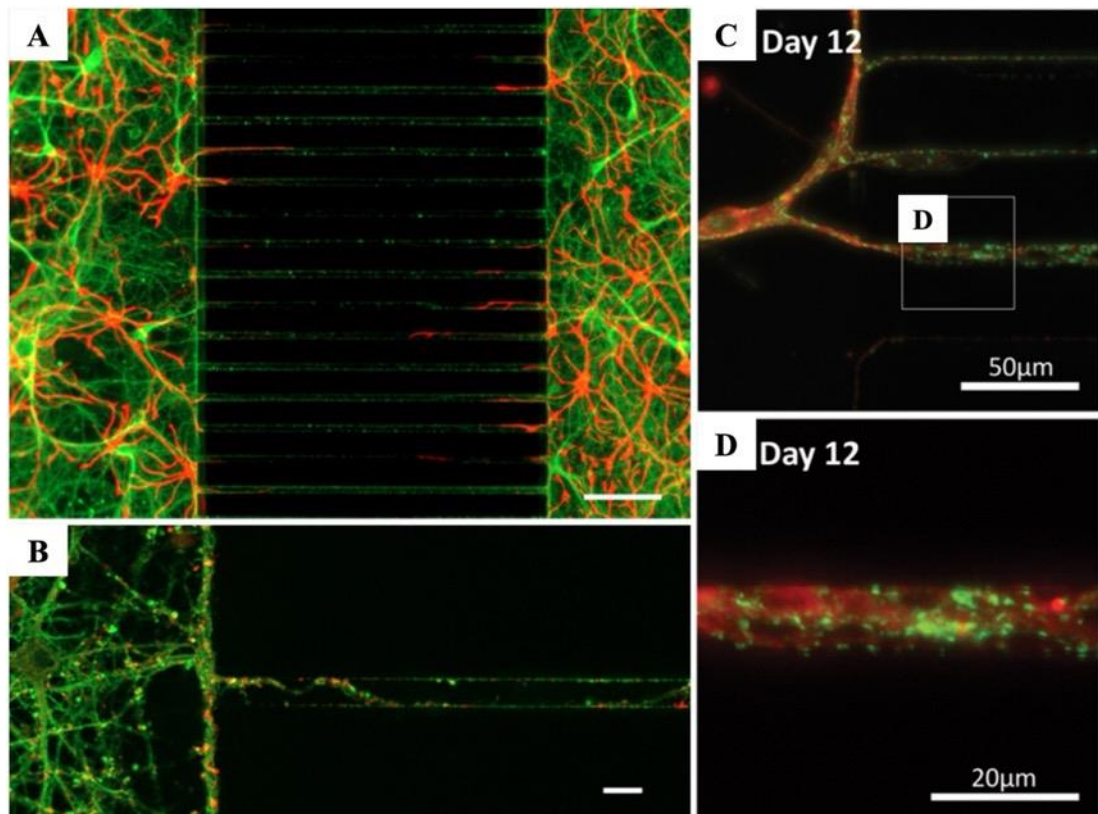


Figure 1.11. Immunofluorescent staining allows visualisation of the cell networks formed and indicates the proteins and structures present. (A) Cellular networks formed within microfluidic culture chambers separated by microchannel arrays, where neurites (green, β III-tubulin) cross between chambers while astrocytes (GFAP, red) do not. (B-D) Immunocytochemistry also enables visualisation of the neurites within microchannels (green, β III-tubulin) and subsequently the presence of synaptophysin (red), which can indicate synapse formation between cell populations. A & B taken from¹²⁵ (open access: CC BY 4.0) and C & D taken with permission from¹³⁴. Scale bars = (A) 100 μ m and (B) 20 μ m.

1.3.5.2. Electrophysiology and interfacing with microelectrode arrays (MEA).

Electrophysiology is performed on live cell cultures and can be used to give functional information pertaining to the cells and networks formed. This technique measures the ionic currents across cells to investigate signalling mechanisms, circuitry and physiological characteristics. Traditional methods for electrophysiological readouts *in vitro* include patch clamping to measure the current or ion flow in whole cells, isolated membrane sections, or tissue sections¹⁷⁷. This is often limited, however, to measuring the activity of individual cells and is a time consuming and labour-intensive method with low-throughput analysis¹⁷⁸.

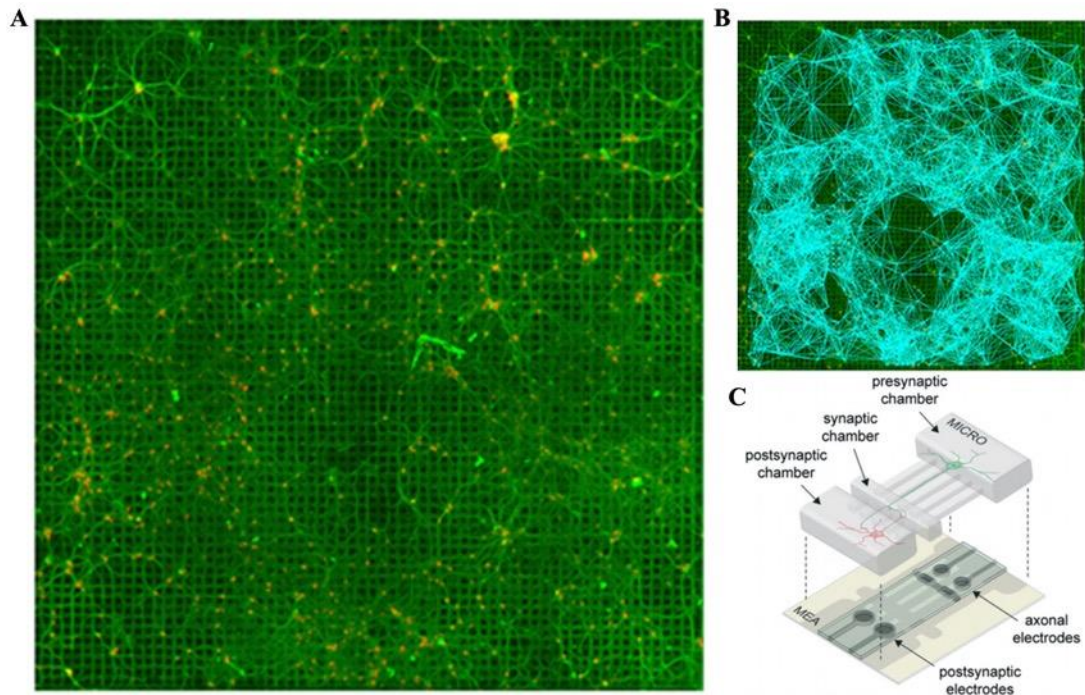


Figure 1.12. Interfacing microfluidic and MEA technology enables stimulation/recording of whole cell population activity as well as spatially and temporally controlled stimulation/recording. (A) Primary rat hippocampal cells cultured on a 3Brain MEA platform. Electrodes shown by black squares, β -III tubulin stained green, and neuron nuclei/NeuN stained red. (B) Structural connectivity of the neuronal network developed, showing a high degree of connectivity and branching between the cells. (C) Example of PDMS microfluidic device and MEA platform for improved spatial and temporal manipulation. A-B taken from¹⁷⁹ (open access CC BY 4.0) and C taken with permission from¹⁸⁰.

In microfluidic devices, electrophysiological activity is often measured by a microelectrode array on which the cells are cultured (**Figure 1.12A**). This enables both stimulation and recording of the activity in larger populations of cells, avoiding invasive mechanical interfacing. The data gained from these recordings can be used to create structural (**Figure**

1.12B) and functional maps of the cell networks¹⁷⁹. Further, compartmentalisation enables temporal and spatial application and recording of activity in specific regions or subpopulations. For example, a two-chamber device similar in design to the Taylor device^{122,126} has been interfaced with an MEA to provide separate pre- and postsynaptic electrode arrays depending on the chamber (**Figure 1.12C**)^{180,181}. Here, the electrodes in the presynaptic chamber can stimulate that neuronal population while the electrodes in the postsynaptic chamber can record the subsequent activity in another environmentally isolated but synaptically connected population. This set-up would also have implications in drug discovery whereby the downstream or indirect effects of a drug could be measured^{182,183}. Here, with controlled drug application to one population, the electrical activity in the adjacent population can be recorded to determine how the stimulation is relayed via synaptic signalling. Further, MEAs are useful tools for studying the origins of epilepsy and real-time analysis of bursting activity, and as screening tools to aid in the development of novel therapeutics^{114,184}. Despite the higher throughput offered using this method, cells must be cultured directly on the MEA. Here, the typical substrate used is polished silicon, which limits microscopic analysis, however recent advances have utilised glass substrates for direct patterning of electrodes to aid in imaging¹⁸⁰.

1.3.5.3. Calcium (Ca²⁺) imaging.

Calcium imaging is a live cell fluorescence imaging method that can be used to provide functional information, without the use of complex equipment. In a similar manner to MEAs, Ca²⁺ imaging can be used to stimulate and monitor activity of whole cell populations or selectively stimulate those in fluidically isolated microenvironments. However, microfluidic devices can be more easily interfaced with standard microscopy set-ups as a means of monitoring cellular activity, and standard culture substrates like glass coverslips can be used. In this technique, a fluorescently labelled Ca²⁺-sensitive dye is used to monitor changes in intracellular calcium, directly related to changes in the fluorescence intensity, to be measured over time. Changes in Ca²⁺ levels correlate with intracellular calcium signalling seen during synaptic activity. Ca²⁺ has a role in almost all cellular tasks and in the nervous system it acts as a secondary messenger, regulating synaptic transmission and plasticity, via neurotransmitter release, and ultimately neuronal survival. This is therefore a useful method for monitoring electrical activity in both individual neurons as well as neuronal networks.

Common fluorescent probes used to monitor changes in intracellular calcium include Fura-2, Fluo-4 and Rhod-2. Fluo-4 is one of the most widely used single wavelength indicators. It has

a peak absorption at around 490 nm and peak emission around 520 nm, making it ideal for use with common 488 and 525 emission/excitation light sources and green fluorescent protein (GFP) filter sets. The relatively low affinity for Ca^{2+} makes it suitable for measuring high Ca^{2+} concentrations without saturation. Loading the dye as an acetoxymethyl (AM) ester enables passage across the cell membrane, improving intracellular delivery^{185,186}. Further, the dye directly binds cytosolic Ca^{2+} leading to a significant increase in fluorescence. Here, the intensity is sensitive to changes in Ca^{2+} concentration relating to calcium signalling. Recently, the fluorescein based Fluo-8 AM has been used due its increased signal intensity over Fluo-4, as well as its ability to be loaded at room temperature.

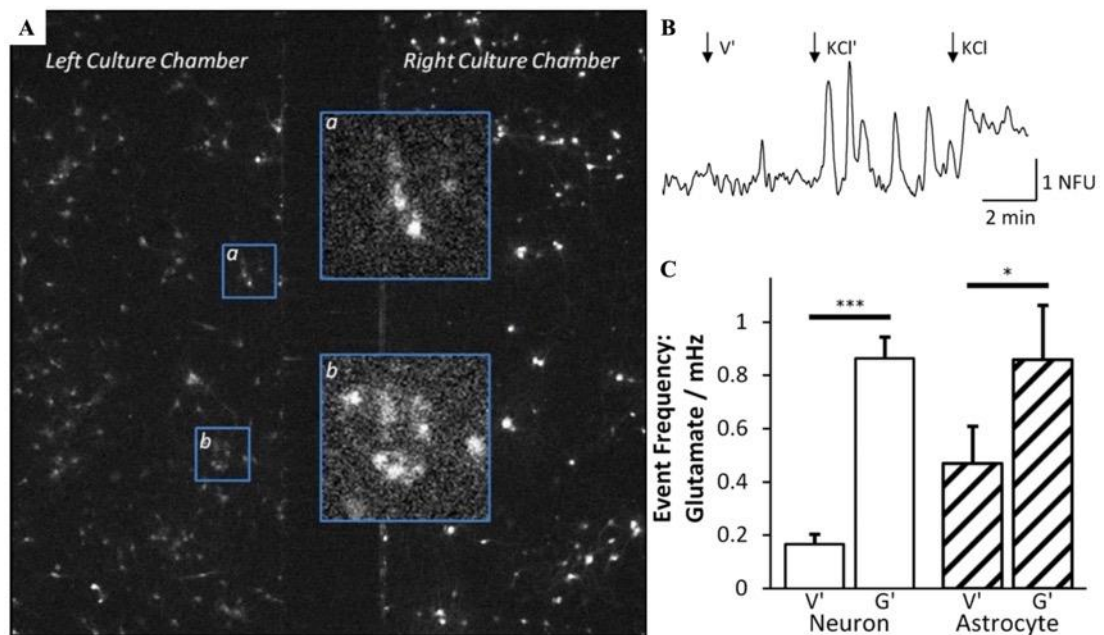


Figure 1.13. Ca^{2+} -sensitive dyes enable the analysis of calcium mediated signalling in neuronal populations cultured in microfluidic devices. (A) Under fluorescence microscopy, the intensity of the dye changes in response to stimulation. The bright white spots highlighted in a and b represent regions of interest corresponding to the neuron/astrocyte soma. (B) Fluorescence intensity trace for a single neuron, showing an increase in intensity following both indirect (KCl') and direct (KCl) stimulation. (C) Analysis confirmed that both neurons and astrocytes show significantly increased frequency of calcium events following indirect stimulation using glutamate (G') compared with direct vehicle (V') application. * = $p < 0.05$, *** = $p < 0.001$. Images taken with permission from¹³⁴.

Ca^{2+} imaging has been used to confirm synaptic connectivity between twin neuronal populations in fluidically isolated and distinct microenvironments¹³⁴. By manipulating fluid volumes across the device, stimulants can be selectively applied to one region and the

fluorescence intensity monitored across multiple chambers (**Figure 1.13**). Following the application of glutamate and high potassium solutions, they showed that both neurons and astrocytes illicit a significant increase in calcium events when indirectly stimulated. As the overall flow across microchannels opposes the diffusion of the stimulant, any response to this in the unstimulated chamber will be caused by synaptic communication between the two neuronal populations. This has applications in both drug discovery and improving the understanding of the mechanisms governing synaptic signalling in disease. Another study created multiple isolated neuronal populations in order to study spreading toxicity induced by glutamate excitotoxicity⁴⁹. Ca²⁺ spikes in the downstream networks confirmed an increased, but deteriorating, excitation of these cells. Further, they demonstrated how this could be used to study neuroprotective mechanisms for acute neuronal death as is the case in stroke and trauma.

1.3.6. Remaining challenges constraining microfluidic use.

Despite the benefits that microfluidics can offer, as well as the plethora of applications demonstrated in the literature, there is still relatively poor uptake within neuroscience labs. Overall, the field has had limited impact outside of specialist labs in academia and little impact directly within the biomedical industry. However, its use is becoming more widespread in applications such as cancer research, where the ability to engineer tumour spheroids and the tumour microenvironment more precisely can provide high throughput, personalised tools for drug screening^{187–189}. Common problems highlighted include the complexity of use and repeatability issues, as well as the high expense and lack of specialist fabrication equipment associated with in-house fabrication^{119,190}. Further, there are limited commercially available devices directed specifically towards neuroscience. Of those available, such as XonaChips® (Xona Microfluidics) or the OrganoPlate® (MIMETAS), the applications are limited, given the fixed device layouts and customisation is typically not available. As a result, there is an opportunity for the development of a more universal microfluidic platform able to cater for a wide array of research activity.

There is also a desire to move towards a whole brain-on-chip style microfluidic system. The majority of models created use neurons from only one brain region, apart from BBB and co-culture models, some of which were highlighted above. These therefore lack the highly ordered connectivity and architecture found *in vivo*. As mentioned previously, organisation in the brain is complex, with multiple regions with distinct structural, functional and cellular organisation³³. Regular brain function is reliant on interactions between hierarchical neuronal

networks across multiple regions. Further, the networks created using cells from multiple regions in microfluidic compartments have shown both different cell composition and electrophysiological activity, compared to networks created from a single region⁴⁴. This highlights the brain region dependent manner of neuronal activity and the importance of multi-regional models for fully recapitulating *in vivo* network dynamics.

Clearly, there are still challenges for recreating *in vivo* networks using human cells³³. For instance, directing the lineage of iPSCs into specific neuronal subtypes has not been fully realised, with low efficiency and the requirement for expensive reagents. Further, viability of the cells is often impacted by the prolonged culture times required for maturation⁹⁷. Whilst these challenges are difficult to overcome, it is possible to focus attention on fabrication and the microsystem components for directing the network formation. A substantial footprint would be required for creating a complete monolithic brain-on-a-chip style device, which would be unattractive and quite daunting for novice users. As such, the ease of use and accessibility must be considered and so a Lego[®]-like microfluidic platform could offer a solution, given its simple design yet endless possibilities and reconfigurability.

1.4. Modular microfluidics.

For a particular field to embrace microfluidic technology, the benefits it can bring must outweigh the difficulties associated and must provide sufficient capabilities above traditional techniques¹⁹¹. Further, devices must be easy to use and provide consistency across all applications. This is where a modular platform has the potential to rapidly improve biomedical research. Such a system could provide flexibility and reconfigurability, as well as ease of assembly and potential reuse of components. Thus, overall costs and time associated with fabrication can also be reduced. Currently, there are discrepancies between modular microfluidic platforms documented in the literature, with little consistency in the overall design, as well as the methods used for fabricating and connecting separate components^{192,193}. Further, there has been a greater focus on diagnostic or fluid mixing applications, as opposed to complex cellular and biological modelling^{119,192,194–202}. This represents an opportunity for the development of an elementary system, utilising plug and play style interconnections, that is aimed towards neuroscience and other organ-on-a-chip applications. The optimal platform would consist of a finite set of components, each with a specific function. This allows for multiple assays to be performed using one system, depending on the order of assembly and type of components used.

Given the specific challenges to drug discovery for brain disorders, owing to the inability to directly probe brain tissue, the translational issues with animal models and the blood-brain barrier, improved and more relevant *in vitro* models are essential. The availability of a modular and customisable platform for neuroscience research would enable a researcher to purchase premade components that can be assembled to produce a fully functioning device, specific to their needs. Subsequently, more complex *in vitro* neuronal networks with defined spatial arrangement can be created, enabling the development of more advanced assays for investigating how they function normally and how the circuitry is implicated in disease. Further, if used in conjunction with human cells (e.g., patient-derived iPSCs), these more advanced and more physiologically relevant *in vitro* models can act as screening tools in drug discovery. This could enable better predictive accuracy in determining the clinical value of results, thus saving time and, vitally, money in the development process. A modular platform therefore enables flexibility in the production of researcher-specific devices and subsequent directed networks, increasing the complexity and relevance of *in vitro* models and improving predictability of physiological response.

1.4.1. Existing modular microfluidic technology.

One of the earliest examples of a modular system came from Rhee and Burns²⁰³. They introduced a concept of microfluidic assembly blocks (MABs) which were produced in PDMS cast directly onto silicon wafers (**Figure 1.14A**). Besides the microfeatures, the wafer also contained taller wall features for moulding the PDMS. Modular components were then assembled onto a PDMS coated glass coverslip. This design was later improved upon by introducing interlocking features on the lateral interfaces and creating silicon ice cube-like trays for casting components¹⁹⁹. These improvements enabled better alignment of modules and sped up the overall production process. A more recent example produced millimetre-sized interlocking and stackable PDMS components²⁰⁰. These modules had a similar concept, with their tongue-and-groove interfacing mechanism, but on a smaller scale. Assembly of these modules was fully reversible, and the small scale ensured interfacing was reliably leak-free without the use of O-rings.

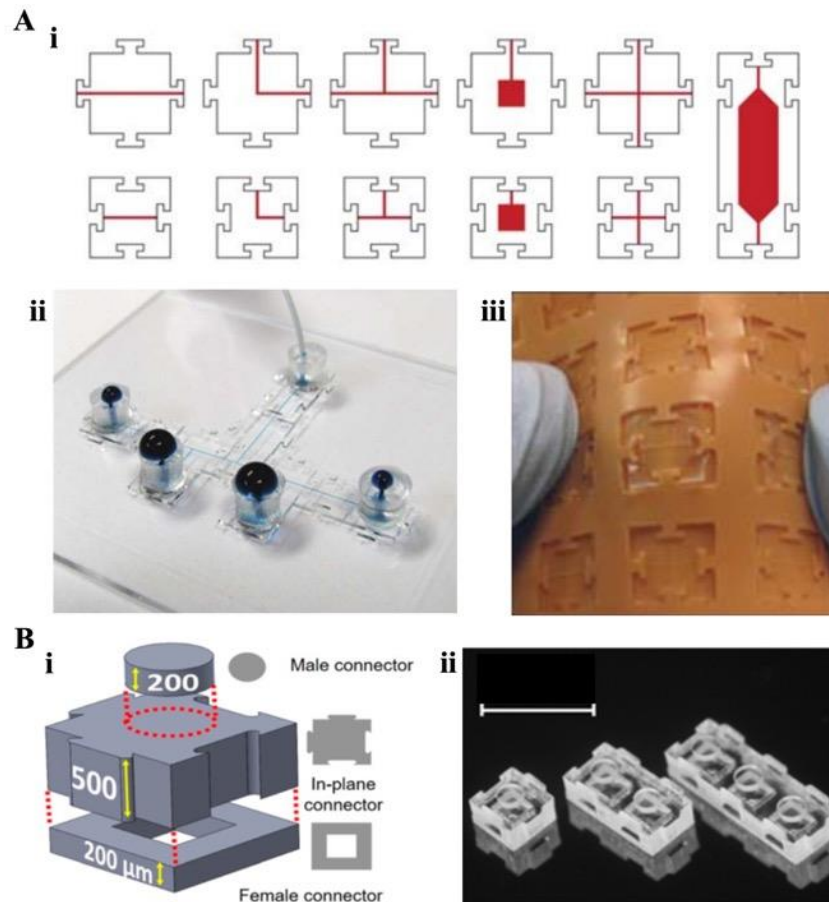


Figure 1.14. Microfluidic assembly blocks provide a good example of interlocking between modular components. (A) Improved MAB concept from ¹⁹⁹ showing (i) individual component layout, (ii) an example of an assembled device and (iii) the silicon mould used to speed up production of the PDMS modules. Images taken with permission from ¹⁹⁹. (B) Recent example of modular PDMS components from ²⁰⁰ showing (i) a schematic of a building block with lateral tongue/groove mechanism and male/female connection for stacking, and (ii) representative examples of PDMS blocks of different footprints. Scale bar shows 2 mm. Images taken from ²⁰⁰ (open access CC BY 4.0).

Whilst this concept provides prefabricated components for assembling user-defined devices, the use of PDMS/adhesive agents for bonding ^{199,203} limits reconfiguration and potential reuse of components. Further, the use of SU8 wall features limits the height of the components that can be produced, with restrictions beyond $\sim 1000 \mu\text{m}$ (1 mm), and so further development would be needed to create well-like features. In another example, the small blocks produced ²⁰⁰ limit the possible applications and would be insufficient for neuronal network formation, given the need for a suitable microchannel array between components (**Figure 1.14B**). However, SU8 does ensure accurate replication and production of microfeatures. Further, the

simple assembly with interlocking features is attractive and it provides interfaces on a flat, continuous substrate.

Other examples have been inspired directly by traditional Lego[®]. These represent the perfect example of an easy to use, consistent and mass producible system of modular component assembly. PDMS modules with the footprint of a typical 2x2 Lego[®] brick have been demonstrated¹⁹⁸ (**Figure 1.15A**). These were cast in 3D printed moulds and assembled on a sheet of laser cut PDMS interfaced on a Lego[®] baseplate. Small protruding/intruding tabs on a given blocks lateral surface confined the interface to a smaller surface area and provided additional pressure to improve bonding and subsequent sealing. Further, they demonstrated the possible 3D stacking of these modules for more complex microfluidic geometries. Whilst the employment of 3D printing moulds provides a rapid method of fabricating, the microfluidic features possible within the geometry of Lego[®] blocks is more limited and would not provide the same degree of accuracy or resolution as photolithography. The studs take up a large portion of the area and so prevent sufficient space for features such as a microchannel array for axonal guidance. The use of a PDMS substrate provides reversible bonding, however, relies on the native hydrophobicity of the material and the conformal bonding with the PDMS blocks. This is weak and typically cannot withstand pressures beyond ~5 psi²⁰⁴.

Another example has utilised Lego[®] bricks directly by micromilling channels in their lateral surfaces (**Figure 1.15B**)²⁰². Channels were sealed on their outer surfaces using a transparent adhesive film and O-rings were used to create a seal between adjacent blocks. Existing bricks were used as the injection moulding process enables rapid, consistent production of components with tolerances less than 50 μm , above that of 3D printing. Further, micromilling enables micron scale dimensions for channels with depths down to 50 μm . Despite the ease of using existing components, this method is still limited to applications directed towards fluid handling and droplets. The injection moulded bricks would not offer the same advantages as PDMS, including gas permeability and optical clarity for microscopic analysis, important features in biomedical analysis. The micromilling procedure used here would not cater for channels <50 μm in depth, and the requirement for O-rings between adjacent bricks does not allow for a continuous flat culture substrate. They have noted, however, that more advanced, industrial milling procedures would allow for features in the 10s of micron range²⁰⁵. This is controlled by the drill bit used and one of such a small scale leads to greater costs and brittleness. Micromilling is also confined to harder plastics such as acrylic and not compatible with elastomeric materials such as PDMS.

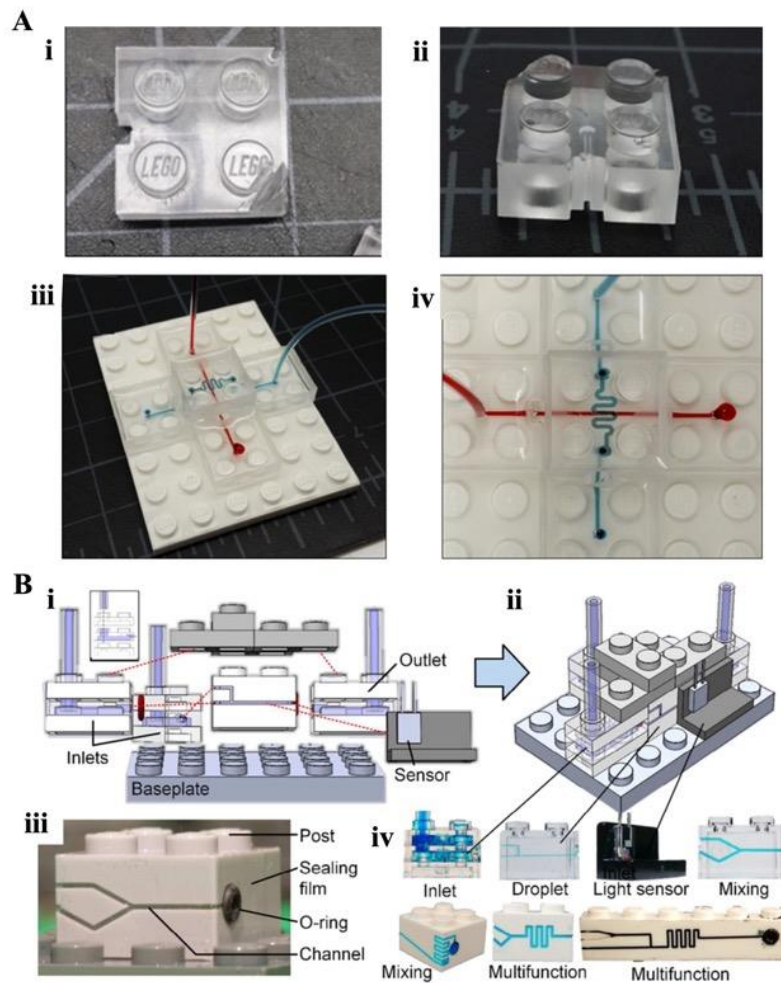


Figure 1.15. Lego[®] has inspired multiple modular microfluidic designs due to its accessibility, consistency between components and ease of use. (A) PDMS blocks have been produced based on the dimensions of a 2x2 Lego[®] brick. (i-ii) Representative example of a PDMS cast, with studs for 3D interfacing and small intruding tabs for 2D interfacing. (iii-iv) Example 3D device assembled using the PDMS Lego[®] bricks, with the blue channel running over the red. Images taken with permission from¹⁹⁸. (B) Existing Lego[®] have also had channels micromilled directly into their sides then sealed using a transparent adhesive film. (i-ii) Schematic of the platform showing individual blocks assembled into a multifunctional device. (iii) An individual Lego[®] brick showing the machined channel and an O-ring for a leak-free seal at the interface between adjacent bricks. (iv) Multiple blocks were produced, each with individual functions. Image taken with permission from²⁰².

One of the most common methods seen for fabricating modular components is 3D printing. For casting PDMS components, this would enable the production of moulds with all the required features. For neuroscience, microstructures for culture chambers, structures for wells, wall features for controlling depth of modules, and interfacing features could all be printed in

one piece. This enables faster production of components with minimal extra processing required. However, affordable and reliable printing is not achievable for features below hundreds of microns, depending on the type of printer used. For instance, stereolithography (SLA) printers offer better resolution but are typically limited to achieving features $\sim 100\ \mu\text{m}$, controlled by the resolution of the light source and the properties of the resin^{206,207}. Recently, a custom SLA 3D printer has demonstrated the reliable creation of channels as small as $18 \times 20\ \mu\text{m}$ ²⁰⁷. On the other hand, fused deposition modelling (FDM) printers cannot create features smaller than $\sim 300\ \mu\text{m}$, controlled by the size of extrusion nozzle. A recent FDM 3D printer designed specifically for microfluidic components by Dolomite is still only able to print down to around $150\ \mu\text{m}$ in width²⁰⁶. In general, 3D printing therefore fails to produce microscale features with the same degree of accuracy as photolithography, and thus would be more suitable for creating larger structures and moulds.

1.4.2. Body-on-a-chip devices.

Beyond the use of modular microfluidic devices for neuroscience applications, such a platform would also have positive implications on the development of body-on-a-chip devices^{208–210}. The ability to combine multiple organ systems *in vitro* allows an analysis of specific organ-organ interactions. Further, whilst specific organ-on-chip devices can enable predictive power for choosing drug candidates with the greatest potential, they provide no information on the effects on whole organisms and toxicity to other systems. In this case, a modular platform would provide the ability to combine multiple components, each with a separate cell type, interconnected to recapitulate *in vivo* organisation. Data obtained from such *in vitro* studies would be useful predicting the systemic response and could reduce the requirement for Phase I trials on healthy individuals²¹⁰. Ultimately, multi-organ-on-a-chip systems will contribute to a reduction in animal use and speed up the drug development process through the improved predictability of response and relevance to human physiology. They also have the potential to make investment in drug discovery more attractive and less risky for complex disorders, such as those associated with the CNS that have higher failure rates.

There have been few attempts at developing full-system models due to the complexity of finding a suitable medium and material that can support the requirements of all organs. However, there are examples of multi-organ platforms in the literature, with varying levels of complexity depending on the number of systems and the components involved^{211–216}. A microphysiological system (MPS) has recently been developed with 4, 7 and 10 different systems integrated, described as a physiome-on-a-chip²¹⁷. The 10 system MPS integrated

liver, immune, intestinal, endometrial, neural, cardiac, pancreatic, kidney, skin and skeletal muscle components (**Figure 1.16B**). They demonstrated the potential of such tools alongside pharmacological modelling to aid in pre-clinical drug discovery and modelling disease. However, challenges remain regarding the long-term functionality and the substantial resources required for high-order (10 systems) interactions. Ultimately, body-on-a-chip systems can prove useful tools in the drug development process and the creation of a modular platform would provide more flexibility in choice of systems that are integrated, depending on the specific drug interactions or disease under investigation.

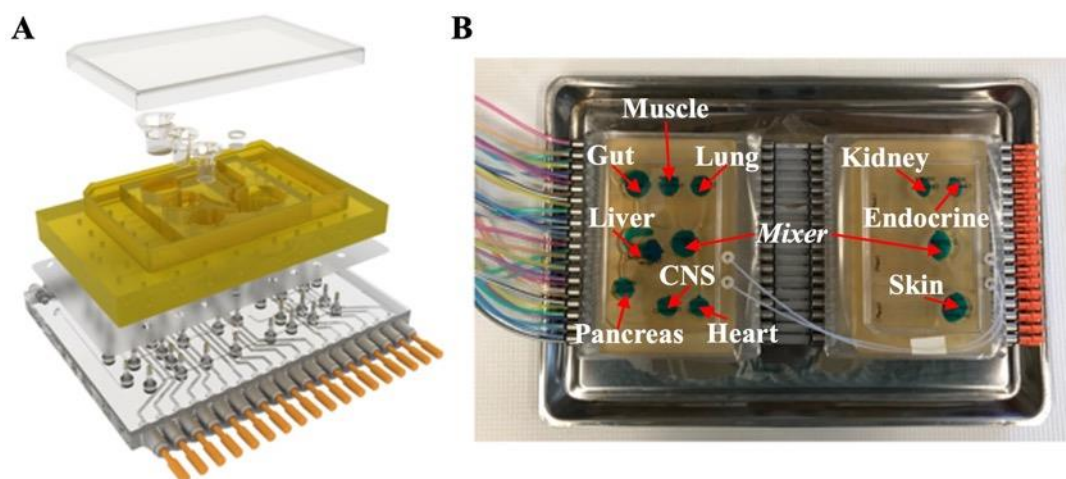


Figure 1.16. Microfluidic multi-system organ-on-a-chip devices have been developed. (A) Schematic of a 4-system physiome-on-a-chip device. (B) 10-system physiome-on-a-chip device comprised of a 7-system chip (left) and 3-system chip (right), each with a mixing well for linking the separate cultures, connected via tubing. Image recreated from²¹⁷ (open access CC BY 4.0).

1.5. Project motivations and objectives.

From existing literature, it is clear there are numerous fabrication and interfacing methods available for creating a modular microfluidic platform. However, one of the main constraints in creating a modular system specific for neuroscience research is the complex geometry required for cell-cell network formation. The interface between separate components must allow physical cellular connectivity and direct axonal outgrowth between separate components, whilst the separate cell populations remain environmentally isolated. Further, the regions enabling this compartmentalisation are in the order of microns, with typical microchannels being no more than 500 μm in length, 10 μm wide and up to 10 μm tall. This helps ensure only axonal connections transverse between compartments and prevents cells entering from the culture chambers. Photolithography therefore remains the most appropriate and reliable method for creating features at this scale¹²¹, however, other fabrication methods

such as 3D printing could prove useful for moulding and creating interlocking structures. For interfacing and creating a seal between separate components, typical methods using tubing and O-ring integration would not enable direct cellular connections between components and so are unsuitable for use here. Further, the size of any interlocking feature must be sufficiently large to accommodate the compartmentalising features and enable leak-free lateral assembly, whilst avoiding dead space. Additionally, the platform must have a suitable biocompatible substrate that runs across the entirety of the assembled device to provide a continuous culture surface between modules.

Given all the above, a modular microfluidic platform must encompass a range of functional modules to have the greatest potential and scope. To achieve this, it is proposed that a modular system of PDMS microfluidic components can be developed, based on Lego[®], and using standard microfabrication techniques. The microfluidic features will be based on the Taylor design and previous studies within our research group^{125,134}. The goal with this is to enable larger *in vitro* neuronal networks to be built beyond those found in the literature, where single networks are the norm. Whilst there are exciting examples of *in vivo*-like circuitry demonstrated, the constraints posed by fixed device layouts limits their use to that which the device was designed for. Further, the ability to control the directionality of networks would be a useful feature, providing more *in vivo*-like circuitry and ability to model specific networks. Further, it is proposed that a modular system should also provide components for 3D culturing to further improve physiological relevancy and enable *in vitro* blood-brain barrier modelling. Ultimately, a modular platform offers greater flexibility, easing the constraints posed by fixed microfluidic layouts in commercially available devices and reducing the need to completely refabricate devices when a new design and layout is required, typical with in-house monolithic device production. A modular platform would therefore enable user-definable device production for the development of more *in vivo*-like conditions and bespoke circuitry. Such a platform would provide a useful tool for assessing network dynamics in both normal and diseased states and ultimately, more relevant pre-clinical models for drug discovery. As the brain relies on complex networks interconnected across multiple regions for normal functioning, any impairment can have wide ranging consequences. Therefore, recreating specific networks *in vitro* would allow a better understanding of the processes behind these functional networks as well as investigating drug interactions, helping develop better therapies. By focusing on the flexibility of a modular platform, there is much greater freedom to build a wide range of these specific circuits and more accurately model their function and dysfunction.

1.5.1. Thesis outline.

Chapter 1 highlighted the complexity of the CNS, the difficulty in treating disorders associated with it and the need for improved *in vitro* models to help better understand underlying function and dysfunction. The chapter then went on to outline current microfluidic technology used in *in vitro* neuroscience research and how this can be improved upon by developing a modular platform to help increase uptake of the technology and ultimately provide greater flexibility for novice users.

Chapter 2 describes the materials and the methods used throughout the project to both produce and assemble the modular devices, and isolate and culture the primary hippocampal cells.

Chapter 3 provides an overview of the development of the modular platform. In particular, this chapter details the selection of a suitable biocompatible substrate for enabling reversible sealing with PDMS and subsequent culturing of primary hippocampal cells. The chapter then goes on to describe the process of producing modular components and their subsequent assembly into devices.

Chapter 4 builds on the work of Chapter 3 to produce more suitable microfluidic geometry that enabled multiple modules to be combined into devices, with subsequent cell connectivity between each. This chapter also provides a critical evaluation of the modular platform produced and highlights some of the remaining challenges.

Chapter 5 provides a characterisation of the modular platform in its current form, using simple assays with primary hippocampal cultures, to demonstrate its potential as well as some of the applications amenable to neuroscience research.

Chapter 6 provides an overall discussion of the project with the major outcomes along with the remaining challenges and future work that should be undertaken to explore further applications, as well as improve the overall platform and ensure its usability.

1.5.2. Publications.

1.5.2.1. Journal articles.

Mearity, D., Vroman, R., Kriek, M., Downey, P., Bushell, T.J., Zagnoni, M. ‘*A modular microfluidic platform to enable complex and customisable in vitro models for neuroscience*’, Lab on a Chip. 2022, 17. doi: 10.1039/d2lc00115b.

1.5.2.2. Conference presentations.

Mearity, D., Bushell, T.J., Zagnoni, M. ‘*Developing a modular neurotechnology*’. BioMedEng19 Conference, 5th – 6th September 2019, London, UK (in-person poster presentation).

Mearity, D., Bushell, T.J., Zagnoni, M. ‘*Developing a modular microfluidic platform for neuroscience research*’. FENS20 Virtual Forum (Federation of European Neuroscience Societies), 11th – 15th July 2020 (virtual poster presentation).

Mearity, D., Bushell, T.J., Zagnoni, M. ‘*Development of a modular microfluidic platform for enabling novel research in neuroscience.*’ SNG21 (Scottish Neuroscience Group Meeting), 27th August 2021 (virtual poster presentation).

Mearity, D., Bushell, T.J., Zagnoni, M. ‘*Development of a modular microfluidic platform for enabling novel research in neuroscience*’. BioMedEng21 Conference, 6th – 7th September 2021, Sheffield, UK (in-person poster presentation).

Chapter 2. Materials and methods.

2.1. Materials.

2.1.1. Equipment and materials.

ARSeal™ 90880 (sample)	Parafix Adhesive Solutions, UK
AxioObserver 5 microscope	Zeiss, Germany
AxioObserver Z1 automated microscope	Zeiss, Germany
Luca R EMCCD camera	Andor Technology, Northern Ireland
ORCA-Flash 4 digital CMOS camera	Hamamatsu Photonics, Japan
Pico A plasma asher	Diener Electric, Germany
Polycarbonate (PC)	Goodfellow, UK
Polymethylmethacrylate (PMMA)	Goodfellow, UK
Silicon wafers	PI-KEM Ltd, UK
ThermalSeal® RTS	Sigma-Aldrich, UK

2.1.2. Chemicals and reagents.

Alexa Fluor 488 donkey anti-rabbit (A21206)	ThermoFisher, UK
Alexa Fluor 488 goat anti-mouse (A32723)	ThermoFisher, UK
Alexa Fluor 555 goat anti-rabbit (A21428)	ThermoFisher, UK
Alexa Fluor 555 donkey anti-mouse (A31570)	ThermoFisher, UK
Alexa Fluor 633 goat anti-chicken (A21103)	ThermoFisher, UK
B27 supplement	ThermoFisher, UK
Bovine serum albumin (BSA)	Sigma-Aldrich, UK
Calcium chloride (CaCl ₂)	VWR, UK
Chicken anti-GFAP antibody (AB5541)	Sigma-Aldrich, UK
Rabbit anti- α -synuclein (pSer129, AB51253)	Abcam, UK
D-glucose	Sigma-Aldrich, UK
Dulbecco's PBS	ThermoFisher, UK
EpoxAcast™ 690 epoxy resin	Bentley Advanced Materials, UK
Ethylene-di-amine tetra-chloro-acetate (EDTA)	Sigma-Aldrich, UK
Fluo-8 AM	Abcam, UK

Foetal bovine serum (FBS)	Sigma-Aldrich, UK
HEPES	Sigma-Aldrich, UK
Hydroxypropyl methylcellulose (HPMC)	Sigma-Aldrich, UK
L-glutamate	Sigma-Aldrich, UK
L-glutamine (200mM)	ThermoFisher, UK
Magnesium chloride (MgCl ₂)	Sigma-Aldrich, UK
Magnesium sulphate (MgSO ₄)	VWR, UK
Methanol	Fisher Scientific, UK
Microposit EC solvent	A-Gas Electronic Materials, UK
Monosodium phosphate (NaH ₂ PO ₄)	VWR, UK
Mouse anti-synaptophysin antibody (AB8049)	Abcam, UK
Neurobasal-A	ThermoFisher, UK
Ostemer 322 resin	A-Gas Electronic Materials, UK
Papain	Sigma-Aldrich, UK
Paraformaldehyde, 4% (PFA)	ThermoFisher, UK
Phosphate-buffered saline (PBS) tablets	Sigma-Aldrich, UK
Poly-L-lysine (PLL) hydrobromide	Sigma-Aldrich, UK
Poly-L-ornithine (PLO)	Sigma-Aldrich, UK
Potassium chloride (KCl)	VWR, UK
Rabbit anti-βII-tubulin antibody (T2200)	Sigma-Aldrich, UK
Mouse anti-βII-tubulin antibody (AB78078)	Abcam, UK
Sodium bicarbonate (NaHCO ₃)	VWR, UK
Sodium chloride (NaCl)	Fisher Scientific, UK
SU8 3005/3010/3035	A-Gas Electronic Materials, UK
Sucrose	VWR, UK
Sylgard™ 184 (PDMS base and curing agent)	Ellsworth Adhesives, UK
Trichloro(1H,1H,2H,2H-perfluorooctyl) silane	Sigma-Aldrich, UK
Triton-X 100	Sigma-Aldrich, UK
Trypan blue	Sigma-Aldrich, UK

2.2. Microfluidic systems.

2.2.1. Design.

All designs were created using CorelDraw computer aided drawing package (multiple versions; Corel, ON, Canada). Dimensions for the x and y plane of the device geometry were integrated into masks (channel length and width), whilst the thickness of the resist determined the dimensions in the z plane (channel height). The photomasks in this project were designed for use with a negative photoresist and created externally by JD Photo Data, UK. Microchannel layouts were printed on glass-chrome masks, as these provide better resolution for smaller features (10 μm width), while the larger culture channel and well layouts were printed on acetate masks (1500 μm width). Designs for all device configurations are based on the Taylor design¹²² (**Figure 1.5**) and those previously used within the group^{125,134}. Masks were designed with features to provide improved alignment between the two layers (**Figure 2.1A**). However, in glass-chrome masks, the microchannels were extended beyond the length required in the final device, allowing for misalignment between this layer and the culture chamber layer (**Figure 2.1B**) due to manual procedures.

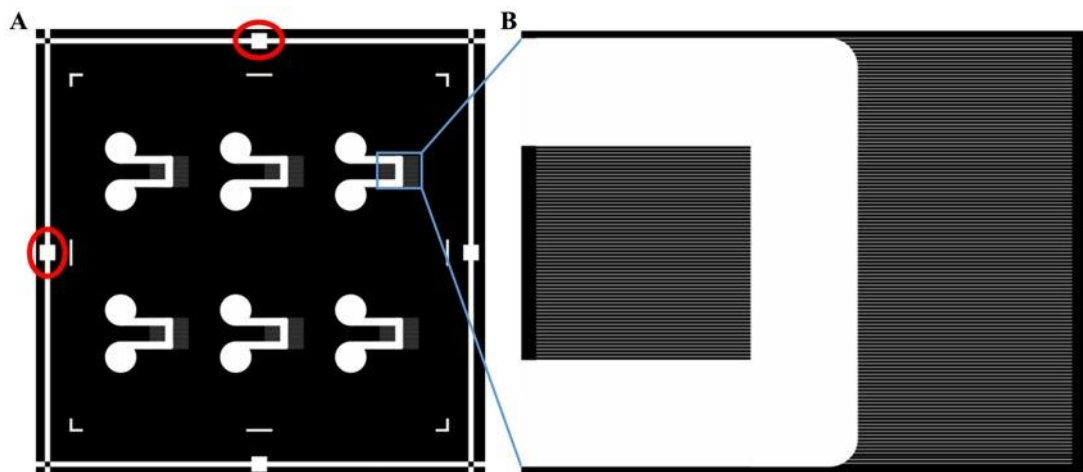


Figure 2.1. Example photomasks used to create devices in a two-layer photolithography process. (A) An example of an acetate mask (well and culture chambers) and glass-chrome mask (microchannels) overlaid to show the positions of the microchannels. Red circles indicate alignment features. (B) The length of microchannels in the glass-chrome mask was 7.5 mm, as opposed to the desired 500 μm between culture chambers. This allows for misalignment of the acetate mask on top and allows multiple designs to work with one glass-chrome mask layout.

2.2.2. Master wafer fabrication.

Master wafers used in this project were fabricated using standard photolithography techniques in a two-stage process, resulting in silicon wafers with patterned SU8 photoresist on their surface (**Figure 2.2**). Wafers were cleaned by sonicating for 3 minutes each in acetone, methanol and isopropanol, then blow-dried with nitrogen gas. Wafers were then dehydrated by placing on a hotplate (180°C, 45-60 minutes) and left to cool to room temperature. The first layer of SU8 (3005), for the microchannels, was spun on the wafer (4000 rpm, 30 s) to create a thickness of ~5 µm (**Figure 2.2Ai and 2.2B**). Alternatively, SU8 3010 was spun at 1500 rpm to achieve a height of ~14 µm. This was soft baked for 1 minute at 65°C followed by 5 minutes at 95°C. Once cooled, the SU8 layer was exposed to collimated UV light, patterned by the photomask, for 60s with an additional optical filter (65CGA-360, Newport Corporation, CA, USA). This helps delivery of parallel, monochromatic light at 365 nm, which minimises diffraction and helps improve resolution of small features. The wafer was then post-baked for 30s at 65°C followed by 3 minutes at 95°C and left to cool completely to reduce internal stress in the resist. Exposed SU8 was developed for 3 minutes in Microposit EC solvent to reveal the microchannel layout. This was hard baked for 5 minutes at 95°C, 5 minutes at 150°C, and 15 minutes at 210°C then was left to cool to room temperature. The hard baking step also dehydrated the wafer, providing good adhesion to the subsequent resist layer. SU8 3035 was spun over the first layer (800 rpm, 30 s) to achieve a height of ~ 100 µm (**Figure 2.2Aii and 2.2C**) for the well and culture chamber layouts. This was soft baked at 65°C for 7 minutes, followed by 25 minutes at 95°C. The acetate mask for the second layer was manually aligned using markers in the first layer, then exposed to collimated UV light for 90s also with the optical filter on top. The resist was baked at 65°C for 1 minute then 95°C for 5 minutes, before being allowed to slowly cool down to room temperature. SU8 was again developed in solvent, and the features checked under an upright microscope to ensure they are fully visible. The development of each layer was tested by rinsing with isopropanol. If a milky substance was observed, then further development was required as this indicates non-crosslinked resin. This was done by placing the wafer in fresh developer then testing again after 1-2 minutes.

The finished wafer was checked under an upright microscope (Nikon Optiphot) to ensure features were fully developed. Finally, the patterned SU8 was hard baked for 5 minutes at 95°C, 5 minutes at 150°C, then 15 minutes at 210°C. The wafer was left to slowly cool to room temperature. Finally, the wafer was exposed to oxygen plasma (100% power/200W, 2 minutes) then placed in a vacuum desiccator with 50 µl of trichloro(1H,1H,2H,2H-

perfluorooctyl) silane for 45 minutes under vacuum. This coating process prevented adhesion of PDMS on the wafer during soft lithography.

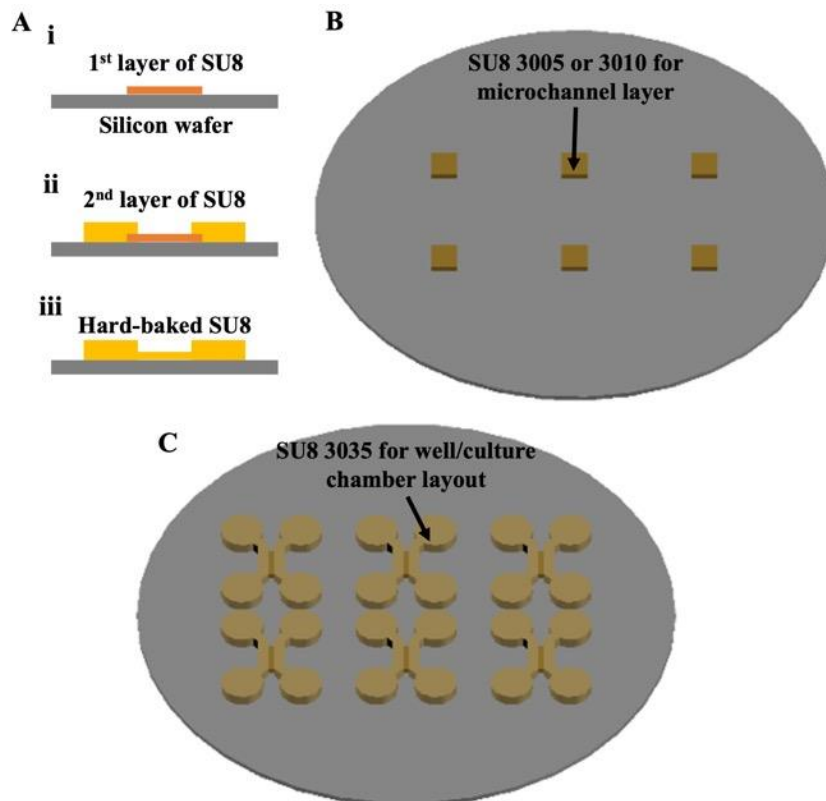


Figure 2.2. Schematic representation of the photolithography procedure for patterning microfluidic features in SU8. (A) The photolithography two-stage process of SU8 deposition. (i) The first layer is patterned onto the silicon wafer then (ii) the second layer is aligned on the first layer and (iii) the final SU8 pattern can be hard baked and silanised prior to soft lithography. (B) First layer of SU8 on the silicon wafer, representing the microchannels. (C) Second layer of SU8 aligned on the first layer to form the channel and well features.

2.2.3. Soft lithography.

PDMS mould was mixed thoroughly with curing agent at a ratio of 10:1 (w/w, PDMS base: curing agent) and poured on the silicon master to achieve a layer of approximately 5 mm. Any trapped air bubbles were removed by placing the wafer with PDMS in a vacuum desiccator and leaving under vacuum for 30-45 minutes. Degassed PDMS was cured at 80°C for 2-3 hours. The SU8 features were replica moulded in the cured PDMS (**Figure 2.3**). Cured PDMS was removed from the master wafer using a scalpel and the layer peeled off. Individual devices were cut out, with inlet and outlet wells for the culture chambers created using a biopsy punch (4-8 mm). Scotch[®] tape was used on the bonding surfaces of PDMS/glass to remove any debris and leave the surfaces clean prior to bonding.

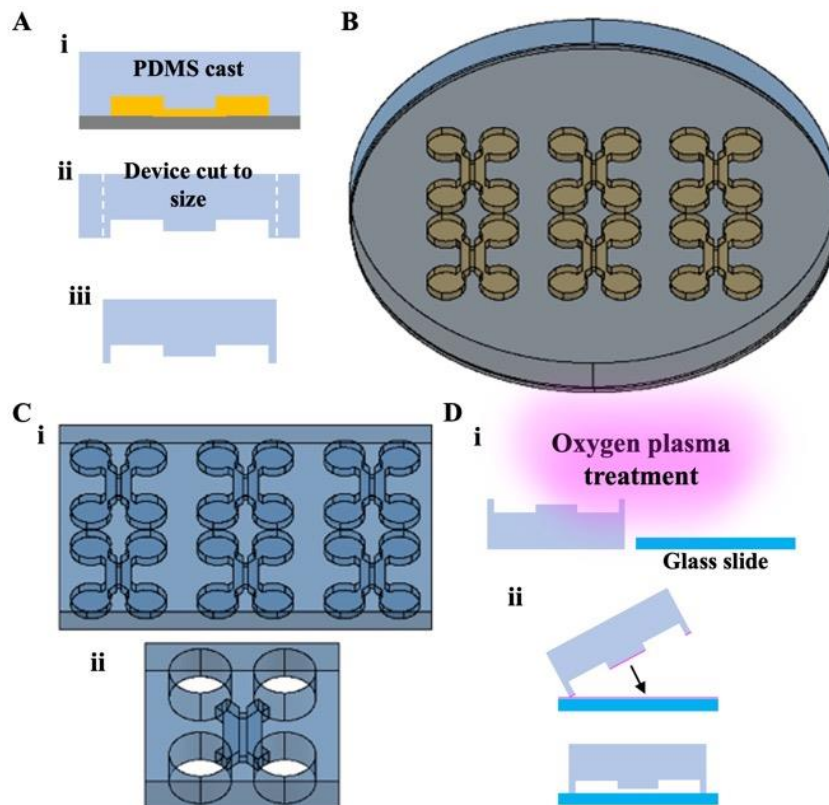


Figure 2.3. Schematic representation of the soft lithography procedure for producing PDMS devices and plasma bonding to glass. (A) Schematic of the soft lithography process. (i) PDMS was cast on the silicon wafer and once cured, (ii-iii) the device cut to size ready for bonding. (B-C) Schematic showing (B) the PDMS on the wafer and (C) individual devices cut from the cured PDMS. (D) To permanently bond devices, (i) the PDMS and a glass coverslip were exposed to oxygen plasma and (ii) brought into contact, forming an enclosed microfluidic device.

2.2.4. Irreversible plasma bonding.

Bonding was carried out using a plasma asher (Pico A, Diener Electronic, Germany). The PDMS and glass coverslips were placed in the asher chamber, feature/bonding side up, and exposed to oxygen plasma (~12 s at ~70% power). The exposed PDMS was then placed on the glass surface feature side down (**Figure 2.3D**), and gentle tapping ensured conformal bonding was achieved over the entire surface. This created the enclosed microfluidic device. Exposure to low-pressure oxygen plasma produced silanol groups (Si-OH) on the surfaces, inducing the formation of Si-O-Si covalent bonds with the loss of water^{204,218,219}, creating a tight and irreversible seal that was able to withstand pressures of 30-50 psi.

2.2.5. Reversible bonding.

To bond devices reversibly, enabling reconfiguration and reuse of devices, pressure-sensitive adhesive (PSA) films were used (ThermalSeal[®] RTS, Sigma Aldrich, UK and ARseal[™] 90880, PARAFIX, UK). Devices were cleaned and prepared as before then carefully placed on a piece of the PSA film with gentle tapping to ensure bonding was achieved between the adhesive and the PDMS. This created an enclosed device, with the PSA film as the culture substrate. Care was taken to avoid applying too much pressure, which could result in channel obstruction.

2.3. Production of modular components.

Moulds for PDMS casting were developed to improve the consistency and size of modular devices with respect to monolithic device fabrication, so to minimise irregularities from hand cutting, which was important for modular device assembly (**Figure 2.4**). All moulds were designed in AutoCAD and exported in STL (for 3D printing) or DXF (for laser cutting) file formats. An Ultimaker FDM (fused deposition modelling) printer operated by technicians in an internal departmental workshop and two SLA/DLP (stereolithography/digital light processing) printers (Bean LCD 3D printer, Kudo3D; ANYCUBIC Photon S, ANYCUBIC, China) were used initially. For improved 3D printing using the SLA printers, models were raised from the print beds and appropriate support points added. SLA 3D printed components were soaked in isopropyl alcohol (IPA) then post-cured using a UV lamp (UV Light Exposure Lamp Unit, Imagepac) and baked at 80°C to remove any uncured resin (24-48 hours). FDM 3D printed components were placed in a solution of hydroxypropyl methylcellulose (HPMC, 0.1% w/v in PBS) for 10-15 minutes to create a non-stick surface for casting PDMS. Once coated, moulds were rinsed in de-ionised water, and dried using nitrogen gas. For a quick non-stick coating on SLA printed moulds, a release agent was sprayed over the surface that contacts the silicon wafer according to the manufacturer's instructions (Ease Release[™] 200, Smooth-On, PA). Alternatively, moulds were laser cut in sheets of polymethylmethacrylate (PMMA/acrylic), also carried out by technicians within internal university workshops (VLS 6.60, Universal Laser Systems, AZ, USA). Moulds were clamped to the silicon wafer to keep them in place (**Figure 2.4A**). PDMS was mixed as before and poured into each individual hole in the mould. This was then degassed and cured as outlined in **Section 2.2.3**. PDMS cast in moulds from the extrusion printer was cured overnight at 50° as the printing material had a lower melting temperature. Once cured, the mould was removed from the wafer and the PDMS blocks were easily removed from the mould, with excess PDMS trimmed as required and holes biopsy punched as before (**Figure 2.4B**).

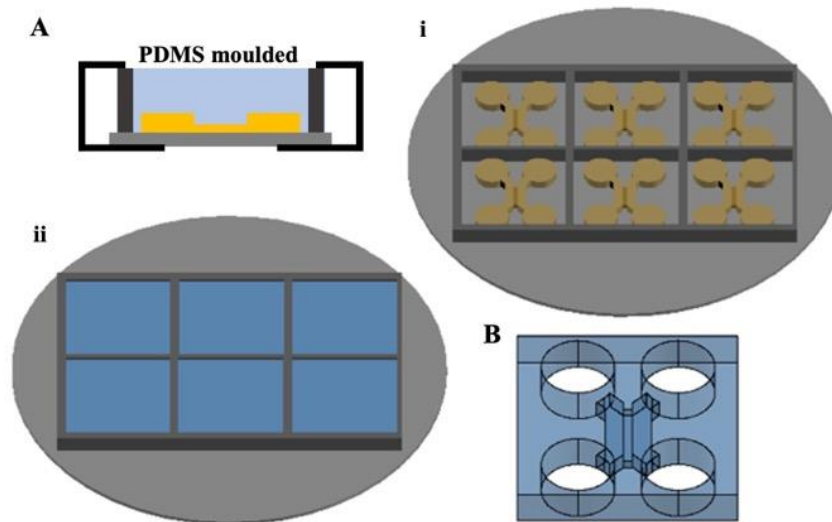


Figure 2.4. Schematic representation demonstrating moulding of PDMS on silicon wafers for more consistent device shape and size. (A) The mould was (i) clamped to the silicon wafer and (ii) PDMS was poured into the holes. After curing, the mould was removed from the wafer, with (B) individual devices dislodged from the mould and wells biopsied as before.

2.3.1. Lego®-like modular platform.

Masks were fabricated to provide square PDMS blocks with microfluidic features and guidance holes. Blocks were initially hand-cut, with the aid of guidance lines around each, or alternatively were moulded as above, with wells and guidance holes biopsied. Guidance holes were 2 mm in diameter and each block was 15x15 mm. Blocks were designed for assembly on a baseplate with studs that interfaced with the guidance holes in the PDMS, providing automatic alignment like that in Lego® (**Figure 2.5A**). Baseplates were designed in AutoCAD software (Autodesk, USA) and 3D printed with both 1 mm and 2 mm diameter studs. The PSA film was cut to the desired size for an assembled device and holes punched to match baseplate studs. The backing film was removed and placed over the baseplate, with individual blocks bonded one at a time to create a fully assembled device. Complete devices were oxygen plasma treated (2 minutes, 100% power/200W) to render the PDMS hydrophilic and food dye added to enable visualisation of sealing between adjacent blocks.

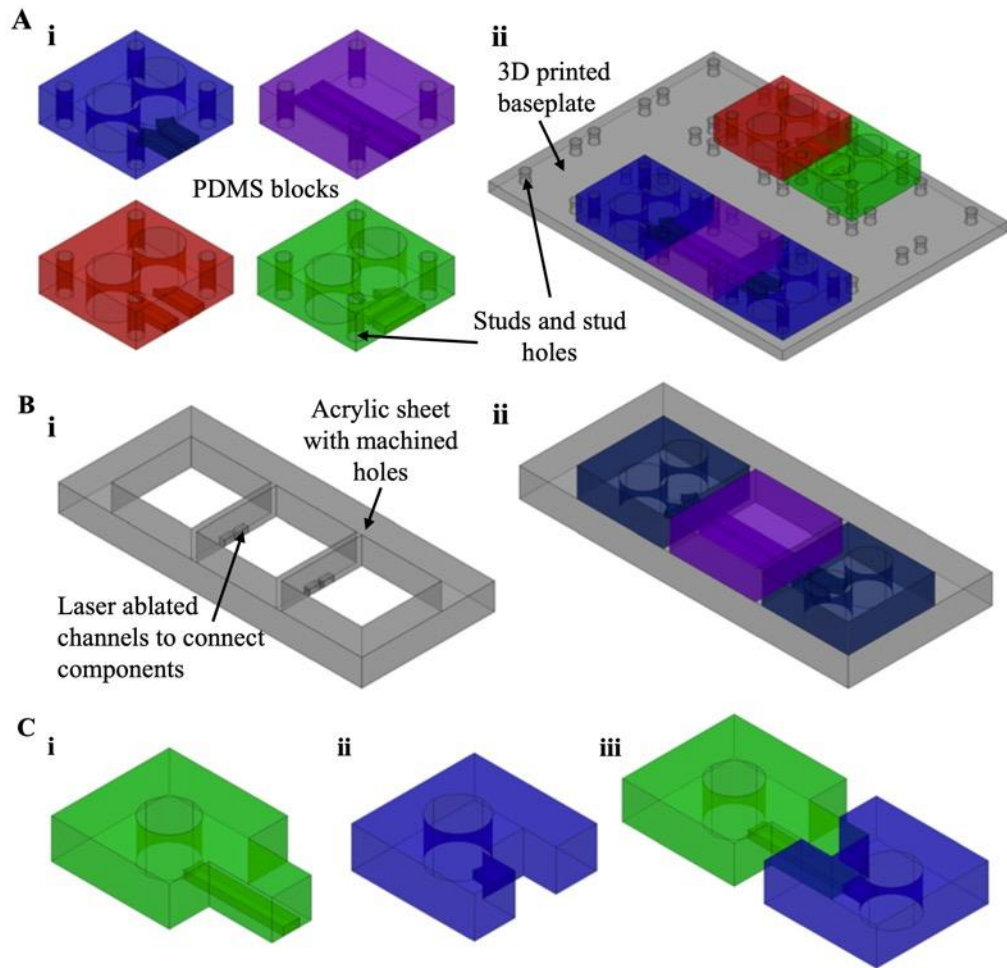


Figure 2.5. Schematic of the various methods tested for developing a modular platform. (A) The initial Lego[®]-like design consisted of (i) PDMS blocks with stud holes for (ii) assembling on a studded baseplate. (B) The second design used the same PDMS blocks, but these were press-fit into acrylic enclosures. (C) The final design consisted of protruding tabs, either as (i) a protrusion or (ii) an intrusion for (iii) interfacing as a complete device.

2.3.2. Press-fit PDMS-PMMA modular platform.

Sheets of 5 mm thick acrylic were cut to the desired size by a departmental workshop. These were milled using a CNC machine to create the 15x15 mm square holes for the PDMS blocks to be press-fit into (Creo Professional 900, NC Machines SRLS, Italy), with 1 mm spacing between each hole (**Figure 2.5B**). Small channels 100 μ m tall and 2 mm wide were then laser ablated between each hole on the lower surface of acrylic sheets, to match the channel layout on PDMS blocks and enable connectivity between them (TruMicro 5050 Femto Edition Laser, TRUMPF, Germany). Both milling and laser ablation were carried out by a research group at the University of Bari Aldo, Italy. The resultant enclosures were sealed to a piece of the PSA

film, with the moulded PDMS blocks press-fit into the holes and also sealed to the film, creating a fully assembled microfluidic device. The assembled configurations were examined for any leaking through the PDMS-PMMA interfaces.

2.3.3. Protrusion-intrusion interfacing modular platform.

Sheets of 5 mm thick acrylic were laser cut to produce moulds with protruding tabs for interfacing (**Figure 2.5C**). Initially, Scotch[®] Tape was used to create channels in the PDMS surface. Small pieces of the tape were cut (~2 mm wide) and placed on a silanised wafer in positions where channels were required, to match the mould layout. Alternatively, photomasks were created for producing devices with a single, uniform channel to connect modules. The laser cut PMMA moulds were clamped to the wafer, and PDMS cast and cured as before. The cured modules were removed from the moulds, with excess PDMS trimmed and wells biopsied. Modules were bonded to the PSA one at a time to create sealed devices. Pressure was also applied horizontally when introducing the next module in series to ensure as tight a fit as possible between adjacent components. Food dye was again used to determine if watertight seals were formed at the interface. Sealing integrity was assessed in freshly assembled devices, devices with a drop of vacuum grease deposited at the interface, and in devices with a thin layer of degassed PDMS brushed around the interface.

2.3.3.1. Double-casting procedure for enclosed interfaces.

Aiming to improve the reliability of the protrusion-intrusion interface, a double-casting procedure using multiple laser cut moulds was used. One mould contained the protrusion and intrusion layout (mould 1), while the other consisted of a simple square to build the height of the PDMS for the larger open wells (mould 2) (**Figure 2.6**). First, mould 1 was clamped to a silicon wafer containing the SU8 microfluidic features (**Figure 2.6A**). PDMS was mixed at the standard ratio and poured into the mould cut-outs (**Figure 2.6B**). This was degassed for 15 minutes and cured at 80°C for 30 minutes, while excess PDMS was left to degas. After curing, the first layer of PDMS was left to cool and the clamps were removed. The second mould was then aligned and clamped onto the first layer mould (**Figure 2.6C**). Degassed PDMS was poured into the new mould set-up and cured at 80°C for 3 hours (**Figure 2.6D**). After cooling, clamps were removed, and the moulds carefully released from the wafer. PDMS modules were dislodged and trimmed as necessary, with holes for wells biopsied (**Figure 2.6E**) and cleaned using Scotch[®] tape or by rinsing in IPA followed by de-ionised water.

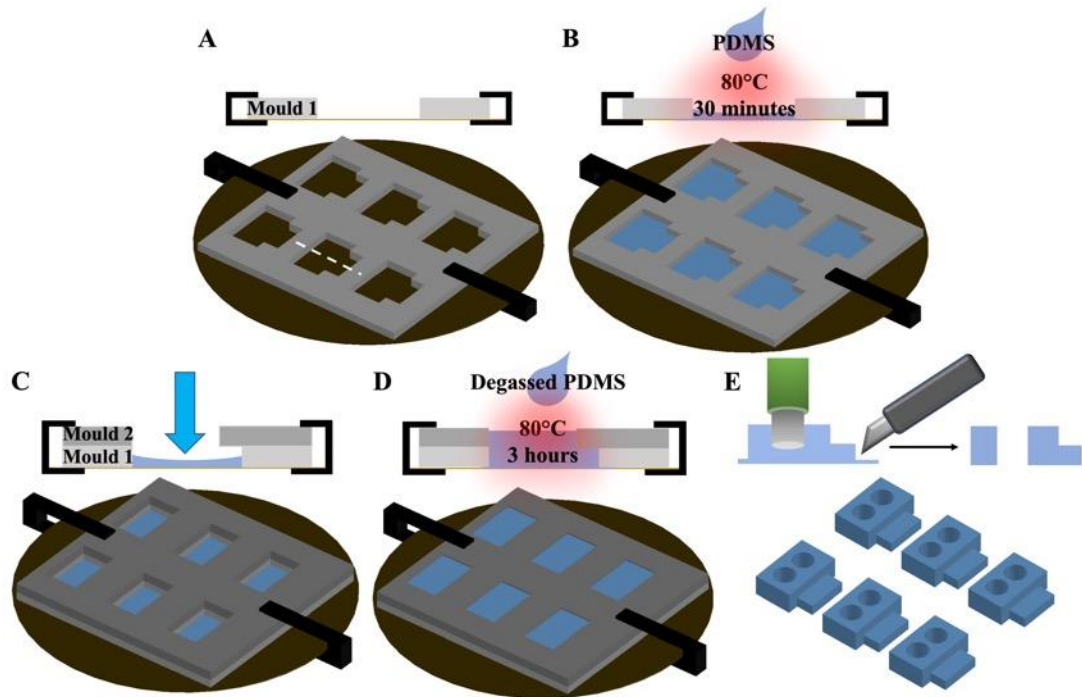


Figure 2.6. Schematic representation of the doubling casting for producing PDMS modules with an enclosed interface. Mould 1 contained the protrusion-intrusion layout to match the SU8-silicon wafer, while mould 2 contained the footprint to build wells only. (A) Mould 1 was clamped to the wafer, with (B) PDMS cast in the holes, degassed and cured for 30 minutes. (C) Mould 2 was aligned on top of mould 1 and re-clamped. (D) Degassed PDMS was poured to fill the holes formed by the sandwiched moulds and cured for 3 hours before demoulding the formed modules. (E) Finally, modules were dislodged from the moulds, with wells biopsied and excess PDMS trimmed.

2.3.3.2. Assembly on glass slides.

To improve the structural stability and facilitate microscopic imaging of devices with multiple modules, a glass coverslip or microscope slide was attached to the ThermalSeal[®] film using a double-sided adhesive film (3M 96042, FindTape, USA), (**Figure 2.7**) prior to assembling the modules. All devices were checked under an inverted microscope prior to use to ensure microchannels were not observably obstructed and were free from debris. If channels were observably obstructed at this point, devices were reconfigured on fresh pieces of adhesive film.

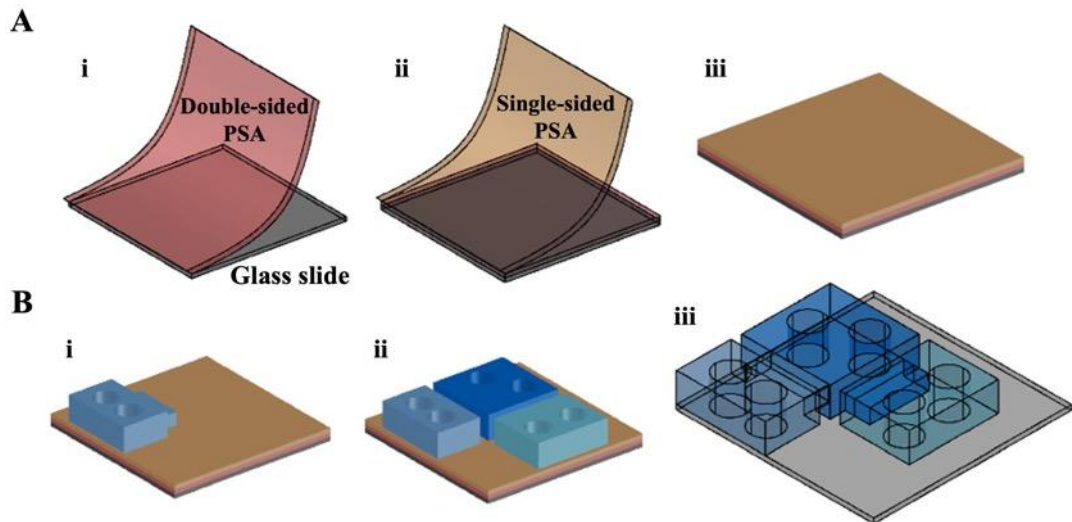


Figure 2.7. Schematic representation of device assembly on glass slides using a double-sided adhesive tape. A glass substrate improves structural stability of modular devices assembled on the ThermalSeal® PSA. (A) To create the stable substrate (i) the 3M 96042 double-sided tape was bonded to a glass-slide followed by (ii) the ThermalSeal® single-sided PSA as the culture substrate (iii) to form the base. (B) (i) Modules were then bonded sequentially (ii-iii) to create the desired device configuration.

2.4. Device preparation for cell culture.

Assembled devices were primed either with a solution of 70% ethanol or with oxygen plasma (Pico A plasma asher, Diener Electric, Germany) to test and compare wettability of the PDMS surfaces and achieve sterile conditions.

2.4.1. Priming devices using oxygen plasma.

Devices were exposed to oxygen plasma (100% power/200W, 2 minutes) and quickly brought into a biological safety cabinet, within 20-25 minutes. Sterile poly-L-lysine (PLL, 10 µg/ml, 1h) or poly-L-ornithine (PLO, 100 µg/ml, 3h) was added to the top two wells of each device and left in an incubator (37°C, 5% CO₂). The PLL/PLO was removed from all devices and the channels rinsed 3x with supplemented Neurobasal-A medium (Neurobasal-A + 2mM L-glutamine and 2% v/v B27). This was added to the top wells of each device and allowed to flow through the channels, then removed and repeated twice more. Devices were left filled with media for use on the day of preparation or left in the incubator to be used in 1-2 days. At this point devices were placed in sterile 4-well Nunc™ cell culture plates surrounded with PBS to reduce evaporation.

2.4.2. Priming devices using 70% ethanol.

70% ethanol was tested to initiate flow through channels and to sterilise devices. For a 2-chamber device, 150 µl of ethanol was added to the top well of one side, followed by 150 µl to the bottom well. 150 µl ethanol was then added to the top well of the other side followed by 150 µl to the bottom well. Devices were sprayed with 70% ethanol in a biological safety cabinet to sterilise the outer PDMS surfaces. Approximately 100 µl was removed from each top well followed by the bottom wells. Top wells were then rinsed with supplemented Neurobasal-A medium (2 mM L-glutamine and 2% v/v B27) to flush out the ethanol from the channels. 150 µl of medium was added to the top wells and allowed to flow through, before removing approximately 100 µl from top wells then bottom wells and repeating twice more. When devices were required, all wells were emptied, and the coating applied. 150 µl of PLL (10 µg/ml) was added to the top well of one side of each device, followed by the top well of the other side and left overnight at 37°C/5% CO₂. This was rinsed off 3x using medium (Neurobasal-A + 2mM L-glutamine and 2% v/v B27) and wells left filled with medium in the incubator prior to cell injection.

2.5. Neuronal cell culture in microfluidic devices.

Neurobasal-A medium was used in all experiments and supplemented with L-glutamine (2 mM) and B27 (2% v/v). This was mixed and filter sterilised (Millex 0.22 µm, Millipore, UK) then incubated in a water bath set at 37°C prior to its use. The enzyme solution used consisted of, in mM: 116 NaCl, 5.39 KCl, 26 NaHCO₃, 1.3 NaH₂PO₄, 1.02 MgSO₄, 0.5 EDTA, 25 Glucose, 1.98 CaCl₂. This was then used to make up solutions of papain and bovine serum albumin (BSA): 7.5 mg of papain was added to 5 ml of enzyme solution and 60 mg of BSA was added to 6 ml of enzyme solution. These were filter sterilised and placed in the 37°C water bath prior to use. The remaining enzyme solution (~2 ml) was kept in the water bath then filter sterilised into a petri dish for storing the hippocampi during tissue isolation.

2.5.1. Hippocampal dissection and cell isolation.

Hippocampal dissection follows techniques previously established^{125,134} and P1-P3 Sprague Dawley rat pups were used throughout this project. Briefly, pups were killed via cervical dislocation (in accordance with Schedule 1 of the Animals (Scientific Procedures) Act 1986) and decapitated. All tools were sterilised by storing in 100% ethanol prior to and during their use. The skin and skull were cut using a scalpel and removed using fine forceps to expose the brain. This was removed and placed on sterile filter paper, ventral side up, using a spatula.

Hemispheres were separated and orientated so that the medial side was facing up. The hippocampus was exposed, removed, and placed in the enzyme solution. This was repeated for the other hemisphere and any other pups used (typically 2 pups per culture). The isolated hippocampus tissue was chopped up into pieces and incubated in the papain solution for 20 minutes at 37°C. The tissue was then removed and placed in the BSA solution to inactivate the papain. Trituration of the tissue, using flame-polished glass pipettes of decreasing diameter, was carried out in BSA, to obtain a cell suspension. The cell suspension was centrifuged (2 minutes), the supernatant removed, and the pellet resuspended in 1 ml of cell culture media. Cells were stained using trypan blue, which can only enter the disrupted membrane of dead cells²²⁰, and live cells counted using a haemocytometer. The cell suspension was once again spun down, and the pellet resuspended to achieve a density of 3-5 x 10⁶ cells/ml.

2.5.2. Seeding devices with cells.

Media from the preparation stage was removed from all wells of a device. For the standard monolithic device^{125,134}, 10 µl of the cell suspension (3-5 x 10⁶ cells/ml) was pipetted into the channel inlet of each top well, allowing cells to flow through the chamber. Devices were then incubated for ~ 10-15 minutes (37°C, 5% CO₂) to allow cell attachment. Media was added to the wells in incremental steps, reducing the flow rate across the newly seeded cells, to obtain a final volume of 200 µl in each well. For modular devices, the seeding volume varied by module and channel geometry (see **Table 4.1**, Chapter 4), and cells were initially seeded in penicillin-streptomycin supplemented media to help avoid bacterial infections (50 U/ml penicillin, 50 µg/ml streptomycin). Here, 9 µl of cell suspension was used for the intrusion module, 17 µl was used for the protrusion module, 30 µl was used for the combined protrusion-intrusion module and 42 µl total was used for the all-intrusion module. Cells were loaded into the device chambers, then incubated for 10-15 minutes at 37°C. Wells were then filled with culture medium in a staggered process, up to 150 µl (50 µl each top well then 50 µl each bottom well), to reduce shear stresses across the cells. 24 hours after seeding, media was completely replaced with antibiotic free media to remove debris and any unattached cells. The devices were kept in Nunc™ cell culture plates, alongside 2-3 ml of phosphate buffered saline (PBS) to help reduce evaporation from the device wells. Media was then refreshed every 2-3 days by removing half the well volume and replacing with fresh antibiotic free media. Devices were kept in a humidified incubator (37°C/5% CO₂) and kept for 10-14 days *in vitro* (DIV) before experimentation.

2.5.3. α -synuclein pre-formed fibril seeding.

Pre-formed fibrils (PFFs) of α -synuclein were prepared as previously described and kindly provided for these experiments²²¹. Hippocampal cultures were prepared as before in devices, with the PFFs added after 7 DIV. Prior to their addition (final concentration 1 μ g/ml), PFF aliquots were wrapped in parafilm and sonicated in a water bath to reduce fibril size and improve seeding (35°C, 37 kHz, 25 minutes – ~5 minutes on, 1 minute off and repeat). Hydrostatic pressure gradients were induced, by appropriately altering well volumes, to prevent flow of PFFs from target chambers to adjacent chambers. PFFs were first added to one open well of the target chambers and incubated for 15 minutes. This was repeated by adding PFFs to the opposite open well of the same chamber, and once again into the initial well. Finally, the PFF solution was washed, and fresh media added to all wells creating a flow gradient across the microchannels to prevent possible contamination of PFFs in the non-target chambers. Cultures were incubated for a further 7 days. Media was refreshed by ensuring the volumes in the target chambers always remained lower than in the adjacent chambers. Immunocytochemical staining was performed on cultures after 14 DIV. To quantify the level of phosphorylated α -synuclein (pSyn), images from target and non-target chambers were first converted to binary in ImageJ. The area of both pSyn and β III-tubulin staining were then found and the level of pSyn expressed as a percentage of the level of β III-tubulin (area of pSyn / area of β III-tubulin). An unpaired t-test was used to compare the level expressed in target and non-target chambers, with a $p < 0.05$ taken as significant.

2.6. Cell viability.

All wells were emptied by removing half the total well volume at a time, reducing flow rate across the cells. A propidium iodide (PI) and Hoechst 33342 staining protocol was used as described previously¹²⁵. Both are fluorescent compounds that bind to cellular DNA, with Hoechst readily crossing the cell membranes of all cells, whereas PI only enters membranes of non-viable cells²²². Therefore, Hoechst staining provides a count of the total number of cells, while PI staining gives a count of dead cells. Cultures were treated with 20 μ M PI and 4.5 μ M Hoechst made up in medium for 15 minutes at 4°C. Liquid was removed from all wells of each device, and cells were rinsed with PBS. This was removed and the wells were filled with PBS prior to imaging to keep them wet. Images were taken of two random locations per chamber of each device (20x, AxioObserver Z1 and ORCA-Flash 4). Cells were counted in Fiji/ImageJ software²²³ and the viability was measured as a proportion of live cells to the total number of cells. This was expressed as a percentage \pm S.E.M, and statistical analysis was

performed in GraphPad Prism using a one-way ANOVA and Tukey's post-hoc test to compare viability on the PSA tapes with the glass control, with significance taken as $p < 0.05$.

2.7. Immunocytochemistry.

Cells were first washed in PBS then fixed using ice-cold paraformaldehyde (4%, PFA, 10 minutes) to fix the cells. Cells were again rinsed with PBS and 0.1% Triton-X 100 was added to the top wells (10 minutes) to permeabilise the cell membranes. Cells were once again rinsed with PBS. To block non-specific binding sites, cells were incubated with a blocking solution (1% w/v BSA and 5% v/v FBS in PBS) added to each well for 1 hour at room temperature. Wells were emptied then primary antibodies were diluted in blocking solution (1:500, unless otherwise indicated) and incubated with the cultures at 4°C overnight. Antibodies used were rabbit anti- β III-tubulin (T2200, Sigma-Aldrich, UK; neuronal marker), mouse anti-synaptophysin (AB8049, Abcam, UK; synaptic vesicle marker) and chicken anti-GFAP (AB5541, Sigma-Aldrich, UK; glial fibrillary acidic protein, marker for astrocytes). For PFF experiments, rabbit anti- α -synuclein (phosphorylated Serine 129; AB51253, Abcam, UK; 1:300 in blocking solution) and mouse anti- β III-tubulin (AB78078, Abcam, UK) primary antibodies were used. Cells were then rinsed with PBS and incubated with complimentary fluorescently labelled secondary antibodies, all diluted 1:200 in blocking solution for 1 hour at room temperature (anti-rabbit or anti-mouse Alexa Fluor 488; anti-rabbit or anti-mouse Alexa Fluor 555; and anti-chicken Alexa Fluor 633). Finally, cells were rinsed 3x in PBS. Wells were left filled with PBS prior to imaging to keep them wet. Devices could be imaged straight away or stored at 4° for a short period (1-2 months) provided wells remain filled with PBS, and devices placed in a dish with PBS-soaked tissue and wrapped in parafilm to preserve sterility. All immunocytochemical imaging in this project was performed using an inverted microscope (AxioObserver Z1, Zeiss). Images were taken using 5x, 10x, 20x and 40x lenses and an ORCA-Flash 4 camera (Hamamatsu Photonics, Japan). Image analysis was undertaken in Zen software (blue edition, Zeiss, Germany) or, alternatively Fiji.

2.8. Ca²⁺ imaging.

Ca²⁺ imaging was used to determine the functionality of cells and visualise the activity between and within separate culture chambers. This was used to determine if there was functional synaptic communication between fluidically isolated cultures. The techniques used are based on those previously developed within the group^{125,134}. As Ca²⁺ imaging is a live cell experiment, a HEPES-buffered saline (HBS) solution was first prepared, so cells remained in

a physiologically relevant environment. This solution consisted of, in mM: 140 NaCl, 2.5 KCl, 2 MgCl₂, 10 HEPES, 10 D-glucose and 1 CaCl₂. To achieve a final pH of 7.4 ± 0.2 , the solution was adjusted by adding NaOH, and for an osmolarity of 310 ± 2 mOsm, sucrose was added sequentially (~100 mg at a time). Media was removed from the wells of each device and channels rinsed using the HBS solution. Cells were loaded with Fluo-8 AM (4 μ M in HBS solution for 1 hour at room temperature), following which they were rinsed with HBS solution.

2.8.1. Microscope set up.

An inverted microscope (AxioObserver A1, Zeiss, Germany) along with a cooled EMCCD camera (LucaR, Andor Technology, NI) were used for all Ca²⁺ imaging experiments. A UV lamp (HBO 100W) was used in conjunction with a yellow fluorescent protein (YFP) filter (Filter Set 46, Zeiss) to image the calcium-bound Fluo-8 in the cells. The light intensity of the lamp was reduced using a neutral density filter (FL attenuator position 5), which helped prevent bleaching of the dye or damage to the live cells. A 5x objective was used, providing a field of view large enough to image the microchannels and part of the culture chambers on either side. Using Andor SOLIS software (Andor Technology), an exposure time of 0.2 s was selected, along with a frame rate of 2 Hz and electron multiplier (EM) gain of 100.

2.8.2. Ca²⁺ imaging protocols.

For a standard two-chamber device, a hydrostatic pressure gradient was created between the left and right culture chambers by removing half the HBS solution from the wells of one side and adding to the wells of another (**Figure 2.8A-B**). The device was loaded onto the microscope, centred around the microchannels, and adjusted so the cells were in focus and the dye visible under UV illumination. L-glutamate (final concentration 100 μ M) was added to the side of the device with the lower well volume, becoming the direct side (A) (**Figure 2.8C**). Approximately one minute later, KCl was added to the indirect side (B) (final concentration 30 mM) (**Figure 2.8D**). Alternatively, a 0 Mg²⁺ HEPES-buffered solution (HBS) was used, as this has previously been demonstrated to induce neuronal bursting activity^{224–226}, and spontaneous Ca²⁺ responses monitored in the indirect chambers. When pipetting these solutions into the wells, caution was taken not to nudge the device with the pipette tip as this would have disrupted the recording. Once completed, recordings were stored as TIF files prior to analysis.

2.8.3. Ca²⁺ imaging analysis.

Recordings were saved as a TIFF and analysed using Fiji, Excel, Minitab and GraphPad Prism software. Regions of interest (ROI) corresponding to cell somas were highlighted in Fiji. ROIs in the A side were selected based on a response to direct glutamate stimulation, whilst ROIs in the B side were selected based on their response to direct KCl. In 0 Mg²⁺ HBS experiments, ROIs were selected based on their response to KCl, which was added to all chambers following the relevant experiments. The mean grey value at each time point was exported to Excel, along with a measurement for background intensity. For each ROI, background intensity was removed at each time point and data normalised by dividing each time point by the mean of the initial 60 data points (initial 30s of recording). Ca²⁺ events calculated and used as a measure to show functional cellular connectivity. An ‘event’ was classed an increase of 0.5 NFU (normalised fluorescence intensity) above the baseline or preceding value for each ROI. Statistical analysis was carried out using Minitab or GraphPad Prism. A one-way ANOVA with Tukey’s post hoc test was used to determine significance between events under the different conditions. P < 0.05 was taken as significant in all cases.

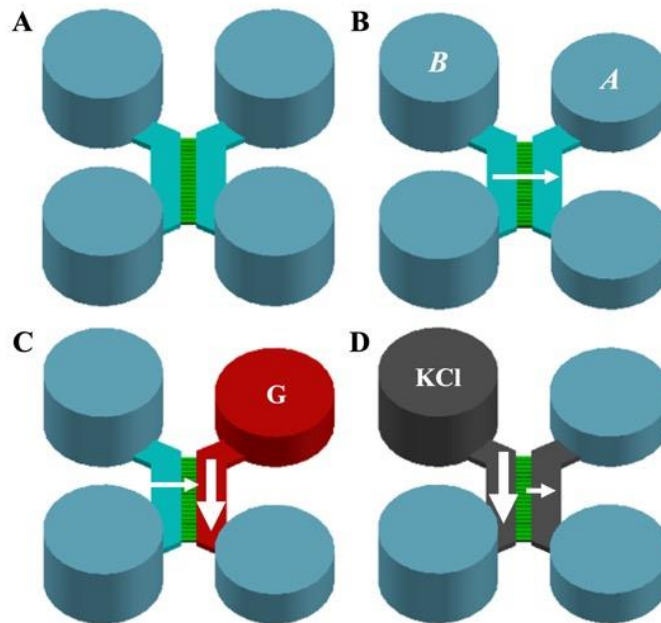


Figure 2.8. Schematic representation of the Ca²⁺ imaging experiment in 2-chamber devices, highlighting fluidic/environmental isolation. (A) All wells have the same volume of HBS at the beginning of the experiment. (B) A fluidic imbalance is created by removing solution from right side wells, this becomes the direct side (A side). (C) Glutamate was added to the top right well and the fluidic imbalance prevents it diffusing into the indirect side. (D) KCl (grey) was added to the top left well (B side).

Chapter 3. Modular microfluidic platform development.

This chapter describes the concepts and ideas around the modular microfluidic platform developed in this project, comprising a substrate that can reversibly bond PDMS components and functions as a biocompatible substrate for primary hippocampal cultures. Various methods were investigated for combining modular microfluidic components on the substrate to create a reconfigurable, easy-to-assemble platform that does not require the use of specialist equipment. Methods of assembly were assessed regarding their ability to create watertight seals between the modules and the interfacing substrates.

3.1. Introduction

For a modular microfluidic platform to be attractive to those with limited experience in microsystems and microfabrication, it must be as simple as possible to use. Individual components would ideally have the same footprint, making the platform universal and devices easy to reconfigure, with a perfect example being Lego[®] building blocks. Such a platform would enable quick assembly of complete devices from individual microfluidic units, ideally with automatic alignment provided by the interconnecting mechanisms on a baseplate. There have been previous attempts at creating such a platform in the literature^{119,192,194–202}. However, none directly addressed the requirements for this project, namely the ability for direct cellular connectivity between components. The use of Lego[®] bricks directly²⁰² or the creation of bricks based on their layout¹⁹⁸ severely limits the size of microfluidic features that can be integrated into individual blocks.

In this project, the main function of the substrate is to support cell growth, form a water-tight seal with PDMS channels and allow interfacing with microscopy equipment. Both PDMS and glass satisfy these requirements and are some of the most widely used materials in microfluidics^{227,228}. The long-established method of permanent PDMS-PDMS or PDMS-glass bonding requires surface activation using oxygen plasma treatment²¹⁸, producing silanol groups on the bonding surfaces, that once combined, form covalent bonds between the two layers. Despite the integrity and longevity of irreversible bonding, it limits the device to a single use and in the case of a modular platform, would not support reconfiguration. Conversely, reversible bonding would enable reuse of PDMS devices as they can be removed from the substrate and repositioned accordingly. Non-permanent, reversible PDMS-PDMS and PDMS-glass bonding in the absence of oxygen plasma is possible, provided both surfaces are flat and clean. However, these conformal contact bonds are weaker than irreversible bonding and so unsuitable for high pressure applications, or those taking place over longer

time periods ²⁰⁴. One way of increasing the native bonding strength of the PDMS is to introduce special contact points on its lower surface, inspired by the bristle-like setae of Gecko feet ²²⁹. This increases the number of contact points, in turn increasing the impact of the native conformal contact bonding between PDMS and PDMS/glass. This was shown to create bonds withstanding pressures up to ~100 psi, 10x higher than standard PDMS reversible bonding ^{204,229}. Other examples have included the use of embedded magnets, or extra channels for vacuum aspiration to reversibly seal devices ²³⁰. However, for a modular platform the complexity of assembly for inexperienced users must be considered. Further, extra equipment would be required for vacuum sealing and the additional bulk associated with embedding magnets would limit portability of the devices and ease of use.

One simple and cheap alternative is the use of adhesive tapes. Three types of commercially available Scotch[®] tape have been shown to create reversible bonds with PDMS microfluidic devices ²³¹. However, to achieve bonding strengths in line with plasma bonding, devices required baking for ~2 hours following adhesion. Even then, the bond failed after minutes to hours when exposed to high pressures. Whilst high pressures are not required in this project, pressure sensitive adhesive (PSA) films are proposed as an appropriate alternative to enable watertight sealing with PDMS and support cell culture. PSA films provide adhesion to a surface upon application of light pressure, without the need for chemical or heat activation ²³². This has been demonstrated previously ²³³, with the films requiring no further processing. Further, as a method for simplifying production, complete microfluidic devices have been produced using PSA films with laser cut channels ²³⁴. These films are further characterised by their ease of removal from the surface they are bonded to without the adhesive rupturing and leaving behind residue. These properties make PSA films suitable substrates for a modular platform, enabling simple, quick assembly with the ability to remove devices and enable reconfiguration of separate components.

Having selected PSA films as an appropriate substrate enabling reversible PDMS binding, I then explored various methods for producing the modular components. In this project, the use of tubing and O-rings for connecting separate modular components would limit cell network formation between separate components, as required for recreating the complex circuitry found in the brain. Therefore, I investigated various methods that could enable conformal PDMS-PDMS bonding between adjacent modules, without requiring additional components:

- 1) A Lego[®]-like design with a studded baseplate (**Figure 3.1A**).
- 2) A press-fitting design using acrylic enclosures (**Figure 3.1B**).

- 3) A design using protruding tabs, termed protrusions and intrusions, for interfacing into complete devices (**Figure 3.1C**).

There was an assumption that conformal PDMS-PDMS bonding between adjacent blocks, along with the PDMS-PSA bond that keeps them in place, would be sufficient to create watertight seals at the interface between blocks for perfusion-free cultures.

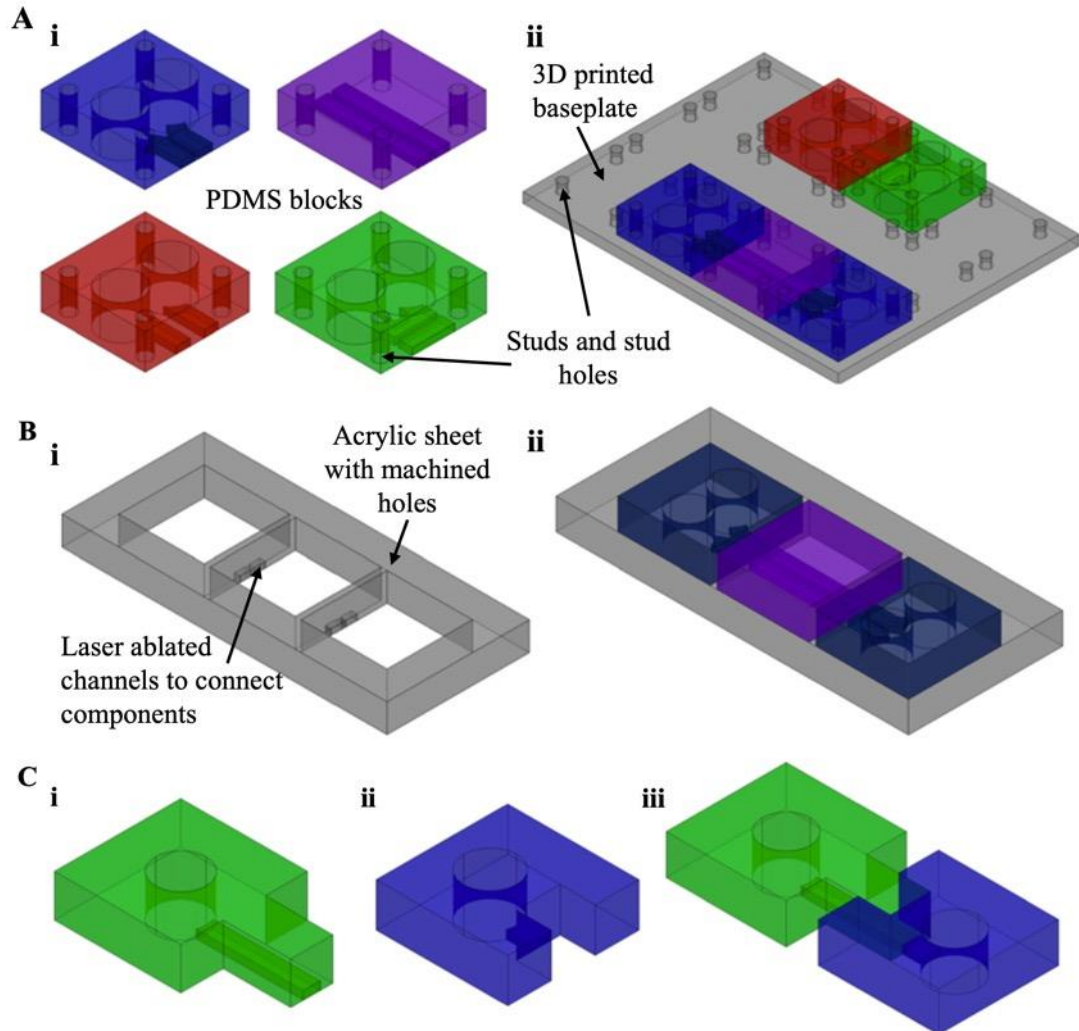


Figure 3.1. Schematic of the various methods tested for developing a modular platform. (A) The initial Lego[®]-like design consisted of (i) PDMS blocks with stud holes for (ii) assembling on a studded baseplate. (B) The second design used the same PDMS blocks, but these were press-fit into acrylic enclosures. (C) The final design consisted of protruding tabs, either as (i) a protrusion or (ii) an intrusion for (iii) interfacing as a complete device.

3.2. PSA film substrates for reversible PDMS bonding and primary hippocampal cultures.

In this project, two silicone-based PSA films were selected for testing. Silicone-based PSAs are generally clear, have excellent humidity and solvent/chemical resistance and can withstand a wide range of temperature variations, all beneficial for microfluidic applications²³². The two PSAs selected were ThermalSeal[®] RTS²³³ from Excel Scientific and ARseal[™] 90880²³⁴ from Adhesives Research, with both films having similar properties. The ThermalSeal[®] film has previously been shown to bond with PDMS as well as a range of thermoplastics such as polymethylmethacrylate (PMMA) and polycarbonate (PC)²³³. Furthermore, previous studies have documented the low autofluorescence and subsequent cell viability following cell culture for both films^{233,235}. However, BeWo b30 placental epithelial cells grown on the ARseal[™] film showed reduced metabolic activity and displayed cell repellent properties, impacting adhesion to its surface²³⁵. Despite this previous characterisation, it was important to demonstrate the bonding and subsequent culture capabilities of the films in this project. Here, primary hippocampal cultures will be used, as opposed to the more robust immortalised cell lines used in the previous studies^{233,235}.

3.2.1. PSA and PDMS bonding.

Initial experiments with the PSA films were performed using monolithic compartmentalised devices used previously in the group^{125,134} to test for watertight, reversible seals between PDMS and the PSA films. PDMS devices were enclosed by placing each microfluidic chip on a piece of either the ARseal[™] or ThermalSeal[®] PSA and then gently tapping down with two fingers flat over the surface of the PDMS, without applying additional force. To observe the seal integrity of PDMS-PSA bonded devices, they were made hydrophilic using a plasma asher (2 minutes, 100% power/200W) and water was added to all wells and left for 1 hour before inspection. The ARseal[™] film had a noticeably sticky and tackier adhesive layer resulting in the roof of channels also bonding to the PSA if blocks were forcefully pushed down, rather than tapping over its surface using two fingers flat. A watertight seal had been assumed with the ARseal[™] film, given this sticky adhesive layer, and was confirmed by no leaks being observed. Similarly, devices bonded to the ThermalSeal[®] film showed no leaking of water. For confirmation, calcein (100 μ M) was added to devices bonded to the less tacky ThermalSeal[®] film, revealing a hermetic seal between PDMS and the PSA (**Figure 3.2A**). Further, microchannels between culture chambers were not blocked by the adhesive, as evident by the presence of calcein within them (**Figure 3.2B**). PDMS devices were easily removeable from both PSA films, however the films themselves were not reusable as channel

imprints were left on its surface resulting in weakened adhesive properties. Subsequent re-use and reconfiguration of PDMS devices was therefore possible, if desired, by bonding to a fresh piece of PSA film.

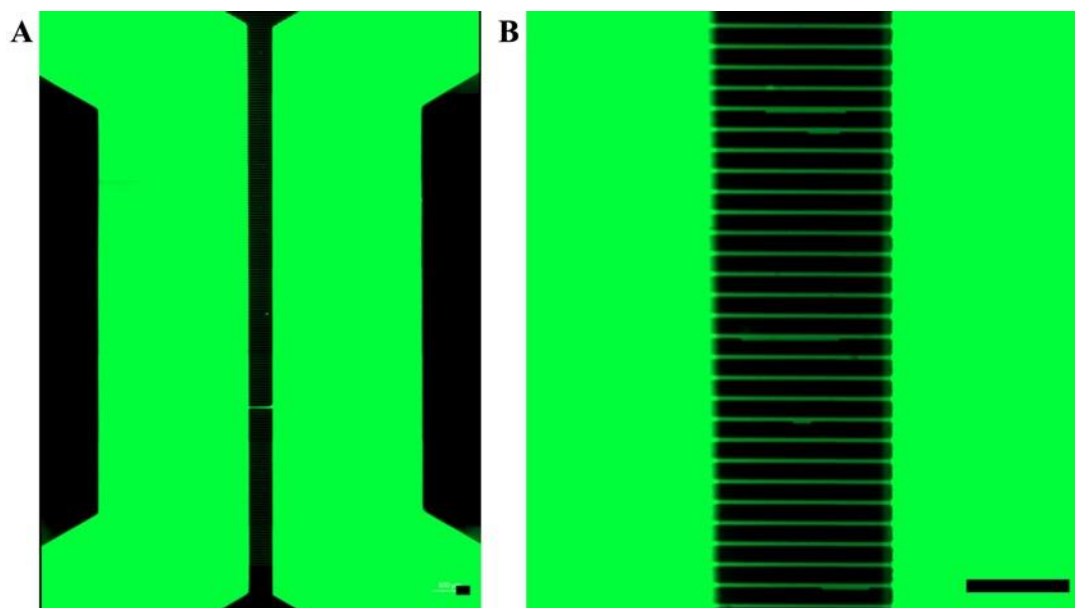


Figure 3.2. Hermetic PDMS-PSA sealing was confirmed using the fluorescent compound *calcein*. (A) *Calcein* remained within the device channels (green), confirming a sufficient seal between PDMS and the ThermalSeal[®] PSA film. (B) Microchannels remain open and are not blocked by the pressure applied for bonding. Scale bars show 250 μm .

3.2.2. Cell growth and functionality on PSA films.

3.2.2.1. Cell viability

Primary hippocampal cells were seeded in monolithic two-chamber devices either plasma bonded to glass or reversibly bonded to the two PSA films, at a density of $3\text{-}5 \times 10^6$ cells/ml. A Hoechst and propidium iodide (PI) staining protocol was used to determine cell viability after 14 days *in vitro* (DIV) (**Figure 3.3F**). In devices plasma bonded to glass the viability was calculated as $88.7 \pm 1.8\%$ ($n = 4$ devices from 3 separate cultures) of the total cell population. For devices bonded to the ARseal[™] PSA viability was calculated as $86.2 \pm 3.2\%$ ($n = 3$ devices/3 separate cultures, $p = 0.8429$ vs glass) and in devices bonded to the ThermalSeal[®] PSA viability was calculated as $81.2 \pm 3.5\%$ ($n = 6$ devices/3 separate cultures, $p = 0.1989$ vs glass). Cells cultured on the ThermalSeal[®] film appeared viable when observed, with neurites extending throughout the culture chambers between cells (**Figure 3.3D**), like that seen in the standard device plasma bonded to glass (**Figure 3.3C**). However, the adhesive layer in the ARseal[™] film appeared to disrupt imaging due to its stickier nature (**Figure 3.3E**), with structures that look like bubbles present during phase contrast imaging. Whilst both PSA films

showed positive results from the viability assay, the poor-quality imaging associated with the ARseal™ film resulted in choosing the ThermalSeal® film for all remaining experiments and throughout the project. In addition, the tackier nature of the double-sided ARseal™ made assembling devices on it more difficult, increasing the likelihood of channel bonding and subsequent blockages to flow.

3.2.2.2. Cell growth on the ThermalSeal® RTS film.

Immunocytochemistry was used to visualise the general growth and morphology of the primary hippocampal cultures grown on the ThermalSeal® PSA. Cultures were stained for β III-tubulin, synaptophysin and glial fibrillary acidic protein (GFAP), alongside DAPI. β III-tubulin is a microtubule element expressed predominantly in neurons and can therefore be used as a marker for distinguishing neurons from glial cells as well as a visualising neurite formation between co-cultures. GFAP is an intermediate filament protein expressed by glial cells in the central nervous system, and so stains astrocytes allowing differentiation between cell types. Synaptophysin is an integral membrane protein found in synaptic vesicles and staining for this gives an indication of synapse formation between cells. DAPI binds to DNA, enabling visualisation of cell nuclei. β III-tubulin and GFAP staining reveals the complex cellular networks formed in primary hippocampal cultures with the presence of both neurons and astrocytes (**Figure 3.4A-C**). Neuronal processes can enter microchannels, creating connections between the cells of environmentally isolated culture chambers (**Figure 3.4B**). The lack of GFAP stained processes within microchannels suggest only neuronal processes are capable of fully traversing the microchannels, as has been shown previously^{124,134}.

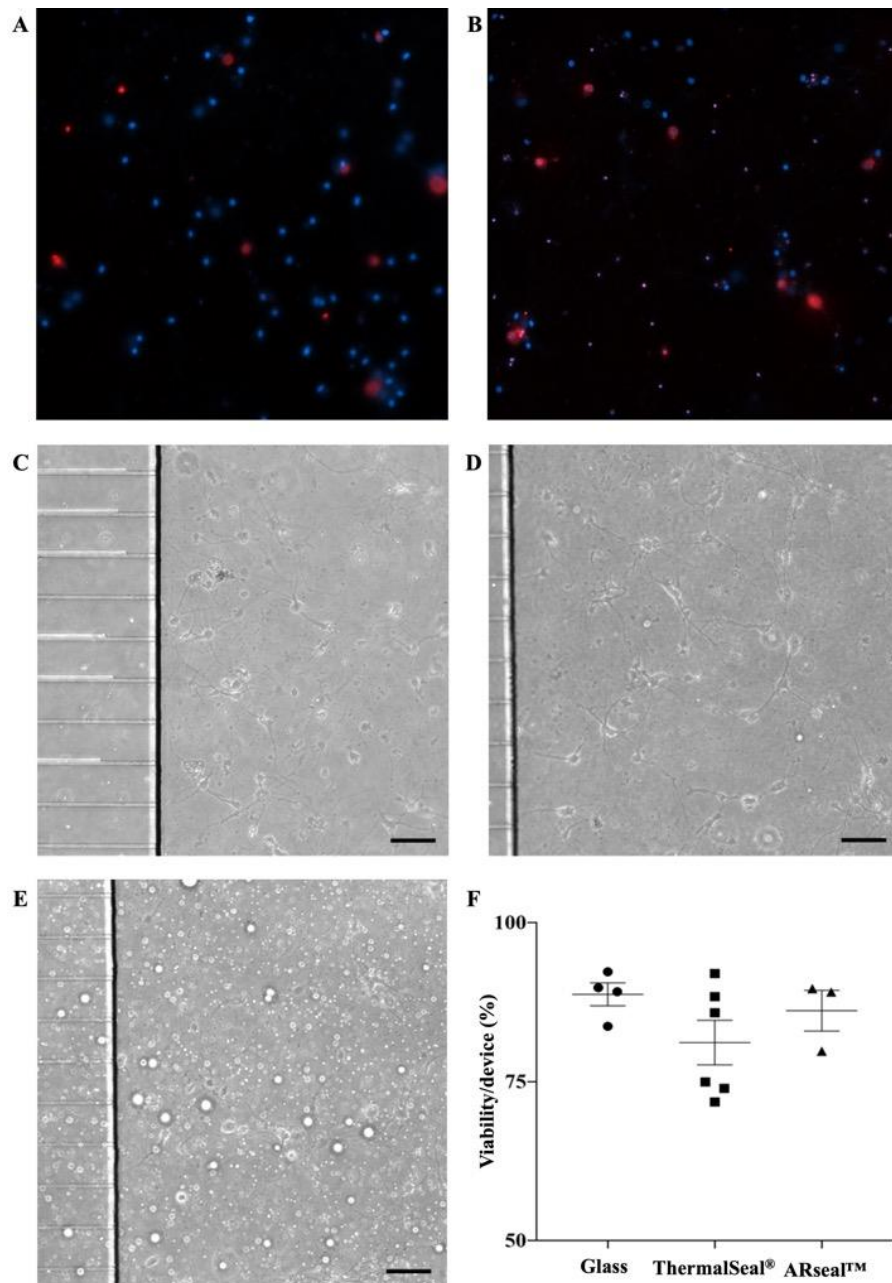


Figure 3.3. PSA substrates enable the growth of healthy primary hippocampal cultures. (A-B) Representative images of hippocampal cultures grown in one device bonded to the ThermalSeal® film and stained with PI (red) and Hoechst (blue). Whilst both images are from the same device and the same culture, the viability calculated in images varied from (A) 94.9% to (B) 43.9%. (C-E) Representative brightfield images of cells in devices plasma bonded to (C) glass, (D) bonded to the ThermalSeal® RTS PSA, or (E) bonded to the ARseal™ 90880 PSA after 10 DIV. Image in (E) demonstrates the poor imaging associated with the adhesive layer in the ARSeal™, with bubbles present on its surface. (F) Cell viability was comparable after 14 DIV when grown on the various substrates. Scatter chart shows mean \pm S.E.M. Scale bars = 100 μ m.

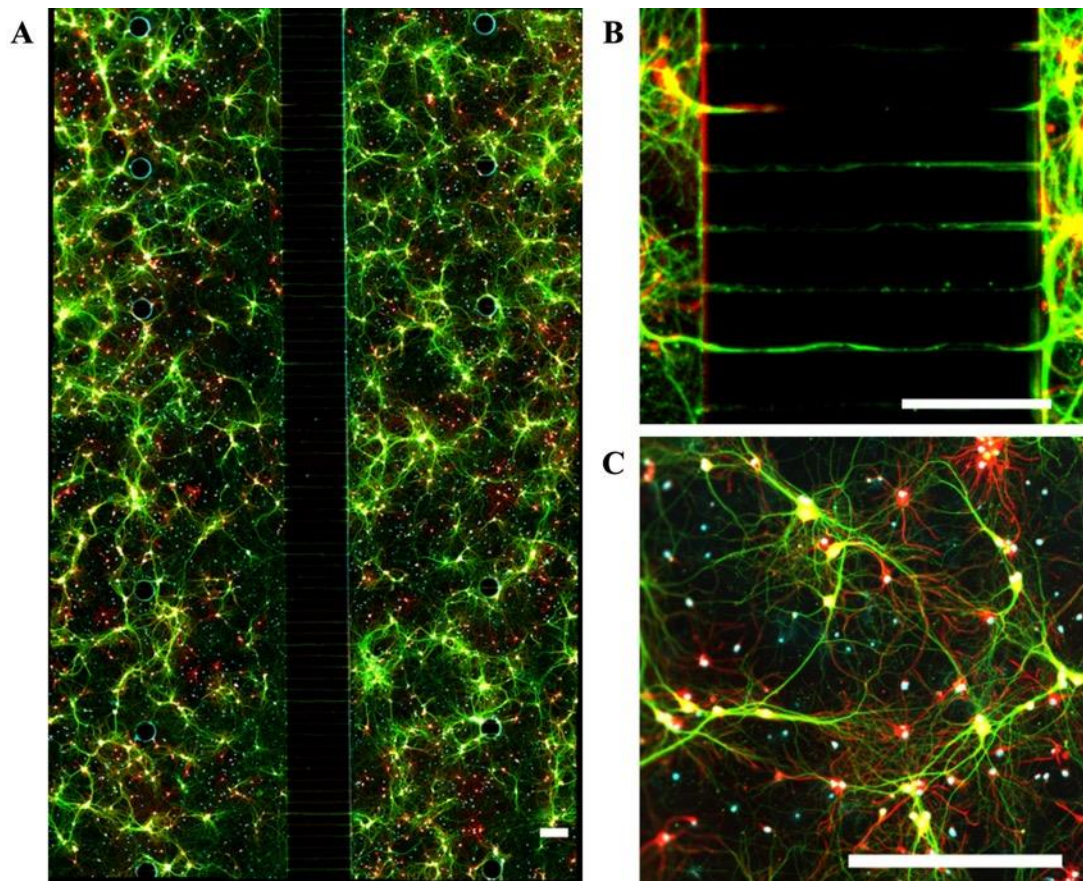


Figure 3.4. Primary hippocampal cultures seeded in monolithic devices bonded to the ThermalSeal® RTS film are healthy with normal growth and morphology after 13 DIV. (A) Cellular distribution is evident throughout culture chambers. (B) β III-tubulin staining shows neurite growth (green) through microchannels, with no evidence of astrocytic processes (red) beyond the channel entrances. (C) growth of both neurons and astrocytes forming intertwined networks in the hippocampal cultures. Green = β III-tubulin, red = GFAP and blue = DAPI. Scale bar shows 200 μ m.

Further, synaptophysin staining within the microchannels indicates the presence of synaptic vesicles shown by punctate staining (white arrows), presumably within synapses, which are required for communication between neurons (**Figure 3.5**). These results show that the ThermalSeal® PSA film is a suitable substrate, with cellular distribution and growth on its surface.

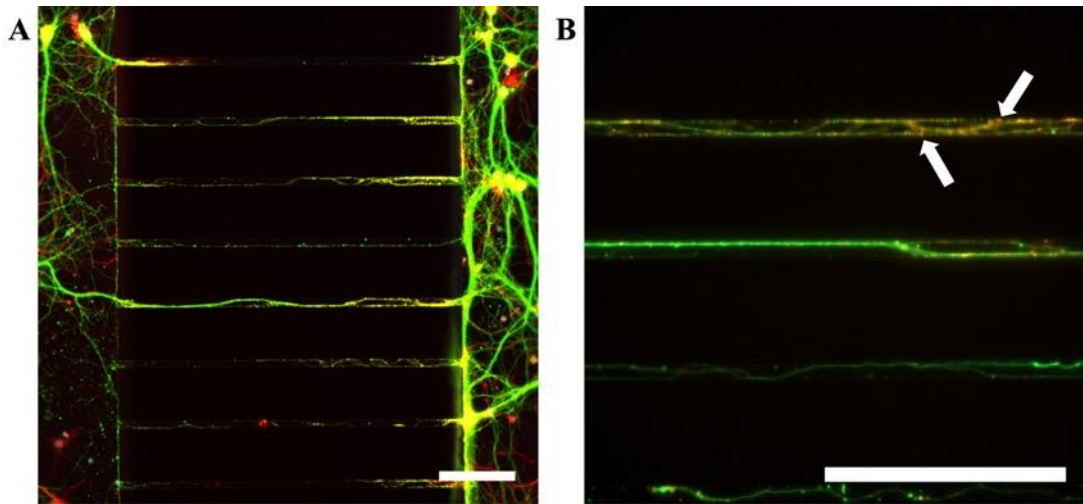


Figure 3.5. Staining in microchannels revealed synaptic vesicle formation in primary hippocampal cultures seeded in monolithic devices on the ThermalSeal® film. (A-B) synaptophysin staining (orange) indicates synaptic vesicle formation within the neurites crossing the microchannels, evident by punctate staining (white arrows). Green = β III-tubulin, red = GFAP, orange = synaptophysin. Scale bar shows 100 μ m.

3.2.2.3. Cell functionality and network connectivity in cultures grown on the ThermalSeal® film.

Calcium (Ca^{2+}) is essential for cell signalling in the nervous system and the use of a fluorescent dye that binds to intracellular Ca^{2+} enables monitoring of cellular and synaptic communication. This provides an indication as to the functionality of the hippocampal cultures. The methods used here have been developed within the group and demonstrated previously to show functional synaptic connectivity between environmentally isolated hippocampal cultures^{125,134}. Hence, cells were loaded with the Ca^{2+} -sensitive dye, Fluo-8 AM (4 μ M, 1 hour at RT), to examine whether synaptic connectivity occurred between cultures grown in devices bonded to ThermalSeal® film. This demonstrated the connectivity between the neuronal populations, with neurites growing across microchannels (**Figure 3.6A**).

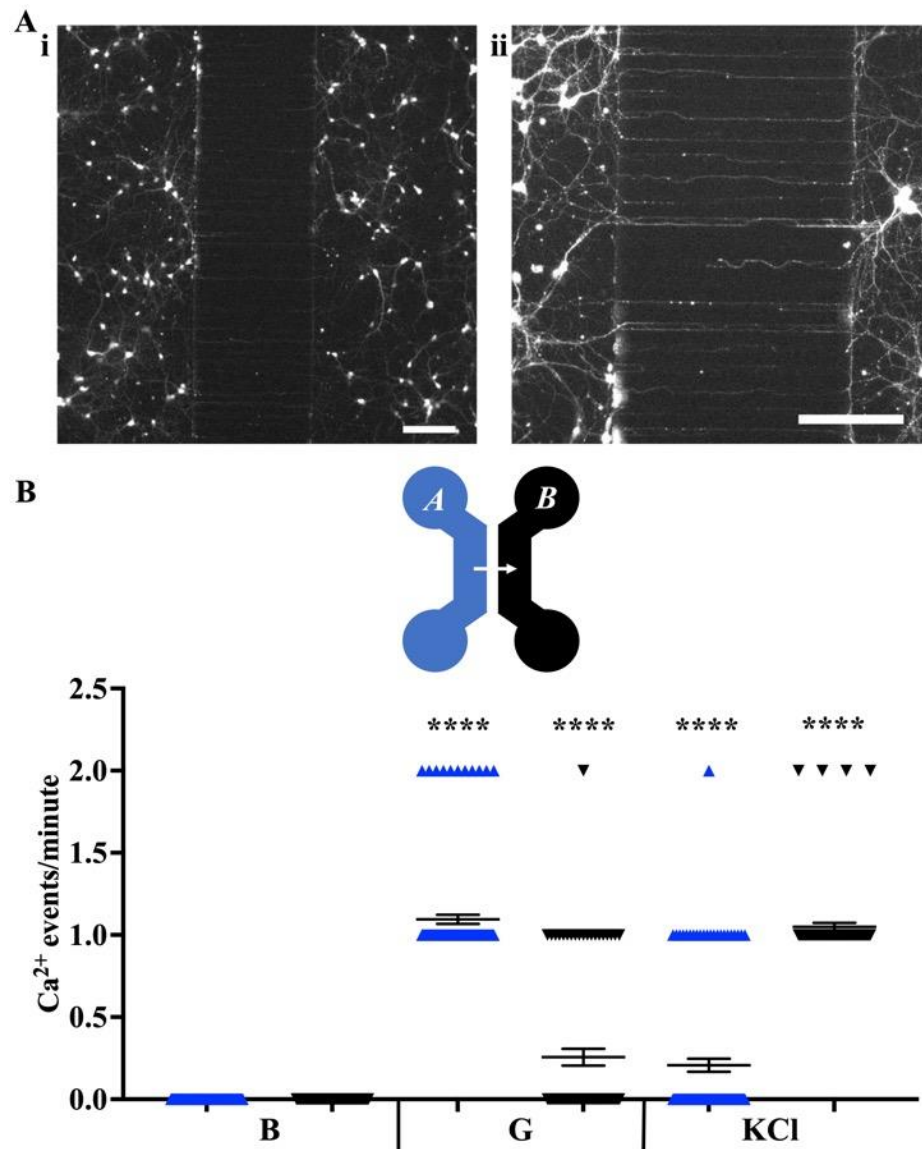


Figure 3.6. Hippocampal cultures grown in monolithic devices bonded to the ThermalSeal® PSA film are functional and synaptically connected. (A) The Fluo-8 AM Ca^{2+} -sensitive dye highlights cellular network formation and neurite outgrowth after 14 DIV. (i) Intracellular calcium can be seen in both cell somas and their processes, with (ii) neurites entering microchannels to enable connectivity between compartments. Scale bars = 200 μ m. (B) The increase in Ca^{2+} events in response to G (applied to chamber A, blue) and KCl (applied to chamber B, black) after 10-12 DIV indicates cells are functional and synaptic communication occurs between environmentally isolated hippocampal cultures. Scatter chart shows mean \pm S.E.M., $n = 116$ cells in chamber A (blue) and 82 cells in chamber B (black) of 3 devices from 3 separate cultures. A one-way ANOVA with Tukey's multiple comparison's test was used to compare values. **** = $p < 0.0001$ vs baseline.

Following the addition of glutamate (G, 100 μM) to one culture chamber of devices (chamber A, blue), there was an increase in Ca^{2+} events from 0 events/minute over the baseline period (B) to 1.09 ± 0.03 events/minute ($p < 0.0001$, B vs G, $n = 116$ responsive cells from 3 devices from 3 separate cultures) in chamber A (blue data points, **Figure 3.6B**) and an increase from 0 events/minute over the baseline period to 0.26 ± 0.05 events/minute ($p < 0.0001$, B vs G, $n = 82$ responsive cells from 3 devices/cultures) in the synaptically connected adjacent chamber B (black data points, **Figure 3.6B**). To further assess functionality, KCl (30 mM) was subsequently added to chamber B (black), which elicited an increase in Ca^{2+} events to 1.05 ± 0.02 events/minute ($p < 0.0001$, B vs KCl). This also elicited an increase in Ca^{2+} events in the opposite culture chamber (chamber A) to 0.21 ± 0.04 events/minute ($p < 0.0001$, B vs KCl). Here, a calcium event was classed as any uninterrupted increase in fluorescence intensity (≥ 0.5 NFU) above the baseline or preceding level. These results highlight the suitability of the ThermalSeal[®] RTS pressure-sensitive adhesive film as an alternative substrate to glass. The increased fluorescence in response to chemical stimulation is indicative of increased intracellular Ca^{2+} . This in turn indicates that cultures are healthy and functional, and demonstrates bidirectional synaptic communication is achieved in hippocampal cultures when grown on the ThermalSeal[®] RTS. Whilst no baseline activity was observed, it is possible that the imaging set up was not sensitive enough to pick up small changes in fluorescence intensity, compared with the large increases observed with direct depolarisation using G/KCl. Further, only cells responsive to direct stimulation were selected.

3.3. Modular device production and assembly.

3.3.1. Lego[®]-like design.

Lego[®] is easily recognisable, with consistent footprints among bricks, and is simple to assemble using a studded baseplate. The initial design in this project was therefore based on this idea and used modular PDMS blocks that were assembled on the PSA using a 3D printed baseplate (**Figure 3.1A**). All the microfluidic blocks were the same shape and size, making devices easy to reconfigure and the studded baseplate provided automatic alignment. However, all combinations tested failed to seal at the interface between blocks (**Figure 3.7A-B**), with dye used to observe leaking. As PDMS is elastomeric, it should be able to conform to the minor imperfections on a flat surface forming a PDMS-PDMS bond via van der Waals forces between the lateral walls of adjacent blocks²⁰⁴. However, by hand-cutting, it was difficult to obtain consistently straight and smooth sidewalls, like the surface achieved in PDMS cast on silicon wafers, and so the uneven interfacing surfaces prevent the creation of a conformal contact bond. Further, it was impossible to guarantee the size or shape of the

resultant blocks, as there is little control over the blade direction given the soft nature of the cured PDMS. This ultimately led to walls on the PDMS blocks of varying angles both horizontally and vertically which cannot combine cleanly at the interface. The difficulty in getting both modules to bond evenly with the PSA at the interface was also observed, due to the pressure generated from the two blocks in close contact (**Figure 3.7C**). Stud dimensions of 1 mm (as opposed to 2 mm) were tested to reduce this deformation. However, these studs were fragile, and in some cases, they could not penetrate the hourglass-shaped holes of the elastomeric PDMS.

3.3.1.1. PDMS blocks cast in 3D printed moulds.

Due to the lack of consistent shape and size of hand cut PDMS blocks, I decided to try moulding the PDMS on the silicon wafers. 3D printing was easily accessible and is quick, cheap and offers a simple method to produce blocks with more defined shape and size. However, the FDM 3D printer available to me produced unsuitable components, as grooves were created where the material had been deposited in layers. This resulted in modules with PDMS walls that were neither smooth nor straight, with the large ridges preventing any PDMS-PDMS sealing between adjacent blocks (**Figure 3.7Ci**). Further, as the material extruded had a low melting temperature, it could not withstand the usual PDMS curing temperature of 80°C and so longer curing times at 40-50°C were required. I then tried an SLA 3D printer (Bean LCD), which provided smoother walls for moulding. With casting holes set to a nominal width of 15 mm in drawing files, the resultant width was 14.79 ± 0.10 (n = 56). However, the PDMS was unable to cure fully, likely due to the UV-curable resin used absorbing the PDMS curing agent²³⁶. Whilst moulds produce more consistent size and shape of modules, it was difficult to align the mould with the silicon wafer and the microfluidic features within. As a result, the positions of stud holes in the PDMS were not aligned sufficiently with the studs on baseplates. Therefore, no consistent seal at the interface could be achieved, with modules either being too far apart or too close together to achieve a flat seal on the substrate. These limitations resulted in leaking at the interface in all cases and as a result, this design was abandoned.

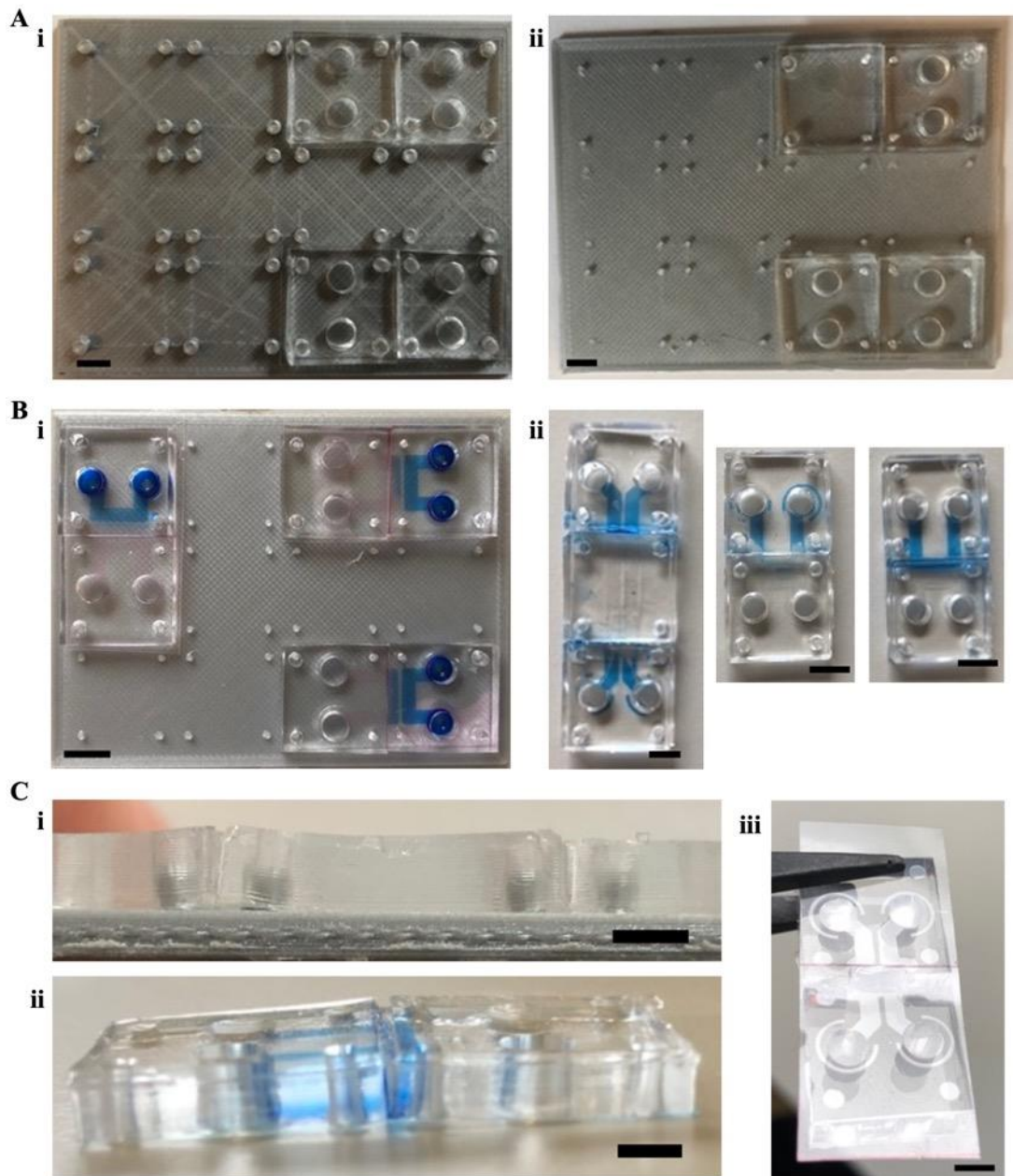


Figure 3.7. A Lego[®]-like method failed to produce a watertight seal at the interface between modules. (A) PDMS blocks assembled into two-chamber devices on a baseplate with (i) 2 mm diameter studs and (ii) 1 mm diameter studs prior to pipetting food dye into wells. (B) Representative examples of multi-module devices following the addition of food dye on (i) a baseplate and (ii) after being removed from the baseplate. All configurations failed to seal, with leakage at the interface between adjacent modules. (C) Representative examples showing (i) the rough, layered surfaces of 3D printed modules that failed to seal fully at the interface both (i-ii) between PDMS modules and (i, iii) to the PSA film. Scale bars = 5 mm.

3.3.2. Press-fitting design with acrylic enclosures.

Due to the issues associated with the Lego[®]-like design, particularly that of aligning the wafer with the mould and the inaccuracies of the stud locations, I then decided to try a press-fitting design (**Figure 3.1B**). This method consisted of press-fitting the individual moulded PDMS blocks into laser cut PMMA/acrylic enclosures to produce a complete device. For this design, I decided to try laser cut acrylic sheets for moulding the PDMS blocks instead of 3D printed moulds, due to the issues highlighted above. CNC milling was chosen to machine the holes for press-fitting the blocks due to the 1 mm spacing required between each hole, which laser cutting could not reliably achieve. Laser ablation was used for channels on the lower surface to connect the blocks in the holes, as it was required to be 100 μm high which neither laser cutting, nor milling was able to achieve. The acrylic enclosures were machined by an external research group (see Materials and Methods, **Section 2.3.2**). In this method, even if the mould is not perfectly aligned with the wafer, the resultant PDMS blocks will be square, and the channels should closely align with the laser ablated channels in the PMMA enclosures. It is worth noting the difficulty in sealing PMMA and PDMS surfaces without treatment^{237,238}. However, for this application, it was assumed that conformal contact aided by the press-fit condition would be achieved between the two materials and be sufficient for watertight sealing.

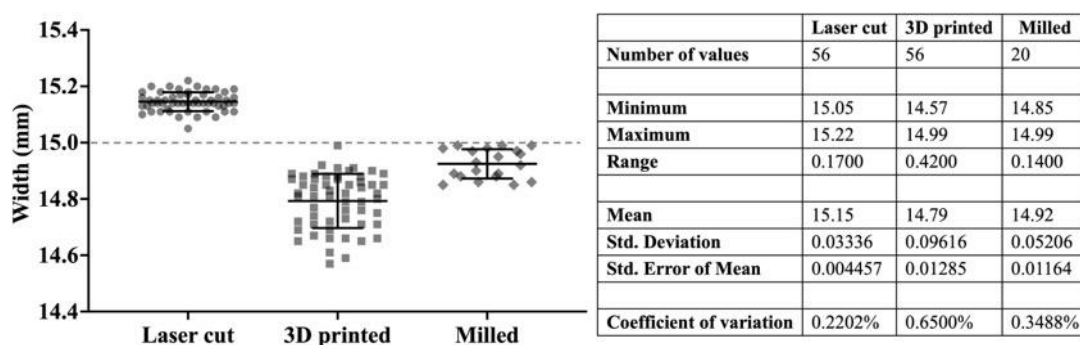


Figure 3.8. Laser cutting provided more consistent feature sizes than 3D printing. The three materials used were 3D printed resin, laser cut acrylic and milled acrylic. Scatter plot shows mean \pm SD with $n \geq 20$ for each condition. Grey dashed line indicates nominal width as set in drawing files.

The laser cut acrylic moulds enabled the production of modules with observably smooth PDMS walls due to the localised melting during laser cutting. For acrylic enclosures, CNC milling was chosen to machine the holes due to the 1 mm spacing required between each hole, which could not be achieved with laser cutting. With a nominal width of 15 mm set in drawing files, the resultant width was 15.15 ± 0.03 ($n = 56$) in laser cut acrylic moulds and $14.92 \pm$

0.05 ($n = 20$) in milled acrylic enclosures (**Figure 3.8**). Milling produced enclosures with widths closer to the desired value of 15 mm than laser cutting, with a smaller range of values (0.14 mm vs 0.17 mm) (**Figure 3.8**). However, both the standard deviation and coefficient of variation were smaller for laser cut dimensions, suggesting this as a suitable fabrication method. Here, the smooth wall surfaces in PDMS blocks moulded using laser cut acrylic should, in theory, improve the likelihood of a seal between interfaces. Conversely, rough surfaces were observed on the machined PMMA surfaces, preventing any conformal sealing between the PMMA and the PDMS. These rough surfaces impeded the formation of a hermetic seal and thus leaking was observed in all cases (**Figure 3.9**). Further, the milling process created rounded corners in the holes as compared to the square moulded blocks. This distorted the PDMS and prevented sufficient sealing to the PSA film. Chopping the corners in the moulded PDMS did not improve the overall fit and so the roughness of the PMMA is the main factor preventing leak-free sealing.

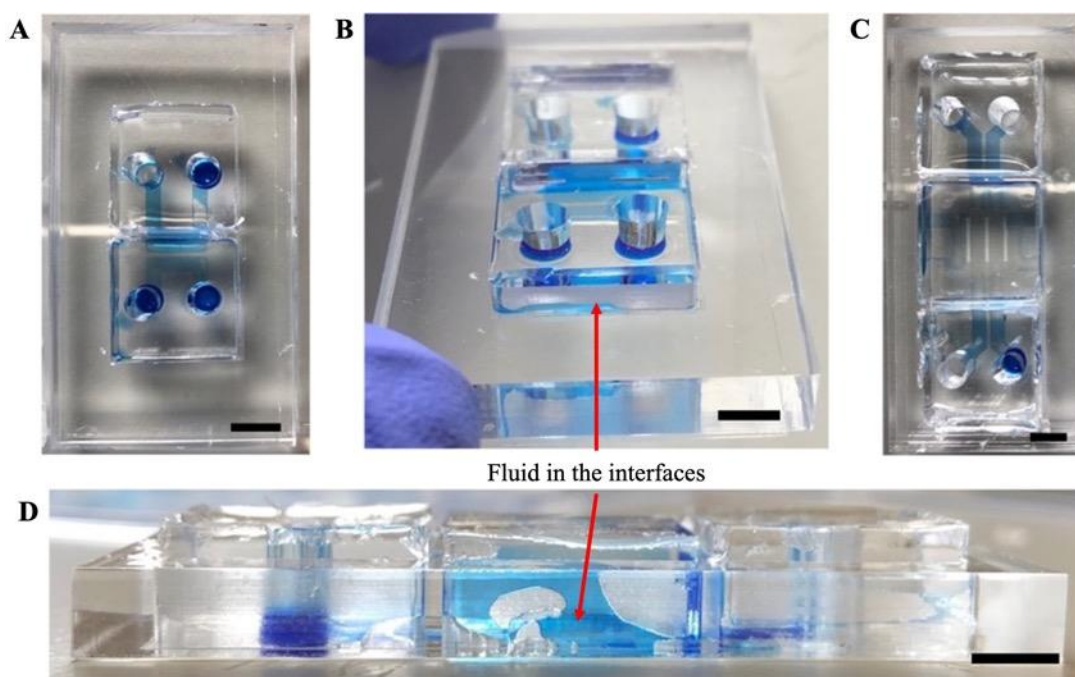


Figure 3.9. Moulded PDMS blocks press-fit into laser cut PMMA did not produce watertight seals. Examples of press-fit modules in the acrylic enclosures showing a lack of seal between PDMS and acrylic, with dye present around the interface. (A-B) two-chamber device configuration assembled from 2 modules and (C-D) two-chamber device configuration assembled from 3 modules.

3.3.3. Protruding tabs for interfacing modular components.

Another approach explored for creating the modular platform was to produce PDMS blocks with protruding tabs for interfacing, termed protrusions and intrusions and I refer to these PDMS blocks as modules (**Figure 3.1C**). Whilst the above results indicated that milling produced features closest to the intended feature size, laser cutting produced smoother surfaces in the cast PDMS and so was chosen as the best moulding method for the PDMS modules. Various protrusion and intrusion widths were tested to find the most appropriate combination for interfacing and creating a press-fit seal. The protrusion-intrusion interface reduces the area of contact between adjacent modules as much as possible, compared with the square blocks used previously. This should have the benefit of localizing the pressure to a smaller surface area and improve overall bonding to PSA tape ¹⁹⁸.

3.3.3.1. Laser-cut acrylic moulds to produce PDMS blocks with protrusions and intrusions.

The width of the protrusion/intrusion of a module was taken as the width of the protrusion/intrusion of the mould in which it was cast. Nominal widths of 6 mm for both protrusions and intrusions were selected initially. The actual protrusion width (P) was 6.19 ± 0.04 mm and the actual intrusion width (I) was 5.72 ± 0.06 mm. Whilst an interference fit was desired, these modules result in a large lateral ‘overlap’ of 0.33-0.64 mm (P-I mm) between the protrusions and intrusions. This can cause the PDMS in the protrusion module to compress, preventing sufficient bonding to the PSA film, or tear the PDMS in the intrusion module. This lateral overlap is defined as how much wider the protrusion is than the intrusion (P-I), where a larger protrusion width is required to create the press-fit condition, whereas a smaller protrusion width would create a gap at the interface (**Figure 3.10A**). Refinement resulted in choosing feature widths of either 5.7 or 5.8 mm for protrusions, with keeping intrusions at 6 mm wide in drawing files (**Figure 3.10B**). Here, actual values from a given feature width of 5.7 mm averaged at 5.85 ± 0.03 mm, while the actual measured value from a feature width of 5.8 mm was 6.00 ± 0.05 mm. Combining these modules enabled a more stable press-fit condition.

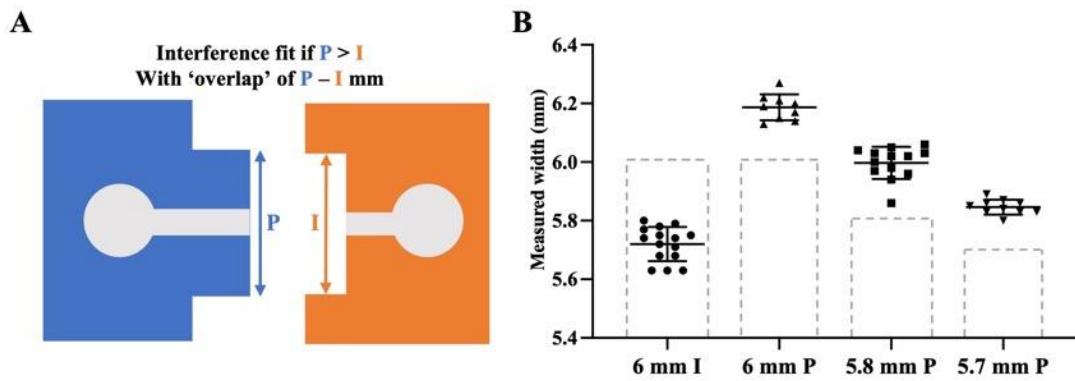


Figure 3.10. Schematic highlighting the interference fit condition between protrusions and intrusions. (A) Schematic to show that an interference or press-fit condition is achieved when $P > I$. (B) A nominal width of 6 mm for both protrusions (P) and intrusions (I) resulted in a large 'overlap' of between 0.33 and 0.64 mm, whereas reducing the nominal protrusion widths to 5.7 mm or 5.8 mm enabled a more stable interference fit of 0 to 0.43 mm. Scatter plot shows mean \pm SD. P = protrusion and I = intrusion. Grey dashed lines indicate nominal dimension given in CAD.

3.3.3.2. Initial proof of concept of the protrusion-intrusion interfacing design.

Prior to producing new photomasks to test this method, channel layouts were produced by depositing strips of Scotch[®] tape, around 2 mm wide, on a silicon wafer in place of SU8 (see Materials and Methods, **Section 2.3.3**). PDMS was then moulded on these wafers to produce blocks with a single straight channel for connectivity between protrusion and intrusion modules (**Figure 3.10A**). Ten assembled devices were tested, with three of these having vacuum grease deposited in the interface to determine if this could reliably prevent leaking (**Figure 3.11**). Of the 7 devices tested without vacuum grease, 2 sealed perfectly (**Figure 3.11C**). The other 5 showed some dye within the interface area but none leaking out of the overall system. I designated these as semi-sealed. It was also observed that the interference fit with the smaller interfacial area provided by protrusions and intrusions does improve sealing to the substrate, compared with the simple square block design.

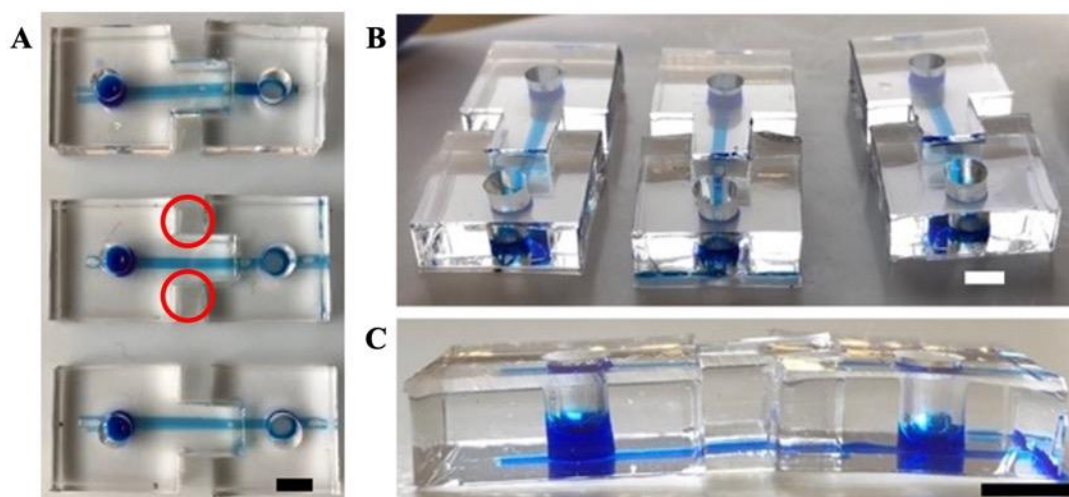


Figure 3.11. Protrusion-intrusion interfacing demonstrated leak-free assembly. This method relies on an interference press-fit condition at the interface with conformal PDMS-PDMS bonding. (A-B) Moulded PDMS modules with simple channels to assess feasibility. Red circles indicate where PDMS/vacuum grease may be deposited to seal the system. (C) An example of a perfectly sealed interface, with no fluid escaping the channel. Scale bars show 5 mm.

3.3.3.3. Testing the robustness of the protrusion-intrusion interfacing with set parameters.

To properly critique this design, photomasks were created so that devices could be produced with a single straight channel connected between modules (**Figure 3.12A**). A set of parameters were also identified at this point that could impact how well two adjacent modules seal together (**Figure 3.12B**). These were the amount of overlap at the interface [P-I, width of protrusions (P) minus width of intrusion (I)], the depth of the interfacing section between the protrusion and the intrusion (A) and the distance between the edge of the channel(s) and the edge of the protrusion (B). From this, it was also of interest to look at the consistency of laser cutting by producing a range of protrusion and intrusion widths. Wafers were fabricated as previously described (see Materials and Methods **Section 2.2.2.**) but in a one-stage process using SU8 3035 to achieve 100 μm tall channels. The PDMS was moulded in laser cut acrylic, and the modules assembled as before.

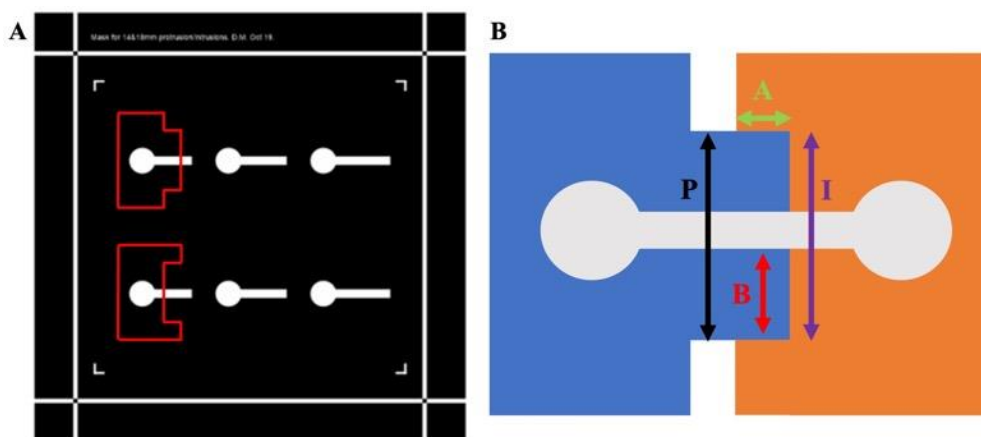


Figure 3.12. Schematic highlighting the parameters identified to help properly test the protrusion-intrusion design. (A) Example mask used to test the protrusion-intrusion system and the effects of the pre-defined parameters. Red outlines indicate the module positions when moulded. (B) Schematic of a device to highlight the parameters – the amount of overlap between protrusion and intrusion (A), the distance between the edges of the channel and the protrusion (B) and the relationship between P and I.

The photomasks for testing the parameters with this protrusion-intrusion design enabled the creation of modules with interfacial widths of 6, 10, 14, and 18 mm. By increasing the width of a protrusion, more microfluidic features can be introduced within the interfacing area. These are the ‘ideal’ values, with nominal dimensions in drawing files set at X+1 mm for intrusion width and X.7 or X.8 mm for protrusion width, based on the initial refinement (**Figure 3.10B**). A measurement of the protrusion/intrusion width was taken from both sides of each hole, using a digital calliper, and the average calculated. The mean measured width for intrusions of 6, 10, 14 and 18 mm was 5.71 ± 0.04 mm (**Figure 3.13A**), 9.62 ± 0.03 mm (**Figure 3.13B**), 13.67 ± 0.06 mm (**Figure 3.13C**) and 17.67 ± 0.04 mm (**Figure 3.13D**) respectively. For protrusions with a nominal width of 5.7, 9.7, 13.7 and 17.7 mm wide, the measured width was 5.90 ± 0.03 mm (**Figure 3.13A**), 9.88 ± 0.03 mm (**Figure 3.13B**), 13.89 ± 0.02 mm (**Figure 3.13C**) and 17.88 ± 0.01 mm (**Figure 3.13D**) respectively. For protrusion with a nominal width of 5.8, 9.8, 13.8 and 17.8 mm, the mean measured width was 5.96 ± 0.02 mm (**Figure 3.13A**), 9.96 ± 0.01 mm (**Figure 3.13B**), 13.97 ± 0.02 mm (**Figure 3.13C**) and 17.97 ± 0.02 mm (**Figure 3.13D**) respectively. For all dimensions tested, a linear regression analysis provided an R^2 value of 0.997 (**Figure 3.13E**) indicating the reliability of laser cutting for achieving consistent results with increasing protrusion and intrusion widths. Moulding in laser cut PMMA therefore remains the most appropriate technique currently available.

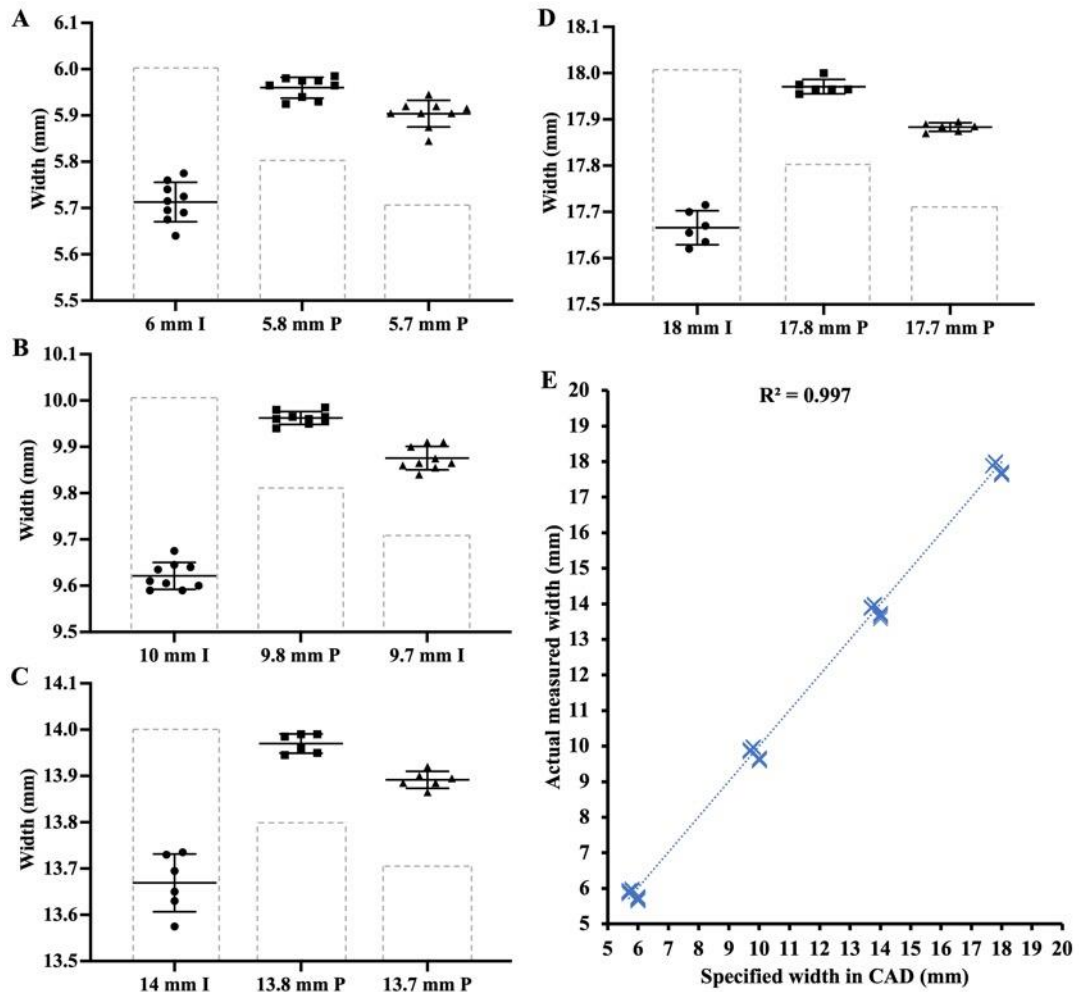


Figure 3.13. Laser cutting produces consistent dimensions for a range of nominal values. (A-D) The measured widths remain consistent for each value tested, with (E) a linear regression plot demonstrating an R^2 value of 0.997 indicating the consistency of laser cutting across a range of values. Graphs created using GraphPad Prism and Excel. Scatter plots show mean \pm SD and $n = 6-9$. Grey dashed lines indicate nominal dimension given in CAD. P = protrusion and I = intrusion.

The sealing integrity was tested for 56 combinations of modules using the nominal protrusion/intrusion widths of 6, 10, 14 and 18 mm and a mix of values for the previously mentioned parameters. The depth of the overlap (A) was 2, 4, or 6 mm and the distance between the edge of the channel and protrusion (B), was 2, 4, 6, or 8 mm (this value increases as the protrusion width increases). All parameters were determined by the fabricated wafer that contained the channel and well features, and the laser cut acrylic moulds. Of the 56 configurations tested, only 9 sealed perfectly (16%, **Figure 3.14A**), with 10 being semi-sealed (18%, **Figure 3.14B**) and the other 37 not sealing (66%, **Figure 3.14C**). For the 9 initial

configurations that had sealed, these were taken apart, re-assembled and then recombined two more times. However, none of these combinations sealed all 3 times without the aid of a sealant at the interface. This suggests that the assembly process is a major factor, i.e the consistency of the force used to push adjacent modules together and the specific alignment at the interface.

The mean P-I value (interfacial overlap) in device combinations that were sealed was 0.28 ± 0.08 compared with 0.25 ± 0.07 in those that were not sealed ($p = 0.2313$, Y vs N) (**Figure 3.14D**). This suggests that a tighter fit between protrusions and intrusions, where there is a greater difference between P and I, creates an improved hermetic seal than in combinations where the fit was looser. The P/I value fell between ~ 1.010 - 1.061 (1.027 ± 0.01), with a range of values for each sealing condition (**Figure 3.14E**). The mean value of P/I in combinations that were sealed was 1.021 ± 0.008 compared with 1.030 ± 0.01 in combinations that were not sealed ($p = 0.0390$ Y vs N). These results suggest that module combinations with P/I values closer to 1 (where $P = I$) are more likely to seal than combinations where there is a greater difference in the widths of P and I. There was no indication that the depth of interface between protrusions and intrusions (A – see **Figure 3.12B**) affects sealing (**Figure 3.14F**). However, it was observed that the larger depth of 6 mm resulted in PDMS not fully bonding to the tape, whilst the smallest value of 2 mm was not guaranteed to create a sufficient fit around the protrusion. This smaller depth of overlap also created more difficulty in aligning the two modules. The middle overlap depth of 4 mm was therefore sufficient for interfacing the two modules and was used to guide further designs. With B (distance between edge of channel and interface – see **Figure 3.12B**), these results suggest the largest distance tested of 8 mm provides the best sealing (75% sealed or semi-sealed vs 25% not sealed) compared with the smallest distance tested of 2 mm (6% sealed or semi-sealed vs 94% not sealed), (**Figure 3.14G**). This is consistent with what was expected, as a smaller distance (2 mm) can result in the channel also bonding to the tape when assembling devices, thus blocking flow. However, it was observed that the larger protrusion modules were more difficult to bond to the PSA film, with regions around the channel and around the edge less likely to fully seal to the substrate. Therefore, a value in between is likely to provide the best compromise and was used to guide further designs.

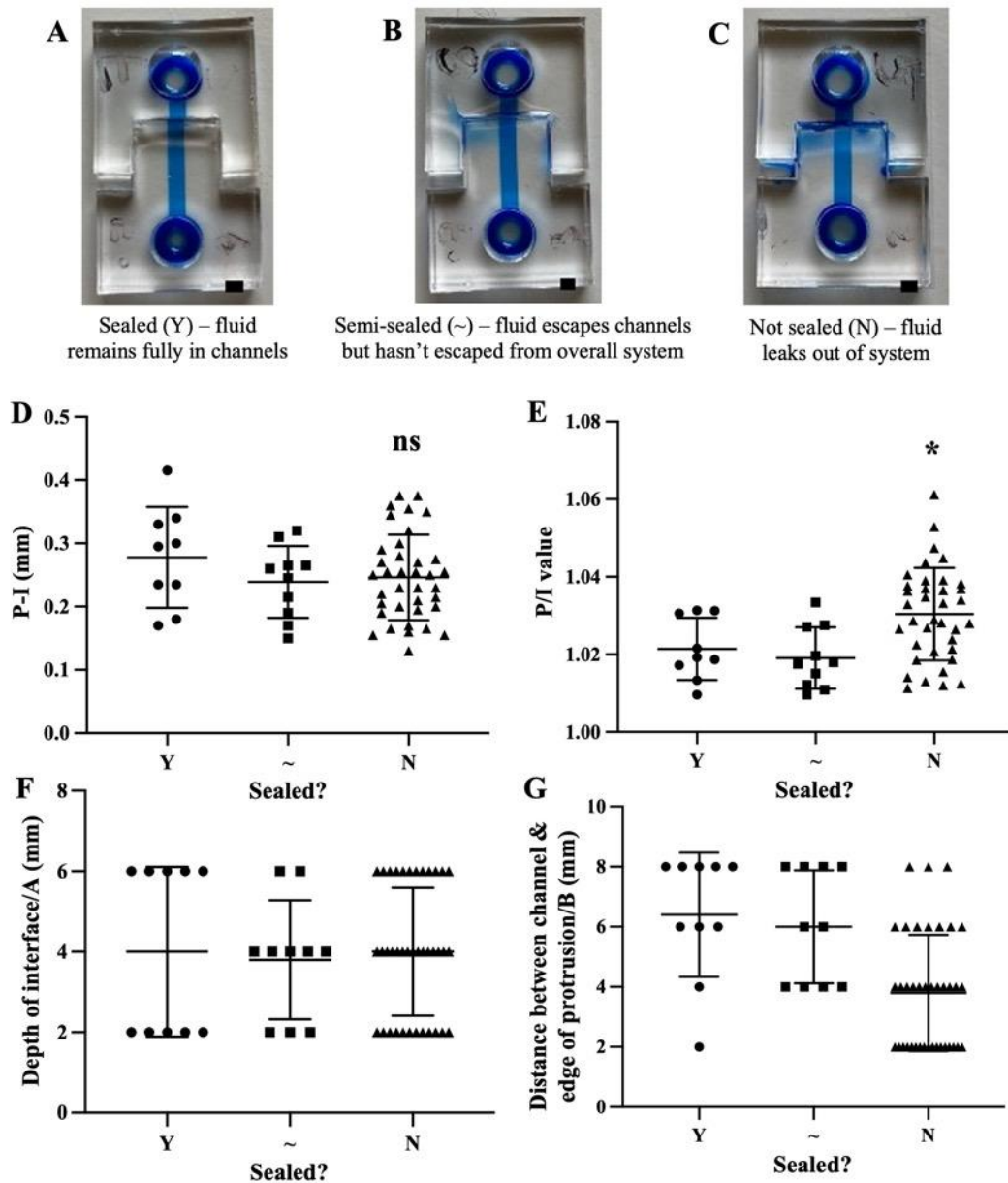


Figure 3.14. The effect of the parameters on sealing was assessed in modular protrusion-intrusion devices. Representative examples given of configurations that were (A) sealed, (B) semi-sealed, and (C) not sealed. (D) Values of P-I (amount of overlap at the interface) plotted according to sealing. (E) P/I (ratio between the widths of the protrusions and intrusions) plotted according to sealing. (F) Depth of interface (A, 2/4/6 mm) plotted according to sealing. (G) Distance between channel and edge of protrusion (B, 2/4/6/8 mm) plotted according to sealing. These results represent a range of protrusion/intrusion widths (6-18 mm). Scatter plots show mean \pm SD. Scale bars = 2 mm. ns = non-significant and * = $p < 0.05$ (Y vs N).

3.4. Discussion.

3.4.1. Cell growth and functionality.

Viability staining revealed both PSA films were able to support primary rat hippocampal cultures, with values comparable to that on the standard glass substrate. The bubble formation observed in the ARseal™ film was likely due to the adhesive becoming disrupted on removal of the backing layer, with a tacky residue left behind. This is contrary to what would be expected with an encapsulated adhesive, where the adhesive is only activated upon application of pressure^{232,235}. Further, the addition of bubbles creates a more variable layer through which imaging must be undertaken. This creates multiple refractive indices within the imaging plane thus making it more difficult to focus on the cellular targets. Hence, the ThermalSeal® was chosen moving forward. Immunocytochemical staining confirmed the presence of both neurons and astrocytes and subsequent network formation between cells after 14 DIV. Further, synaptophysin staining indicated the presence of synaptic vesicles formed in microchannels between culture chambers, with punctate staining suggesting the formation of synapses^{125,134}. Ca²⁺ imaging confirmed that hippocampal cultures were functional following the addition of glutamate and KCl to devices, based on protocols that have been developed previously for microfluidic cultures^{125,134}. Subsequent Ca²⁺ activity following indirect stimulation confirmed that environmentally isolated culture chambers were connected by functional synapses via microchannels as observed previously in similar devices plasma bonded to glass^{125,134}.

The direct addition of glutamate, the main excitatory neurotransmitter in the CNS, depolarises the cell membrane, activating cell surface receptors and allowing positively charged ions through, including Ca²⁺. which enters through voltage gated channels. Ca²⁺ may also be released from internal stores, mainly the endoplasmic reticulum^{239,240}. The depolarisation will help generate action potentials along the axon resulting in the opening of voltage gated Ca²⁺ channels at the presynaptic membranes and propagation of the signal. As a result, there is an overall increase in intracellular Ca²⁺ and subsequent intensity of the fluorescent signal. Further, the hydrostatic pressure gradient created by altering well volumes ensures glutamate cannot flow from the direct side into the indirect side. As a result, the response following glutamate addition to the direct side seen in the indirect side must be from functional synaptic connectivity between cultures of the two fluidically isolated chambers. The rise in activity in the direct side following addition of KCl to the indirect side further indicates functional synaptic connectivity. These results confirm that primary hippocampal cultures are healthy and functional when grown on the ThermalSeal® RTS PSA film.

These results indicate the suitability of the ThermalSeal[®] RTS pressure-sensitive adhesive film as an alternative substrate to glass. The film permits hermetic, reversible sealing with PDMS and has no detrimental effect on the growth and culture of primary hippocampal cultures. Cells can grow and extend neurites between culture compartments, and the subsequent synaptic vesicle formation and functional communication between culture chambers indicates these cells remain healthy and viable when cultured on the substrate surface.

3.4.2. Modular device assembly.

Both initial Lego[®]-like and enclosure designs proved unsuitable. The reliance of multiple fabrication methods for a Lego[®]-like design resulted in poor alignment between the blocks and the baseplate. This led to assembled devices that are unable to create seals at the interfaces between blocks and difficulty obtaining a sufficient seal to the PSA film. Similarly, with the enclosure design, press fit PDMS blocks were unable to create seals with the rough, machined PMMA surface. As a result, both options were abandoned whilst keeping the same moulding procedure with laser cut acrylic. This provided the most accessible method for creating the PDMS modules.

3.4.2.1. Lego[®]-like design.

Moulding the PDMS for this assembly did not aid in sealing due to the difficulty of aligning the separate mould on top of the silicon wafer that contains the microfluidic features. Further, due to the variable nature of 3D printing, the positions of studs on the baseplate did not align perfectly with the positions of holes on PDMS blocks. Due to its mechanical properties, the PDMS becomes compressed when punching, resulting in hourglass shaped holes. This, along with the different positioning of studs and holes caused the blocks to become stretched, affecting sealing with the PSA and further disrupting bonding at the interface. Overall, the limitations of this process could not provide a reliable leak-free assembly and this design was abandoned.

A previous design used components with the same dimensions as Lego[®] blocks and matching baseplates¹⁹⁸. They used 3D printed master moulds with simple straight channels to produce PDMS components that combined to produce hermetically sealed devices. However, my design relied on various fabrication methods as opposed to producing the device using one mould. Here, SU8 masters were required to reliably produce the microchannels and so any subsequent moulding had to be carried out on top of these. Further, the inclusion of culture chambers, microchannel arrays, and open wells (for pump-free, static culture), whilst keeping

the overall block geometry as small as possible for ease-of-use and to prevent dead space, meant there was limited space for integrating alignment holes. In my design, blocks were 15x15 mm with 2 mm diameter studs, compared with 16x16 mm blocks and 4.9 mm diameter studs. Their larger studs are more likely to keep the blocks in place with a greater bond to the substrate, while their smaller fluidic features provided more surface PDMS for bonding to the substrate. Another design used Lego® bricks directly by micromachining channels in their surface and using PSA films to seal the channels²⁰². However, connections between blocks relied on O-rings and tubing, which is not applicable to my project as a flat substrate and larger interfacial system was required to enable neurite outgrowth and synaptic connectivity between separate components.

3.4.2.2. Press-fitting design with acrylic enclosures.

For this design, CNC milling was chosen to machine the holes due to the 1 mm spacing required between each hole and the inability for laser cutting to perform this. Laser ablation was used for channels on the lower surface to connect the blocks in the holes, as it was required to be 100 µm high which neither laser cutting, nor milling was able to achieve. It was assumed here that the resultant interference fit between the blocks and the enclosures would enable improved sealing between the PDMS and the PMMA at the interfacing areas. However, the rough surfaces produced prevented any conformal bonding between the PDMS and PMMA, leaving spaces for fluid to leak. There are options available to alleviate the surface roughness of the PMMA, such as wet etching by submersing the material in a solution of acetone and ethanol at an elevated temperature²⁴¹. However, this design did not provide a truly modular platform, limiting the potential applications and overall scope. These limitations could not provide a reliable leak-free assembly and this design was abandoned.

3.4.2.3. Protruding tabs for interfacing modular components.

The protrusion-intrusion design was chosen to reduce the size of the interface between modules. Doing this should localise the pressure to a smaller surface area, creating a tighter seal, and aid in alignment of adjacent modules^{198,199}. Further, this localised interfacial area was expected to alleviate the issue with square blocks in close contact failing to seal to the PSA (**Figure 3.7C**). The proof-of-concept study was carried out to test the feasibility of such a system prior to creating photomasks, enabling the production of modular devices with sealed interfaces between components. It was apparent however that there was no guarantee of a hermetic seal between modules without the use of a sealant at the interfacial gap.

P-I (the interfacial overlap) did not appear to be the major factor in seal integrity, as there is a wide range of values for each sealing condition. However, results do suggest that a tighter fit between protrusions and intrusions created an improved hermetic seal in the combinations tested. Here, there is a greater chance of forming a conformal bond between the PDMS in the two modules with the added pressure, helping to seal the interface. It was expected here that as P-I increases, sealing would be more likely achieved, up until a point where this overlap becomes too large. Here, the PDMS in either module becomes distorted, either leaving space between the two modules at the interface or preventing sufficient sealing to the PSA. Comparatively, if P-I was negative then the intrusion would be larger than the protrusion, leaving space for fluid to easily escape through. P/I was used to compare the different values of protrusion and intrusion widths (6, 10, 14 and 18 mm) for finding the ideal combination for persistent sealing. Here, there is a range of values for each sealing condition, but results suggest that module combinations with P/I values closer to 1 (where $P = I$) are more likely to seal than combinations where there is a greater difference in the widths of P and I.

Observations when assembling devices indicated that the larger depth (A) of 6 mm prevented PDMS fully sealing to the tape, whilst the smaller value of 2 mm did not guarantee a sufficient fit around the protrusion and creates difficulty in aligning the two modules. A middle overlap value therefore provides the best compromise for further designs. A larger distance between edge of channel and interface (B) better prevents the channels collapsing, as there is a greater region of PDMS away from the channel for pressing the module to the tape. Conversely, a much smaller distance can result in the channel bonding to the tape when pressing down and thus blocking flow. However, if B is large then the device becomes unnecessarily bulky with wasted space compared to traditional monolithic devices. Again, a value in between therefore provides the best compromise for further designs.

I used laser cut acrylic to mould the modules as it was easily accessible internally. However, it was observed that despite the smooth sidewalls produced, there was not always conformal contact achieved between the PDMS components cast in these moulds. Each interface, whether a protrusion or an intrusion, takes the shape of the laser cut PMMA and so any imperfections present on its surface will be replicated in the PDMS. This is in comparison to PDMS that has been cast on a silicon wafer which provides the smooth, flat finish required for consistent conformal bonding. The surface irregularities present along with the larger interface in my modules (12+ mm wide) compared with others (~3 mm wide)¹⁹⁸ have a greater area over which leaking may occur. Another example demonstrated leak-free assembly with a

submillimetre sized ‘tongue and groove’ mechanism ²⁰⁰. However, the larger protrusion/intrusion width in my design was necessary to integrate the microchannel array that enables soma isolation and cellular network formation between culture chambers of separate modules. As there was no guarantee of universal leak-free assembly amongst devices, I decided to use a sealant in the interfacial space to ensure fluid remains within devices moving forward. As the use of vacuum grease left an oily residue on device surfaces, a small amount of PDMS deposited at the interface offered a better solution.

Further, the excess PDMS that runs under the mould requires trimming to create flush interfaces (**Figure 3.15**). This was done by hand, using either a blade or a scalpel. Correspondingly, the interface can become damaged, with small tears on the lower interfacing surface next to the channel, allowing fluid to escape. This trimming may not be fully sufficient, with small lips left that can subsequently prevent the opposite module fully sealing to the film. Neither condition may be noticeable by eye, but they ultimately contribute to failure of the seal, hence the deposition of PDMS at the interface. Again, this was unavoidable owing to the use of SU8 silicon wafers for reliably producing the microchannels and subsequent moulding on top, compared with casting blocks in a single mould ¹⁹⁸.

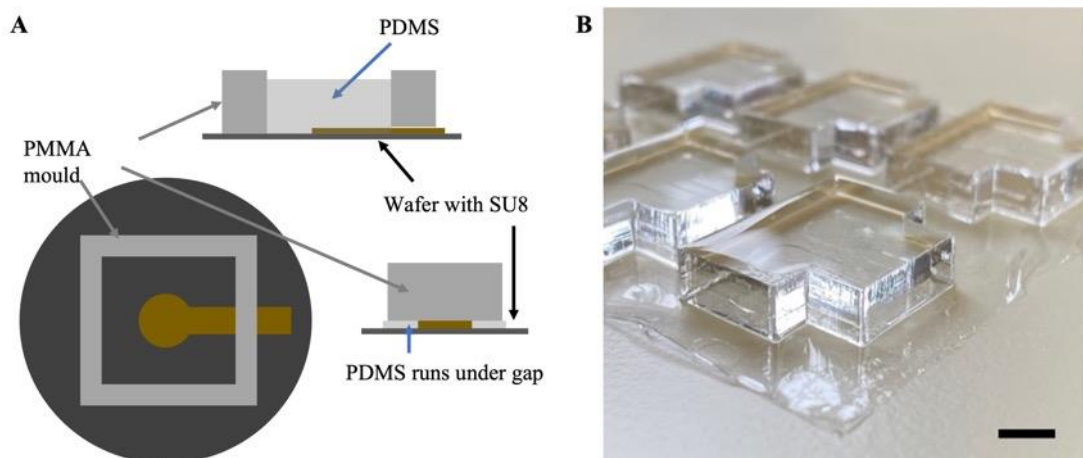


Figure 3.15. Schematic demonstrating the excess PDMS that runs under moulds. (A) Schematic representation of moulds sitting above SU8. (B) Representative example of cast PDMS modules. Once cured, the excess PDMS requires trimming which can damage the interfacing surfaces. Scale bar shows 5 mm.

3.5. Conclusion.

This chapter has detailed the selection of a suitable culture substrate for creating enclosed microfluidic devices, whilst enabling disassembly and reconfiguration, and not impacting the growth or functionality of primary hippocampal cultures. The ThermalSeal[®] RTS PSA film is

suitable for primary hippocampal cultures, with functional synaptic communication observed between cells cultured on its surface. Further, the selection of the protrusion-intrusion interfacing method for modular assembly enables the production of devices with a suitable press-fit seal between modules. Given that above information I decided to select a nominal interface width of 12 mm, with a value of 3 mm for both parameters A (the depth of the interfacing section between the protrusion and the intrusion) and B (the distance between the edge of the channel(s) and the edge of the protrusion). This will provide an optimal width for integrating the microchannel array feature between modules and provide sufficient space around the channels to help prevent collapse. A width of 12 mm also eliminates, as much as possible, the excess PDMS provided by larger interfaces that serves no function and makes modules unnecessarily bulky.

Chapter 4. Modular devices for neuronal network formation.

Having established the protrusion-intrusion design enabling a sealed interface on PSA film for reversible device assembly, I designed modules that would enable multiple blocks to be assembled into complete devices, with subsequent cell connectivity between each module. The new design was based on common features and applications seen in the literature, aiming to produce a versatile platform suitable for multiple neuroscience assays using a small number of different modules. I also developed a new casting procedure to create an improved inter-module interface, aiming to improve the seal integrity between protrusion and intrusion features.

4.1. Modules for neuronal network formation.

The aim of the newly designed modules is to provide flexibility in device production and enable more complex network formation between modules, enabling culture of neuronal networks both in series and in parallel configurations. The availability of series and parallel configurations increases the complexity of the devices that can be created, enabling recapitulation of more specific *in vivo*-like organisation and circuitry. Common applications in the literature include co-cultures with both CNS and other cell types^{127–130}, recapitulation of specific networks^{43,44,131,132}, studying axonal and synaptic connectivity^{133,137} and onset and spreading of injury or disease^{49,242,243}, as discussed in Chapter 1 and briefly outlined in **Table 4.2** at the end of this chapter. The modules I designed enable the development of such assays within one reconfigurable platform using four different modular geometries, assembled in various configurations. Further, the basic module geometry is amenable to the integration of edge-guidance microchannels (for unidirectional axonal growth between modules) or micropillars, for potentially creating 3D models and for the *in vitro* development of structures including the blood-brain barrier in the future^{169,171,173}. With more complex *in vitro* neuronal network formations in mind, it is anticipated that this modular system will enable the development of a vast array of assays within one easy to use, reconfigurable platform.

4.1.1. Double casting for enclosed modular interfaces.

Aiming to improve the reliability of the press-fit protrusion-intrusion interface, I developed a procedure to enclose the interface between modules, inspired by the enclosed protruding tabs demonstrated previously¹⁹⁸. This feature is expected to increase the success rate of conformal PDMS bonding between components and to reduce the occurrence of leaks at the interface without requiring any additional sealant. To achieve this, PDMS was cast in a double layer

using multiple moulds, where one mould contained the protrusion and intrusion layout (mould 1), while the other consisted of a simple square to build the height of the PDMS for the larger open wells (mould 2) (see Materials and Methods, **Section 2.3.3.1** and **Figure 2.6**).

4.1.2. Resultant PDMS modules.

The modules were designed to consist of either one or multiple cell culture chambers with an intrusion (**Figure 4.1Ai**), culture chambers with small microchannels and a protrusion (**Figure 4.1Aii**), or a combination of both. Each module has a height of approximately 6 mm (dictated by the acrylic moulds the PDMS is cast in). For the interfacing section between protrusion and intrusion features an arbitrary width of 12mm was selected, as this was sufficient for integrating the microchannel array (6 mm), with a height of 3 mm (again dictated by the acrylic mould). Further, this provided a value of 3 mm for both parameters A (the depth of the interfacing section between the protrusion and the intrusion) and B (the distance between the edge of the channel(s) and the edge of the protrusion), as defined in Chapter 3 (**Figure 4.1B**). For laser cutting, the nominal width in drawing files was set as 12 mm for intrusions (11.65 ± 0.03 , $n = 26$) and 11.7 mm for protrusions (11.95 ± 0.02 , $n = 10$). By interfacing protrusion and intrusion features of different modules, several configurations of microfluidic devices could be obtained, enabling serial and parallel culture conditions. Overall, as proof-of-concept, four different modules were designed (**Figure 4.2**) to create a wide range of device configurations and subsequent assays. The approximate dimensions of individual modules are as follows: the single protrusion module (**Figure 4.2A**) is 18 x 16 mm (including protrusion); the single intrusion module (**Figure 4.2B**) is 18 x 14 mm (including intrusion); the combined protrusion-intrusion module (**Figure 4.2C**) is 18 x 23 mm (including protrusion and intrusion); and the module with four intrusions combined (**Figure 4.2D**) is 24 x 24 mm. These modules, when combined, provided an interference fit, where $P > I$ (**Figure 4.1B**). The reduced area of contact given by the enclosed interface will help provide a stable press-fit seal, aided by PDMS-PDMS conformal bonding.

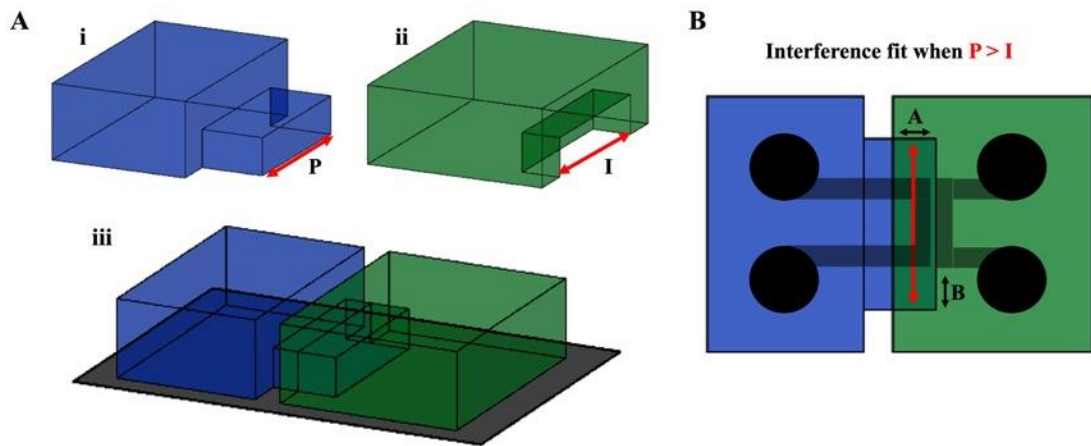


Figure 4.1. Schematic representation of the interface between protrusion and intrusion modules. (A) The main (i) protrusion and (ii) intrusion modules with widths P and I respectively and (iii) a combined two-module protrusion-intrusion device with enclosed interface. (B) A press-fit condition is achieved if $P > I$.

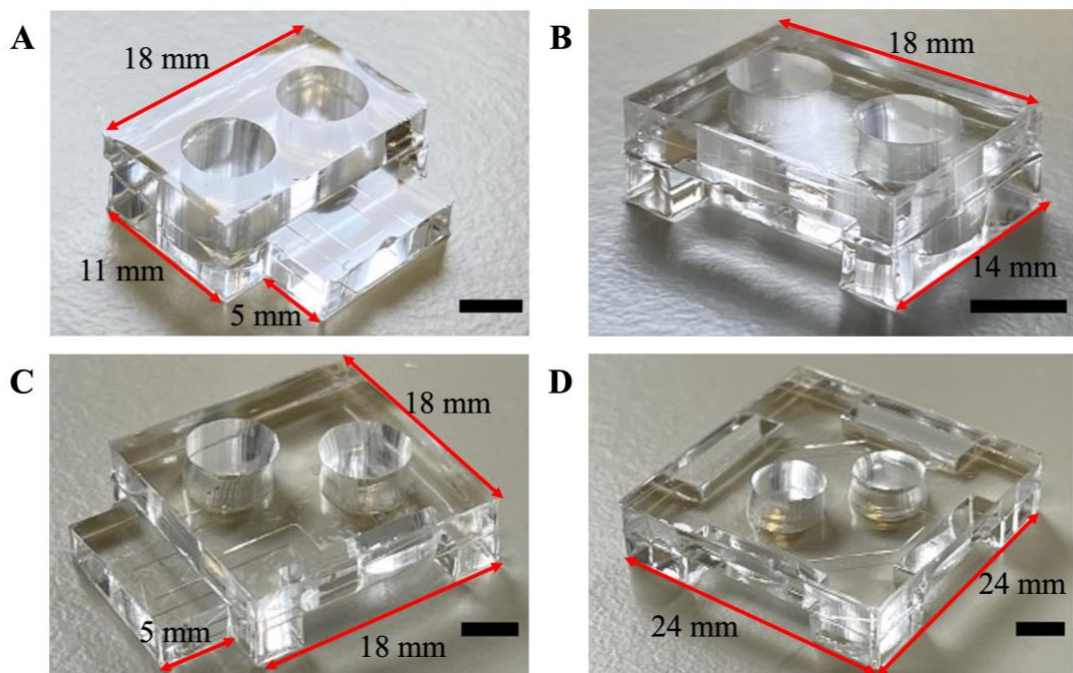


Figure 4.2. Representative examples of the four individual PDMS modules moulded in laser cut acrylic. The four main module types include (A) one protrusion, (B) one intrusion, (C) one protrusion and one intrusion combined and (D) four intrusions combined. Scale bars = 5 mm.

4.2. Modular assembly and device production.

The four modules can be assembled in various configurations on the ThermalSeal® single-sided PSA film to create enclosed microfluidic devices. Further, to improve the structural stability and facilitate microscopic imaging of devices with more than two modules, a glass coverslip or microscope slide was attached to the ThermalSeal® film using a double-sided adhesive film (3M 96042, FindTape, USA), (see Materials and Methods, **Section 2.3.3.2** and **Figure 2.7**). The high degree of flexibility created using these modules enables a large range of device configurations (**Figure 4.3**). To demonstrate this potential, I produced a range of examples. This included the common two-chamber (18 x 27 mm, **Figure 4.3A**) and three-chamber (34 x 31 mm, **Figure 4.3B**) devices alongside larger configurations including a four-chamber device, with all modules connected in series (34 x 38 mm, **Figure 4.3C**) and a six-chamber device (38 x 67 mm, **Figure 4.3E**). Finally, to demonstrate parallel module connectivity, I also produced a five-chamber device with four modules independently connected to a fifth central all-intrusion module (50 x 50 mm, **Figure 4.3D**). The combined protrusion-intrusion module type (**Figure 4.2C**) enables multiple cell network formation in series, whilst the central all-intrusion module type (**Figure 4.2D**) enables parallel cell network formation. It was also observed that the enclosed interfaces make the alignment and subsequent assembly of components quicker and more straight-forward than the initial protrusion-intrusion modules outlined in Chapter 3.

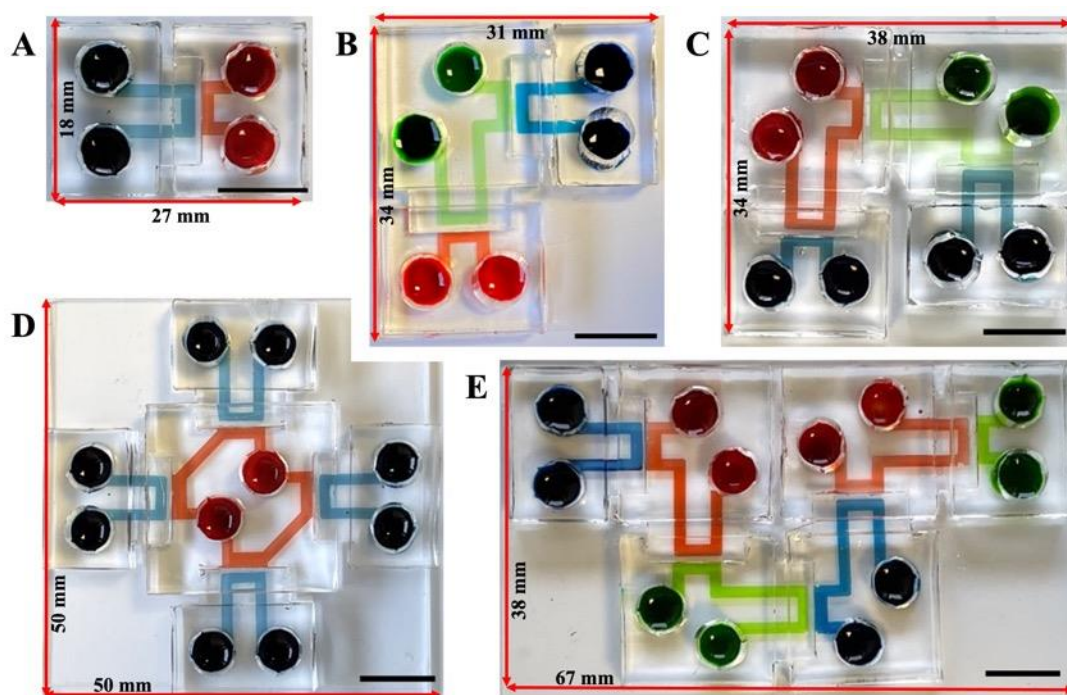


Figure 4.3. Representative examples of devices using the four module styles in various configurations. Examples include (A) the common two-chamber and (B) three-chamber devices, along with (C) a four-chamber device with modules connected in series. Larger configurations include (D) a five-chamber device, with four modules independently connected to the central intrusion module, demonstrating parallel network formation, and (E) a six-chamber device with modules connected in series. Scale bar = 10 mm.

To ensure the interface between protrusion and intrusion modules was not obstructed during assembly, I used calcein in two-module devices that were bonded to the ThermalSeal® PSA and exposed to oxygen plasma. Calcein was added to one empty well of the intrusion chamber (**Figure 4.4**, right of microchannel boundary) and a hydrostatic pressure gradient was formed across the microchannels, shown by calcein entering the protrusion chamber (left of microchannel boundary, **Figure 4.4Ai-ii**). With the addition of water to the protrusion side (**Figure 4.4Bi**), the calcein gradient was initially pushed back towards the intrusion module (**Figure 4.4Bii**). Calcein then began to re-enter the protrusion chamber (**Figure 4.4Biii**) as the water level equilibrated between inlet and outlet wells and due to the overall larger volume of calcein in the intrusion module creating greater hydrostatic pressure. However, when a larger volume of water was added to the protrusion module (**Figure 4.4Ci**), a larger hydrostatic pressure gradient was formed from the protrusion module to the intrusion module and the calcein began to fully rescind, as the water flowed across the microchannels towards the intrusion chamber (**Figure 4.4Cii**). This confirmed that channels were not blocked following

assembly on the pressure-sensitive adhesive film. Further, the modular devices can be used to induce fluidic isolation of adjacent culture chambers and create appropriate hydrostatic pressure gradients between modules, enabling regional isolation and analysis.

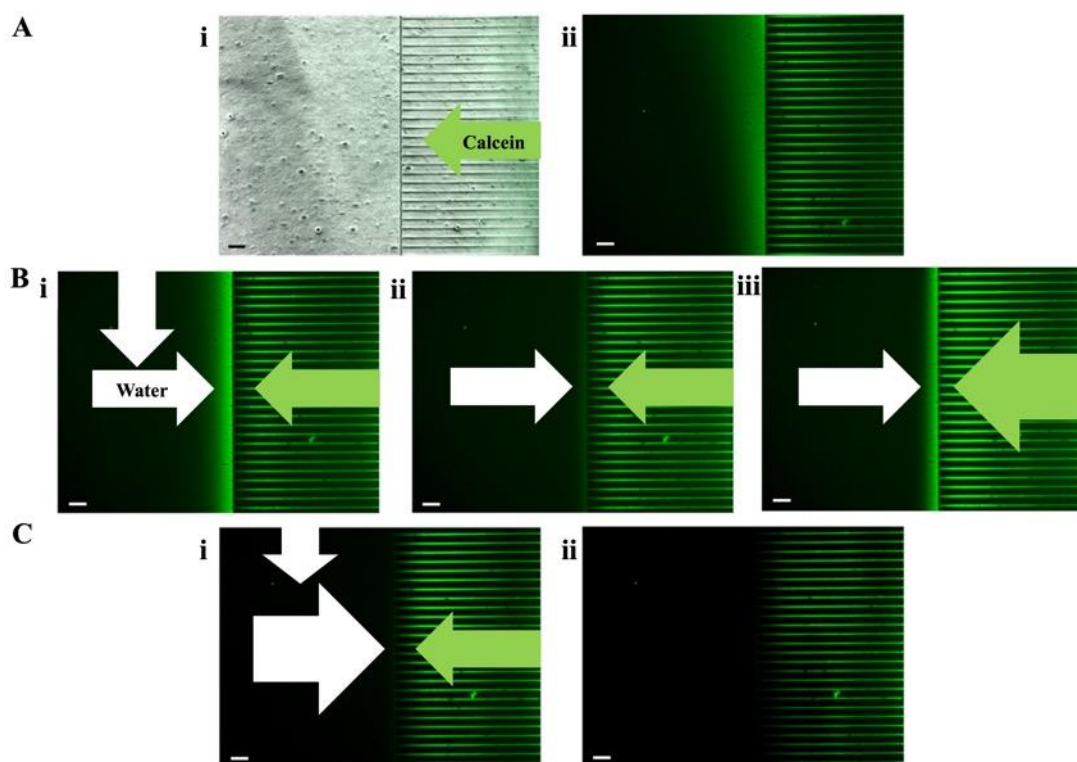


Figure 4.4. *Microchannels were not blocked by the adhesive following assembly of modular devices. Results here are for a two-module device that was oxygen plasma treated and the chamber shown is from a protrusion module with integrated microchannels. The calcein was added to the intrusion module to the right of the microchannel array, not shown in these images. (A) Beginning with empty wells, (i) 75 μ l of calcein was added to the top right well followed by the bottom right well. (ii) This caused calcein to flow across the microchannels to the left side. (B) (i) 75 μ l of water was added to the left top well, (ii) causing the gradient to retract. (iii) The water in the left chamber stabilised and the gradient reformed due to the still larger volume on the right side. (C) (i) The top left well was filled with water (ii) forcing the calcein to fully retract due to the larger volume on the left compared with the right. Scale bars = 100 μ m.*

To assess the stability of any fluidic isolation between culture chambers of separate modules, I examined the interface between two modules after a period of 30 minutes. This provided an indication as to the ability for regional manipulation and robust separation between target and non-target chambers. In the example below (**Figure 4.5**), the non-target chamber (Chamber 2) had wells filled with de-ionised water (150 μ l), whilst 75 μ l of calcein was added to the target

chamber (Chamber 1). After 30 minutes, there was a reduction in the fluorescence intensity in the target chamber, with no increase in the non-target chamber, indicating that water in fact flowed from the non-target to target chambers (**Figure 4.5C**). This demonstrates that a stimulant in the place of calcein would not be able to flow into non-target chambers, confirming the capability to produce environmentally isolated conditions.

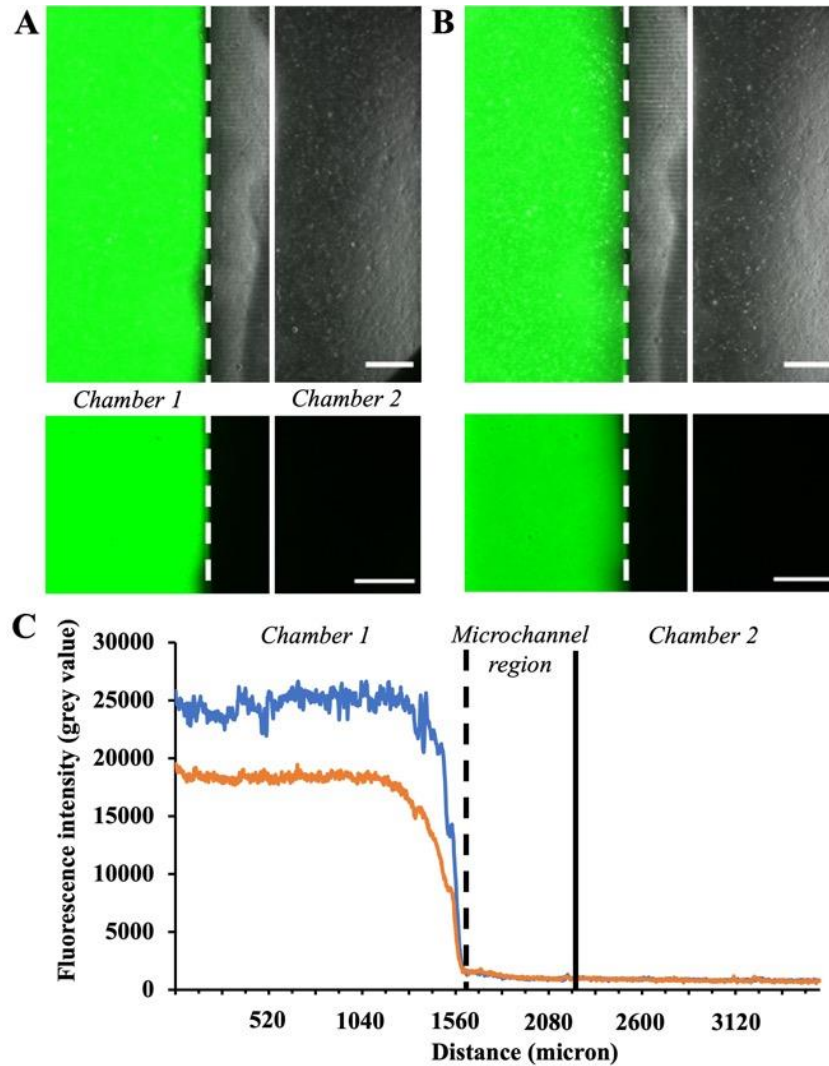


Figure 4.5. Well imbalances between culture chambers were maintained over the course of 30 minutes. Calcein was added to chamber 1 (target chamber) and a fluorescent image taken (A) immediately and after (B) 30 minutes. Images with (top) and without (bottom) brightfield. (C) Fluorescence intensity chart across the 2 chambers initially (blue) and after 30 minutes (orange). This highlights that there was no increase in fluorescence in chamber 2 and a reduction in chamber 1, indicating that passive flow does not occur from target to non-target chambers. Dashed white/black line indicates location of modular interface and beginning of microchannel region whilst solid line indicates end of microchannel region and beginning of chamber 2. Scale bars = 500 μm .

Given that researchers are unlikely to have access plasma asher equipment, I wanted to determine if priming devices using a more accessible method such as ethanol was practical. This is a universal option that is readily applicable in all research labs and would also obtain a sterile microchannel environment for subsequent cell culture. Devices were primed by adding 70% ethanol in de-ionised water to top wells, ensuring it flowed through the channels, then all wells were emptied. Upon addition of calcein to the intrusion module, a hydrostatic pressure gradient was formed across the microchannels and calcein began to fill the protrusion chamber as expected (**Figure 4.6Ai-ii**). Following the addition of water to the protrusion module, the calcein was initially pushed back (**Figure 4.6Bi**), before reforming (**Figure 4.6Bii**), as the water level equilibrated and there was greater hydrostatic pressure from the larger volume of calcein in the intrusion module. This confirms that ethanol priming is sufficient to initiate flow through PDMS channels.

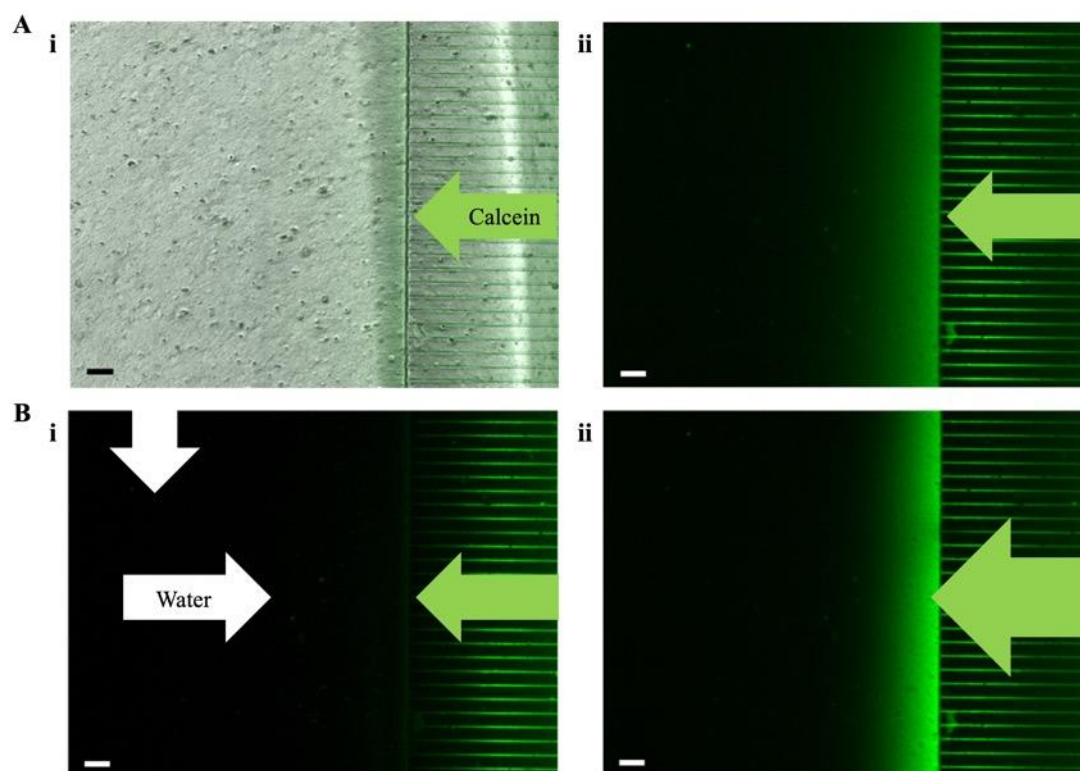


Figure 4.6. 70% ethanol is a suitable alternative to oxygen plasma treatment for initiating flow through devices. (A) Beginning with empty wells, (i) 75 μl of calcein was added to the top right well followed by the bottom right well (ii) forcing calcein to flow across the microchannels to the left side. (B) (i) 75 μl of water was added to the left top well, causing the gradient to retract. (ii) The water level in the left chamber stabilises and the gradient reforms due to the still larger volume of calcein on the right side. Scale bars = 100 μm .

4.3. Primary hippocampal culture in modular devices.

4.3.1. Cell seeding in the different modules.

The cell seeding parameters were adjusted prior to cell culture experiments in modular devices. This was to ensure a consistent flow rate across the various channels to achieve uniform cell distribution throughout the culture chambers of the different modules. Initial adjustments were made based on monolithic devices used previously¹³⁴. Here, 10 μl of cell suspension ($3\text{-}5 \times 10^6$ cells/ml) was added to each culture chamber ($\sim 16 \text{ mm}^2$) representing ~ 2500 cells/ mm^2 (at 4×10^6 cells/ml). The seeding volume was then calculated for each module based on its channel area to provide approximately 2500 cells/ mm^2 (**Table 4.1**). The flow rate (Q) was also calculated (equation 1) to assess consistency across the separate modules. The adjusted seeding volumes produce consistent flow rates across all modules (2.44 ± 0.02 $\mu\text{L}/\text{min}$) and is comparable to the flow created in monolithic devices (2.36 $\mu\text{L}/\text{min}$). Assumptions taken were for the properties of water: dynamic viscosity = 1 mPas (at 20°C) and density = $1000 \text{ kg}/\text{m}^3$. To calculate the fluidic resistance in the culture chambers, equation 2 was used as the width (w) was greater than the height (h) of the channels. Further, to calculate the hydrostatic pressure (P), equation 3 was used, with the height of the fluid body in wells calculated using equation 4 and assuming perfectly cylindrical wells. Here, the pressure is generated by the difference across the inlet and outlet wells, with gravity (g) acting on the height of the fluid (h). This in turn creates a flow across the culture chambers and microchannels. These adjustments enable uniform cell distribution in the different channels by altering the volume of cell suspension added, whilst keeping cell density of suspension constant.

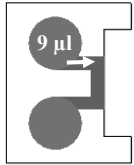
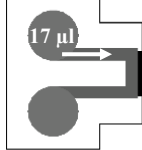
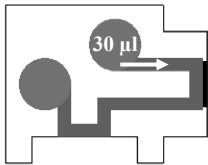
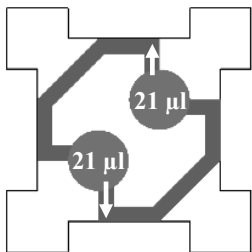
Flow rate, Q	$Q = \frac{\Delta P}{R}$	<i>Equation 1</i>
--------------	--------------------------	-------------------

Fluidic resistance, R	$R = \frac{12\mu L}{wh^3(1 - 0.63\frac{h}{w})}$	<i>Equation 2</i>
-----------------------	---	-------------------

Hydrostatic pressure, P	$\Delta P = \rho gh$	<i>Equation 3</i>
-------------------------	----------------------	-------------------

Volumetric height in wells, h	$h = \frac{V}{\pi r^2}$	<i>Equation 4</i>
-------------------------------	-------------------------	-------------------

Table 4.1. Due to their variable geometry, the seeding volume was adjusted for each module. Seeding volume was adjusted for the individual modules to ensure uniform cell distribution without changing the cell suspension density.

Module	Cell suspension
<p>Intrusion module</p> 	<p>Channel area ~ 14 mm². Cells required ~ 35,000. Cell suspension required ~ 9 µl. Q = ~ 2.49 µl/min</p>
<p>Protrusion module</p> 	<p>Channel area ~ 27 mm². Cells required ~ 67,500. Cell suspension required ~ 17 µl. Q = ~ 2.44 µl/min</p>
<p>Protrusion and intrusion combined module</p> 	<p>Channel area ~ 48 mm². Cells required ~ 120,000 Cell suspension required (4M cells/ml) ~ 30 µl. Q = ~ 2.43 µl/min</p>
<p>Four-intrusion module</p> 	<p>Total channel area ~ 67 mm². Cells required ~ 167,500. Cell suspension required ~ 42 µl. 21 µl added to each channel region. Q = ~ 2.38 µl/min</p>

4.3.2. Primary hippocampal cultures in ethanol treated devices.

Having determined that ethanol priming enabled flow through the modular devices in a similar fashion to that seen with oxygen plasma treated devices, it was essential to ensure this method is suitable for sterilisation and subsequent cell culture. Again, this is a method used extensively in neuroscience labs and contributes to the goal of allowing use of microfluidic devices outside labs with specialist equipment. Two-module devices were used, with an assessment of cell growth within the channels and neurite outgrowth across the modular interface. The existing protocol for functionalising the substrate surface and increasing adhesion of cells relied on plasma treatment immediately prior to adding the solution with an adhesion molecule (e.g.,

PLL). Initial results showed this coating procedure was insufficient for modular devices where flow was initiated using ethanol in place of plasma treatment. Here, cellular adhesion to the PSA substrate was disrupted, with more clumping and less distribution of cells (**Figure 4.7A**) compared with previous cultures subject to coating immediately following plasma treatment. This is likely a result of a lack of functionalisation that the plasma treatment provides with subsequent insufficient time for the coating to bind to the substrate. However, immunocytochemical staining revealed neurites transecting between chambers across the microchannels where cells had adhered (**Figure 4.7B**).

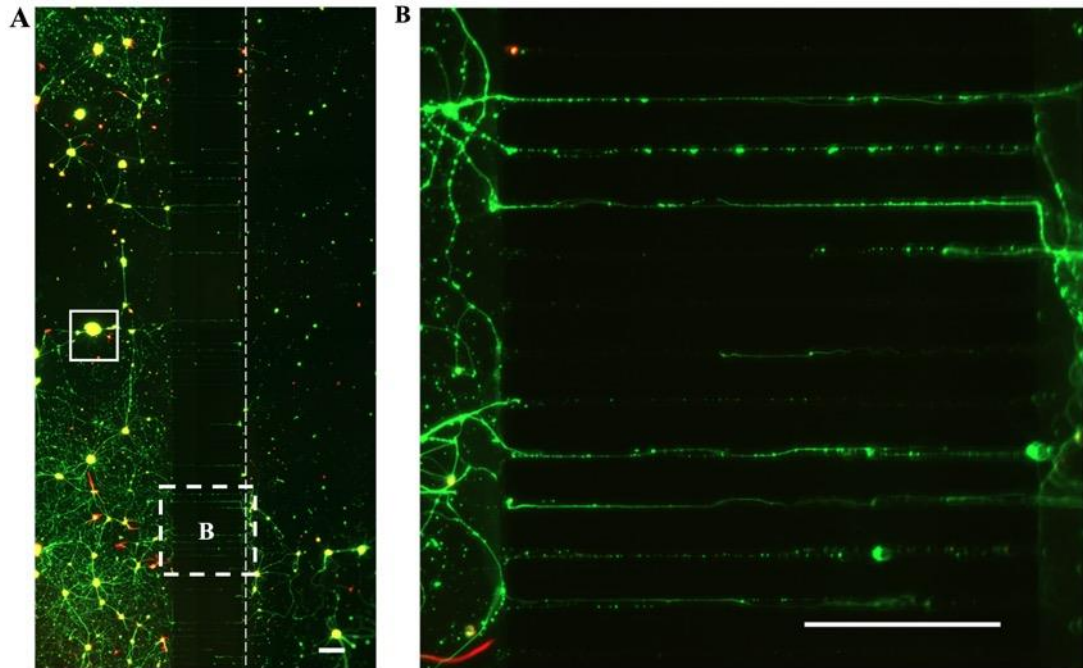


Figure 4.7. *Poor cell adhesion was observed with initial cultures in modular devices that had been primed with ethanol. Primary hippocampal cultures stained after 13 DIV with β III-tubulin shown in green and GFAP shown in red. (A) A two-chamber modular device bonded to PSA film was primed using 70% ethanol followed by addition of PLL for 1 hour. Large cellular aggregates were observed in culture chambers (white solid box) with poor cell distribution overall. White dashed line represents the interface. (B) However, neurites enter microchannels between compartments indicating the modular interface does not pose a barrier to cellular connectivity between components. Scale bars = 200 μ m.*

Adjusting the coating protocol and leaving the PLL in devices overnight in a 37°C/5% CO₂ incubator improved the culture conditions. This compensates for the adhesive properties and the altered surface chemistry provided by plasma treatment. Whilst some clumping was still observed, cells cultured on surfaces with the longer treatment time had improved overall distribution (**Figure 4.8A**) and more consistent neurite outgrowth across microchannels

(**Figure 4.8B**), as compared with the cultures above. These results highlight ethanol priming as a suitable alternative to oxygen plasma treatment. The ethanol treatment appears to have no effect on cellular growth, provided the PLL coating is left on for an appropriate length of time, and provides suitable sterilisation. This provides greater potential for microfluidic technologies to be used outside specialist laboratories.

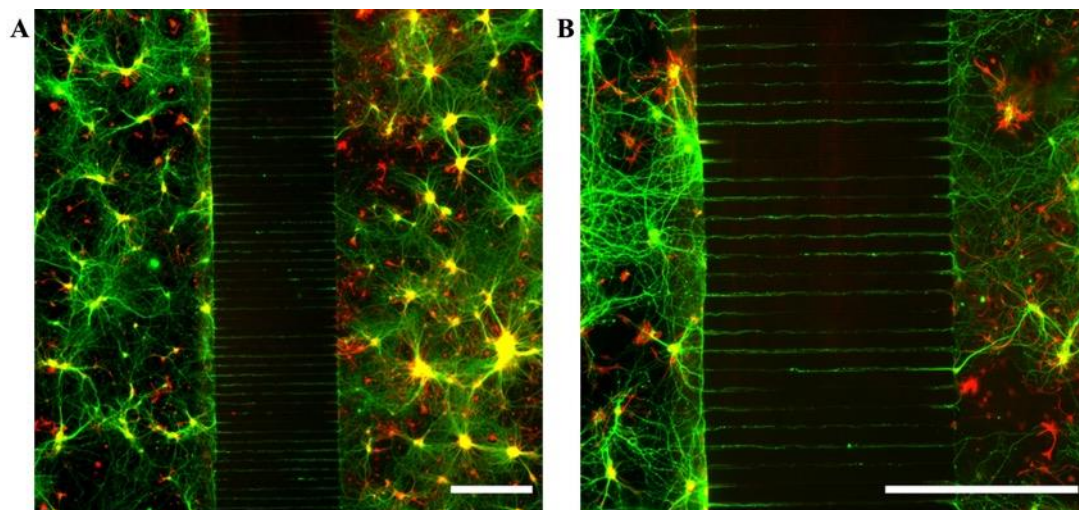


Figure 4.8. *An increased incubation time with PLL demonstrated improved cellular distribution in modular devices primed with ethanol. Improved cellular distribution throughout culture chambers of both the intrusion (left) and protrusion modules of a two-chamber device, with subsequent neurite outgrowth through microchannels. Green = β III-tubulin and red = GFAP. Scale bar = 500 μ m.*

4.4. Design and production evaluation.

Whilst the laser cut acrylic provided a smooth surface for casting PDMS, the persistent surface irregularities prevent fully complimentary protrusion and intrusion interfaces. The enclosed interface made assembly and alignment overall simpler, but it could not resolve these issues. As a result, no consistent conformal PDMS-PDMS bonding could be achieved at the interface, increasing the likelihood of leaking. In devices that were primed using 70% ethanol, leaking was less frequent than in devices that were plasma treated, due to the PDMS remaining hydrophobic. Here, the enclosed interface with the hydrophobic PDMS was sufficient for preventing a full failure of the seal in 4 of 6 two-module devices initially tested (~ 66%). However, as with the regular protrusion-intrusion interface, this could not be replicated with the same combinations of blocks more than once. Further, for larger device configurations where multiple modules are all interconnected, this increases the area over which seal-compromising defects occur. As a result of the issues highlighted and lack of a consistent leak-free seal, particularly in larger device configurations, I decided to brush PDMS (cured at RT,

24-48 hours) around the interfaces to achieve hermetic sealing across devices for my remaining cell culture experiments. This layer of PDMS fills any small gaps between irregular interfacing surfaces and once cured provides a barrier to leaking. The use of PDMS improved the success rate to around 90%. However, even if small leaks were present, they could be compensated for and did not disrupt cell culture experiments. Further, devices could still be dis-assembled with careful detachment of modules sequentially from the ThermalSeal® PSA, enabling re-use of modules after cleaning in IPA. Overall, this protrusion-intrusion interface design does provide a modular platform to create larger devices containing multiple, fluidically isolated culture chambers with cellular network formation throughout.

Despite 70% ethanol initiating flow through devices and demonstrating a suitable sterilisation procedure for primary hippocampal cultures in modular devices, the formation of air gaps in culture chambers was more frequent than in plasma treated devices. In two-module devices, disruptive air gaps were most often seen forming in the intrusion modules close to the interface. Here bubble nucleation was directly observed forming in the corner of a channel over the course of 3 minutes (**Figure 4.9A**) or observed in the form of an air gap across the length of the channel, forming within 1 minute (**Figure 4.9B**). This suggests the occurrence is due to insufficient, non-hermetic sealing around the modular interface with areas open to the environment, which allows introduction of air to the system. However, bubble formation was also observed in monolithic devices, albeit to a lesser extent (**Figure 4.10Ai-ii**), and in modular devices sealed with a layer of PDMS around the interface (**Figure 4.10B**). This then suggests that the surface tension between the untreated, hydrophobic PDMS and the liquid influences bubble formation. Bubble formation was reduced when rinsing with supplemented media in place of water, where the B27 component appeared to enable better wetting of the PDMS surface, compared with water and media without B27. Other mitigations included ensuring all liquids for priming were at room temperature and careful observation when rinsing to ensure wells were not fully emptied, so as not to disrupt the flow path into channels. In some instances, bubbles could also be dislodged by pushing the fluid through the channel with a pipette placed close to the entrance. However, even with these mitigations, bubbles persisted to form in more than half of modules upon introduction to an incubator environment, resulting in channels drying out and preventing their immediate use (**Figure 4.10B**) Further, as larger devices have a greater number of modules, the likelihood of one of these failing and bubble nucleation occurring increases, preventing use of the entire device. Major and disruptive bubble formation must therefore be from a combinatory effect of poorly sealed devices, a lack of functionalisation of the hydrophobic PDMS surface and the static, perfusion free conditions.

At this point, I decided to plasma treat devices and store them at 4°C filled with de-ionised water prior to using them for my remaining cell culture experiments.

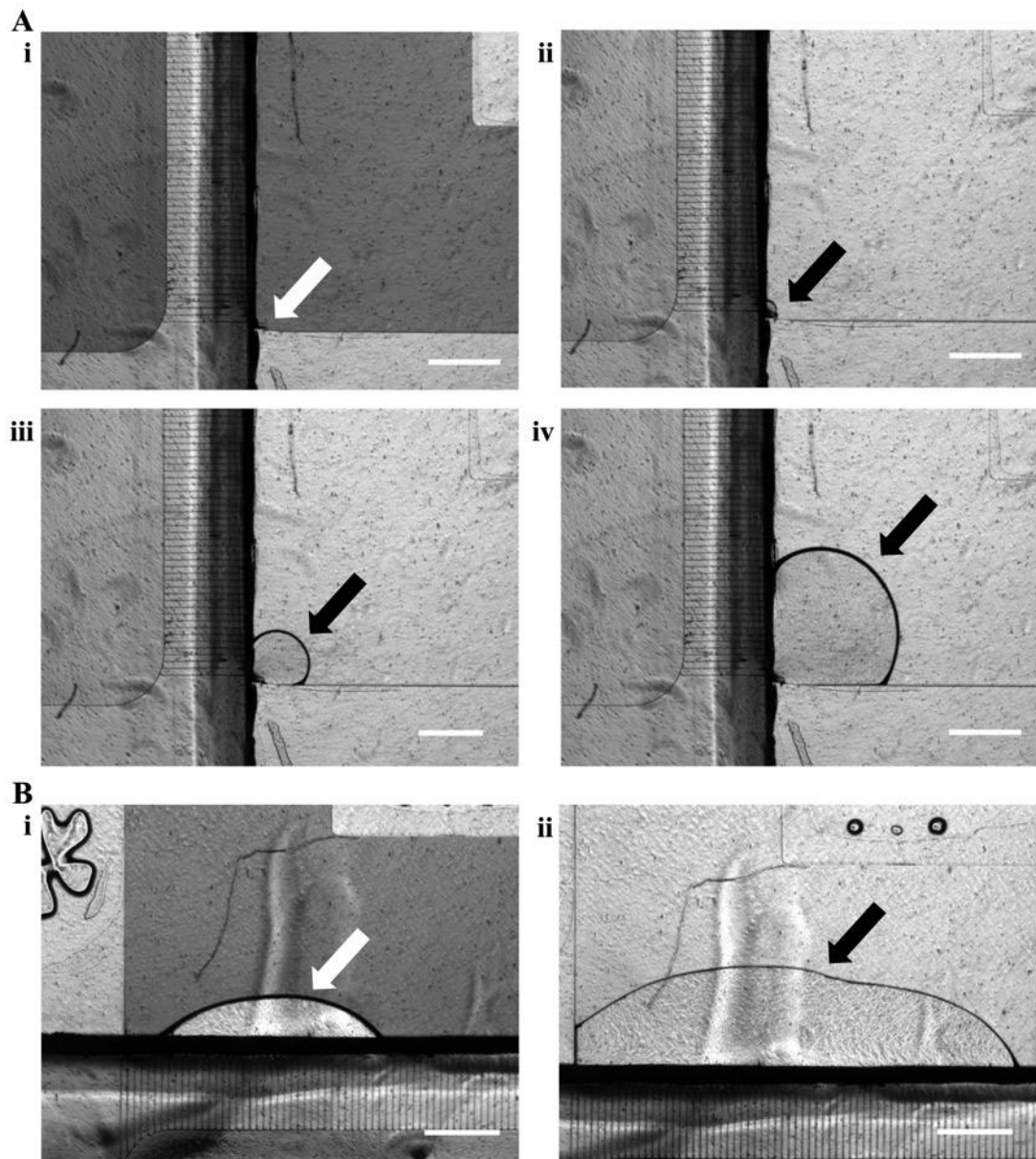


Figure 4.9. Priming modular components with ethanol can lead to disruptive bubble formation in culture chambers. (A) Bubble nucleation was observed in the corner of channels at the modular interface, suggesting insufficient sealing. (B) Air gaps were seen forming along the length of culture chambers suggesting surface tension effects also contribute to this problem, with the hydrophobic PDMS repelling the water. Arrows indicate air gaps and bubbles in chambers. Scale bars = 500 μm .

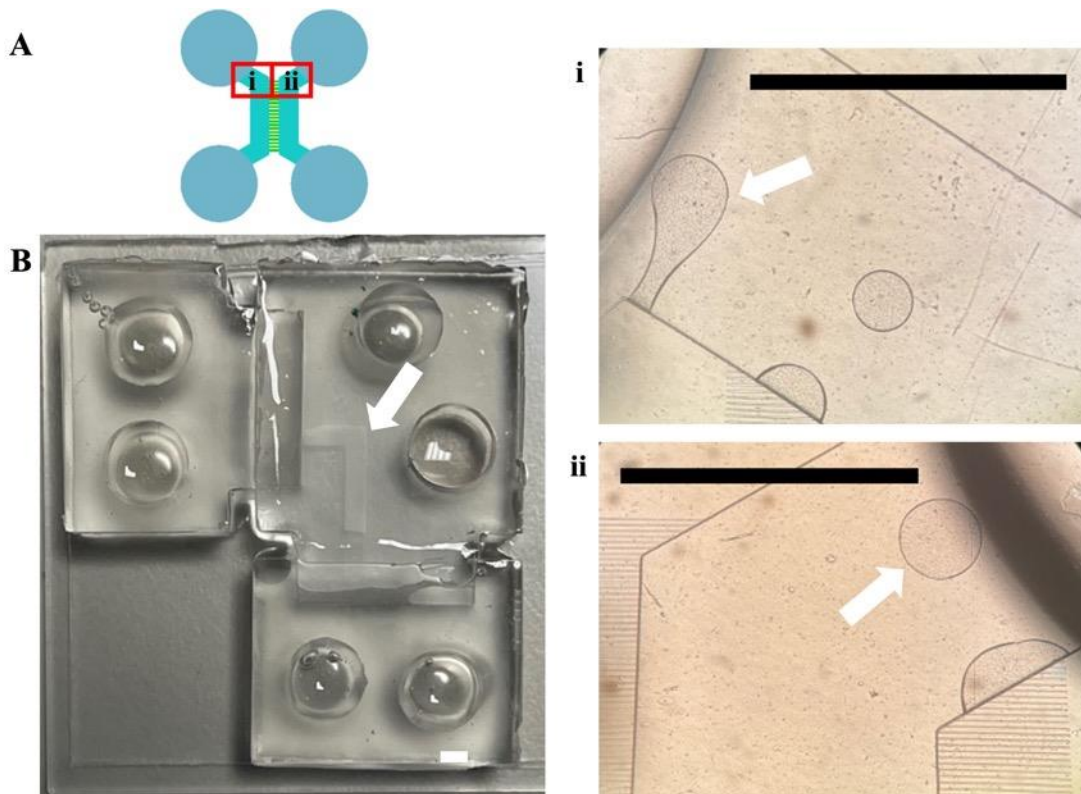


Figure 4.10. *Bubble/air gap formation was observed in monolithic devices and modular devices sealed with PDMS. (A) Small bubbles were observed in culture chambers of hermetically sealed monolithic devices. (B) Air gap in a channel of a modular device sealed with PDMS after incubation overnight at 5% CO₂/37°C. This represents a major disruption to flow through the device thus making it unusable. Arrows indicate air gaps and bubbles. Scale bars = 2 mm.*

4.5. Discussion.

At this stage, the enclosed protrusion-intrusion design offered the most appropriate solution for creating a modular platform. This interfacing method offers simple alignment and subsequent assembly without the need for additional mechanical components or tubing for connecting components. Further, the direct connection between the separate PDMS modules ensures culture chambers are separated by the microchannel arrays enabling somal isolation with guided neurite growth through microchannels between culture compartments and subsequent cellular connectivity. This in turn ensures that individual culture chambers can be fluidically isolated and spatial/regional stimulation and analysis is possible. Using various combinations of modules, this platform would allow the recreation of devices used for co-cultures^{127–130} and recapitulation of specific networks^{43,44,131,132}, studying axonal and synaptic connectivity^{133,137}, and onset and spreading of injury or disease^{49,242,243}.

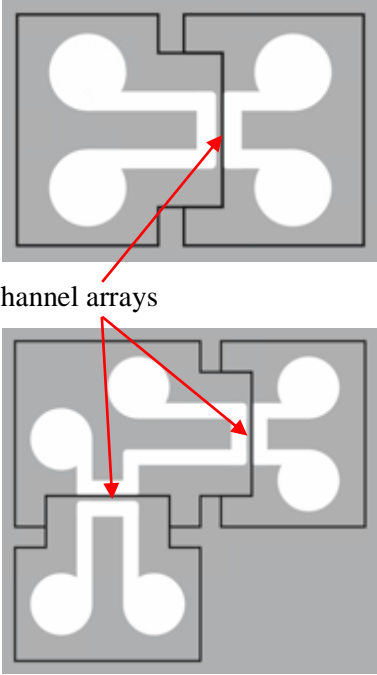
For priming devices, plasma treatment alters the surface chemistry, oxidising it and making the surface hydrophilic²⁴⁴. This helps improve coating with the adhesion molecule and subsequently cell attachment, compared with the ethanol treatment. Using the original protocol in ethanol treated devices (PLL incubated in devices for 1-1.5 hours), cells were observed detaching from the substrate surface and the remaining cells formed large aggregates. This in turn vastly reduces cellular distribution and the subsequent likelihood for consistent functional network connectivity. Therefore, adjusting the coating protocol and leaving the PLL in devices overnight was essential for ensuring continued growth and health of cells. Cells grown in these devices showed more consistent cellular distribution, reduced cell aggregate formation and greater neurite outgrowth through microchannels. For consistency, plasma exposed devices (both modular pre-assembled devices and monolithic devices plasma bonded to glass) had the same coating procedure applied. This does not have a negative influence on cell growth and functionality and was deemed suitable as devices were stored at 4°C and filled with de-ionised water prior to use, rather than having the PLL immediately applied.

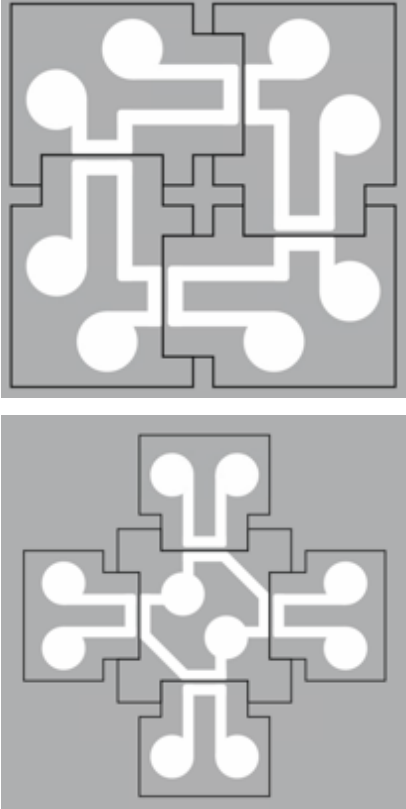
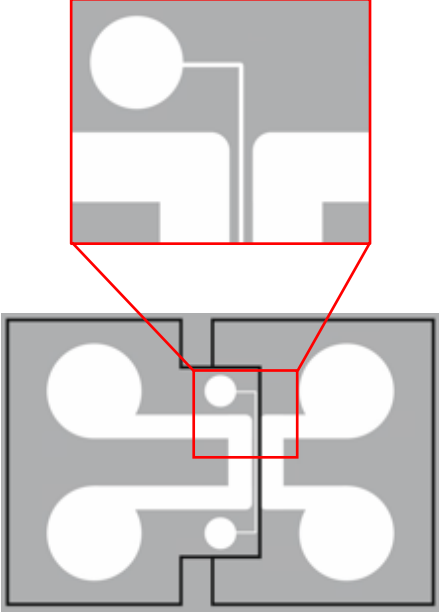
Priming devices with ethanol can offer an accessible alternative to oxygen plasma treatment, enabling sterilisation and cell culture in the absence of complex and expensive equipment. However, the formation of air gaps in culture chambers was more frequent using ethanol priming, which in turn can disrupt subsequent flow and culture conditions. Even with mitigations, in some cases bubbles may not be visible, but upon introduction to an incubator during the coating procedure, channels may dry out and prevent the immediate use of those devices. Overall, major and disruptive bubble formation is from a combinatory effect of poorly sealed devices, a lack of functionalisation of the hydrophobic PDMS surface and the perfusion free conditions. Therefore, for future experiments, I decided to brush PDMS around the interface of devices then plasma treat, and store devices filled with de-ionised water at 4°C until required. This did not impact the reconfigurability, as PDMS modules could be carefully removed from the PSA and each other. For reusing modules, these were cleaned in IPA then rinsed in de-ionised water and blow dried, prior to reassembling on a fresh piece of PSA film. Previous examples of modular systems have also used PDMS as a sealant to ensure a hermetic seal between adjacent components^{199,203}. However, to make the platform truly accessible, further work will be needed to fabricate modules with more consistent interfacing surfaces that can produce consistent hermetic seals and prevent the introduction air from the environment. In addition, it is necessary to test alternative coating methods in the absence of oxygen plasma treatment, to aid flow through devices and prevent surface tension effects giving rise to bubble nucleation.

4.5. Conclusion.

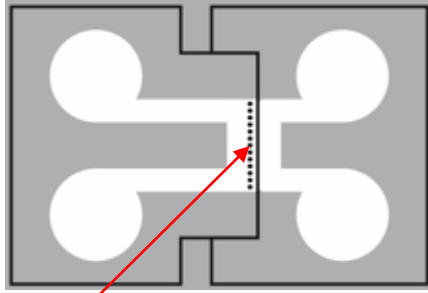
This chapter has set out the design of improved channel and module geometry for ensuring cellular network connectivity across the modular interface. Whilst the new enclosed protrusion-intrusion interface did not fully resolve issues with sealing, it improves the alignment and subsequent assembly of modules. In ethanol treated two-module devices, around 66% showed no leaking. However, any small leaks could be compensated for, by keeping well volumes topped up, and did not disrupt cultures. Further, the use of extra PDMS at the interface, particularly in larger configurations, provided a success rate closer to 90%. I have shown the possibility to create multiple interconnected *in vitro* neuronal cultures with distinct microenvironments using the modular components and appropriate fluidic manipulation. Further, the proposed modules provide the ability to produce more complex *in vitro* neuronal cultures beyond the capabilities of current monolithic equivalents. To improve the sealing between individual modules and produce consistent, hermetic, leak-free seals without the use of PDMS around the interface, further work is needed with regards to module fabrication and channel coating. This could take the form of testing more advanced 3D printers for mould production, using thick film SU8 resists to produce moulds with combined wall and microfluidic features²⁴⁵⁻²⁴⁷, using alternative materials for soft lithography^{248,249}, as well as modifying the PDMS²⁵⁰ or coating the modules with a material such as PVA to improve hydrophilicity²⁵¹.

Table 4.2. Common applications of microfluidic devices for neuroscience research. A literature search enabled investigation into the most common microfluidic features used in the literature and provided a better idea of how to design a more universal platform for multiple applications.

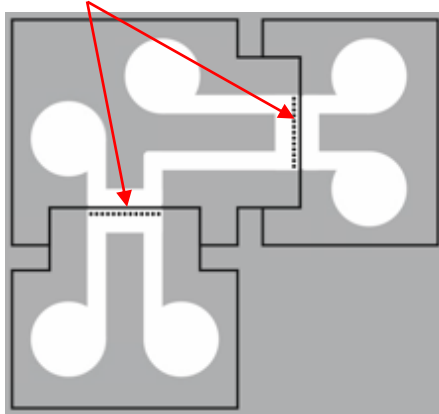
Device features	Example applications in the literature
<p>2+ culture chambers separated by microchannel arrays.</p> <p>This is the major device configuration in use given its ease of fabrication and commercial availability.</p> <p>Microchannels either linear, for bidirectional synaptic connectivity, or tapered (diodes) to enable directed connectivity between compartments.</p>  <p>Microchannel arrays</p>	<p><u>Co-cultures.</u></p> <p>Environmentally isolated neuronal populations for studying neurodegenerative disease propagation. ^{40,133,141,143,146,152–155,252}</p> <p>Neurons and glial cells for studying myelination. ^{128,253}</p> <p>Co-culture of neurons and microglia for studying microglial recruitment and response to disease. ^{127,151,254}</p> <p>Recapitulation of specific <i>in vivo</i> networks including:</p> <ul style="list-style-type: none"> • Cortical-thalamic ^{47,132} • Cortical-striatal ^{45,46} • Cortical-hippocampal-amygdala ⁴⁴ • Basal ganglia ⁴³ <p>Spread of chemical injury and investigating neuroprotective mechanisms of the network. ⁴⁹</p> <p><u>Co-cultures with non-neuronal cells.</u></p> <p>Co-culture of motor neurons and muscle cells for studying neuromuscular junction. ^{129,255–259}</p>

	<p>Co-culture of neurons and cardiomyocytes for studying cardiac function. ^{130,260}</p>
<p>Axotomy channel transecting the microchannel array.</p> 	<p>Axotomy via detergent in central chamber for studying injury and regeneration. ^{261,262}</p>
<p>2+ main chambers separated by phase guides in place of microchannels. This enables gel</p>	<p>3D neuronal cultures to improve extracellular environment. ¹⁶³</p>

insertion and polymerisation for 3D culture conditions.



Phase guides in place of microchannels to enable addition of gel for 3D culture.



Blood-brain barrier. Multiple examples in the literature, varying in complexity based on the cell types used. Here, the use of endothelial cells, pericytes and astrocytes would give the most accurate representation of *in vivo* environment.

169–171,173,263

Chapter 5. Research capabilities of the modular platform for neuroscience.

Having developed an appropriate module geometry to enable cell network formation across the protrusion-intrusion interface, modular devices were examined to ensure functional synaptic connectivity is achieved between the separate components. Primary rat hippocampal cultures were used, with subsequent immunocytochemical staining and calcium imaging used to assess cell growth across the interface and functional synaptic connectivity between environmentally isolated populations. The aim is to demonstrate that the modular platform performs as seen in monolithic device equivalents, with the added attraction of flexibility and reconfigurability. This will enable user-defined device production without the need for specialist knowledge and facilities, thus enabling and widening the use of microfluidic technology and its associated benefits within the neuroscience research community.

5.1. Connectivity and functional synaptic communication across the modular interface.

Immunocytochemical staining indicated uniform cellular distribution throughout the two separate culture chambers of a 2-module device (**Figure 5.1A**), with β III-tubulin staining indicating neurite outgrowth across the modular interface and between the environmentally isolated cell populations (**Figure 5.1B-C**). To ensure functional synaptic connectivity was achieved across the modular interface, Ca^{2+} imaging protocols previously developed for probing connectivity between fluidically isolated hippocampal cultures were adapted^{125,134}. The initial flow rate across the microchannels was negligible and was calculated to be 0.10 $\mu\text{l}/\text{min}$. Following the addition of glutamate (G, 100 μM) to chamber A (blue chamber highlighted in **Figure 5.2A**), the initial flow rate from inlet to outlet well was calculated as 6.92 $\mu\text{l}/\text{min}$. There was an increase in Ca^{2+} events from 0 events/minute over the baseline period (B) to 1.11 ± 0.01 events/minute ($p < 0.0001$, B vs G, $n = 223$ cells from 3 separate devices/cultures) in the directly stimulated side/chamber A (**Figure 5.2C**, blue data points) and an increase from 0 events/minute over the baseline period to 0.27 ± 0.04 events/minute ($p < 0.0001$, B vs G, $n = 170$ cells from 3 separate devices/cultures) in the synaptically connected adjacent side/chamber B (**Figure 5.2C**, black data points). Subsequently, following the addition of KCl (30 mM) to chamber B (black chamber highlighted in **Figure 5.2A**), the initial flow rate across the culture chamber was calculated as 6.92 $\mu\text{l}/\text{min}$, and once stabilised, the flow rate across the microchannels towards the glutamate-stimulated side (A) was calculated as 0.12 $\mu\text{l}/\text{min}$. There was an increase in events from 0 events/minute over the baseline period

to 1.07 ± 0.02 events/minute in chamber *B* ($p < 0.0001$, *B* vs KCl) (**Figure 5.2C**, black data points). This also elicited a response in culture chamber *A* (**Figure 5.2C**, blue data points), from 0 events/minute over the baseline period to 0.35 ± 0.04 events/minute ($p < 0.0001$, *B* vs KCl), indicating bidirectional synaptic connectivity across the modular interface.

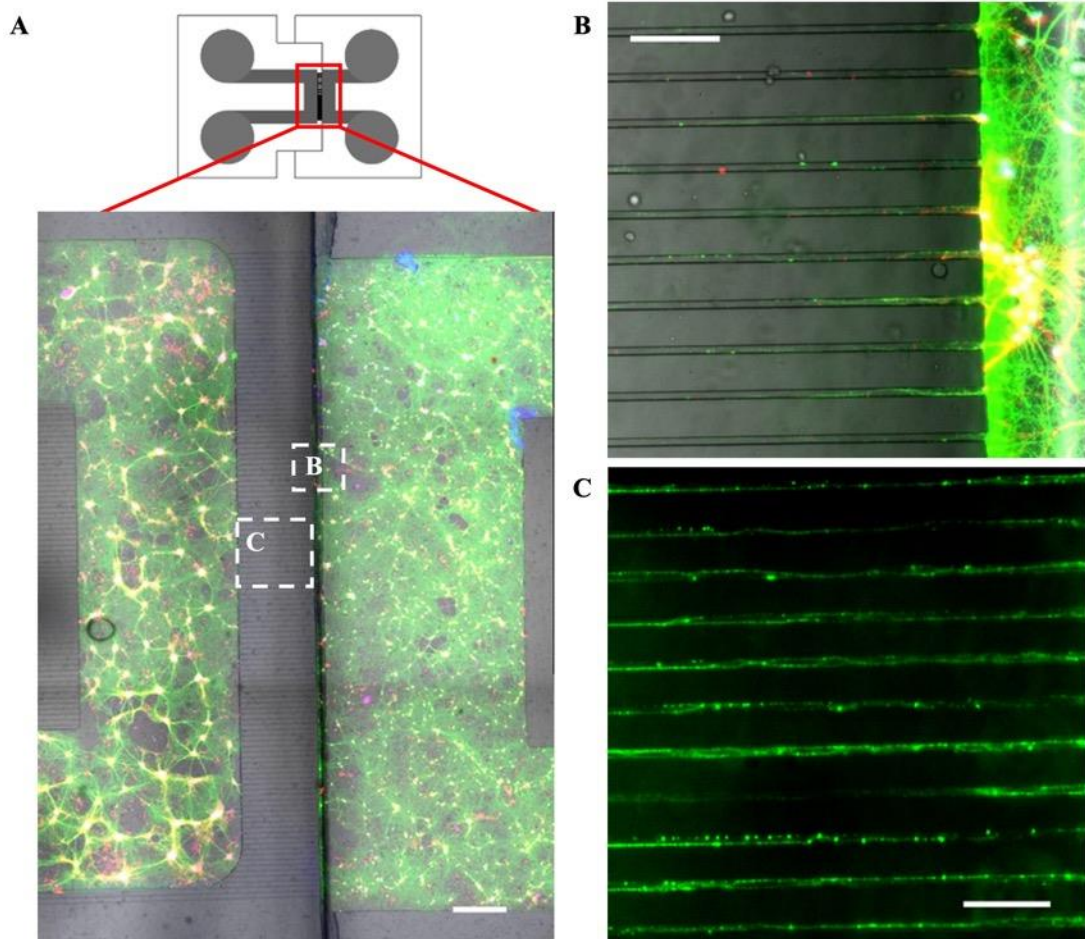


Figure 5.1. Healthy growth and morphology of primary hippocampal cultures is observed in 2-module devices. (A) Cellular distribution was evident throughout culture chambers of both the protrusion (left) and intrusion (right) modules, with neurites (B) able to cross the modular interface and (C) grow throughout the microchannels. Green = β -III tubulin, red = GFAP and blue = DAPI. Scale bars = 500 μ m (A) and 100 μ m (B-C).

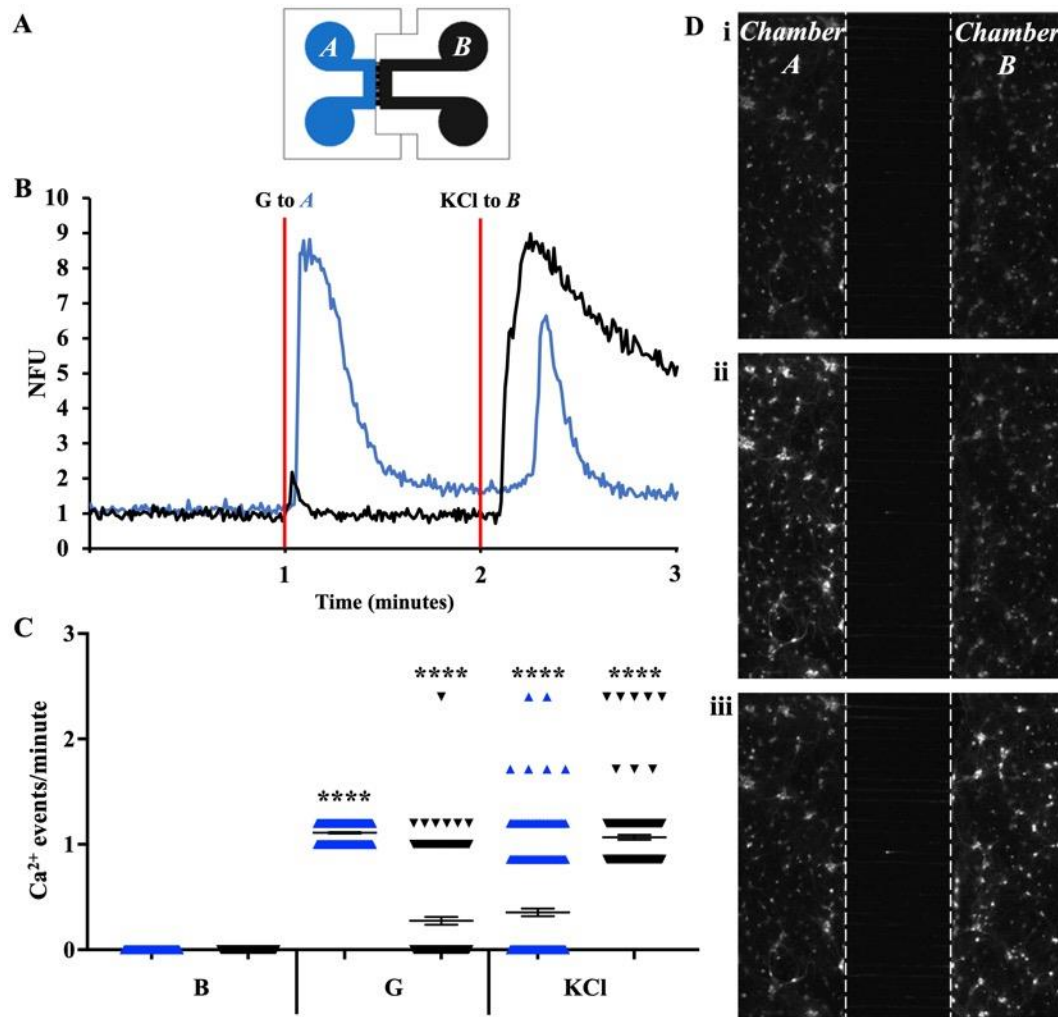


Figure 5.2. Hippocampal cultures grown in modular devices are functional and synaptically connected across the protrusion-intrusion interface. (A) Schematic of a 2-module device. (B) Representative fluorescence intensity traces for a synaptically connected cell in chamber A (blue) and chamber B (black). NFU = normalised fluorescence units. (C) An increase in Ca²⁺ events in response to G and KCl indicates hippocampal cultures are functional and synaptic connectivity occurred between the cultures of separate modules. Scatter chart shows mean \pm S.E.M. $n = 223$ cells in chamber A and 170 cells in chamber B of 3 separate devices/cultures. **** = $p < 0.0001$. (D) Representative images during (i) the baseline period; (ii) the period following addition of G to chamber A; and (iii) the period following the addition of KCl to chamber B. White dashed lines indicate boundary between culture chambers and microchannel region in the centre.

5.1.1. Functional synaptic connectivity across multiple modular interfaces.

To further assess the capabilities of the platform and ensure functional connectivity in larger device configurations, 3-module devices were examined. This is important as it will

demonstrate functional synaptic connectivity can be achieved across multiple interconnected modules, ensuring the relevance and usability of larger devices. As with the 2-module devices, primary hippocampal cultures showed uniform cellular distribution throughout the three culture chambers, with neurite processes again crossing the modular interface and the presence of neurites throughout microchannels (**Figure 5.3**).

To examine functional synaptic connectivity in these 3-module devices, a 0 Mg²⁺ HBS solution was tested. This stimulation approach has been demonstrated previously to induce an increase in neuronal excitability, due to the reduced external Mg²⁺ unblocking NMDA receptors^{224–226,264}. For the purpose of this demonstration, an increase in neuronal excitability will improve the likelihood of seeing indirect cellular responses, compared with a single large response and subsequent desensitisation observed using glutamate in the 2-module device. This was particularly important given the length of the central protrusion-intrusion chamber and subsequently the large number of cells that any signal would travel through between the two outer chambers. The experiment using 0 Mg²⁺ HBS was tested in both 2-module and 3-module devices to assess whether increased neuronal activity was observed following an incubation period as mentioned in previous studies²²⁶.

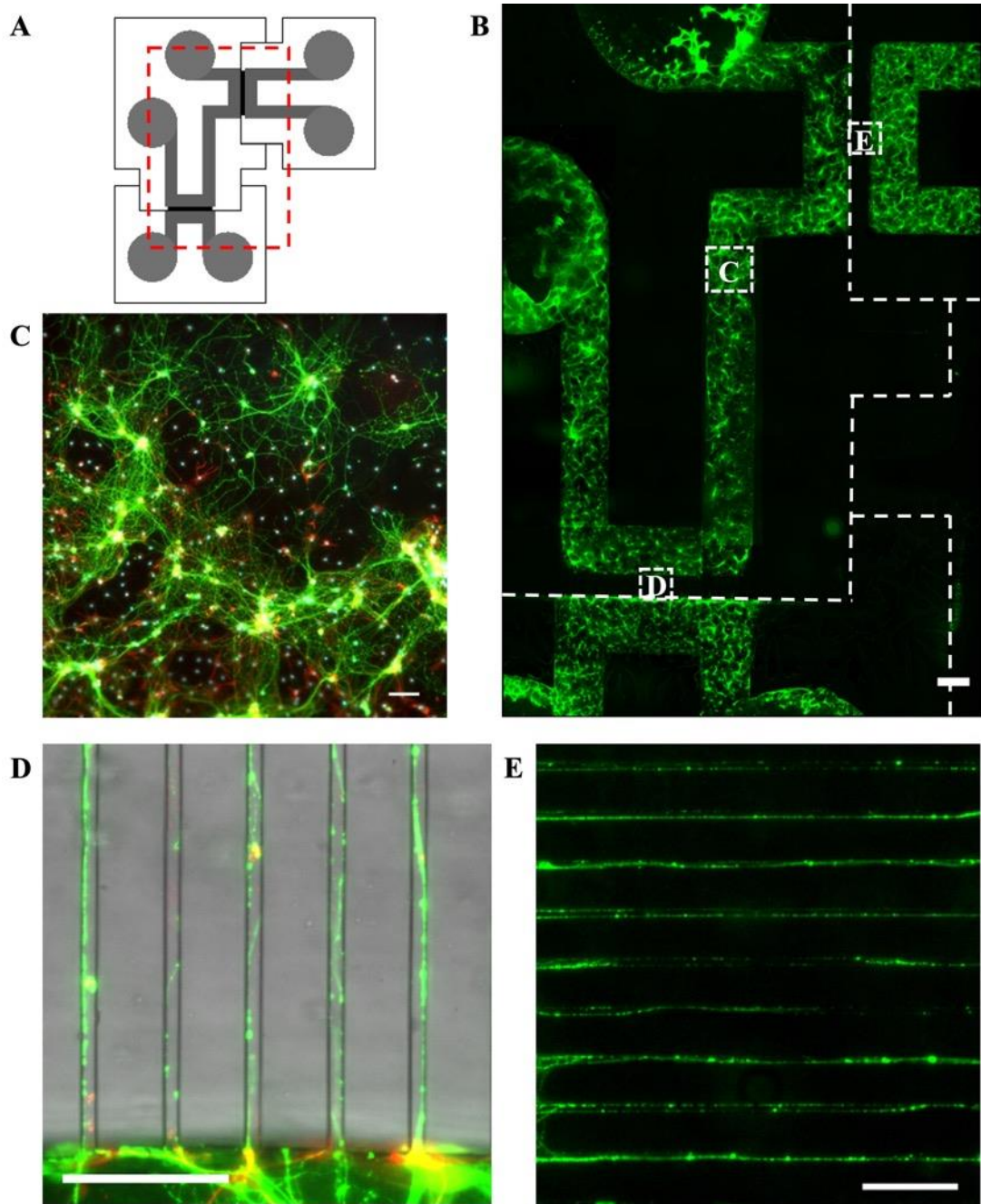


Figure 5.3. *Healthy growth of hippocampal cultures in a 3-module device, with neurites observed across multiple protrusion-intrusion interfaces. (A-C) Uniform neuronal cell distribution throughout the culture chambers of the three individual components. (D) Neurites are again able to cross the modular interface with (E) a presence throughout microchannels indicating connectivity across the three modules. Green = β III-tubulin, red = GFAP, blue = DAPI. Scale bars = 2 mm (B) and 100 μ m (C-E).*

The 0 Mg^{2+} HBS was added to one culture chamber of a 2-module device (chamber A, blue chamber highlighted in **Figure 5.4A**), with recordings captured between this and the adjacent

culture chamber (chamber *B*, black chamber highlighted in **Figure 5.4A**). The indirect chamber was filled with approximately 150 μl normal Mg^{2+} HBS, initiating a flow rate across the microchannels of 0.20 $\mu\text{l}/\text{min}$. Beginning with empty wells in chamber *A* at $t = 0$ minutes, 0 Mg^{2+} HBS was added at $t = 2$ and 3 minutes and recordings were captured periodically over a period of 30 minutes (**Figure 5.4A**). As the wells of chamber *B* were left filled with normal HBS, the hydrostatic pressure gradient created prevents flow or diffusion of the 0 Mg^{2+} HBS into chamber *B* (see Chapter 4, **Figures 4.5**). The flow rate across the microchannels, following the addition of 0 Mg^{2+} HBS, was reduced to 0.14 $\mu\text{l}/\text{min}$. In chamber *A*, there was an increase in Ca^{2+} events from 0 events/minute over the baseline period ($t = 0 - 2$ minutes) to 0.13 ± 0.01 events/minute in the period following the addition of 0 Mg^{2+} HBS ($t = 2 - 10$ mins. $p < 0.0001$, B vs 0 Mg^{2+} , $n = 63$ cells from 1 device/culture) and 0.07 ± 0.02 events/minute in the post-incubation period ($t = 20 - 30$ mins. $p = 0.0012$, B vs 0 Mg^{2+}) (**Figure 5.4B**, left, blue data points). This also elicited an increase in the synaptically connected adjacent side (chamber *B*) from 0 events/minute over the baseline period to 0.01 ± 0.01 events/minute in the period following the addition of 0 Mg^{2+} ($p = 0.1899$, B vs 0 Mg^{2+} , $n = 37$ cells from 1 device/culture) and to 0.03 ± 0.01 events/minute in the post-incubation period ($p = 0.0273$, B vs 0 Mg^{2+}) (**Figure 5.4B**, left, black data points).

In a control device, normal HBS (2 mM Mg^{2+}) was added to chamber *A* in place of the 0 Mg^{2+} HBS solution. Whilst this elicited an increase in chamber *A* from 0 events/minute over the baseline period to 0.05 ± 0.01 events/minute following the addition of normal HBS ($p = 0.0053$, B vs 0 Mg^{2+} , $n = 19$ cells from 1 device/culture) and to 0.02 ± 0.01 events/minute in the post-incubation period ($p = 0.1861$, B vs 0 Mg^{2+}) (**Figure 5.4B**, right, blue data points) there was no increase in activity in the indirectly stimulated side (**Figure 5.4B**, right, black data points). Further, the magnitude of events in cells directly stimulated with the 0 Mg^{2+} HBS was 5.41 ± 0.42 NFU, compared with a magnitude of 1.46 ± 0.16 NFU in cells directly stimulated using the control normal Mg^{2+} HBS. These results suggest the use of 0 Mg^{2+} HBS as a suitable tool to determine functional connectivity in larger device configurations. The increased activity achieved over a longer period will decrease the likelihood of dissipation of the signal before reaching the downstream neurons of indirect chambers in a 3-module device.

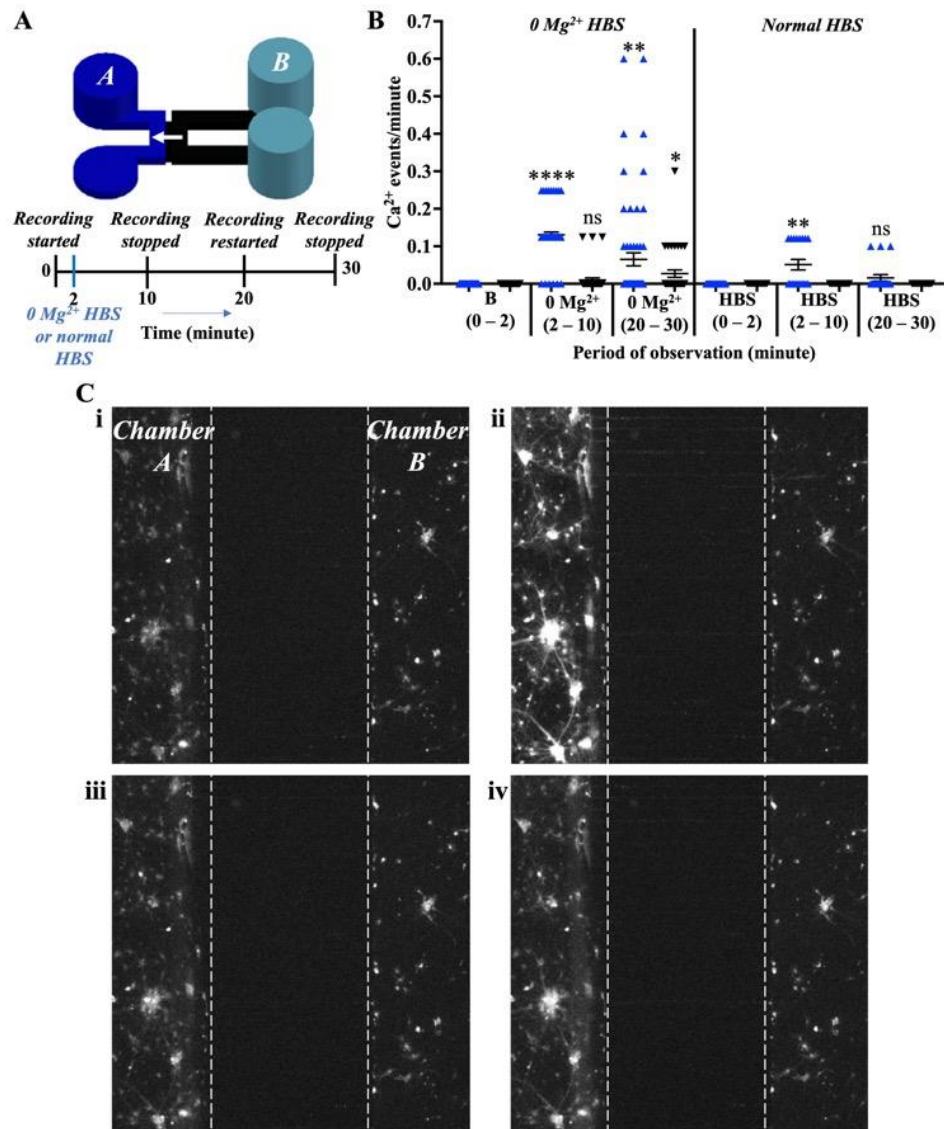


Figure 5.4. 0 Mg^{2+} HBS induced an increase in calcium response in 2-module devices following an incubation period. (A) Schematic and timeline of the experiment. (B) 0 Mg^{2+} HBS induced continued activity in the directly stimulated chamber A (blue points) and an increase in activity in the synaptically connected chamber B (black points) following an incubation period, which was absent with a control (normal HBS, right). Charts show mean \pm S.E.M., $n = 63$ cells in direct chamber and 37 cells in the indirect chamber from 1 device loaded with 0 Mg^{2+} and 19 cells in direct chamber and 15 cells in the indirect chamber from 1 device loaded with the control. A one-way ANOVA was used to compare events over baseline period ($t = 0 - 2$ minutes), the period following addition of the stimulant/control ($t = 2 - 10$ mins) and the post-incubation period ($t = 20 - 30$ mins). * = $p < 0.05$, ** = $p < 0.01$ and **** = $p < 0.0001$. (C) Representative images taken during the Ca^{2+} imaging experiment at (i) $t = 0$ minutes; (ii) $t = 2$ minutes, after 0 Mg^{2+} HBS addition; (iii) $t = 10$ minutes; and (iv) $t = \sim 20$ minutes, following the incubation period.

In 3-module devices, the 0 Mg^{2+} HBS was added to chamber 1 (red chamber) and recordings were taken of the microchannel region between chamber 2 (green chamber) and chamber 3 (blue chamber) (**Figure 5.5A**). This enabled observation of secondary effects in chamber 2, which had direct connectivity with cells in chamber 1, and tertiary effects in chamber 3, which did not have direct connectivity with cells in chamber 1. Wells of chamber 1 were emptied, whilst those of chambers 2 and 3 were filled with normal HBS, inducing a hydrostatic pressure gradient towards chamber 1 and preventing flow or diffusion of the 0 Mg^{2+} solution into the indirect chambers over the course of the experiment (see Chapter 4, **Figure 4.5**). The initial flow rate across microchannels was calculated as approximately $0.20 \mu\text{l}/\text{min}$. This was reduced to approximately $0.14 \mu\text{l}/\text{min}$ following the addition of 0 Mg^{2+} HBS to chamber 1.

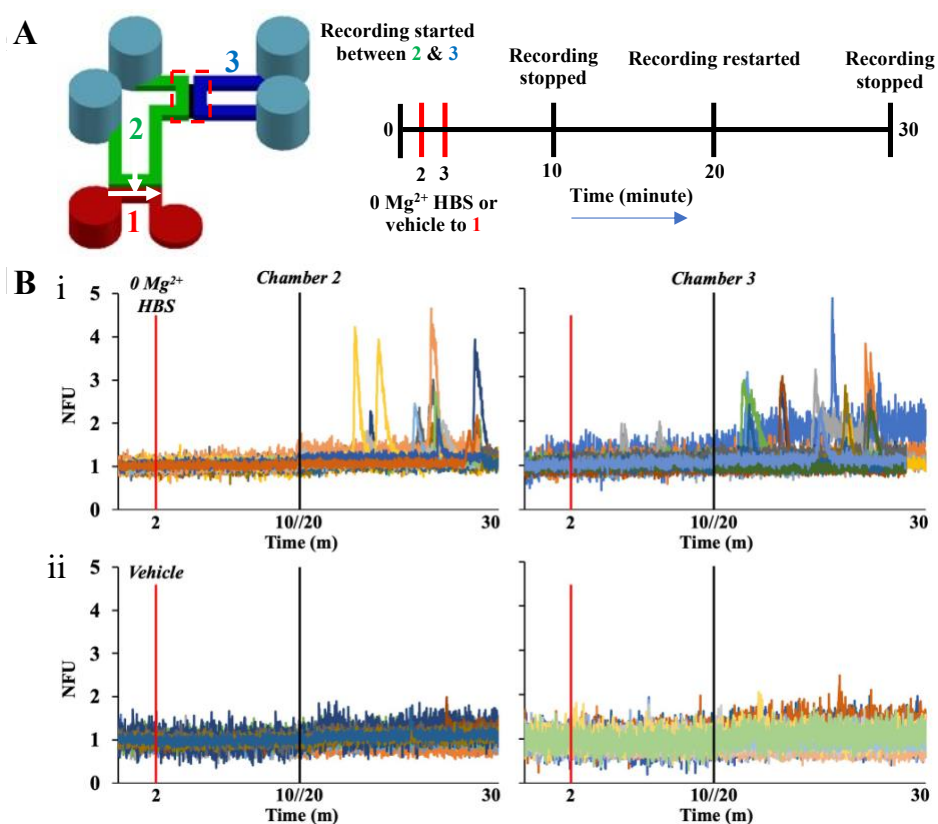


Figure 5.5. Functional synaptic connectivity was observed in 3-module devices. (A) Schematic and timeline of Ca^{2+} imaging experiments in 3-module devices. (B) (i) 0 Mg^{2+} HBS induced increased activity in both chamber 2 (left) and chamber 3 (right) following an incubation period, (ii) which was absent with normal Mg^{2+} HBS.

Following the incubation period with the 0 Mg^{2+} HBS, there was an increase in activity observed in both chamber 2 (**Figure 5.5Bi**, left) and chamber 3 (**Figure 5.5Bi**, right). In chamber 2, there was an increase in Ca^{2+} events from 0 events/minute over the baseline period ($t = 0 - 2$ minutes) to 0.04 ± 0.01 events/minute over the post-incubation period ($t = 20 - 30$

minutes) ($p < 0.0001$, B vs 0 Mg^{2+} , $n = 65$ cells from 2 separate devices from 2 separate cultures) (**Figure 5.6**, left, green data points) and in chamber 3 there was an increase from 0 events/minute over the baseline period to 0.04 ± 0.01 events/minute over the post-incubation period ($p = 0.0001$, B vs 0 Mg^{2+} , $n = 57$ cells from 2 separate devices/cultures) (**Figure 5.6**, left, blue data points). Conversely, in a control device with normal Mg^{2+} HBS added to chamber 1, there was no significant increase in activity observed in the cell populations of either chamber 2 or chamber 3 (**Figure 5.5Bii**). In chamber 2, there was a small increase in Ca^{2+} events from 0 events/minute over the baseline period ($t = 0 - 2$ minutes) to 0.01 ± 0.01 events/minute over the post-incubation period ($t = 20 - 30$ minutes) ($p = 0.3357$, B vs V, 13 cells from 1 device/culture) (**Figure 5.6**, right, green data points) and in chamber 3 there was a small increase from 0 events/minute over the baseline period to 0.01 ± 0.00 events/minute over the post-incubation period ($p = 0.3346$, B vs V, $n = 30$ cells from 1 device/culture) (**Figure 5.6**, right, blue data points). These results suggest that functional synaptic connectivity was achieved across all modules in the 3-module devices, highlighting the usability of larger device configurations for producing more complex, connected cultures.

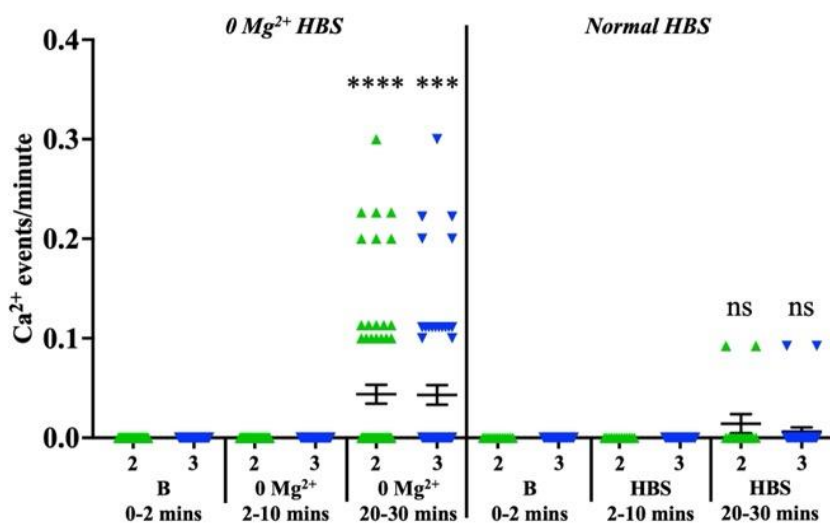


Figure 5.6. Functional synaptic connectivity was observed across the three chambers in 3-module devices. Increase in Ca^{2+} events in both chambers 2 (green) and 3 (blue) with addition of the 0 Mg^{2+} HBS (0 Mg^{2+} , left), compared with normal HBS (HBS, right). Chart shows mean \pm S.E.M., $n = 65$ cells in chamber 2 and 57 cells in chamber 3 from 2 devices/cultures loaded with 0 Mg^{2+} HBS and 13 cells in chamber 2 and 30 cells in chamber 3 from 1 device/culture loaded with normal HBS. One-way ANOVA used to compare events over the baseline period ($t = 0 - 2$ mins), the period following addition of the 0 Mg^{2+} HBS/normal HBS ($t = 2 - 10$ mins) and the post-incubation period ($t = 20 - 30$ mins). *** = $p < 0.001$, **** = $p < 0.0001$, ns = non-significant.

5.2. Modular devices as tools to study neurodegenerative disease mechanisms *in vitro*.

To show proof-of-concept suitability of the platform for studying mechanisms of neurodegeneration, a modular 3-chamber device was used where one chamber (red protrusion module, **Figure 5.7**) was seeded with pre-formed fibrils (PFFs) to induce phosphorylation of α -synuclein at serine-129 (pSer-129- α Syn), a disease-specific post-translational modification observed in Parkinson's disease. PFFs were seeded in the target chamber after 7 DIV, with the recommended time frame being 6-10 DIV due to limited primary culture lifespans but the need for mature synapses²⁶⁵. At 7 DIV it is anticipated that neurites will have begun to fully transverse the microchannel barrier, with network connectivity established between separate neuronal populations in the immediate vicinity of the microchannel barriers across culture chambers²⁶⁶.



Figure 5.7. Modular devices can be used as tools for investigating neurodegenerative disease mechanisms. PFFs were added to one module (red highlighted chamber 1) after 7 DIV, with cells fixed and stained after 14 DIV. Hydrostatic pressure gradients were induced towards the target chamber, ensuring environmental isolation, and preventing flow of PFFs into non-target chambers.

In the target chamber, the PFFs produced pSer-129- α Syn, evident by the typical punctate and thread-like pSer129 staining^{157,221} (**Figure 5.8A** and **Figure 5.8i-iii**). Further, pSer-129 staining was also evident in the adjacent synaptically connected but fluidically isolated chamber 2 (**Figure 5.8B** and **Figure 5.8iv-vi**), with a reduced level of $0.12\% \pm 0.01\%$ compared with $0.46\% \pm 0.08\%$ in the target chamber ($p = 0.03$, target vs non-target) (**Figure 5.8D**). This indicates that either transport or transfer of pathology occurred between the cultured neurons. Undesired transport of PFF solution between the target and adjacent chambers was prevented by creating a hydrostatic pressure gradient towards the target chamber (see Chapter 4, **Figures 4.5**). Further, no punctate or thread-like pSer-129 staining was observed in the non-target chamber 3 (calculated as $0.00\% \pm 0.00\%$), whilst the antibody used has previously been demonstrated for its robustness in specifically targeting the phosphorylated α -synuclein and not wild-type α -synuclein¹⁷⁵. These results indicate that the

modular platform can serve as a suitable tool for *in vitro* neurodegenerative disease modelling and investigation into mechanisms of pathological spread.

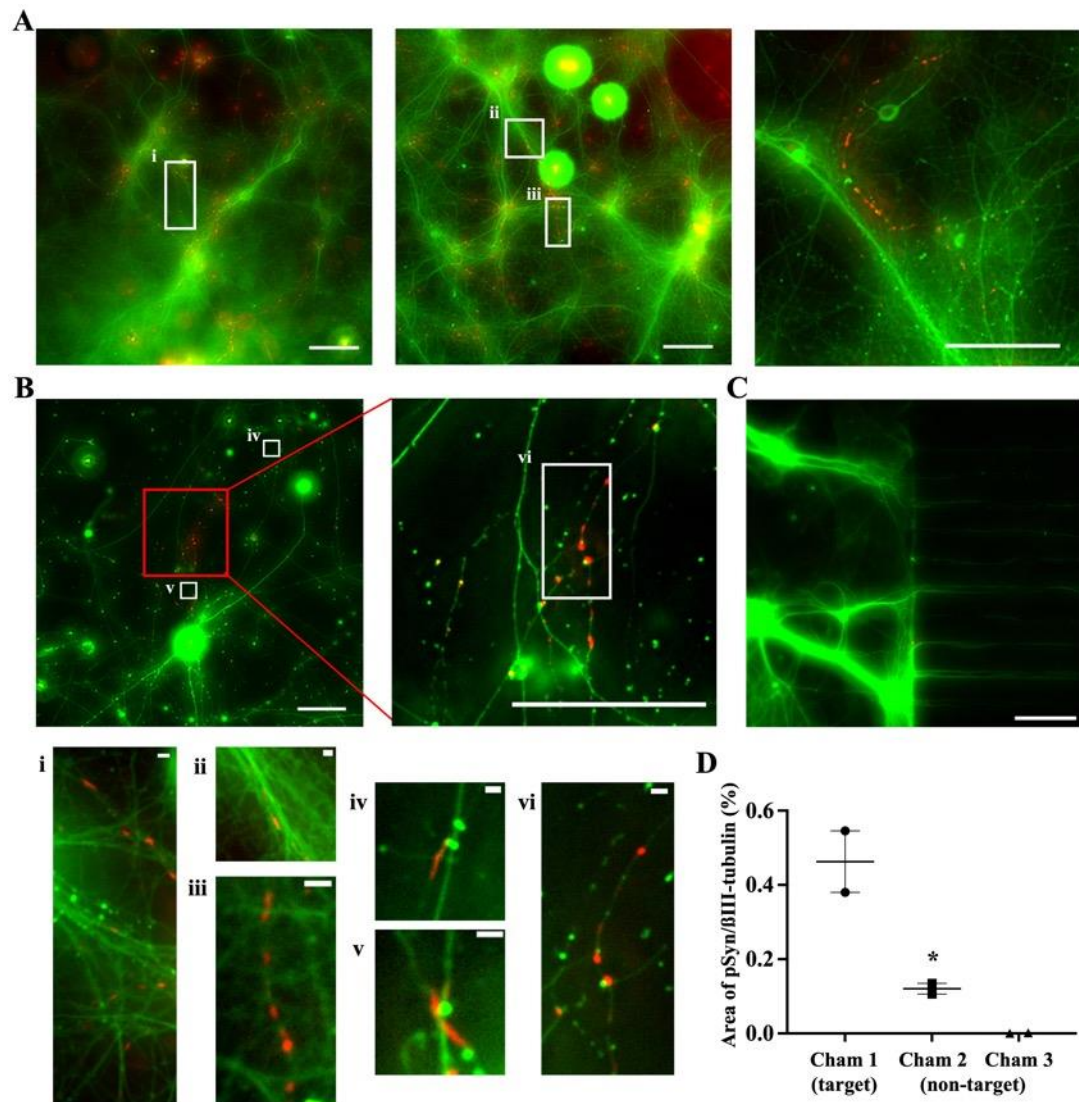


Figure 5.8. The addition PFFs induced phosphorylation of α -synuclein in primary hippocampal cells cultured in a modular device. Representative images taken in (A) target chamber (Chamber 1); (B) non-target chamber 2; and (C) non-target chamber 3 of a 3-module device (Figure 5.7) 7 days after the addition of PFFs to the target chamber (14 DIV). pSer129 staining in the target chamber indicated internalisation and phosphorylation of α -synuclein fibrils, with subsequent transfer of pathology to a fluidically isolated but synaptically connected non-target chamber 2, evident by both punctate and thread-like features (red). Pathological staining was absent in chamber 3. Red = pSer-129- α Syn and green = β III-tubulin. Scale bars = 100 μ m (top and middle row of images) and 5 μ m (i-vi). (D) The level of pSyn was calculated as a percentage of the level of β III-tubulin, demonstrating a reduction in the non-target chamber 2 ($n = 2$ images from each chamber of 1 device).

5.3. Controlling neurite outgrowth to produce defined network connectivity.

In addition to linear microchannels that enable bidirectional synaptic connectivity, diode microstructures were designed to provide edge-guidance of neurites for either permitting or prohibiting growth between culture chambers. These allow the formation of more defined networks, increasing the ability to recapitulate specific *in vivo* connectivity. Typical structures include ‘heart’, ‘arrow’, ‘zig-zag’ and ‘triangle’ shaped features^{138,139}. Here, as a proof-of-concept example, I chose to combine heart and arrow shaped features (**Figure 5.9A**) as these have previously been demonstrated to be effective at blocking and stalling outgrowth in the prohibitive direction¹³⁹. Fabrication was performed as before in a two-step process, with SU8 3005 (10 μm) used for the microchannel layer as it produced defined heart-arrow features compared with SU8 3010. Primary hippocampal cultures were prepared as before in a 2-module device, with culture chambers connected by the edge-guiding microchannels, then fixed and stained after 14 DIV.

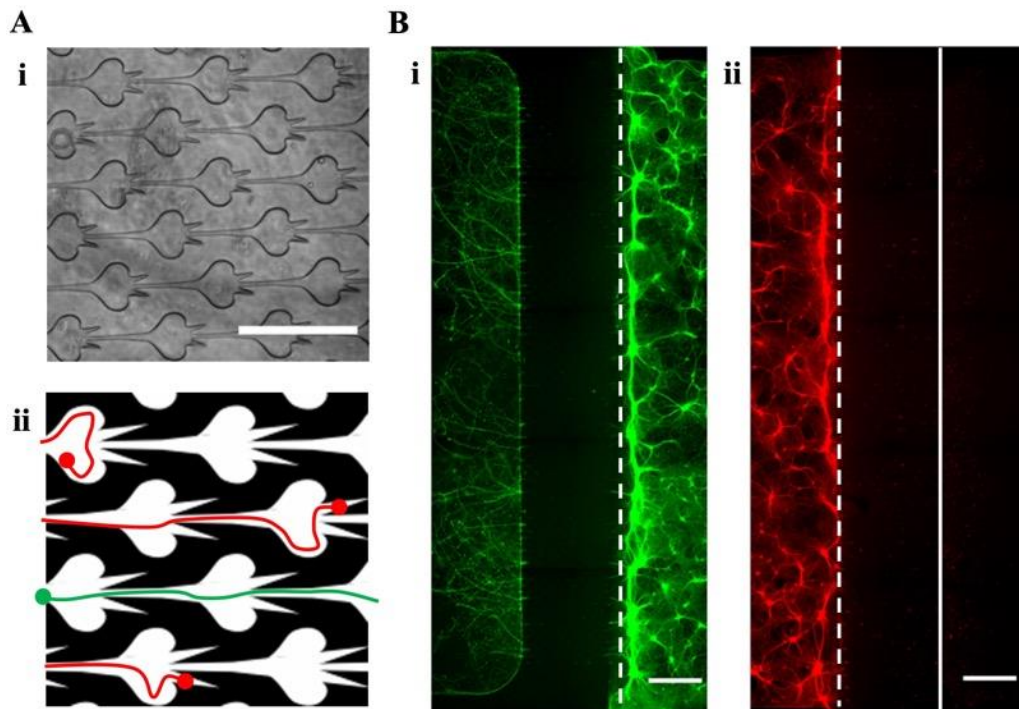


Figure 5.9. Edge-guided microchannels can be used in modular devices to either permit or inhibit neurite outgrowth between culture chambers. (A) Representative (i) brightfield image of PDMS heart-arrow microchannels and (ii) schematic highlighting permissive (green) and inhibitive outgrowth (red). (B) Confirmation of microstructure abilities, with (i) permissive neurite growth in the forward orientation (green) and (ii) inhibited neurite growth in the reverse orientation (red). Red and green = β III-tubulin. White dashed line indicates the modular interface and edge of microchannel region, while solid white line indicates edge of adjacent culture chamber in a 2-module device. Scale bars = 200 μm (A) and 500 μm (B).

Results here confirm the capabilities of the combined heart-arrow microstructures for directing neurite outgrowth. With cells seeded in the forward or growth enabling chamber, neurite outgrowth was permitted, and neurites are seen entering the adjacent unseeded chamber (Figure 5.9Bi and Figure 5.10Ai). Conversely, when cells were seeded in the reverse or growth inhibiting chamber, neurite outgrowth was blocked between culture chambers and no neurites fully crossed the microchannels to the unseeded adjacent chamber after 14 DIV (Figure 5.9Bii and Figure 5.10Aii). The heart-arrow structures can be seen successfully stalling and blocking the neurites from fully crossing the microchannel region to the adjacent culture chamber (Figure 5.10B).

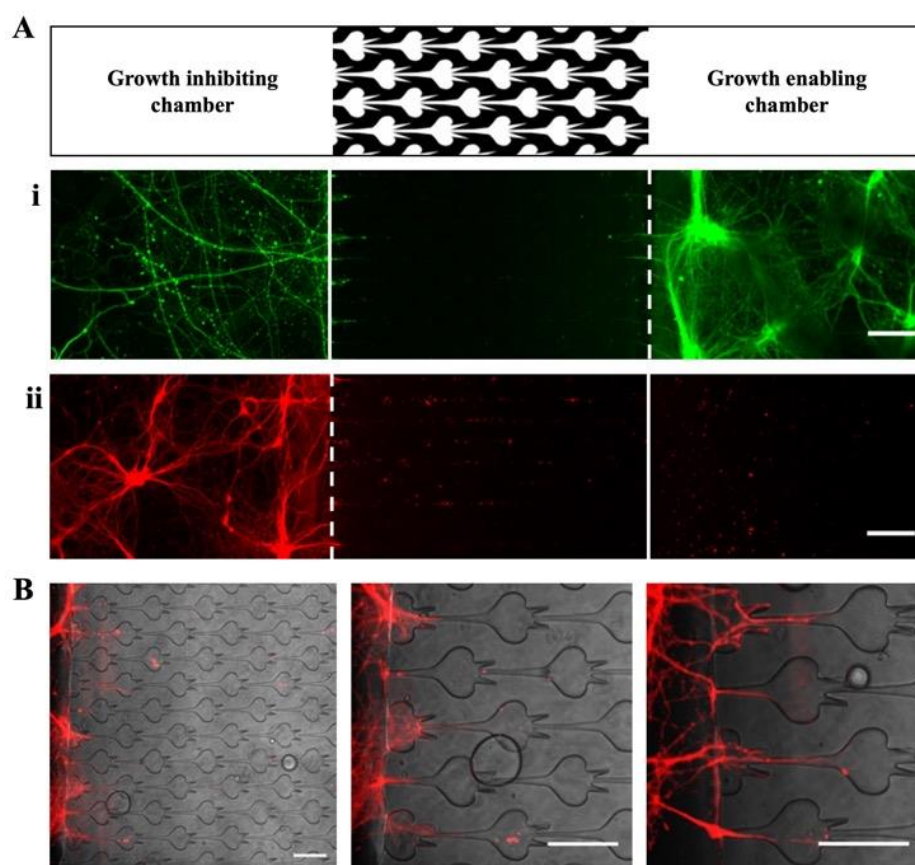


Figure 5.10. *The heart-arrow microstructures stalled neurite outgrowth when cells were seeded in the inhibitive chamber. (A) Edge guidance of neurites, highlighting (i) permissive growth with cells seeded in the growth enabling chamber, but (ii) blocking/stalling of neurite growth when cells were seeded in the growth inhibiting chamber. (B) Representative images of the microstructures with cells seeded in the growth inhibiting chamber highlighting where the neurites have been stalled and blocked from crossing the entirety of the microchannel region. Red = β III-tubulin. White dashed line indicates the modular interface and edge of microchannel region, while solid white line indicates edge of adjacent culture chamber. Scale bars = 100 μ m.*

5.4. Multi-module configurations for more complex *in vitro* models.

To further demonstrate the potential of the modular platform, I produced devices with more complex geometries comprised of multiple modules. These included a 4-chamber device with all chambers interconnected in series (**Figure 5.11**), a 5-chamber device using the central all-intrusion module to highlight parallel connectivity (**Figure 5.12**) and a 6-chamber device to show a more complex device where the culture chambers are connected in series (**Figure 5.13**). These more complex configurations showed cellular distribution throughout culture chambers with neurites entering and crossing the microchannel barrier at the modular interface to connect the cultures in separate modules.

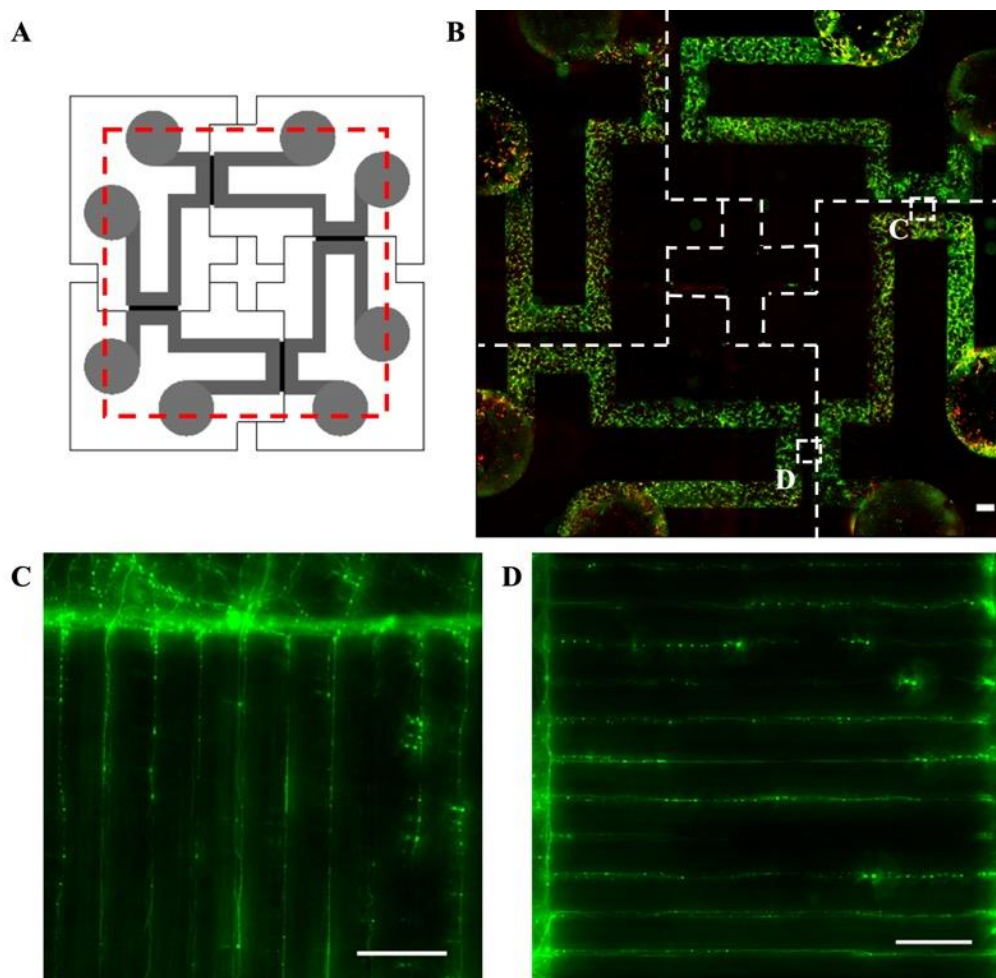


Figure 5.11. Uniform cell distribution throughout a multi-module 4-chamber device configuration. The modular platform provides greater flexibility to design user-specific devices above monolithic equivalents. Here, all modules are interconnected in series as shown in (A). (B) Uniform cell distribution throughout the individual modules with (C-D) neurites able to cross the modular interface. Red dashed box indicates area imaged. White dashed lines indicate the outline of individual modules. Green = β III-tubulin, red = GFAP. Scale bars = 2 mm (B) and 100 μ m (C-D).

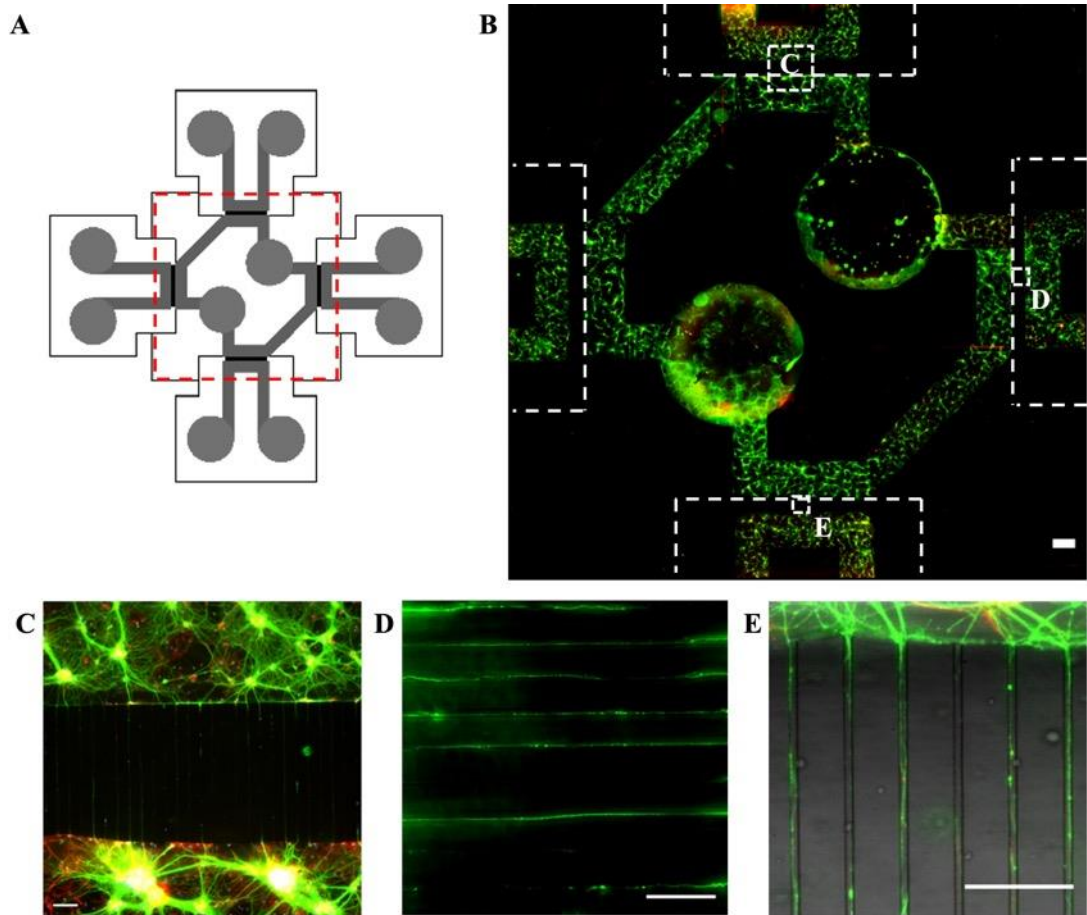


Figure 5.12. Parallel cell network formation is possible using the modular platform. In addition to serial connectivity, the modular platform enables the production of devices with modules connected in parallel. Here, a 5-chamber device was produced with 4 protrusion modules each independently connected to a central all-intrusion module as shown in (A). (B) Uniform cell distribution evident throughout all modules and (C-E) neurites can cross the modular interfaces, which enables connectivity between cells of the separate modules. Red dashed box indicates device area imaged. White dashed lines indicate the outline of individual modules. Green = β III-tubulin and red = GFAP. Scale bars in = 2 mm (B) and 100 μ m (C-E).

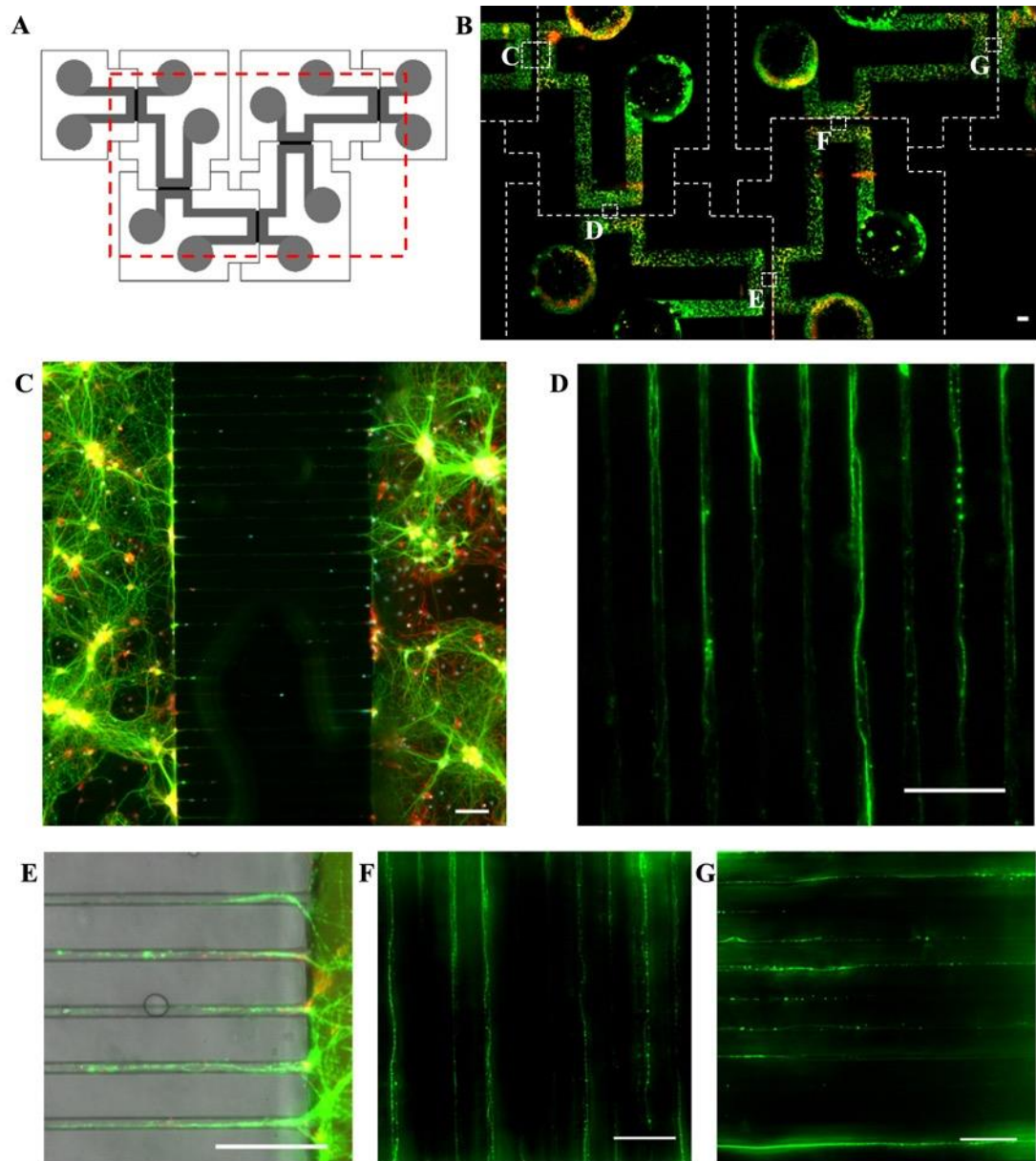


Figure 5.13. Uniform cell distribution with module-module connectivity can be achieved in larger device configurations. The modular platform enables the production of much larger devices, as demonstrated by a 6-chamber device with all modules connected in series, shown in (A). This provides the flexibility to create more complex *in vitro* networks and subsequent novel assays, beyond that available with typical monolithic equivalents. (B) Uniform cell distribution evident throughout all modules and (C-G) neurites again cross the modular interface enabling connectivity between cells of separate modules. Red dashed box indicates device area imaged. White dashed lines indicate the outline of individual modules. Green = β III-tubulin and red = GFAP. Scale bars = 2 mm (B) and 100 μ m (C-G).

5.5. Discussion.

A range of device configurations have been shown in this chapter to show the complex neuronal cultures possible using the modular platform and highlighting both serial and parallel chamber connectivity. The maximum number of modules tested here was six due to the dimensions of the glass slides used. However, the protrusion-intrusion interfacing system would enable extended designs, beyond the maximum number shown here, providing an even greater degree of flexibility for multi-module connectivity. Immunocytochemical staining has shown uniform cellular growth and distribution throughout the culture chambers. It is expected that after 12-14 DIV, network connectivity will be established across multiple modules. Neurites begin to enter microchannels after 3 DIV and will have fully transversed the microchannel barrier after 12-14 DIV^{134,266}. This enables direct connectivity between neurons in the separate culture chambers on either side of the barrier, with connectivity throughout central modules completing the network. Whilst there is an observable difference in clumping between protrusion and intrusion chambers in the 2-module device, this can be resolved by altering the volume of media added/removed and create a more consistent flow rate, given the increasing resistance in longer channels. In the 3-module device (**Figure 5.3**) the cellular distribution is more even throughout the 3 different modules geometries by changing the volume added across each module, from 30 μ l in the smallest intrusion module up to 60 μ l in the largest central intrusion-protrusion modules. Alternatively, redesigning the channel geometry to make their lengths more consistent may improve this. Immunocytochemistry has been demonstrated previously in microfluidic devices^{122,124,134}, however these results show that the interfacing between separate modules does not present a barrier to neurite outgrowth between culture chambers. The modular devices examined in **Section 5.4** highlight the possibility for creating large, interconnected networks with increasing levels of complexity. Further, there is a greater degree of flexibility to create multiple regions and subsequent spatial manipulation, beyond that of the traditional monolithic devices currently available.

Ca²⁺ imaging experiments have confirmed that functional synaptic connectivity is achieved between the individual modules, again demonstrating that the modular protrusion-intrusion interface does not present a barrier to neurite outgrowth and connectivity. The use of a 0 Mg²⁺ solution increases neuronal activity, thus creating a favourable condition to observe responses to indirect stimulation in downstream modules, as opposed to the one large response seen when using glutamate, that failed to elicit an observable response in the downstream modules of 3-module devices¹³⁴. This has previously been used to induce synchronous and spontaneous neuronal bursting activity shown by increased fluorescence intensity and levels of intracellular

calcium²²⁴⁻²²⁶. The increased excitability is due to greater probability of neurotransmitter release and the unblocking of NMDA receptors in the absence of Mg²⁺²²⁵. At rest, NMDA receptors are ordinarily blocked from initiating Ca²⁺ entry into the cell due to the presence of external Mg²⁺, therefore reducing the Mg²⁺ concentration unblocks these receptors and enables Ca²⁺ entry into the cell and initiation of an action potential²⁶⁴. The 0 Mg²⁺ induced spiking activity enabled observation of secondary cellular responses in the central intrusion-protrusion chamber and subsequently tertiary responses seen in the protrusion chamber. The increased activity observed in both indirectly stimulated chambers in fluidic isolation is indicative of functional synaptic connectivity across the three modules, as this was absent in the control.

Whilst there is an observed delay in the response of cells in chambers 2 and 3, where a response would be expected to take a matter of seconds, a previous study has shown increased activity over a period of 30 minutes²²⁶. In this study, neuronal cultures were incubated in a 0 Mg²⁺ solution for 30 minutes to model epileptic activity, after which the 0 Mg²⁺ solution was replaced with a 2 mM Mg²⁺ solution. They observed an increased frequency of Ca²⁺ transients, with more synchronous bursting. It is therefore possible that the initial activity observed in 2-module devices following direct addition of 0 Mg²⁺ was not strong enough to illicit an observable response in downstream modules of a 3-module device, as with glutamate. However, over the 30-minute observation window, given the established fluidic gradient from chambers 2/3 towards chamber 1, some of the normal HBS solution in chambers 2/3 (containing 2 mM Mg²⁺) will begin to enter chamber 1. This would have a similar affect as the aforementioned study²²⁶, to stimulate the neurons in close proximity to the microchannel barrier and create the synchronous activity they observed. Other studies have also pointed to the role of 0 Mg²⁺ solutions inducing permanent changes in neuronal activity maintained for 12-17 DIV post-incubation, with extended epileptic-like activity demonstrated by spontaneous and rapid firing patterns²⁶⁷.

The integration of edge-guiding microstructures demonstrates the ability to control network formation between culture chambers, by either permitting or prohibiting neurite outgrowth, depending on microstructure orientation. This control over neurite outgrowth improves the ability to create more defined *in vitro* networks and the establishment of more *in vivo*-like organisation, as a step to recreating the complexity of the brain circuitry. For example, in progressive neurodegenerative disorders such as Parkinson's, Alzheimer's and motor neuron disease, a greater understanding of the mechanisms underlying the pathological spread between cells and regions would be highly valuable^{40,268}. As discussed previously, edge-

guidance features have been used previously in monolithic devices, by using tapered microchannels and various diode microstructures^{43,138,139}. However, integrating these features into my modular platform enhances their potential by creating devices with a greater number of separate regions. The edge-guidance microchannels, combined with both parallel and serial connectivity, enable more control over the interconnectivity than traditional *in vitro* techniques, with improved network dynamics and replication of the specific interregional circuitry seen *in vivo*.

The use of pre-formed fibrils to induce α -synuclein pathology has been well documented for its ability to study misfolding and aggregation in cultures with normal levels of endogenous α -synuclein^{40,156–158}. Here, I demonstrated the induction of α -synuclein pathology and subsequent spread of pathology across the modular interface between fluidically isolated but synaptically connected neurons. However, I acknowledge in this study it is difficult to truly determine if pathological features imaged in chamber 2 are from this side or in neurites projecting from chamber 1. Despite no indication of pathology generation in the third chamber (intrusion module, **Figure 5.7**), these results still demonstrate the potential of the modular interfacing system as a platform for *in vitro* modelling of neurodegenerative disease and the subsequent transfer of pathology between isolated regions of neurons. This was a relatively short experiment, with imaging only 7 days after PFF addition. Whilst the hippocampal cultures will show synaptic maturity after 7 DIV (when PFFs were added)^{110,265} and connectivity will be established across microchannel barriers²⁶⁶, the long chambers between the central and intrusion chambers provides a large population through which the pathology must spread. Longer experimental times associated with iPSCs may be more appropriate to sufficiently study spread between multiple regions, with a previous study showing increased accumulation over a 30-day period post-exposure in smaller microfluidic channels⁴⁰. Overall, our results shows that the functionality obtained by this modular system is equivalent to that of previous monolithic devices but will allow examination in more complex *in vitro* networks. Combining this with the edge-guidance microchannels, will enable a better study of the underlying mechanisms behind the suspected prion-like spreading to be examined between separate, synaptically connected neuronal populations. Further, this can be applied to other progressive disorders with pathological protein misfolding and aggregation. Examples include Alzheimer's disease, where the propagation of misfolded amyloid- β or the hyperphosphorylated tau could be examined in depth.

5.6. Conclusion.

As proof-of-concept, a selection of modular device configurations has been demonstrated in this chapter using my modular protrusion-intrusion interfacing system. The main attraction of this platform is the ability to produce bespoke devices and assays within one researcher-friendly system that does not require fabrication facilities. These characteristics present a step forward for researchers to design devices suitable to their needs, above that available with monolithic devices. Ultimately more widespread use of microfluidic technology to create more advanced *in vitro* models will contribute to a greater understanding of brain circuitry and its alteration in CNS disorders. Further, an increased uptake in such systems that provide enhanced experimental capabilities will contribute to a reduction in animal use and speed up the drug development process through the improved predictability of response and relevance to human physiology.

Chapter 6. General discussion and evaluation.

This thesis set out to develop a modular microfluidic platform for neuroscience applications. Whilst microfluidic technology has been well established in the neuroscience field^{41,108,140,269}, there remain limitations on its use outside laboratories with the microfabrication knowledge and specialist equipment necessary for in-house fabrication. Further, there are limited commercially available options, which generally lack the flexibility required for researcher-designed device production. Modular microfluidic platforms are of interest given the flexibility and reconfigurability offered, and so producing such a system with microfluidic geometry specific for neuroscience studies can enable a wider uptake of the technology in neuroscience labs where no engineering expertise is available. I first set out to find a suitable substrate that enables growth and maturation of primary rat hippocampal cultures, as well as providing a method of non-permanent bonding with PDMS. Various methods were then explored to find a suitable way of assembling separate PDMS components, followed by designing specific microfluidic geometry applicable to neuronal network and microenvironment production. Here, an interlocking protrusion-intrusion system was created that enables modular device production on a PSA substrate. Finally, the overall platform was assessed to ensure functional synaptic connectivity can be achieved across the modular interface and demonstrate the flexibility offered to enable the production of a vast array of user-specific devices and subsequent novel assays. This work, to the best of my knowledge, presents the first microfluidic platform that enables complex neuronal connectivity between separate modular components.

6.1. Main thesis outcomes.

6.1.1. A substrate for reversible PDMS bonding and primary hippocampal cultures.

Typical PDMS-based microfluidic device production relies on plasma bonding between the device and a substrate^{219,270}. However, this is a permanent bonding mechanism and prevents disassembly and reuse of components. For a microfluidic platform to have universal outreach and be attractive to novice users, a reversible bonding mechanism would enable reconfiguration of devices and equipment free device assembly. PSA films were investigated for reversible PDMS bonding and as a biocompatible culture substrate, as they were easily accessible, enabling quick and simple assembly. A single-sided PSA, ThermalSeal® RTS, was selected as this had previously been found to have similar bonding strengths to plasma bonded PDMS-glass²³³. PDMS can be reversibly bonded to this substrate, enabling disassembly and subsequent re-bonding with a fresh piece of the film. Further, there is no adhesive residue left

on the PDMS surface after removal. Existing protocols for immunocytochemistry and Ca^{2+} imaging^{125,134} were adapted to assess its capabilities as a culture substrate. After 14 DIV, primary rat hippocampal cultures are healthy and functional when cultured directly on the PSA, as highlighted by synaptic connectivity between fluidically isolated cell populations. Overall, I demonstrated the suitability of pressure-sensitive adhesives for cost-effective and simple assembly, with the non-permanent bonding mechanism allowing disassembly of PDMS components for their potential reuse. Further, whilst PSA films have been demonstrated previously for organ-on-a-chip applications^{233,235}, I have highlighted their use as a suitable substrate for equipment free, modular device production and as a culture substrate for the healthy growth and maturation of primary hippocampal cultures.

6.1.2. Modular components for reversible assembly.

Various methods were assessed for creating modular PDMS components that can be combined on the PSA film. Whilst modularity has been explored in the literature^{119,192,194–202}, there is a lack of suitable examples that would enable the complex cell-cell connectivity required for neuroscience studies. Initial designs were based on Lego[®] as this would provide an easy method of assembly with consistent block dimensions. However, issues resulted in difficulty achieving hermetic sealing at the interface. The use of protruding tabs (protrusion and intrusion features) between microfluidic components has been demonstrated previously for self-alignment and to localise the area of contact to a smaller surface, increasing the pressure at overlapping regions to help reduce the likelihood of defects that may affect the seal^{198–200}. The idea was built upon in this thesis, to produce PDMS modules with a larger protrusion-intrusion interface, increasing the range of features that could be integrated into components. This enables researcher-specific device production using the four different modules in a variety of configurations and provides more flexibility in the range of assays that can be conducted using one platform. The modules designed in this thesis would enable the replication of various microfluidic based studies including co-cultures with both CNS and other cell types^{127–130}, recapitulation of specific networks^{43,44,131,132}, studying axonal and synaptic connectivity^{133,137} and onset and spreading of injury or disease^{49,242,243}. The novelty herein is the ability to produce larger and more complex neuronal cultures for researcher-specific assays, above that possible with traditional monolithic device equivalents, and without requiring specialist equipment and facilities for in-house fabrication.

Whilst my design enables somal-axonal and fluidic isolation, the relatively large interface compared with other examples increased the area over which seal-compromising defects may occur^{198,200}. It was also observed that whilst laser cut acrylic enabled smooth surfaces in the cast PDMS for improving conformal bonding, localised melting of the acrylic produced irregular features in the vertical walls. This resulted in weak seals at the interface and, whilst the enclosed protrusion-intrusion design enabled a press-fit, self-sealing mechanism, it did not improve sealing. Previous modular systems have made use of O-rings and tubing to connect separate components for leak-free sealing^{195,196,201,202}. However, these are only useful for connecting fluid reservoirs and simple channels and do not offer a platform for direct cellular connectivity. The protrusion-intrusion style interface was therefore the most appropriate system to enable cell culture and subsequent neuronal connectivity between modules. To counteract the weak sealing, at this stage a small amount of PDMS was used around the interface to enable consistent sealing across devices. Sealants have been used previously in modular components^{199,203}, and I was able to take devices apart with careful removal of modules from the PSA, demonstrating that reconfigurability remains possible. This represents equipment free device production, as no specialist equipment was needed to assemble devices on the PSA or to apply the thin PDMS layer over interfaces. Overall, this modular platform, with the protrusion-intrusion interfacing tabs, provides a suitable area for integrating larger microfluidic features and enables directed neuronal connectivity between separate modular components, features not previously demonstrated.

6.1.3. Microfluidic priming in the absence of oxygen plasma.

Device production using the modular protrusion-intrusion interface offered equipment free and simple assembly. However, to enable universal use of the platform, protocols are needed for priming devices and enabling cell culture conditions in the absence of oxygen plasma treatment. Ethanol is an option readily available to all research labs and can initiate capillary flow in hydrophobic PDMS channels, due to its lower surface tension than aqueous solutions²⁷¹. I was able to demonstrate use of 70% ethanol for inducing flow in microchannels and for sterilising devices. Further, regarding the coating procedure with PLL, similar results to oxygen plasma treated devices were achieved when incubation was performed overnight, obtaining improved culture conditions with uniform cellular distribution throughout chambers. Whilst most cultures were successful using 70% ethanol, the occurrence of air bubbles was more frequent than in oxygen plasma treated devices. There are several factors that have an impact on bubble formation including the material surface properties, channel geometry and the microstructures present, as well as the specific reagents used and their associated properties

^{271–275}. However, ethanol priming has been demonstrated successfully in monolithic PDMS devices for neuron cultures ^{139,276}, suggesting the main issue in my modular devices is the presence of trapped air at the interface and non-hermetic sealing. Despite rinsing the channels with media, the use of PLL (in de-ionised water) likely contributes to the reformation of surface tension effects and dislodging bubbles that had formed, by flushing more ethanol, was difficult in the longer channels. Further work is therefore essential to perfect the protocols and reduce the likelihood of disruptive bubble formation in culture chambers for ensuring 70% ethanol is a complete alternative to plasma treatment for modular devices.

6.1.4. Functional neuronal connectivity and disease modelling in modular devices.

In Chapter 5, a comprehensive characterization of the protrusion-intrusion modular system was undertaken to ensure functional synaptic connectivity between hippocampal cultures in separate modules and demonstrate potential applications for complex network formation. Uniform cellular growth and distribution was evident throughout all culture chambers of the devices tested (2-6 chamber configurations with both parallel and serial network conditions), with neurites able to grow across the modular interface. Ca^{2+} imaging using glutamate, KCl and a 0 Mg^{2+} HBS demonstrated that cells are functional in modular devices and synaptic connectivity occurs across multiple modular protrusion-intrusion interfaces. Whilst primary hippocampal cultures and their subsequent synaptic connectivity has been demonstrated in monolithic microfluidic devices ^{122,124,125,134}, these results demonstrate that my modular interface design does not present a barrier to neurite outgrowth between separate device modules, and highlights the possibility for creating larger, interconnected networks above that possible in monolithic devices, with a greater degree of flexibility and control over regional manipulation. Whilst there are modular platforms aimed at cell culture and organ-on-a-chip applications ^{194,196,200,277}, this represents the first modular system specifically for connecting complex neuronal cultures between components. One example demonstrated a platform that enables a vast number of modules to be connected with subsequent cell culture and drug toxicity assays, however the homogeneity and minute size of components limits its applications ²⁰⁰.

The integration of edge-guiding microstructures in modular devices demonstrates the ability to control neurite outgrowth in this platform, with both enabled and blocked axonal growth shown after 14 DIV, depending on channel orientation. I used a combined heart-arrow structure here as a proof-of-concept design, as these shapes have previously been demonstrated to stall neurite outgrowth in the inhibitive direction in primary hippocampal cultures ¹³⁹. Whilst

tapered microchannels and other similar structures have been demonstrated previously^{43,138,139}, the results here demonstrate the use of these features in a modular platform. These previous examples represent an exciting development in reconstructing more *in vivo*-like circuitry; however, the fixed device layout ultimately restricts the use of the device to that which it was designed for. Conversely, a modular system enables the creation of larger, more complex networks without redesigning and refabricating to a specific specification. This then enables the establishment of more *in vivo*-like organisation, with directed interregional circuitry, as a step to recreating the complexity of the brain circuitry.

The use of pre-formed fibrils to induce α -synuclein pathology has been well documented for its ability to study misfolding and aggregation in cultures with normal levels of endogenous α -synuclein^{156–158}. However, the results in this thesis demonstrate induction of α -synuclein pathology and subsequent spread of pathology across a modular interface between separate components. Despite no indication of pathology generation in the tertiary chamber (probably due to the short-term assay), given the lack of pSer129 staining, the modular platform shows promise for *in vitro* modelling of neurodegenerative disease and the subsequent transfer of pathology between isolated regions of synaptically connected neurons. The functionality obtained in modular devices is therefore equivalent to that of previous monolithic devices that have modelled pathological spread in Parkinson's disease^{39,40,152–155}, but would allow examination in larger, more complex *in vitro* networks. Further, these results indicate its use for other, similar neurodegenerative disorders such as Alzheimer's disease²⁵². Common applications here include investigating the propagation and spread of pathology^{133,141–143,146}, whilst other studies have looked at amyloid- β induced synaptotoxicity¹⁴⁸, clearance of amyloid- β aggregates¹⁴⁷ and effect of amyloid- β aggregates on signalling¹⁴⁹ and microglial migration¹⁵¹. Such applications could be replicated with the modular platform but with the added flexibility to design larger, more complex networks specific to the assay in question or integrate directionality of synaptic connectivity using the edge-guiding microchannels. Ultimately, using the modular platform would enable production of more complex *in vitro* networks to further study the underlying mechanisms behind neurodegenerative and other disorders as well as further investigation into regional propagation of pathology. The enhanced translational validity and greater depth of information gained using larger networks will help reduce animal use and aid in the drug discovery process, reducing costs and time associated with therapeutic development.

6.2. Future work.

Further work should focus initially on demonstrating additional assays and more advanced applications of the platform. This should involve creating co-cultures both with other cell types within the CNS as well as those in the rest of the body. Examples include culturing neurons and glial cells in separate modules for investigating myelination^{128,253}, or microglial recruitment in disease states^{151,254}, as well as culturing multi-regional neurons in separate modules to recreate specific brain networks. These have been used to model cortical-thalamic interactions¹³², cortical-striatal interactions^{45,46}, as well as a cortical-hippocampal-amygdala network⁴⁴ and a more complex basal ganglia model⁴³, all to help investigate normal function as well as dysfunction in disease states. Furthermore, it is worth exploring 0 Mg^{2+} further to create *in vitro* epilepsy models^{224–226,264}. In microfluidic devices, the ability to guide neurite growth would enable development of more relevant models for both focal seizures, between isolated functional networks, or more generalised seizures, between multiple interconnected regions, as well as an investigation of anti-epileptic drugs and their effectiveness^{184,278,279}.

Other applications of interest include demonstrating gel-based 3D culture conditions and working towards developing *in vitro* blood-brain barrier equivalents both for studying normal functioning of the BBB, developing therapeutics and for investigating dysfunction in CNS disorders^{81,280,281}. The ability to replicate and advance these applications will demonstrate the flexibility and highlight the potential and exciting nature of researcher-designed device production using a modular, reconfigurable platform. Beyond neuroscience research, it is of interest to demonstrate co-cultures with non-CNS cell types to replicate higher order organ-organ interactions, as a step towards body-on-a-chip applications^{208–210,282}. Microfluidic co-culture models have developed to study an array of interactions including the neuromuscular junction^{129,255–259,283} and the gut-brain axis^{284,285} as well as cardiac function^{130,260}. Recently, there have been attempts at developing larger multi-organ systems including a 10-system ‘physiome-on-a-chip’ device integrating liver, immune, intestinal, endometrial, neural, cardiac, pancreatic, kidney, skin and skeletal muscle components²¹⁷. For such applications, a modular platform would provide the ability to combine multiple components, each with a separate cell type, interconnected to recapitulate *in vivo* organisation.

Further, whilst the use of primary postnatal rat cultures enables rapid and easily accessible source of information, they do not offer an optimal system for studying age-dependent diseases such as Alzheimer’s and Parkinson’s^{90,109,110,286}. It is therefore of interest to test the modular platform using human cells, in particular iPSC’s. Whilst these are still considered

developmentally immature, they can offer patient-specific studies, are more representative of human disorders and their greater relevance can help improve translatability for drug discovery^{96,287}. Further, as iPSCs can be differentiated into various cell lines, they could also be used for modelling other systems using non-neuronal cell types, increasing the applications of the modular platform^{208,288}.

6.2.1. Fabrication and device preparation.

It may be of interest to redesign the platform to a more universal footprint such as that of a 96-well plate. This has the advantage of enabling higher-throughput analysis and integration with robotic systems for dispensing. Further, a smaller module footprint improves mass production, is more applicable to existing imaging systems and creates more consistent microfluidic geometry between modules. Reducing the footprint of the culture chambers, particularly that of the central combined protrusion-intrusion chamber, would also reduce the number of cells required and enable more consistent seeding volumes. In the immediate term, investigation into alternative fabrication methods for moulding is required to produce more consistent modules, ensuring consistent hermetic sealing and provide scalability of the modules for mass production. Methods of interest include using more advanced 3D printers, injection moulding and the use of hard plastics to improve consistency and reduce the deformation associated with PDMS. The use of hard plastic for module production would also reduce small molecule absorption by PDMS in any future work that involves drug screening²⁸⁹. Inspiration could also be drawn from an example that produced blocks directly on SU8 wafers²⁰⁰. The added benefit of producing more consistent modules would be in reducing the deformation observed when assembling devices with multiple modules. Here the thick glass slides in combination with the double-sided adhesive and PSA film were required to add stability and ensure a flat surface for imaging. However, this thicker surface presents a barrier to imaging, with difficulty obtaining sharp, consistent images. Conversely, the reduced deformation achieved with more consistent modules could enable the use of thinner glass coverslips, alongside a single double-sided PSA, for minimising the overall substrate thickness and improving the sharpness and sensitivity in imaging.

Recently, the use of a newer 3D printer (Form3, Formlabs) has enabled the production of more complimentary interfacing surfaces, without the irregularities caused by melting of the acrylic during laser cutting. These surfaces enable better PDMS-substrate bonding at the interface and sufficient processing with UV post-curing and baking (80°C) for 24-48 hours alleviates any issues with uncured resin (mould sticking to the silicon wafer and PDMS not fully curing).

The Form3 can print layer thicknesses as small as 25 microns with an XY resolution of 25 microns, offering higher quality printing with smoother surfaces compared with the Kudo3D and Ultimaker 3D printers used previously. Further, the actual dimensions produced are more in line with the nominal dimensions with more consistency between features than laser cutting (**Figure 6.1**) and previous 3D printing. For a nominal width of 12 mm, the resultant width was 11.65 ± 0.03 in laser cut acrylic and 11.87 ± 0.01 in a 3D printed component (**Figure 6.1A**). Using the Form3, the protrusions were 0.17 ± 0.01 mm smaller than the nominal CAD value and intrusions were 0.13 ± 0.01 mm smaller. In the laser cut acrylic, protrusions were 0.23 ± 0.04 mm larger than the CAD dimensions whilst intrusions were 0.35 ± 0.03 mm smaller (**Figure 6.1B**). However, the PDMS cast in these moulds is not as observably smooth as in laser cut acrylic, reducing the likelihood of conformal PDMS-PDMS bonding at the interface. It is possible to process these 3D prints with progressively smaller grit sandpaper, but the protrusion/intrusion components make it difficult to obtain an even level of sanding across the entire mould surface. Other methods to improve the surface qualities could include spraying the moulds with an acrylic-based lacquer to obtain a smooth surface for casting PDMS. Further investigation is required to assess the sealing of components cast in these moulds and determine if they alleviate the reliance on PDMS brushing at the interface.

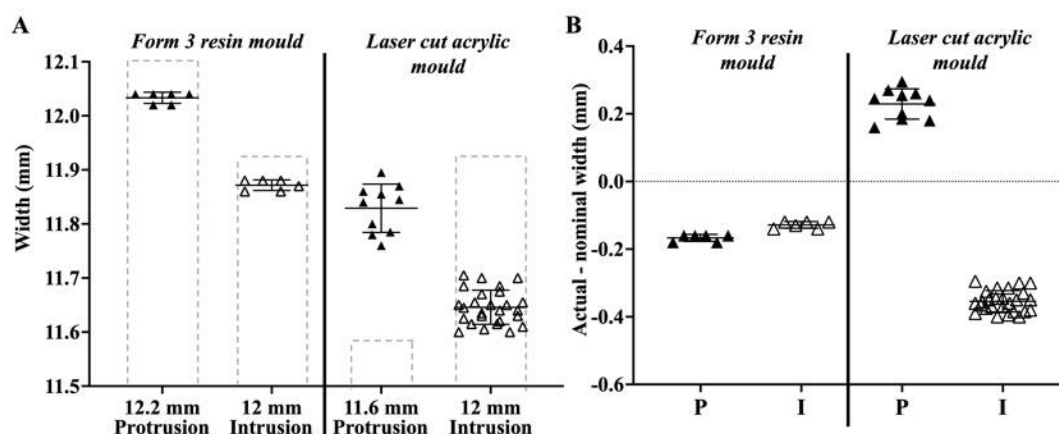


Figure 6.1. The Form3 produces more consistent moulds with values closer to the desired width than those produced by laser cutting acrylic sheets. (A) The Form3 printer (left) produces moulds with dimensions closer to the intended values than laser cutting (right). Dashed outlines indicate the intended nominal values. (B) Difference between intended and actual dimensions of protrusions (P) and intrusions (I) using the Form3 and laser cut acrylic. Scatter plot shows mean \pm SD, $n = 6-26$.

Whilst the production of blocks directly using SU8 wafer moulds would limit the height of the modules that could be produced, the straighter walls achievable via photolithography would improve the surface qualities of the PDMS cast on these moulds²⁰⁰. A lack of hand cutting at

the protrusion-intrusion interfacial region in combination with these smoother PDMS surfaces may improve the likelihood of a hermetic seal. Further, the greater accuracy achievable with SU8 photolithography would enable the creation of more complex interfacing shapes to improve the seal between the protrusion and intrusion features (**Figure 6.2**). Whilst conventional SU8 photolithography cannot reliably produce uniform features taller than 100s of microns, the use of thick film resists presents an opportunity to create taller walls (**Figure 6.2**)^{245–247}. These films are typically available in sheets 200 – 1000 μm thick and features could be created using single or multiple applications to achieve the desired height. Further, laser cut-acrylic or 3D printed moulds could still be used in association with these wafers to cast PDMS in a layered process, like that of the double-casting procedure in Chapter 4, to produce taller modules with appropriate open wells (**Figure 6.2C**).

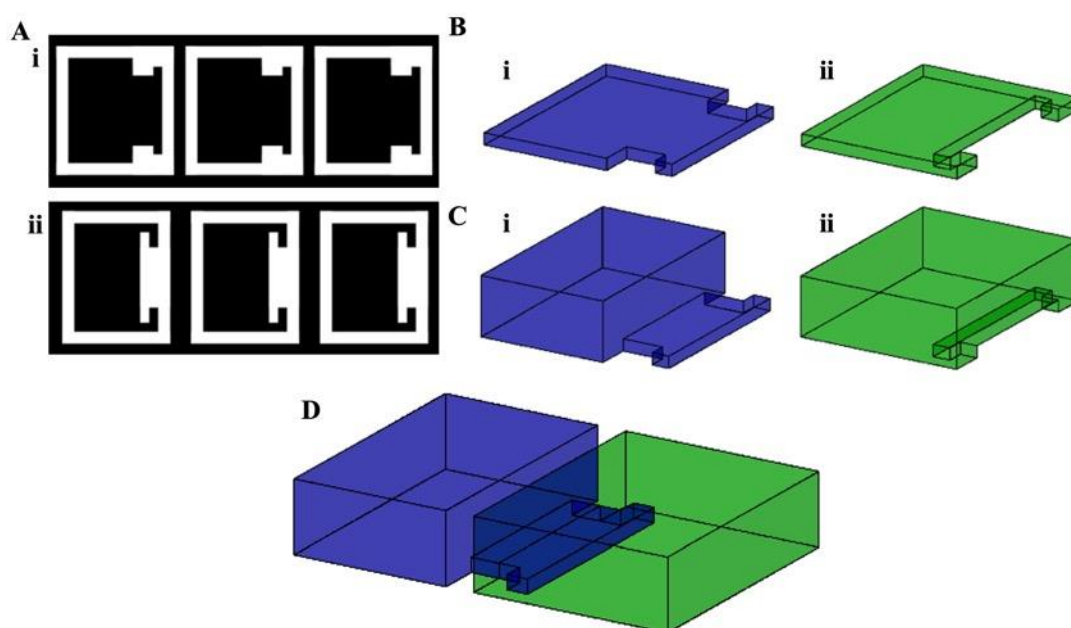


Figure 6.2. Schematic representation demonstrating the use thick film resists for creating smaller interfacing regions with improved alignment features. (A) Example mask design for (i) protrusion and (ii) intrusion. (B) PDMS could first be cast directly on the wafer to produce the interfacing features, then (C) further PDMS moulded to build the modules height and integrate open wells for (D) an enclosed device.

As PDMS is elastomeric and liable to deformation, the thin protrusion-intrusion section (e.g., 1 mm thick cast on thick film resist wafer) may be difficult to seal, and so alternative materials could be explored to create the initial protrusion-intrusion features. For example, a photosensitive thermoset polymer, Ostemer 322, that is applicable to soft lithography has been demonstrated for microfluidic device applications^{248,249}. Ostemer 322 can be cast on silicon wafers and replica moulded like PDMS and is curable in a two-stage process using UV and

oven baking. The main advantages over PDMS are its greater mechanical properties, with a final modulus of 2.3 GPa compared with 1.8 MPa for PDMS, and its lower permeability^{290,291}. Further, it is biocompatible and amenable to cell culture and organ-on-a-chip applications^{248,249}. This is worth investigating as an alternative to PDMS in association with the thick film resist moulds.

Further work is also needed to overcome the issue of bubble formation to make ethanol priming a more attractive option and sufficient alternative to oxygen plasma treatment. Reducing the native hydrophobicity of PDMS has been demonstrated by mixing a PDMS-PEG (polyethylene glycol) copolymer into the PDMS prior to curing, shown by a reduction in water contact angle²⁵⁰. This may be worth investigating with thorough contact angle measurements in association with ethanol flooding. Initial observations with the addition of PEG polymer directly into PDMS presented difficulty in mixing the two polymers together, with an increased viscosity making it difficult to pour into moulds and a greasy residue on the surfaces after curing. Other methods have included surface modification of PDMS using polyvinyl chloride (PVA) which also showed a reduction in water contact angle²⁵¹.

6.2.2. Microfluidic features.

Whilst I was able to demonstrate the use of combined heart-arrow edge-guiding microchannel features, it may be useful to integrate more complex microstructures for longer experimental times associated with iPSCs. The heart-arrow features delay the outgrowth of primary hippocampal neurites after 14 DIV. However, to fully prohibit outgrowth in the unwanted direction, re-routing has been proposed¹³⁹. Suitable microstructures for this include pretzel-like designs that re-direct the neurites back to their source chamber. The mask designs shown include tapered microchannels as an additional feature to prevent the re-routed neurites progressing forward again (**Figure 6.3A**). Another feature of interest is a central channel that runs perpendicular to microchannels to enable axonal dissection/degeneration (**Figure 6.3B**). As discussed earlier, this is useful to study regeneration properties and response to injury¹³⁵. Methods for axotomy include mechanical dissection (e.g., vacuum aspiration) or through addition of a detergent such as Triton X-100²⁶², or another chemical such as acrylamide²⁹². This would require an assessment of the flow properties to ensure any chemical applied in the perpendicular axotomy channel cannot spread to the adjacent culture chambers. A simple test for this could be the application of a fluorescent compound, such as calcein, in the axotomy chamber and observation to ensure it does not spread beyond the microchannels.

Beyond the use microchannel arrays at the modular interfaces, the integration of phase guides or micropillars would enable the creation of 3D models and the *in vitro* development of structures including the blood-brain barrier^{169,171,173}. As discussed previously, these structures sit between culture chambers and enable the controlled addition of a hydrogel (e.g., collagen or Matrigel) by preventing it spreading from the desired channel prior to polymerisation (**Figure 6.3C**). Cells are suspended in these gels to provide 3D culture conditions and the creation of more *in vivo* like environments. The mask designs shown have been based on previous examples from the literature but have yet to be tested in their ability to control gels and prevent cross-contamination from the target chamber prior to polymerising. Despite the focus on neuroscience applications, a modular platform with 3D culture capabilities would also offer a major step forward in developing body-on-chip style systems, as reviewed elsewhere²⁰⁸. The ability to combine multiple organ systems *in vitro* allows an analysis of specific organ-organ interactions. Further, whilst specific organ-on-chip devices can enable predictive power for choosing drug candidates with the greatest potential, they provide no information on the effects on whole organisms and toxicity to other systems. In this case, a modular platform would provide the ability to combine multiple components, each with a separate cell type, interconnected to recapitulate *in vivo* organisation.

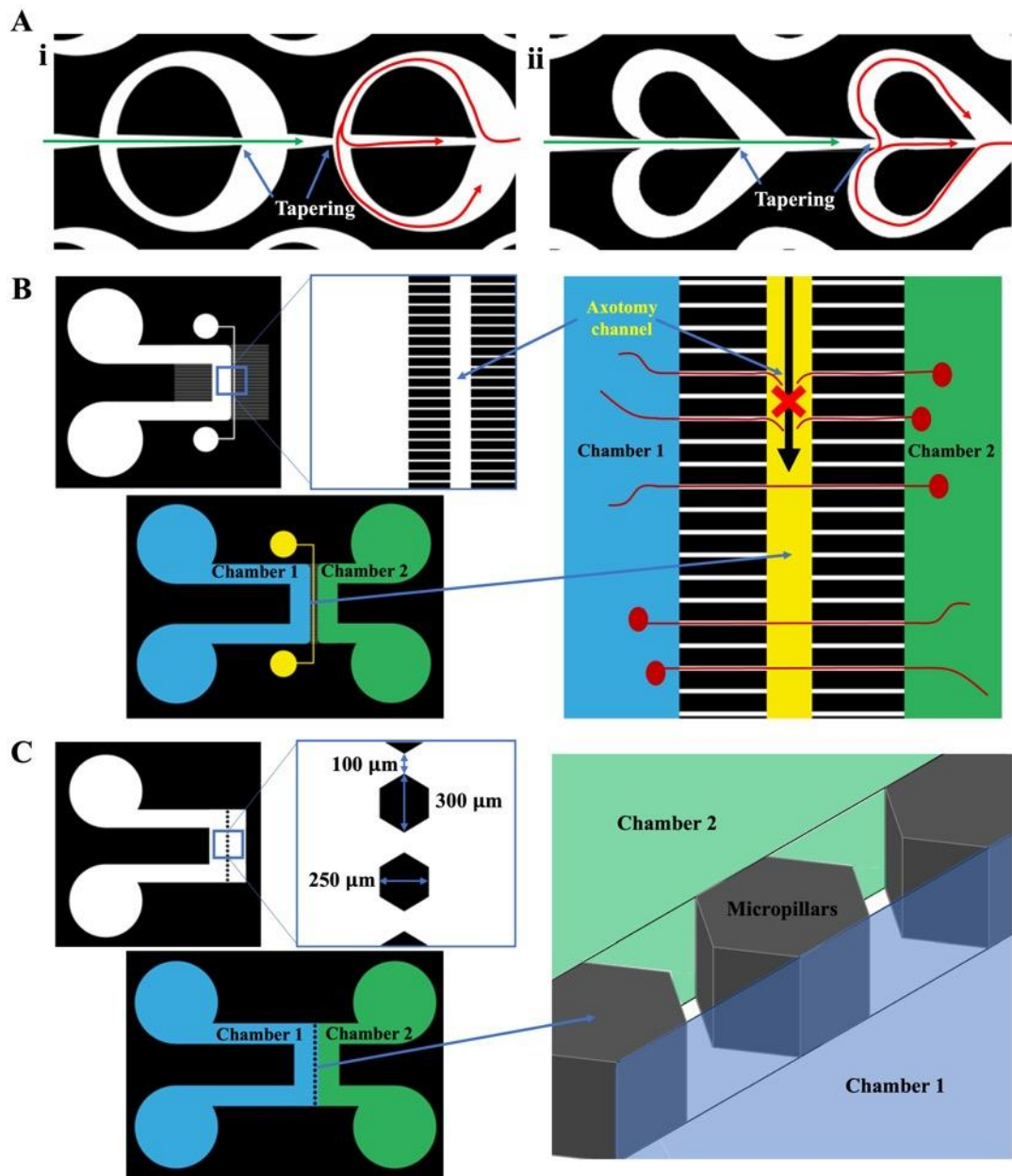


Figure 6.3. Schematic representation highlighting other features of interest for integrating into the modular platform and increasing the potential applications. This includes (A) more complex edge-guiding patterns with tapering to encourage re-routing and long-term inhibitive outgrowth, (B) micropillars in place of the microchannels to enable 3D culture conditions, and (C) an axotomy channel that runs perpendicular to the straight-edge microchannels to allow an investigation of axonal regenerative properties and response to injury.

6.3. Conclusion.

In this thesis, a novel proof-of-concept modular microfluidic platform has been developed to enable the production of complex, user-defined cell culture patterns. The platform consists of multiple microfluidic PDMS modules that interface via a simple protrusion-intrusion mechanism on a pressure sensitive adhesive film substrate. Results here have shown the successful growth of primary rat hippocampal cultures within devices and subsequent functional synaptic connectivity across the modular protrusion-intrusion interface. Further results have demonstrated the potential for larger, interconnected devices than currently available monolithic equivalents, with the possibility to direct neurite outgrowth for more defined circuitry and enable more complex neurodegenerative pathological spreading assays between fluidically isolated but syntactically connected groups of cells. The main attraction of this platform is the ability to produce bespoke devices and assays within one researcher-friendly system without the need for specialist fabrication facilities. This provides an ability for researchers to design devices suitable to their needs and ultimately contribute to a greater understanding of brain circuitry and its alteration in CNS disorders. Given the specific challenges in brain disorder drug discovery and the translational issues with animal models, improved *in vitro* models are likely to play a pivotal role by recapitulating specific circuitry and microenvironmental conditions. Future opportunities include the development of modules that can provide features such as 3D culture to enable the development of structures such as the blood-brain barrier. Further work is needed to fully validate the platform, including demonstration of more advanced assays with both CNS and non-CNS cell types, as well as human iPSCs, and increasing the sample number to ensure the results are more robust and improve the statistical findings and reliability. Finally, work is also required with regards to fabrication and assembly to ensure consistency between modules, bubble-free channel priming and hermetic sealing at the interface without the need for extra PDMS. Overall, despite our focus on neuroscience applications, this development of a modular platform also offers a step forward in developing multi-organ-on-a-chip and subsequently body-on-chip systems using non-neuronal cell types. In this case, a modular platform would provide the ability to combine multiple components, each with a separate cell type, interconnected to recapitulate the *in vivo* organisation. Ultimately, the development of a modular microfluidic platform for organ-on-a-chip applications can provide enhanced experimental capabilities, contribute to a reduction in animal use and speed up the drug development process through the improved predictability of response and relevance to human physiology.

References

1. Azevedo, F. A. C. *et al.* Equal numbers of neuronal and nonneuronal cells make the human brain an isometrically scaled-up primate brain. *Journal of Comparative Neurology* **513**, 532–541 (2009).
2. Boto, T. & Tomchik, S. M. The Excitatory, the Inhibitory, and the Modulatory: Mapping Chemical Neurotransmission in the Brain. *Neuron* **101**, 763–765 (2019).
3. Marieb, E. N. & Hoehn, K. *Human Anatomy & Physiology. Physiology* (2016). doi:10.1038/nnano.2011.234.
4. Ming, G. li & Song, H. Adult Neurogenesis in the Mammalian Brain: Significant Answers and Significant Questions. *Neuron* **70**, 687 (2011).
5. *Fundamental Neuroscience. Fundamental Neuroscience* (Academic Press, 2013). doi:10.1016/c2010-0-65035-8.
6. OpenStax *et al.* Biology. 985–992 https://cnx.org/contents/GFy_h8cu@10.4:c9j4p0aj@3/Neurons-and-Glial-Cells (2016).
7. Jäkel, S. & Dimou, L. Glial cells and their function in the adult brain: A journey through the history of their ablation. *Front Cell Neurosci* **11**, 24 (2017).
8. Thompson, K. K. & Tsirka, S. E. The Diverse Roles of Microglia in the Neurodegenerative Aspects of Central Nervous System (CNS) Autoimmunity. *Int J Mol Sci* **18**, (2017).
9. Snaidero, N. & Simons, M. Myelination at a glance. *J Cell Sci* **127**, 2999–3004 (2014).
10. Siracusa, R., Fusco, R. & Cuzzocrea, S. Astrocytes: Role and functions in brain pathologies. *Front Pharmacol* **10**, 1114 (2019).
11. Garwood, C. J. *et al.* Review: Astrocytes in Alzheimer’s disease and other age-associated dementias: a supporting player with a central role. *Neuropathol Appl Neurobiol* **43**, 281–298 (2017).
12. Kimelberg, H. K. & Nedergaard, M. Functions of astrocytes and their potential as therapeutic targets. *Neurotherapeutics* **7**, 338–353 (2010).
13. Scimemi, A. The Role of Astrocytes in Neurotransmitter Uptake and Brain Metabolism. in 309–328 (Springer, Cham, 2019). doi:10.1007/978-3-030-00817-8_12.
14. Farhy-Tselnicker, I. & Allen, N. J. Astrocytes, neurons, synapses: a tripartite view on cortical circuit development. *Neural Development* *2018 13:1* **13**, 1–12 (2018).
15. Fletcher, A. Action potential: generation and propagation. *Anaesthesia & Intensive Care Medicine* **20**, 243–247 (2019).
16. Pivovarov, A. S., Calahorra, F. & Walker, R. J. Na⁺/K⁺-pump and neurotransmitter membrane receptors. *Invertebrate Neuroscience* *2018 19:1* **19**, 1–16 (2018).
17. Seidl, A. H. Regulation of conduction time along axons. *Neuroscience* **276**, 126–134 (2014).
18. Sol-Foulon, N., Foulon, N. & Desmazières, A. Nodes of Ranvier during development and repair in the central nervous system. *Nat Rev Neurol* **16**, (2020).
19. Purves, D. *et al.* Increased Conduction Velocity as a Result of Myelination. (2001).
20. Montero-Crespo, M. *et al.* Three-dimensional synaptic organization of the human hippocampal ca1 field. *Elife* **9**, 1–31 (2020).
21. Brini, M., Calì, T., Ottolini, D. & Carafoli, E. Neuronal calcium signaling: Function and dysfunction. *Cellular and Molecular Life Sciences* **71**, 2787–2814 (2014).
22. Nair, J. D., Wilkinson, K. A., Henley, J. M. & Mellor, J. R. Kainate receptors and synaptic plasticity. *Neuropharmacology* **196**, 108540 (2021).
23. Pittaluga, A. Presynaptic release-regulating NMDA receptors in isolated nerve terminals: A narrative review. *Br J Pharmacol* **178**, 1001–1017 (2021).
24. Hampe, C. S., Mitoma, H. & Manto, M. GABA and Glutamate: Their Transmitter Role in the CNS and Pancreatic Islets. in *GABA And Glutamate - New Developments In Neurotransmission Research* (InTech, 2018). doi:10.5772/intechopen.70958.

25. Niciu, M. J., Kelmendi, B. & Sanacora, G. Overview of glutamatergic neurotransmission in the nervous system. *Pharmacology Biochemistry and Behavior* vol. 100 656–664 Preprint at <https://doi.org/10.1016/j.pbb.2011.08.008> (2012).
26. Huang, Y. & Thathiah, A. Regulation of neuronal communication by G protein-coupled receptors. *FEBS Lett* **589**, 1607–1619 (2015).
27. Niswender, C. M. & Conn, P. J. Metabotropic Glutamate Receptors: Physiology, Pharmacology, and Disease. *Annu Rev Pharmacol Toxicol* **50**, 295–322 (2010).
28. Betke, K. M., Wells, C. A. & Hamm, H. E. GPCR Mediated Regulation of Synaptic Transmission. *Prog Neurobiol* **96**, 304 (2012).
29. Hamid, E. *et al.* Modulation of Neurotransmission by GPCRs Is Dependent upon the Microarchitecture of the Primed Vesicle Complex. *The Journal of Neuroscience* **34**, 260 (2014).
30. Wu, C. & Sun, D. GABA receptors in brain development, function, and injury. *Metab Brain Dis* **30**, 367–379 (2015).
31. Martinez, P. & Sprecher, S. G. Of Circuits and Brains: The Origin and Diversification of Neural Architectures. *Front Ecol Evol* **8**, 82 (2020).
32. Hartlaub, A. M., McElroy, C. A., Maitre, N. L. & Hester, M. E. Modeling human brain circuitry using pluripotent stem cell platforms. *Front Pediatr* **7**, 57 (2019).
33. Ndyabawe, K. & Kisaalita, W. S. Engineering microsystems to recapitulate brain physiology on a chip. *Drug Discovery Today* vol. 24 1725–1730 Preprint at <https://doi.org/10.1016/j.drudis.2019.06.008> (2019).
34. Small, S. A., Schobel, S. A., Buxton, R. B., Witter, M. P. & Barnes, C. A. A pathophysiological framework of hippocampal dysfunction in ageing and disease. *Nat Rev Neurosci* **12**, 585 (2011).
35. Basu, J. & Siegelbaum, S. A. The Corticohippocampal Circuit, Synaptic Plasticity, and Memory. *Cold Spring Harb Perspect Biol* **7**, a021733 (2015).
36. Pignataro, A. & Middei, S. Trans-Synaptic Spread of Amyloid- β in Alzheimer's Disease: Paths to β -Amyloidosis. *Neural Plast* **2017**, (2017).
37. Catarina Silva, M. & Haggarty, S. J. Tauopathies: Deciphering Disease Mechanisms to Develop Effective Therapies. *Int J Mol Sci* **21**, 1–49 (2020).
38. Mezas, C., LoCastro, E., Xia, C. & Raj, A. Connectivity, not region-intrinsic properties, predicts regional vulnerability to progressive tau pathology in mouse models of disease. *Acta Neuropathol Commun* **5**, 61 (2017).
39. Wu, Q. *et al.* Neuronal activity modulates alpha-synuclein aggregation and spreading in organotypic brain slice cultures and in vivo. *Acta Neuropathol* **140**, 831–849 (2020).
40. Griboado, S. *et al.* Propagation of α -Synuclein Strains within Human Reconstructed Neuronal Network. *Stem Cell Reports* **12**, 230–244 (2019).
41. Fantuzzo, J. A., Hart, R. P., Zahn, J. D. & Pang, Z. P. Compartmentalized Devices as Tools for Investigation of Human Brain Network Dynamics. *Developmental Dynamics* **248**, 65–77 (2019).
42. Mateos-Aparicio, P. & Rodríguez-Moreno, A. The impact of studying brain plasticity. *Frontiers in Cellular Neuroscience* vol. 13 66 Preprint at <https://doi.org/10.3389/fncel.2019.00066> (2019).
43. Kamudzandu, M., Köse-Dunn, M., Evans, M. G., Fricker, R. A. & Roach, P. A micro-fabricated *in vitro* complex neuronal circuit platform. *Biomed Phys Eng Express* **5**, 045016 (2019).
44. Dauth, S. *et al.* Neurons derived from different brain regions are inherently different in vitro: a novel multiregional brain-on-a-chip. *J Neurophysiol* **117**, 1320–1341 (2017).
45. Virlogeux, A. *et al.* Reconstituting Corticostriatal Network on-a-Chip Reveals the Contribution of the Presynaptic Compartment to Huntington's Disease. *Cell Rep* **22**, 110–122 (2018).

46. Lassus, B. *et al.* Glutamatergic and dopaminergic modulation of cortico-striatal circuits probed by dynamic calcium imaging of networks reconstructed in microfluidic chips. *Scientific Reports* 2018 8:1 **8**, 1–11 (2018).
47. Kanagasabapathi, T. T. *et al.* An experimental approach towards the development of an in vitro cortical-thalamic co-culture model. in *Proceedings of the Annual International Conference of the IEEE Engineering in Medicine and Biology Society, EMBS* 648–651 (2011). doi:10.1109/IEMBS.2011.6090144.
48. Fantuzzo, J. A. *et al.* μ Neurocircuitry: Establishing in vitro models of neurocircuits with human neurons. *Technology (Singap World Sci)* **5**, 87 (2017).
49. Samson, A. J., Robertson, G., Zagnoni, M. & Connolly, C. N. Neuronal networks provide rapid neuroprotection against spreading toxicity. *Sci Rep* (2016) doi:10.1038/srep33746.
50. Feigin, V. L. *et al.* Global, regional, and national burden of neurological disorders, 1990–2016: a systematic analysis for the Global Burden of Disease Study 2016. *Lancet Neurol* **18**, 459 (2019).
51. DiLuca, M. & Olesen, J. The cost of brain diseases: A burden or a challenge? *Neuron* vol. 82 1205–1208 Preprint at <https://doi.org/10.1016/j.neuron.2014.05.044> (2014).
52. European Commission. Brain research. https://ec.europa.eu/info/research-and-innovation/research-area/health-research-and-innovation/brain-research_en (2020).
53. Alzheimer's Research UK. Alzheimer's Research UK. <https://www.alzheimersresearchuk.org/>.
54. Alzheimer's Research UK. Dementia Statistics Hub. <https://www.dementiastatistics.org/>.
55. Deture, M. A. & Dickson, D. W. The neuropathological diagnosis of Alzheimer's disease. *Molecular Neurodegeneration* 2019 14:1 **14**, 1–18 (2019).
56. Kametani, F. & Hasegawa, M. Reconsideration of amyloid hypothesis and tau hypothesis in Alzheimer's disease. *Frontiers in Neuroscience* vol. 12 Preprint at <https://doi.org/10.3389/fnins.2018.00025> (2018).
57. Busche, M. A. & Hyman, B. T. Synergy between amyloid- β and tau in Alzheimer's disease. *Nature Neuroscience* 2020 23:10 **23**, 1183–1193 (2020).
58. Parkinson's UK. The prevalence and incidence of Parkinson's in the UK. (2017).
59. Rocca, W. A. The burden of Parkinson's disease: a worldwide perspective. *The Lancet Neurology* vol. 17 928–929 Preprint at [https://doi.org/10.1016/S1474-4422\(18\)30355-7](https://doi.org/10.1016/S1474-4422(18)30355-7) (2018).
60. Raza, C., Anjum, R. & Shakeel, N. ul A. Parkinson's disease: Mechanisms, translational models and management strategies. *Life Sciences* vol. 226 77–90 Preprint at <https://doi.org/10.1016/j.lfs.2019.03.057> (2019).
61. Pan, L., Meng, L., He, M. & Zhang, Z. Tau in the Pathophysiology of Parkinson's Disease. *Journal of Molecular Neuroscience* 2021 71:11 **71**, 2179–2191 (2021).
62. Recasens, A. & Dehay, B. Alpha-synuclein spreading in Parkinson's disease. *Frontiers in Neuroanatomy* vol. 8 Preprint at <https://doi.org/10.3389/fnana.2014.00159> (2014).
63. Stafstrom, C. E. & Carmant, L. Seizures and Epilepsy: An Overview for Neuroscientists. *Cold Spring Harb Perspect Med* **5**, a022426 (2015).
64. Pressler, R. M. *et al.* The ILAE classification of seizures and the epilepsies: Modification for seizures in the neonate. Position paper by the ILAE Task Force on Neonatal Seizures. *Epilepsia* **00**, 1–14 (2021).
65. Epilepsy Research UK. Epilepsy Statistics. <https://epilepsyresearch.org.uk/about-epilepsy/epilepsy-statistics/>.
66. Ellis, C. A., Petrovski, S. & Berkovic, S. F. Epilepsy genetics: clinical impacts and biological insights. *Lancet Neurol* **19**, 93–100 (2020).
67. Gribkoff, V. K. & Kaczmarek, L. K. The Need for New Approaches in CNS Drug Discovery: Why Drugs Have Failed, and What Can Be Done to Improve Outcomes HHS Public Access. *Neuropharmacology* **120**, 11–19 (2017).

68. Miller, G. Is Pharma Running Out of Brainy Ideas? *Science* (1979) **329**, 502–504 (2010).
69. Khachaturian, Z. S. 40 Years of Alzheimer’s Research Failure: Now What? | MedPage Today. *MedPage Today* <https://www.medpagetoday.com/neurology/alzheimersdisease/75075> (2018).
70. Luengo-Fernandez, R., Leal, J. & Gray, A. UK research spend in 2008 and 2012: comparing stroke, cancer, coronary heart disease and dementia. *BMJ Open* **5**, e006648 (2015).
71. Cummings, J., Lee, G., Zhong, K., Fonseca, J. & Taghva, K. Alzheimer’s disease drug development pipeline: 2021. *Alzheimer’s & Dementia: Translational Research & Clinical Interventions* **7**, e12179 (2021).
72. Marucci, G. *et al.* Efficacy of acetylcholinesterase inhibitors in Alzheimer’s disease. *Neuropharmacology* **190**, 108352 (2021).
73. Sharma, K. Cholinesterase inhibitors as Alzheimer’s therapeutics. *Mol Med Rep* **20**, 1479 (2019).
74. Ferreira-Vieira, T. H., Guimaraes, I. M., Silva, F. R. & Ribeiro, F. M. Alzheimer’s Disease: Targeting the Cholinergic System. *Curr Neuropharmacol* **14**, 101 (2016).
75. Pardridge, W. M. The blood-brain barrier: Bottleneck in brain drug development. *NeuroRx* **2**, 3–14 (2005).
76. Whelan, R., Hargaden, G. C. & Knox, A. J. S. Modulating the Blood–Brain Barrier: A Comprehensive Review. *Pharmaceutics* **13**, (2021).
77. Ballabh, P., Braun, A. & Nedergaard, M. The blood-brain barrier: An overview: Structure, regulation, and clinical implications. *Neurobiology of Disease* vol. 16 1–13 Preprint at <https://doi.org/10.1016/j.nbd.2003.12.016> (2004).
78. Daneman, R. & Prat, A. The blood–brain barrier. *Cold Spring Harb Perspect Biol* **7**, (2015).
79. Wong, A. D. *et al.* The blood-brain barrier: An engineering perspective. *Front Neuroeng* **0**, 7 (2013).
80. Banks, W. A. Characteristics of compounds that cross the blood-brain barrier. in *BMC Neurology* vol. 9 S3 (BioMed Central, 2009).
81. Bagchi, S. *et al.* In-vitro blood-brain barrier models for drug screening and permeation studies: An overview. *Drug Design, Development and Therapy* vol. 13 3591–3605 Preprint at <https://doi.org/10.2147/DDDT.S218708> (2019).
82. Prabhakarparandian, B. *et al.* SyM-BBB: A microfluidic blood brain barrier model. *Lab Chip* **13**, 1093–1101 (2013).
83. Abbott, N. J., Patabendige, A. A. K., Dolman, D. E. M., Yusof, S. R. & Begley, D. J. Structure and function of the blood–brain barrier. *Neurobiol Dis* **37**, 13–25 (2010).
84. Zhang, J. Basic Neural Units of the Brain: Neurons, Synapses and Action Potential. *arXiv Preprint* at (2019).
85. Colicos, M. A. & Syed, N. I. Neuronal networks and synaptic plasticity: Understanding complex system dynamics by interfacing neurons with silicon technologies. *Journal of Experimental Biology* vol. 209 2312–2319 Preprint at <https://doi.org/10.1242/jeb.02163> (2006).
86. Ressler, K. J. & Mayberg, H. S. Targeting abnormal neural circuits in mood and anxiety disorders: From the laboratory to the clinic. *Nature Neuroscience* vol. 10 1116–1124 Preprint at <https://doi.org/10.1038/nn1944> (2007).
87. Caban, A. *et al.* Filling the gap in CNS drug development: evaluation of the role of drug repurposing. <https://doi.org/10.1080/20016689.2017.1299833> **5**, 1299833 (2017).
88. Zhao, Y., Demirci, U., Chen, Y. & Chen, P. Multiscale brain research on a microfluidic chip. *Lab on a Chip* vol. 20 1531–1543 Preprint at <https://doi.org/10.1039/c9lc01010f> (2020).

89. Fisher, E. M. C. & Bannerman, D. M. Mouse models of neurodegeneration: Know your question, know your mouse. *Science Translational Medicine* vol. 11 Preprint at <https://doi.org/10.1126/scitranslmed.aag1818> (2019).
90. Ransohoff, R. M. All (animal) models (of neurodegeneration) are wrong. Are they also useful? *Journal of Experimental Medicine* **215**, 2955–2958 (2018).
91. Cummings, J. L., Morstorf, T. & Zhong, K. Alzheimer’s disease drug-development pipeline: Few candidates, frequent failures. *Alzheimers Res Ther* **6**, (2014).
92. Booth, R. & Kim, H. Characterization of a microfluidic in vitro model of the blood-brain barrier (μ BBB). *Lab Chip* **12**, 1784–1792 (2012).
93. Mullard, A. 2020 FDA drug approvals. *Nature reviews. Drug discovery* vol. 20 85–90 Preprint at <https://doi.org/10.1038/d41573-021-00002-0> (2021).
94. Pardridge, W. M. The blood-brain barrier: Bottleneck in brain drug development. *NeuroRx* **2**, 3–14 (2005).
95. Zeng, X. *et al.* Concise Review: Modeling Central Nervous System Diseases Using Induced Pluripotent Stem Cells. *Stem Cells Transl Med* **3**, 1418–1428 (2014).
96. Li, L., Chao, J. & Shi, Y. Modeling neurological diseases using iPSC-derived neural cells: iPSC modeling of neurological diseases. *Cell Tissue Res* **371**, 143–151 (2018).
97. de Leeuw, S. M. *et al.* Increased maturation of iPSC-derived neurons in a hydrogel-based 3D culture. *J Neurosci Methods* **360**, 109254 (2021).
98. Lines, G., Casey, J. M., Preza, E. & Wray, S. Modelling frontotemporal dementia using patient-derived induced pluripotent stem cells. *Molecular and Cellular Neuroscience* **109**, 103553 (2020).
99. Drouin-Ouellet, J., Piracs, K., Barker, R. A., Jakobsson, J. & Parmar, M. Direct neuronal reprogramming for disease modeling studies using patient-derived neurons: What have we learned? *Front Neurosci* **11**, 530 (2017).
100. Yi, B., Xu, Q. & Liu, W. An overview of substrate stiffness guided cellular response and its applications in tissue regeneration. *Bioact Mater* **15**, 82–102 (2022).
101. Jiang, X. *et al.* Cell Growth in Response to Mechanical Stiffness is Affected by Neuron-Astroglia Interactions. *Open Neurosci J* **1**, 7–14 (2007).
102. Smith, L. R., Cho, S. & Discher, D. E. Stem cell differentiation is regulated by extracellular matrix mechanics. *Physiology* **33**, 16–25 (2018).
103. Lancaster, M. A. & Huch, M. Disease modelling in human organoids. *DMM Disease Models and Mechanisms* **12**, (2019).
104. Wray, S. Modelling neurodegenerative disease using brain organoids. *Semin Cell Dev Biol* **111**, 60–66 (2021).
105. Koo, B., Choi, B., Park, H. & Yoon, K. J. Past, Present, and Future of Brain Organoid Technology. *Mol Cells* **42**, 617 (2019).
106. Hyun, I., Scharf-Deering, J. C. & Lunshof, J. E. Ethical issues related to brain organoid research. *Brain Res* **1732**, 146653 (2020).
107. Millet, L. J. & Gillette, M. U. New perspectives on neuronal development via microfluidic environments. *Trends Neurosci* **35**, 752–761 (2012).
108. Holloway, P. M. *et al.* Advances in microfluidic in vitro systems for neurological disease modeling. *Journal of Neuroscience Research* vol. 99 1276–1307 Preprint at <https://doi.org/10.1002/jnr.24794> (2021).
109. Moutin, E. *et al.* Procedures for Culturing and Genetically Manipulating Murine Hippocampal Postnatal Neurons. *Front Synaptic Neurosci* **12**, 19 (2020).
110. Grabrucker, A., Vaida, B., Bockmann, J. & Boeckers, T. M. Synaptogenesis of hippocampal neurons in primary cell culture. *Cell Tissue Res* **338**, 333–341 (2009).
111. Bradley, J. A., Luithardt, H. H., Metea, M. R. & Strock, C. J. In Vitro Screening for Seizure Liability Using Microelectrode Array Technology. *Toxicological Sciences* **163**, 240–253 (2018).

112. Pyka, M., Busse, C., Seidenbecher, C., Gundelfinger, E. D. & Faissner, A. Astrocytes are crucial for survival and maturation of embryonic hippocampal neurons in a neuron-glia cell-insert coculture assay. *Synapse* **65**, 41–53 (2011).
113. Bond, A. M. *et al.* Differential Timing and Coordination of Neurogenesis and Astrogenesis in Developing Mouse Hippocampal Subregions. *Brain Sci* **10**, 1–14 (2020).
114. Grainger, A. I. *et al.* In vitro models for seizure-liability testing using induced pluripotent stem cells. *Front Neurosci* **12**, 590 (2018).
115. Chiu, D. T. *et al.* Small but Perfectly Formed? Successes, Challenges, and Opportunities for Microfluidics in the Chemical and Biological Sciences. *Chem* vol. 2 201–223 Preprint at <https://doi.org/10.1016/j.chempr.2017.01.009> (2017).
116. Soe, A. K., Nahavandi, S. & Khoshmanesh, K. Neuroscience goes on a chip. *Biosensors and Bioelectronics* vol. 35 1–13 Preprint at <https://doi.org/10.1016/j.bios.2012.02.012> (2012).
117. Bhatt, G. *et al.* Microfluidics overview. in *Microfluidics for Biologists: Fundamentals and Applications* 33–83 (Springer International Publishing, 2016). doi:10.1007/978-3-319-40036-5_2.
118. Mao, X. & Huang, T. J. Microfluidic diagnostics for the developing world. *Lab on a Chip* vol. 12 1412–1416 Preprint at <https://doi.org/10.1039/c2lc90022j> (2012).
119. Fernandes, A. C., Gernaey, K. v. & Krühne, U. “Connecting worlds – a view on microfluidics for a wider application”. *Biotechnology Advances* vol. 36 1341–1366 Preprint at <https://doi.org/10.1016/j.biotechadv.2018.05.001> (2018).
120. Gale, B. K. *et al.* A review of current methods in microfluidic device fabrication and future commercialization prospects. *Inventions* Preprint at <https://doi.org/10.3390/inventions3030060> (2018).
121. Miccoli, B., Braeken, D. & Li, Y.-C. E. Brain-on-a-chip Devices for Drug Screening and Disease Modeling Applications. *Curr Pharm Des* **24**, 5419–5436 (2019).
122. Taylor, A. M. *et al.* Microfluidic multicompartiment device for neuroscience research. *Langmuir* **19**, 1551–1556 (2003).
123. Campenot, R. B. Local control of neurite development by nerve growth factor. *Proc Natl Acad Sci U S A* **74**, 4516–4519 (1977).
124. Taylor, A. M. *et al.* A microfluidic culture platform for CNS axonal injury, regeneration and transport. *Nat Methods* **2**, 599–605 (2005).
125. MacKerron, C., Robertson, G., Zagnoni, M. & Bushell, T. J. A Microfluidic Platform for the Characterisation of CNS Active Compounds. *Sci Rep* **7**, (2017).
126. Taylor, A. M., Dieterich, D. C., Ito, H. T., Kim, S. A. & Schuman, E. M. Microfluidic Local Perfusion Chambers for the Visualization and Manipulation of Synapses. *Neuron* **66**, 57–68 (2010).
127. Hosmane, S. *et al.* Toll/interleukin-1 receptor domain-containing adapter inducing interferon- β mediates microglial phagocytosis of degenerating axons. *J Neurosci* **32**, 7745–57 (2012).
128. Ristola, M. *et al.* A compartmentalized neuron-oligodendrocyte co-culture device for myelin research: design, fabrication and functionality testing. *Journal of Micromechanics and Microengineering* **29**, 065009 (2019).
129. Ionescu, A., Zahavi, E. E., Gradus, T., Ben-Yaakov, K. & Perlson, E. Compartmental microfluidic system for studying muscle–neuron communication and neuromuscular junction maintenance. *Eur J Cell Biol* **95**, 69–88 (2016).
130. Sakai, K. *et al.* Functional innervation of human induced pluripotent stem cell-derived cardiomyocytes by co-culture with sympathetic neurons developed using a microtunnel technique. *Biochem Biophys Res Commun* **494**, 138–143 (2017).
131. Zhao, X. *et al.* TRiC subunits enhance BDNF axonal transport and rescue striatal atrophy in Huntington’s disease. *Proc Natl Acad Sci U S A* **113**, E5655–64 (2016).

132. Kanagasabapathi, T. T. *et al.* Selective pharmacological manipulation of cortical-thalamic co-cultures in a dual-compartment device. *J Neurosci Methods* **214**, 1–8 (2013).
133. Kunze, A., Meissner, R., Brando, S. & Renaud, P. Co-pathological connected primary neurons in a microfluidic device for alzheimer studies. *Biotechnol Bioeng* **108**, 2241–2245 (2011).
134. Robertson, G., Bushell, T. J. & Zagnoni, M. Chemically induced synaptic activity between mixed primary hippocampal co-cultures in a microfluidic system. *Integrative Biology (United Kingdom)* **6**, 636–644 (2014).
135. Shrirao, A. B. *et al.* Microfluidic platforms for the study of neuronal injury in vitro. *Biotechnology and Bioengineering* vol. 115 815–830 Preprint at <https://doi.org/10.1002/bit.26519> (2018).
136. Tong, Z. *et al.* A microfluidic neuronal platform for neuron axotomy and controlled regenerative studies. *RSC Adv* **5**, 73457–73466 (2015).
137. Coquinco, A. *et al.* A microfluidic based in vitro model of synaptic competition. *Molecular and Cellular Neuroscience* **60**, 43–52 (2014).
138. Gladkov, A. *et al.* Design of Cultured Neuron Networks in vitro with Predefined Connectivity Using Asymmetric Microfluidic Channels. *Sci Rep* **7**, 1–14 (2017).
139. Holloway, P. M. *et al.* Asymmetric confinement for defining outgrowth directionality. *Lab Chip* **19**, 1484–1489 (2019).
140. Osaki, T., Shin, Y., Sivathanu, V., Campisi, M. & Kamm, R. D. In Vitro Microfluidic Models for Neurodegenerative Disorders. *Adv Healthc Mater* **7**, 1700489 (2018).
141. Wang, Y. *et al.* The release and trans-synaptic transmission of Tau via exosomes. *Mol Neurodegener* **12**, (2017).
142. Wu, J. W. *et al.* Neuronal activity enhances tau propagation and tau pathology in vivo. *Nat Neurosci* **19**, 1085 (2016).
143. Takeda, S. *et al.* Neuronal uptake and propagation of a rare phosphorylated high-molecular-weight tau derived from Alzheimer’s disease brain. *Nat Commun* **6**, (2015).
144. Dujardin, S. *et al.* Neuron-to-neuron wild-type Tau protein transfer through a trans-synaptic mechanism: relevance to sporadic tauopathies. *Acta Neuropathol Commun* **2**, 14 (2014).
145. Wu, J. W. *et al.* Small Misfolded Tau Species Are Internalized via Bulk Endocytosis and Anterogradely and Retrogradely Transported in Neurons. *J Biol Chem* **288**, 1856 (2013).
146. Katsikoudi, A. *et al.* Quantitative propagation of assembled human Tau from Alzheimer’s disease brain in microfluidic neuronal cultures. *Journal of Biological Chemistry* **295**, 13079–13093 (2020).
147. Lee, J. S. & Park, C. B. Microfluidic dissociation and clearance of Alzheimer’s β -amyloid aggregates. *Biomaterials* **31**, 6789–6795 (2010).
148. Kilinc, D. *et al.* Pyk2 overexpression in postsynaptic neurons blocks amyloid β 1–42-induced synaptotoxicity in microfluidic co-cultures. *Brain Commun* **2**, (2020).
149. Poon, W. W. *et al.* β -Amyloid impairs axonal BDNF retrograde trafficking. *Neurobiol Aging* **32**, 821–833 (2011).
150. Zilberzwige-Tal, S. & Gazit, E. Go with the Flow—Microfluidics Approaches for Amyloid Research. *Chem Asian J* **13**, 3437–3447 (2018).
151. Cho, H. *et al.* Microfluidic chemotaxis platform for differentiating the roles of soluble and bound amyloid- β on microglial accumulation. *Sci Rep* **3**, 1–7 (2013).
152. Cavaliere, F. *et al.* In vitro α -synuclein neurotoxicity and spreading among neurons and astrocytes using Lewy body extracts from Parkinson disease brains. *Neurobiol Dis* **103**, 101–112 (2017).
153. Fernandes, J. T. S., Chutna, O., Chu, V., Conde, J. P. & Outeiro, T. F. A novel microfluidic cell co-culture platform for the study of the molecular mechanisms of Parkinson’s disease and other synucleinopathies. *Front Neurosci* **10**, 511 (2016).

154. Dauer née Joppe, K. *et al.* Brain iron enrichment attenuates α -synuclein spreading after injection of preformed fibrils. *J Neurochem* **159**, 554–573 (2021).
155. Freundt, E. C. *et al.* Neuron-to-neuron transmission of α -synuclein fibrils through axonal transport. *Ann Neurol* **72**, 517–524 (2012).
156. Luk, K. C. *et al.* Exogenous α -synuclein fibrils seed the formation of Lewy body-like intracellular inclusions in cultured cells. *Proceedings of the National Academy of Sciences* **106**, 20051–20056 (2009).
157. Volpicelli-Daley, L. A. *et al.* Exogenous α -Synuclein Fibrils Induce Lewy Body Pathology Leading to Synaptic Dysfunction and Neuron Death. *Neuron* **72**, 57 (2011).
158. Duffy, M. F. *et al.* Quality over quantity: Advantages of using alpha-synuclein preformed fibril triggered synucleinopathy to model idiopathic Parkinson’s disease. *Front Neurosci* **12**, 621 (2018).
159. Li, X., Valadez, A. v., Zuo, P. & Nie, Z. Microfluidic 3D cell culture: Potential application for tissue-based bioassays. *Bioanalysis* vol. 4 1509–1525 Preprint at <https://doi.org/10.4155/bio.12.133> (2012).
160. Hughes, C. S., Postovit, L. M. & Lajoie, G. A. Matrigel: a complex protein mixture required for optimal growth of cell culture. *Proteomics* **10**, 1886–1890 (2010).
161. Lam, D. *et al.* Optimizing cell encapsulation condition in ECM-Collagen I hydrogels to support 3D neuronal cultures. *J Neurosci Methods* **329**, 108460 (2020).
162. Slater, K., Partridge, J. & Nandivada, H. *Tuning the Elastic Moduli of Corning® Matrigel® and Collagen I 3D Matrices by Varying the Protein Concentration Application Note.* (2018).
163. Wevers, N. R. *et al.* High-throughput compound evaluation on 3D networks of neurons and glia in a microfluidic platform. *Sci Rep* **6**, 38856 (2016).
164. Huang, C. P. *et al.* Engineering microscale cellular niches for three-dimensional multicellular co-cultures. *Lab Chip* **9**, 1740–1748 (2009).
165. Vulto, P. *et al.* Selective sample recovery of DEP-separated cells and particles by phaseguide-controlled laminar flow. *Journal of Micromechanics and Microengineering* (2006) doi:10.1088/0960-1317/16/9/013.
166. Vulto, P. *et al.* Phaseguides: A paradigm shift in microfluidic priming and emptying. *Lab Chip* **11**, 1596–1602 (2011).
167. Trietsch, S. J., Israëls, G. D., Joore, J., Hankemeier, T. & Vulto, P. Microfluidic titer plate for stratified 3D cell culture. *Lab Chip* **13**, 3548–3554 (2013).
168. Bang, S. *et al.* A Low Permeability Microfluidic Blood-Brain Barrier Platform with Direct Contact between Perfusable Vascular Network and Astrocytes. *Sci Rep* **7**, 1–10 (2017).
169. Shin, Y. *et al.* Blood–Brain Barrier Dysfunction in a 3D In Vitro Model of Alzheimer’s Disease. *Advanced Science* **6**, 1900962 (2019).
170. Adriani, G., Ma, D., Pavesi, A., Kamm, R. D. & Goh, E. L. K. A 3D neurovascular microfluidic model consisting of neurons, astrocytes and cerebral endothelial cells as a blood–brain barrier. *Lab Chip* **17**, 448–459 (2017).
171. Campisi, M. *et al.* 3D self-organized microvascular model of the human blood-brain barrier with endothelial cells, pericytes and astrocytes. *Biomaterials* **180**, 117–129 (2018).
172. Ding, Y., Shusta, E. v. & Palecek, S. P. Integrating in vitro disease models of the neurovascular unit into discovery and development of neurotherapeutics. *Curr Opin Biomed Eng* **20**, 100341 (2021).
173. Wevers, N. R. *et al.* A perfused human blood–brain barrier on-a-chip for high-throughput assessment of barrier function and antibody transport. *Fluids Barriers CNS* **15**, 23 (2018).

174. Maiuolo, J. *et al.* The “frail” brain blood barrier in neurodegenerative diseases: Role of early disruption of endothelial cell-to-cell connections. *International Journal of Molecular Sciences* vol. 19 Preprint at <https://doi.org/10.3390/ijms19092693> (2018).
175. Fayyad, M. *et al.* Generation of monoclonal antibodies against phosphorylated α -Synuclein at serine 129: Research tools for synucleinopathies. *Neurosci Lett* **725**, 134899 (2020).
176. Choi, S. H. *et al.* A three-dimensional human neural cell culture model of Alzheimer’s disease. *Nature* **515**, 274–278 (2014).
177. Rubaiy, H. N. A short guide to electrophysiology and ion channels. *Journal of Pharmacy and Pharmaceutical Sciences* **20**, 48–67 (2017).
178. Spira, M. E. & Hai, A. Multi-electrode array technologies for neuroscience and cardiology. *Nature Nanotechnology* vol. 8 83–94 Preprint at <https://doi.org/10.1038/nnano.2012.265> (2013).
179. Ullo, S. *et al.* Functional connectivity estimation over large networks at cellular resolution based on electrophysiological recordings and structural prior. *Front Neuroanat* **8**, 137 (2014).
180. Moutaux, E., Charlot, B., Genoux, A., Saudou, F. & Cazorla, M. An integrated microfluidic/microelectrode array for the study of activity-dependent intracellular dynamics in neuronal networks. *Lab Chip* **18**, 3425–3435 (2018).
181. Moutaux, E. *et al.* AN INTEGRATED MICROELECTRODE ARRAY AND MICROFLUIDIC PLATFORM FOR STIMULATING AND RECORDING RECONSTRUCTED NEURONAL NETWORKS. <https://hal.archives-ouvertes.fr/hal-01692984> (2017).
182. Biffi, E. *et al.* A microfluidic platform for controlled biochemical stimulation of twin neuronal networks. *Biomicrofluidics* **6**, 24106–2410610 (2012).
183. Bruno, G. *et al.* Microfluidic Multielectrode Arrays for Spatially Localized Drug Delivery and Electrical Recordings of Primary Neuronal Cultures. *Front Bioeng Biotechnol* **8**, (2020).
184. Liu, J., Sternberg, A. R., Ghiasvand, S. & Berdichevsky, Y. Epilepsy-on-a-chip System for Antiepileptic Drug Discovery. *IEEE Trans Biomed Eng* **66**, 1231 (2019).
185. Hamad, M. I. K., Krause, M. & Wahle, P. Improving AM ester calcium dye loading efficiency. *J Neurosci Methods* **240**, 48–60 (2015).
186. AAT Bioquest. What is an AM ester? <https://www.aatbio.com/resources/faq-frequently-asked-questions/What-is-an-AM-ester> (2020).
187. Paterson, K., Zanivan, S., Glasspool, R., Coffelt, S. B. & Zagnoni, M. Microfluidic technologies for immunotherapy studies on solid tumours. *Lab Chip* **21**, 2306–2329 (2021).
188. Ortseifen, V., Viefhues, M., Wobbe, L. & Grünberger, A. Microfluidics for Biotechnology: Bridging Gaps to Foster Microfluidic Applications. *Front Bioeng Biotechnol* **8**, 1324 (2020).
189. Mathur, L., Ballinger, M., Utharala, R. & Merten, C. A. Microfluidics as an Enabling Technology for Personalized Cancer Therapy. *Small* **16**, (2020).
190. Mark, D., Haeberle, S., Roth, G., Stetten, F. von & Zengerle, R. Microfluidic lab-on-a-chip platforms: Requirements, characteristics and applications. *Chem Soc Rev* **39**, 1153–1182 (2010).
191. Sackmann, E. K., Fulton, A. L. & Beebe, D. J. The present and future role of microfluidics in biomedical research. *Nature* vol. 507 181–189 Preprint at <https://doi.org/10.1038/nature13118> (2014).
192. Dekker, S. *et al.* Standardized and modular microfluidic platform for fast Lab on Chip system development. *Sens Actuators B Chem* **272**, 468–478 (2018).
193. Nie, J. *et al.* 3D printed Lego® -like modular microfluidic devices based on capillary driving. *Biofabrication* **10**, 035001 (2018).

194. Abhyankar, V. v., Wu, M., Koh, C. Y. & Hatch, A. v. A reversibly sealed, easy access, modular (SEAM) microfluidic architecture to establish in vitro tissue interfaces. *PLoS One* **11**, e0156341 (2016).
195. Bhargava, K. C., Thompson, B. & Malmstadt, N. Discrete elements for 3D microfluidics. *Proc Natl Acad Sci U S A* **111**, 15013–8 (2014).
196. Shang, W., Chen, C. Y., Lo, K., Payne, G. F. & Bentley, W. E. Chip modularity enables molecular information access from organ-on-chip devices with quality control. *Sens Actuators B Chem* **295**, 30–39 (2019).
197. Hernández Vera, R., O’Callaghan, P., Fatsis-Kavalopoulos, N. & Kreuger, J. Modular microfluidic systems cast from 3D-printed molds for imaging leukocyte adherence to differentially treated endothelial cultures. *Sci Rep* **9**, 11321 (2019).
198. Vittayarukskul, K. & Lee, A. P. A truly Lego®-like modular microfluidics platform. *Journal of Micromechanics and Microengineering* **27**, (2017).
199. Langelier, S. M. *et al.* Flexible casting of modular self-aligning microfluidic assembly blocks. *Lab Chip* **11**, 1679–1687 (2011).
200. Xie, X., Maharjan, S., Liu, S., Zhang, Y. S. & Livermore, C. A modular, reconfigurable microfabricated assembly platform for microfluidic transport and multitype cell culture and drug testing. *Micromachines (Basel)* **11**, 2 (2020).
201. Song, R., Abbasi, M. S. & Lee, J. Fabrication of 3D printed modular microfluidic system for generating and manipulating complex emulsion droplets. *Microfluid Nanofluidics* **23**, 92 (2019).
202. Owens, C. E. & Hart, A. J. High-precision modular microfluidics by micromilling of interlocking injection-molded blocks. *Lab Chip* **18**, 890–901 (2018).
203. Rhee, M. & Burns, M. A. Microfluidic assembly blocks. *Lab Chip* **8**, 1365–1373 (2008).
204. McDonald, J. C. *et al.* Fabrication of microfluidic systems in poly(dimethylsiloxane). *Electrophoresis* (2000) doi:10.1002/(SICI)1522-2683(20000101)21:1<27::AID-ELPS27>3.0.CO;2-C.
205. Venkatesh, V., Swain, N., Srinivas, G., Kumar, P. & Barshilia, H. C. Review on the machining characteristics and research prospects of conventional microscale machining operations. *Materials and Manufacturing Processes* **32**, 235–262 (2017).
206. Bhattacharjee, N., Urrios, A., Kang, S. & Folch, A. The upcoming 3D-printing revolution in microfluidics. *Lab on a Chip* vol. 16 1720–1742 Preprint at <https://doi.org/10.1039/c6lc00163g> (2016).
207. Gong, H., Bickham, B. P., Woolley, A. T. & Nordin, G. P. Custom 3D printer and resin for 18 μm \times 20 μm microfluidic flow channels. *Lab Chip* **17**, 2899–2909 (2017).
208. Sung, J. H. *et al.* Recent advances in body-on-a-chip systems. *Anal Chem* **91**, 330 (2019).
209. Kimura, H., Sakai, Y. & Fujii, T. Organ/body-on-a-chip based on microfluidic technology for drug discovery. *Drug Metab Pharmacokinet* **33**, 43–48 (2018).
210. Dehne, E. M. & Marx, U. Human body-on-a-chip systems. *Organ-on-a-chip: Engineered Microenvironments for Safety and Efficacy Testing* 429–439 (2020) doi:10.1016/B978-0-12-817202-5.00013-9.
211. Skardal, A. *et al.* Multi-tissue interactions in an integrated three-tissue organ-on-a-chip platform. *Sci Rep* **7**, (2017).
212. Xiao, S. *et al.* A microfluidic culture model of the human reproductive tract and 28-day menstrual cycle. *Nat Commun* **8**, (2017).
213. Sung, J. H., Kam, C. & Shuler, M. L. A microfluidic device for a pharmacokinetic-pharmacodynamic (PK-PD) model on a chip. *Lab Chip* **10**, 446–455 (2010).
214. Coppeta, J. R. *et al.* A Portable and Reconfigurable Multi-Organ Platform for Drug Development with Onboard Microfluidic Flow Control. *Lab Chip* **17**, 134 (2016).
215. Miller, P. G. & Shuler, M. L. Design and demonstration of a pumpless 14 compartment microphysiological system. *Biotechnol Bioeng* **113**, 2213–2227 (2016).

216. Zhang, Y. S. *et al.* Multisensor-integrated organs-on-chips platform for automated and continual in situ monitoring of organoid behaviors. *Proc Natl Acad Sci U S A* **114**, E2293–E2302 (2017).
217. Edington, C. D. *et al.* Interconnected Microphysiological Systems for Quantitative Biology and Pharmacology Studies. *Scientific Reports* 2018 8:1 **8**, 1–18 (2018).
218. Katzenberg, F. Plasma-bonding of poly(dimethylsiloxane) to glass. *e-Polymers* (2014) doi:10.1515/epoly.2005.5.1.638.
219. Duffy, D. C., McDonald, J. C., Schueller, O. J. A. & Whitesides, G. M. Rapid prototyping of microfluidic systems in poly(dimethylsiloxane). *Anal Chem* (1998) doi:10.1021/ac980656z.
220. Strober, W. Trypan blue exclusion test of cell viability. *Current protocols in immunology / edited by John E. Coligan ... [et al.] Appendix 3*, (2001).
221. Chen, Y. *et al.* Engineering synucleinopathy-resistant human dopaminergic neurons by CRISPR-mediated deletion of the SNCA gene. *European Journal of Neuroscience* **49**, 510–524 (2019).
222. Lema, C., Varela-Ramirez, A. & Aguilera, R. J. Differential nuclear staining assay for high-throughput screening to identify cytotoxic compounds. *Curr Cell Biochem* **1**, 1–14 (2011).
223. Schindelin, J. *et al.* Fiji: an open-source platform for biological-image analysis. *Nature Methods* 2012 9:7 **9**, 676–682 (2012).
224. Mangan, P. S. & Kapur, J. Factors Underlying Bursting Behavior in a Network of Cultured Hippocampal Neurons Exposed to Zero Magnesium. *J Neurophysiol* **91**, 946–957 (2004).
225. Johnson, S. E., Hudson, J. L. & Kapur, J. Synchronization of action potentials during low-magnesium-induced bursting. *J Neurophysiol* **113**, 2461–2470 (2015).
226. Mele, M. *et al.* Transient incubation of cultured hippocampal neurons in the absence of magnesium induces rhythmic and synchronized epileptiform-like activity. *Scientific Reports* 2021 11:1 **11**, 1–14 (2021).
227. Nielsen, J. B. *et al.* Microfluidics: Innovations in Materials and Their Fabrication and Functionalization. *Anal Chem* **92**, 150 (2020).
228. Ren, K., Zhou, J. & Wu, H. Materials for Microfluidic Chip Fabrication. *Acc Chem Res* **46**, 2396–2406 (2013).
229. Wasay, A. & Sameoto, D. Gecko gaskets for self-sealing and high-strength reversible bonding of microfluidics. *Lab Chip* (2015) doi:10.1039/C5LC00342C.
230. Anwar, K., Han, T. & Kim, S. M. Reversible sealing techniques for microdevice applications. *Sensors and Actuators, B: Chemical* Preprint at <https://doi.org/10.1016/j.snb.2010.11.002> (2011).
231. Thompson, C. S. & Abate, A. R. Adhesive-based bonding technique for PDMS microfluidic devices. *Lab Chip* **13**, 632–635 (2013).
232. Czech, Z. & Kowalczyk, A. Pressure-Sensitive adhesives. in *Adhesives: Types, Mechanics and Applications* (2011). doi:10.1016/b978-044451140-9/50011-1.
233. Serra, M. *et al.* A simple and low-cost chip bonding solution for high pressure, high temperature and biological applications. *Lab Chip* **17**, 629–634 (2017).
234. Walsh, D. I., Kong, D. S., Murthy, S. K. & Carr, P. A. Enabling Microfluidics: from Clean Rooms to Makerspaces. *Trends in Biotechnology* vol. 35 383–392 Preprint at <https://doi.org/10.1016/j.tibtech.2017.01.001> (2017).
235. Kratz, S. R. A. *et al.* Characterization of four functional biocompatible pressure-sensitive adhesives for rapid prototyping of cell-based lab-on-a-chip and organ-on-a-chip systems. *Sci Rep* **9**, (2019).
236. Venzac, B. *et al.* PDMS Curing Inhibition on 3D-Printed Molds: Why? Also, How to Avoid It? *Anal Chem* **93**, 7180–7187 (2021).
237. Zhang, W. *et al.* PMMA/PDMS valves and pumps for disposable microfluidics. *Lab Chip* **9**, 3088–3094 (2009).

238. Tan, H. Y., Loke, W. K. & Nguyen, N. T. A reliable method for bonding polydimethylsiloxane (PDMS) to polymethylmethacrylate (PMMA) and its application in micropumps. *Sens Actuators B Chem* **151**, 133–139 (2010).
239. Grienberger, C. & Konnerth, A. Imaging Calcium in Neurons. *Neuron* vol. 73 862–885 Preprint at <https://doi.org/10.1016/j.neuron.2012.02.011> (2012).
240. Kawamoto, E. M., Vivar, C. & Camandola, S. Physiology and pathology of calcium signaling in the brain. *Front Pharmacol* **3 APR**, (2012).
241. Wang, Z. K., Zheng, H. Y., Lim, R. Y. H., Wang, Z. F. & Lam, Y. C. Improving surface smoothness of laser-fabricated microchannels for microfluidic application. *Journal of Micromechanics and Microengineering* **21**, 095008 (2011).
242. Charier, D. *et al.* Memantine plus vitamin d prevents axonal degeneration caused by lysed blood. *ACS Chem Neurosci* **6**, 393–397 (2015).
243. Sauer, B. M., Schmalstieg, W. F. & Howe, C. L. Axons are injured by antigen-specific CD8+ T cells through a MHC class I- and granzyme B-dependent mechanism. *Neurobiol Dis* **59**, 194–205 (2013).
244. Lerman, M. J., Lembong, J., Muramoto, S., Gillen, G. & Fisher, J. P. The Evolution of Polystyrene as a Cell Culture Material. *Tissue Eng Part B Rev* **24**, 359–372 (2018).
245. Figura, D. & Bartel, J. Fabrication of High Aspect Ratio SU-8 Structures Using UV Lithography and Megasonic-Enhanced Development. *ECS Trans* **25**, 29–35 (2010).
246. Johnson, D., Goettert, J., Singh, V. & Yemane, D. SUEX for High Aspect Ratio Micro-Nanofluidic Applications. *TechConnect Briefs* **2**, 404–407 (2012).
247. Kim, J. J. K., al Thuwaini, H. & Almuslem, M. Photolithography of SU-8 microtowers for a 100-turn, 3-D toroidal microinductor. *Micro and Nano Systems Letters* **6**, 1–9 (2018).
248. Sticker, D., Rothbauer, M., Lechner, S., Hehenberger, M. T. & Ertl, P. Multi-layered, membrane-integrated microfluidics based on replica molding of a thiol–ene epoxy thermoset for organ-on-a-chip applications. *Lab Chip* **15**, 4542–4554 (2015).
249. Bastiaens, A., Frimat, J.-P., van Nunen, T. & Luttge, R. Exploiting nanogroove-induced cell culture anisotropy to advance in vitro brain models COLLECTIONS ARTICLES YOU MAY BE INTERESTED IN Exploiting nanogroove-induced cell culture anisotropy to advance in vitro brain models. *J. Vac. Sci. Technol. B* **37**, 61802 (2019).
250. Gökaltun, A., Kang, Y. B. (Abraham), Yarmush, M. L., Usta, O. B. & Asatekin, A. Simple Surface Modification of Poly(dimethylsiloxane) via Surface Segregating Smart Polymers for Biomicrofluidics. *Scientific Reports 2019 9:1* **9**, 1–14 (2019).
251. Trantidou, T., Elani, Y., Parsons, E. & Ces, O. Hydrophilic surface modification of PDMS for droplet microfluidics using a simple, quick, and robust method via PVA deposition. *Microsystems & Nanoengineering 2017 3:1* **3**, 1–9 (2017).
252. Prasanna, P. *et al.* Microfluidic Platforms to Unravel Mysteries of Alzheimer’s Disease: How Far Have We Come? *Life 2021, Vol. 11, Page 1022* **11**, 1022 (2021).
253. Park, J., Koito, H., Li, J. & Han, A. Multi-Compartment Neuron-Glia Co-culture Platform for Localized CNS Axon-glia Interaction Study. *Lab Chip* **12**, 3296 (2012).
254. Gu, R. *et al.* Probing the Bi-directional Interaction Between Microglia and Gliomas in a Tumor Microenvironment on a Microdevice. *Neurochem Res* **42**, 1478–1487 (2017).
255. Hyun Sung Park, Su Liu, McDonald, J., Thakor, N. & In Hong Yang. Neuromuscular junction in a microfluidic device. in *2013 35th Annual International Conference of the IEEE Engineering in Medicine and Biology Society (EMBC)* 2833–2835 (IEEE, 2013). doi:10.1109/EMBC.2013.6610130.
256. Southam, K. A., King, A. E., Blizzard, C. A., McCormack, G. H. & Dickson, T. C. Microfluidic primary culture model of the lower motor neuron–neuromuscular junction circuit. *J Neurosci Methods* **218**, 164–169 (2013).

257. Osaki, T., Uzel, S. G. M. & Kamm, R. D. On-chip 3D neuromuscular model for drug screening and precision medicine in neuromuscular disease. *Nat Protoc* **15**, 421–449 (2020).
258. de Jongh, R., Spijkers, X. M., Pasteuning-Vuhman, S., Vulto, P. & Pasterkamp, R. J. Neuromuscular junction-on-a-chip: ALS disease modeling and read-out development in microfluidic devices. *J Neurochem* **157**, 393–412 (2021).
259. Dittlau, K. S. *et al.* Generation of Human Motor Units with Functional Neuromuscular Junctions in Microfluidic Devices. *JoVE (Journal of Visualized Experiments)* **2021**, e62959 (2021).
260. Takeuchi, A. *et al.* Device for co-culture of sympathetic neurons and cardiomyocytes using microfabrication. *Lab Chip* **11**, 2268 (2011).
261. Kilinc, D. *et al.* Wallerian-like degeneration of central neurons after synchronized and geometrically registered mass axotomy in a three-compartmental microfluidic chip. *Neurotox Res* **19**, 149–161 (2011).
262. Deleglise, B. *et al.* Synapto-Protective Drugs Evaluation in Reconstructed Neuronal Network. *PLoS One* (2013) doi:10.1371/journal.pone.0071103.
263. Koo, Y., Hawkins, B. T. & Yun, Y. Three-dimensional (3D) tetra-culture brain on chip platform for organophosphate toxicity screening. *Sci Rep* **8**, 2841 (2018).
264. Nikolaev, M. v., Magazanik, L. G. & Tikhonov, D. B. Influence of external magnesium ions on the NMDA receptor channel block by different types of organic cations. *Neuropharmacology* **62**, 2078–2085 (2012).
265. Volpicelli-Daley, L. A., Luk, K. C. & Lee, V. M. Y. Addition of exogenous α -Synuclein Pre-formed fibrils to Primary Neuronal Cultures to seed recruitment of endogenous α -Synuclein to Lewy body and Lewy Neurite-like aggregates. *Nat Protoc* **9**, 2135 (2014).
266. Robertson, G. Development of microfluidic systems for studying functional connectivity between in vitro neuronal co-cultures. (2015) doi:10.48730/414E-6E53.
267. Sombati, S. & DeLorenzo, R. J. Recurrent spontaneous seizure activity in hippocampal neuronal networks in culture. *J Neurophysiol* **73**, 1706–1711 (1995).
268. McAlary, L., Plotkin, S. S., Yerbury, J. J. & Cashman, N. R. Prion-Like Propagation of Protein Misfolding and Aggregation in Amyotrophic Lateral Sclerosis. *Front Mol Neurosci* **12**, 262 (2019).
269. Neto, E. *et al.* Compartmentalized microfluidic platforms: The unrivaled breakthrough of in vitro tools for neurobiological research. *Journal of Neuroscience* **36**, 11573–11584 (2016).
270. Temiz, Y., Lovchik, R. D., Kaigala, G. v. & Delamarche, E. Lab-on-a-chip devices: How to close and plug the lab? *Microelectron Eng* **132**, 156–175 (2015).
271. Pereiro, I., Fomitcheva Khartchenko, A., Petrini, L. & Kaigala, G. v. Nip the bubble in the bud: a guide to avoid gas nucleation in microfluidics. *Lab Chip* **19**, 2296–2314 (2019).
272. Sung, J. H. & Shuler, M. L. Prevention of air bubble formation in a microfluidic perfusion cell culture system using a microscale bubble trap. *Biomed Microdevices* **11**, 731–738 (2009).
273. Wang, Y. *et al.* Systematic Prevention of Bubble Formation and Accumulation for Long-Term Culture of Pancreatic Islet Cells in Microfluidic Device. *Biomed Microdevices* **14**, 419 (2012).
274. Zheng, W., Wang, Z., Zhang, W. & Jiang, X. A simple PDMS-based microfluidic channel design that removes bubbles for long-term on-chip culture of mammalian cells. *Lab Chip* **10**, 2906–2910 (2010).
275. Hagemeyer, B., Zechall, F. & Stelzle, M. Towards plug and play filling of microfluidic devices by utilizing networks of capillary stop valves. *Biomicrofluidics* **8**, (2014).

276. Hallinan, G. I., Lopez, D. M., Vargas-Caballero, M., West, J. & Deinhardt, K. Co-culture of Murine Neurons Using a Microfluidic Device for The Study of Tau Misfolding Propagation. *Bio Protoc* **10**, (2020).
277. Vit, F. F. *et al.* A modular, reversible sealing, and reusable microfluidic device for drug screening. *Anal Chim Acta* **1185**, 339068 (2021).
278. van de Wijdeven, R. *et al.* A novel lab-on-chip platform enabling axotomy and neuromodulation in a multi-nodal network. *Biosens Bioelectron* **140**, 111329 (2019).
279. Pelkonen, A. *et al.* A modular brain-on-a-chip for modelling epileptic seizures with functionally connected human neuronal networks. *Biosens Bioelectron* **168**, 112553 (2020).
280. Wang, X. *et al.* Potential applications of microfluidics based blood brain barrier (BBB)-on-chips for in vitro drug development. *Biomedicine & Pharmacotherapy* **132**, 110822 (2020).
281. Oddo, A. *et al.* Advances in Microfluidic Blood–Brain Barrier (BBB) Models. *Trends Biotechnol* **37**, 1295–1314 (2019).
282. Kolahchi, A. R. *et al.* Microfluidic-Based Multi-Organ Platforms for Drug Discovery. *Micromachines* **2016**, Vol. 7, Page 162 **7**, 162 (2016).
283. Li, Y.-T. *et al.* Real-time Monitoring of Discrete Synaptic Release Events and Excitatory Potentials within Self-reconstructed Neuromuscular Junctions. *Angewandte Chemie International Edition* **54**, 9313–9318 (2015).
284. Kim, M. H., Kim, D. & Sung, J. H. A Gut-Brain Axis-on-a-Chip for studying transport across epithelial and endothelial barriers. *Journal of Industrial and Engineering Chemistry* **101**, 126–134 (2021).
285. Raimondi, M. T., Albani, D. & Giordano, C. An Organ-On-A-Chip Engineered Platform to Study the Microbiota–Gut–Brain Axis in Neurodegeneration. *Trends Mol Med* **25**, 737–740 (2019).
286. Chesselet, M. F. & Carmichael, S. T. Animal Models of Neurological Disorders. *Neurotherapeutics* **9**, 241 (2012).
287. Cornacchia, D. & Studer, L. Back and Forth in Time: Directing Age in iPSC-Derived Lineages. *Brain Res* **1656**, 14 (2017).
288. Ramme, A. P. *et al.* Autologous induced pluripotent stem cell-derived four-organ-chip. *Future Sci OA* **5**, (2019).
289. van Meer, B. J. *et al.* Small molecule absorption by PDMS in the context of drug response bioassays. *Biochem Biophys Res Commun* **482**, 323 (2017).
290. Schneider, F., Fellner, T., Wilde, J. & Wallrabe, U. Mechanical properties of silicones for MEMS. *Journal of Micromechanics and Microengineering* **18**, 065008 (2008).
291. Sandström, N. *et al.* Reaction injection molding and direct covalent bonding of OSTE+ polymer microfluidic devices. *Journal of Micromechanics and Microengineering* **25**, 075002 (2015).
292. Li, L. *et al.* Spatiotemporally controlled and multifactor involved assay of neuronal compartment regeneration after chemical injury in an integrated microfluidics. *Anal Chem* **84**, 6444–6453 (2012).